# Physics-Based Turbulence Anisotropy Closure Including Nonlocal and Nonequilibrium Effects in Turbulent Flows

by

Peter Edward Hamlington

A dissertation submitted in partial fulfillment
of the requirements for the degree of
Doctor of Philosophy
(Aerospace Science)
in The University of Michigan
2009

Doctoral Committee:

        Professor Werner J.A. Dahm, Chair
        Professor Charles R. Doering
        Professor Wei Shyy
        Assistant Professor Matthias Ihme
        Professor Jörg Schumacher, Ilmenau University of Technology

To Barbara, my parents, and Ben.
Thank you for your love, support, and patience.

# ACKNOWLEDGEMENTS

# TABLE OF CONTENTS

# LIST OF FIGURES

# LIST OF TABLES

# CHAPTER I

# Introduction

The vast majority of fluid flows found in nature and engineering are not smooth, steady, or organized. Everything from smoke billowing from a fire to water rushing through a pipe involves highly complex motions that are seemingly impossible to understand. Such complex flow is referred to as *turbulent*, by contrast to the smooth and steady fluid behavior found in *laminar* flows. Turbulent flows are characterized by highly unsteady and chaotic fluid motions, and the underlying dynamics are dominated by nonlinear inertial processes. The Reynolds number, defined as

$$Re \equiv \frac{\rho U L}{\mu} \, ,  \tag{1.1}$$

characterizes the ratio of nonlinear inertial effects to linear viscous effects in the flow, where $\rho$ and $\mu$ are, respectively, the density and viscosity of the fluid, and $U$ and $L$ are characteristic velocity and length scales of the mechanism by which the turbulence is generated. For shear-driven turbulent flows – which comprise the majority of the flows considered in this dissertation – $U$ and $L$ are determined by the imposed mean shear. When the Reynolds number is large, the dynamics are dominated by nonlinear effects and the flow is turbulent. In addition to a wide range of natural occurrences, turbulence also plays a critical role in many practical applications, particularly within aerospace engineering. For instance, combustion processes in gas turbine engines, the sequence of shocks in supersonic jet inlets, and the flow over aircraft all involve turbulent fluid flow.

Despite the ubiquity of turbulence in nature and engineering however, prior attempts to computationally simulate turbulent flows have been notoriously problematic. The difficulty stems in large part from the wide-range of spatial scales that must be predicted in simulations of most practical problems. Energy input at the largest scales – which are typically on the order of the system geometry in many applications – cascades to smaller scales until it is dissipated as heat by viscous processes at the very small scales. The ratio of the energy input to viscous scales increases with Reynolds number as $Re^{3/4}$, and for the high Reynolds numbers found in many engineering problems the range of spatial scales can be substantial.

Some progress in simulating this wide range of scales has been made over the last several decades as computing power has increased, resulting in the increasing use of direct numeri-

cal simulations (DNS) for the study of turbulent flows. In DNS, all scales of the turbulence are calculated directly from the Navier-Stokes equations, and every year increasingly ambitious DNS studies of increasingly complex flows are undertaken. However, due to the overwhelming computational resources required for DNS of even the most basic problems – as indicated by the $Re^{9/4}$ scaling of the number of spatial grid points in such simulations – this approach is not viewed as a viable computational tool for practical engineering turbulent flow problems where the flow geometry can become quite complicated and the Reynolds number is, in nearly all instances, very large. Indeed, essentially all DNS studies to date have focused on relatively basic flows at only low to moderate Reynolds numbers, and it is unclear if DNS will ever be an option for simulations of practical aerospace applications.

As a result, computational simulations of practical problems will continue to require physically-accurate models for all – or at least some – of the scales in turbulent flows. The formulation of such models, which effectively reduce the range of scales calculated in computational simulations, has been the goal of turbulence researchers for over half a century. However, a high-fidelity, universally accurate approach has yet to be developed. The failure of existing turbulence model approaches has become particularly problematic over the last several decades, as simulations of practical applications involving turbulent fluid flow have become an increasingly important aspect of the design process for a variety of problems. For example, it is much more time- and cost-efficient to conduct computational design analyses of new aerospace propulsion systems than it is to carry out real-world manufacture and testing, which can be expensive, time-consuming, and hazardous. However, such computational analyses require physically-accurate predictions of various turbulent processes, and to date standard turbulence models have been unreliable in essentially all such simulations.

Currently the most widely-used simulation approaches are based on the Reynolds-averaged Navier-Stokes (RANS) equations, where closure of the governing equations requires a representation for the ensemble-averaged Reynolds stress anisotropy. The exact transport equation for the anisotropy is readily derived, but additional higher-order terms are introduced which prevent closure. As a result, it has been common to model these unclosed terms, or to simply model the anisotropy directly beginning either from the exact anisotropy transport equation or physical considerations. In contrast to DNS, RANS approaches only attempt to provide predictions of the mean flow and turbulence statistics, which in many cases are all that is required from simulations of practical problems. Such approaches generally provide reasonably accurate predictions of the flow statistics within a computationally-simple framework, and consequently RANS models have been common in engineering practice for several decades. Despite their popularity however, the accuracy of these approaches is limited by the fidelity of the modeled representation for the anisotropy. In many cases, physical accuracy is sacrificed in the interest of obtaining a computationally-simple closure model, resulting in generally unreliable simulations of complex problems.

In response to the inaccuracy of existing RANS approaches, large eddy simulations

(LES) have been viewed as a promising alternative for turbulent flow simulations. In such approaches only the smallest scales of the flow are modeled, and the increasing popularity of LES is due in large part to the increased accuracy that is obtained by calculating the largest scales of the flow directly. For the practical user however, the computational resources required even for LES can be prohibitive, and for many problems there remain issues concerning the physically-accurate modeling of the small scale motions. As a result, RANS approaches remain the "state of the practice" for simulating practical turbulent flow problems, due in large part to their computational simplicity. This situation is expected to continue for the foreseeable future as the complexity and ambitiousness of simulations for practical applications continue to outpace the development, and more importantly the availability, of the high-power computational resources required for DNS and LES.

There thus continues to be substantial demand, especially from the user community, for new high-fidelity, computationally-efficient turbulence closure models. In particular, physically-accurate representations for the turbulence anisotropy in strongly nonequilibrium and inhomogeneous flows are critical for obtaining reliable flow predictions in a wide range of practical applications. For example, the interaction of a shock wave impinging on a turbulent boundary layer plays a key role in the flow-field of embedded propulsion systems for next-generation supersonic and hypersonic air vehicles [15]. However, most existing turbulence models are largely incapable of capturing effects due to the rapid and large straining of the shock in the near-wall region of the flow. Inhomogeneities in the imposed mean strain rate, such as those created by the solid wall in shock-boundary layer interactions, have posed particular problems for existing approaches, since such inhomogeneities lead to spatially nonlocal effects that are difficult to predict within simple single-point model frameworks. While efforts have been made to develop closure models that account for nonlocal and nonequilibrium effects on the anisotropy, a physically-accurate and computationally-efficient solution approach has yet to be formulated.

In response to the need for novel turbulence closure strategies in complex problems, a new representation for the turbulence anisotropy that is directly aimed at providing improved predictions of nonlocal and nonequilibrium effects in turbulent flows is outlined in this dissertation. The new approach is based on fundamental considerations of turbulence physics and vortex dynamics, and is intended to provide a physically-accurate, computationally-efficient alternative to existing simulation strategies by bridging the gap between relatively inaccurate, currently popular RANS models, and more computationally-demanding LES approaches. If turbulence modeling is to continue as a common simulation strategy for practical problems over the next decade and beyond – as seems likely – then new high-fidelity closure approaches such as that developed in this dissertation will be critical for enabling the reliable computational design of next-generation aerospace applications.

## 1.1  The Reynolds-Averaged Navier-Stokes (RANS) Equations

Simulation approaches based on the RANS equations are likely to remain, for the foreseeable future at least, the primary computational design tool used by the majority of engineers for the majority of practical problems. Focusing here for purposes of clarity on incompressible turbulent flows, ensemble-averaging the continuity and momentum equations leads to the single-point RANS equations for the mean-flow velocity components $\overline{u}_i(\mathbf{x}, t)$ and kinematic pressure $\overline{p}(\mathbf{x}, t)$, namely

$$\frac{\partial \overline{u}_i}{\partial x_i} = 0 \,, \tag{1.2}$$

$$\frac{D\overline{u}_i}{Dt} = -\frac{\partial \overline{p}}{\partial x_i} + \frac{\partial}{\partial x_j}\left[2\nu \overline{S}_{ij} - \overline{u_i' u_j'}\right] \,, \tag{1.3}$$

where $D/Dt \equiv (\partial/\partial t + \overline{u}_j \partial/\partial x_j)$ denotes the mean-flow material derivative, and

$$\overline{S}_{ij} \equiv \frac{1}{2}\left(\frac{\partial \overline{u}_i}{\partial x_j} + \frac{\partial \overline{u}_j}{\partial x_i}\right) \tag{1.4}$$

is the mean strain rate tensor. The overbar in (1.2)-(1.4) and elsewhere herein is understood to be an ensemble average at location $\mathbf{x}$ and time $t$ over infinitely many realizations of the "same" turbulent flow having nominally identical initial and boundary conditions, despite the fact that this average is often implemented in practice via time or space averaging. Much of this dissertation will focus primarily on incompressible turbulent flows, with the understanding that all model developments are readily extended to transonic and supersonic flows where compressible effects on the mean flow may be important. Compressibility very seldom has a direct impact on the turbulence itself, since the turbulence Mach number $M_T \equiv u'_{rms}/a$ is typically substantially below about 0.3, where $u'_{rms}$ is the characteristic velocity of the turbulence and $a$ is the speed of sound. In such cases, compressibility effects can still be important in the mean flow, but the turbulence fluctuations are essentially incompressible. As a result, compressible effects on the evolution of the turbulence anisotropy will not be addressed herein.

Solving (1.2)-(1.4) requires a representation for the Reynolds stresses $\overline{u_i' u_j'}$ in (1.3), where primes denote fluctuations relative to the average. This stress tensor can be written in terms of its isotropic form $\frac{2}{3}k\delta_{ij}$ and the deviations from isotropy as

$$\overline{u_i' u_j'} = \frac{2}{3}k\delta_{ij} - \left(\overline{u_i' u_j'}\right)_{aniso} \,, \tag{1.5}$$

where $k \equiv \frac{1}{2}\overline{u_i' u_i'}$ is the turbulence kinetic energy. The anisotropic part $(\overline{u_i' u_j'})_{aniso}$ can be equivalently expressed in terms of the Reynolds stress anisotropy tensor

$$a_{ij} \equiv -\frac{(\overline{u_i' u_j'})_{aniso}}{k} = \frac{\overline{u_i' u_j'}}{k} - \frac{2}{3}\delta_{ij} \,, \tag{1.6}$$

4

where due to the symmetry of the tensor there are six independent components of $a_{ij}$. The closure required in (1.2)-(1.5) thus amounts to constructing a representation for the anisotropy tensor $a_{ij}$ in (1.6). It has been a major goal of fluid dynamics research for well over a century to solve the resulting 'closure problem' by developing a turbulence model that is reliably accurate over the range of conditions encountered in essentially all practical problems. As will be seen in the following, the exact transport equation for $a_{ij}$ is readily derived, although additional unclosed terms are introduced. Formulating physically-accurate representations for these terms, and then solving the subsequent modeled equation for $a_{ij}$, remains one of the greatest challenges in turbulence modeling research.

## 1.2 The Exact Anisotropy Transport Equation

From the definition of the Reynolds stress anisotropy tensor in (1.6), the exact anisotropy transport equation can be obtained from

$$\frac{Da_{ij}}{Dt} = \frac{1}{k}\left(\frac{D\overline{u_i'u_j'}}{Dt} - \frac{\overline{u_i'u_j'}}{k}\frac{Dk}{Dt}\right). \tag{1.7}$$

On the right-hand side, the transport equation for the Reynolds stress tensor $\overline{u_i'u_j'}$ can be written [24, 42, 78, 96] as

$$\frac{D\overline{u_i'u_j'}}{Dt} = P_{ij} + \Pi_{ij} - \epsilon_{ij} + D_{ij}. \tag{1.8}$$

In (1.8), $P_{ij}$ is the production tensor

$$P_{ij} \equiv -\overline{u_i'u_l'}\frac{\partial \overline{u}_j}{\partial x_l} - \overline{u_j'u_l'}\frac{\partial \overline{u}_i}{\partial x_l}, \tag{1.9}$$

$\Pi_{ij}$ is the pressure-strain rate correlation tensor given by

$$\Pi_{ij}(\mathbf{x}) \equiv \frac{2}{\rho}\overline{p'(\mathbf{x})S_{ij}'(\mathbf{x})}, \tag{1.10}$$

with the fluctuating strain rate tensor $S_{ij}'$ defined as

$$S_{ij}' \equiv \frac{1}{2}\left(\frac{\partial u_i'}{\partial x_j} + \frac{\partial u_j'}{\partial x_i}\right), \tag{1.11}$$

$\epsilon_{ij}$ is the dissipation rate tensor given by

$$\epsilon_{ij} \equiv 2\nu\overline{\frac{\partial u_i'}{\partial x_l}\frac{\partial u_j'}{\partial x_l}}, \tag{1.12}$$

and $D_{ij}$ accounts for viscous, turbulent, and pressure transport and is defined as

$$D_{ij} \equiv -\frac{\partial}{\partial x_l}\left(\overline{u'_i u'_j u'_l} + \frac{\overline{p' u_j}}{\rho}\delta_{li} + \frac{\overline{p' u'_i}}{\rho}\delta_{jl} - \nu\frac{\partial \overline{u'_i u'_j}}{\partial x_l}\right). \tag{1.13}$$

The corresponding transport equation for the turbulence kinetic energy $k$ is obtained from the trace of (1.8) as

$$\frac{Dk}{Dt} = P - \epsilon + D, \tag{1.14}$$

where $P \equiv P_{nn}/2$, $D \equiv D_{nn}/2$, $\epsilon \equiv \epsilon_{nn}/2$, and $\Pi_{nn} = 0$ in incompressible turbulence. Substituting (1.8) and (1.14) into (1.7), and employing the definition of the anisotropy tensor in (1.6), gives the exact anisotropy transport equation

$$\frac{Da_{ij}}{Dt} = -\left(\frac{P}{\epsilon} - 1\right)\frac{\epsilon}{k}a_{ij} + \frac{1}{k}\left[P_{ij} - \frac{2}{3}P\delta_{ij}\right] + \frac{1}{k}\Pi_{ij} - \frac{1}{k}\left[\epsilon_{ij} - \frac{2}{3}\epsilon\delta_{ij}\right] \tag{1.15}$$

$$+ \frac{1}{k}\left[D_{ij} - \left(a_{ij} + \frac{2}{3}\delta_{ij}\right)D\right].$$

The production term in (1.15) can be exactly written in terms of $a_{ij}$, $\overline{S}_{ij}$, and the antisymmetric part of the mean velocity gradient tensor $\overline{W}_{ij}$, defined as

$$\overline{W}_{ij} \equiv \frac{1}{2}\left(\frac{\partial \overline{u}_i}{\partial x_j} - \frac{\partial \overline{u}_j}{\partial x_i}\right), \tag{1.16}$$

to obtain the exact form

$$\left[P_{ij} - \frac{2}{3}P\delta_{ij}\right] = -\frac{4}{3}k\overline{S}_{ij} - k(a_{il}\overline{S}_{lj} + \overline{S}_{il}a_{lj} - \frac{2}{3}a_{nl}\overline{S}_{nl}\delta_{ij}) + k(a_{il}\overline{W}_{lj} - \overline{W}_{il}a_{lj}), \tag{1.17}$$

where the kinetic energy production $P$ is given by

$$P = -k\,a_{ij}\,\overline{S}_{ij}. \tag{1.18}$$

With (1.17), the transport equation in (1.15) is then written as

$$\frac{Da_{ij}}{Dt} = -\left(\frac{P}{\epsilon} - 1\right)\frac{\epsilon}{k}a_{ij} - \frac{4}{3}\overline{S}_{ij} - \left(a_{il}\overline{S}_{lj} + \overline{S}_{il}a_{lj} - \frac{2}{3}a_{nl}\overline{S}_{nl}\delta_{ij}\right) \tag{1.19}$$

$$+ \left(a_{il}\overline{W}_{lj} - \overline{W}_{il}a_{lj}\right) + \frac{1}{k}\Pi_{ij} - \frac{1}{k}\left[\epsilon_{ij} - \frac{2}{3}\epsilon\delta_{ij}\right] + \frac{1}{k}\left[D_{ij} - \left(a_{ij} + \frac{2}{3}\delta_{ij}\right)D\right].$$

In (1.19), $k$ is given by (1.14), $P$ is given by (1.18), and the remaining unclosed terms are $\epsilon_{ij}$, $D_{ij}$, and $\Pi_{ij}$. If physically-accurate closed representations for these terms can be obtained then the transport equation in (1.19) can be used to solve (1.2)-(1.4) for any flow.

## 1.3 Prior Anisotropy Closure Models

Nearly all standard approaches for modeling the anisotropy and closing (1.2)-(1.4) can be related to the exact transport equation in (1.19). In the following various prior approaches are outlined, beginning with second-order Reynolds stress transport models. These approaches model the $\epsilon_{ij}$, $D_{ij}$, and $\Pi_{ij}$ terms in (1.19) and obtain the anisotropy from solution of the subsequent closed system of partial differential equations for the six independent components of $a_{ij}$. An outline of prior two-equation linear and nonlinear eddy viscosity closure models is then provided. These models are obtained as convective equilibrium solutions to (1.19) and are overwhelmingly the most widely-used RANS models in standard engineering practice.

### 1.3.1 Second-Order Reynolds Stress Transport Models

Reynolds stress transport models are the highest commonly-used level of closure for the anisotropy, and seek to retain much of the physics contained in the exact transport equation in (1.19). The dissipation tensor $\epsilon_{ij}$, transport term $D_{ij}$, and pressure-strain correlation $\Pi_{ij}$ are the only unclosed terms in (1.19), and Reynolds stress transport models provide closed representations for each of these terms.

For high Reynolds number flow, the dissipation tensor $\epsilon_{ij}$ is concentrated at the smallest scales of the flow, which are assumed to be isotropic by the Kolmogorov hypotheses [49, 78]. As a result, the dissipation is given in nearly all Reynolds stress transport models (e.g. Refs. [51, 98]) by its isotropic form, namely

$$\epsilon_{ij} = \frac{2}{3}\epsilon\delta_{ij}\,. \tag{1.20}$$

The transport terms $D_{ij}$ and $D$ in (1.15) are typically represented using gradient-transport hypotheses (e.g. Daly and Harlow [17], Hanjalic and Launder [35], and Mellor and Herring [65]), and an overview of these prior representations is given in Ref. [99].

The only remaining unclosed term in (1.19) is thus the pressure-strain correlation $\Pi_{ij}$, defined in (1.10). Physically-accurate closures for $\Pi_{ij}$ have been the focus of turbulence researchers since the pioneering works of Chou [14] and Rotta [85, 86]. Chou proposed splitting $\Pi_{ij}$ into slow and rapid parts, denoted $\Pi_{ij}^{(s)}$ and $\Pi_{ij}^{(r)}$, respectively, as

$$\Pi_{ij} = \Pi_{ij}^{(s)} + \Pi_{ij}^{(r)}\,. \tag{1.21}$$

While the exact integral representations for both parts of $\Pi_{ij}$ are readily derived (and will be discussed in more detail in Chapter III), it has been common to express $\Pi_{ij}^{(s)}$ and $\Pi_{ij}^{(r)}$ in terms of local variables only, with little regard to the nonlocality inherent in the exact integrals for these terms.

Nearly all existing models for $\Pi_{ij}^{(s)}$ rely on insights obtained from the decay of the

anisotropy in unstrained turbulence, for example during the relaxation of grid turbulence. Rotta [86] proposed a simple linear "return-to-isotropy" model as

$$\Pi_{ij}^{(s)} = -C_1 \epsilon a_{ij} \,, \tag{1.22}$$

and in unstrained homogeneous turbulence, substitution of (1.22) into (1.19) with $\epsilon_{ij}$ given by (1.20) yields the simplified anisotropy transport equation

$$\frac{da_{ij}}{dt} = -(C_1 - 1)\frac{\epsilon}{k}a_{ij} \,, \tag{1.23}$$

resulting in decay of the anisotropy on a time scale determined by the turbulence time scale $k/\epsilon$. Sarkar and Speziale [89, 98] have argued that additional higher order quadratic terms should also be included in (1.22) to yield better agreement with experimental results, but it has been noted [99] that these terms are typically small. As a result, models for $\Pi_{ij}^{(s)}$ remain relatively simple, and the standard form in (1.22) continues to be widely used.

To date, models for $\Pi_{ij}^{(r)}$ have typically been obtained by assuming that the mean velocity gradient is spatially invariant (as in homogeneous flows), and the subsequent general form for $\Pi_{ij}^{(r)}$ that is linear in $a_{ij}$ is given by [24, 51, 96, 98]

$$\Pi_{ij}^{(r)} = C_2 k \overline{S}_{ij} - C_3 k \left( a_{il}\overline{S}_{lj} + \overline{S}_{il}a_{lj} - \frac{2}{3}a_{nl}\overline{S}_{nl}\delta_{ij} \right) + C_4 k \left( a_{il}\overline{W}_{lj} - \overline{W}_{il}a_{lj} \right) \,, \tag{1.24}$$

where all variables are evaluated locally at point $\mathbf{x}$ and time $t$. With the exception of $C_2$, which has been shown by Crow [16] to have an exact value of $C_2 = 4/5$ based on consideration of turbulence in the rapid distortion limit, the $C_i$ coefficients in (1.24) are typically not determined in a systematic manner, and are often based on comparisons with experimental or computational data.

With (1.22), the rapid pressure-strain correlation in (1.24) gives the commonly-used local homogeneous model for $\Pi_{ij}$ as

$$\Pi_{ij} = -C_1 \epsilon a_{ij} + C_2 k \overline{S}_{ij} - C_3 k \left( a_{il}\overline{S}_{lj} + \overline{S}_{il}a_{lj} - \frac{2}{3}a_{nl}\overline{S}_{nl}\delta_{ij} \right) + C_4 k \left( a_{il}\overline{W}_{lj} - \overline{W}_{il}a_{lj} \right) \,, \tag{1.25}$$

where the $C_i$ are constants that may depend on invariants of $a_{ij}$, $\overline{S}_{ij}$, and $\overline{W}_{ij}$. For the most common second-order Reynolds stress transport closures, the constants $C_i$ are taken as

$$C_1 = 1.5, \quad C_2 = 0.8, \quad C_3 = 0.875, \quad C_4 = 0.655 \,, \tag{1.26}$$

in the Launder, Reece, and Rodi (LRR) model [51], and as

$$C_1 = 0.9\frac{P}{\epsilon} + 1.7, \quad C_2 = 0.8 - 0.65\,(II_a)^{1/2}, \quad C_3 = 0.625, \quad C_4 = 0.2 \,, \tag{1.27}$$

in the Speziale, Sarkar, and Gatski (SSG) model [98], where $II_a \equiv a_{nl}a_{ln}$ is the second invariant of the anisotropy tensor. It should be noted that the SSG model typically includes an additional quadratic $a_{il}a_{lj}$ term in the slow pressure-strain correlation in (1.22), but as noted previously this term is typically small and can be neglected for most flows.

Substituting (1.20) and (1.25) into (1.19) and rearranging terms gives the conventional modeled anisotropy transport equation that forms the basis of nearly all Reynolds stress transport models, namely

$$\frac{Da_{ij}}{Dt} = -\alpha_1 \frac{\epsilon}{k} a_{ij} + \alpha_2 \overline{S}_{ij} + \alpha_3 (a_{il}\overline{S}_{lj} + \overline{S}_{il}a_{lj} - \frac{2}{3}a_{nl}\overline{S}_{nl}\delta_{ij})$$
$$-\alpha_4 \left( a_{il}\overline{W}_{lj} - \overline{W}_{il}a_{lj} \right) + \frac{1}{k} \left[ D_{ij} - \left( a_{ij} + \frac{2}{3}\delta_{ij} \right) D \right], \quad (1.28)$$

where common representations for $D_{ij}$ are summarized in [99] and the $\alpha_i$ are given by

$$\alpha_1 = \frac{P}{\epsilon} - 1 + C_1, \ \alpha_2 = \left( C_2 - \frac{4}{3} \right), \ \alpha_3 = (C_3 - 1), \ \alpha_4 = (C_4 - 1). \quad (1.29)$$

The coefficients $C_i$ in (1.29) are given by the specific choice of pressure-strain model, for example (1.26) for the LRR [51] model or (1.27) for the SSG [98] model. Thus, while the exact anisotropy transport equation in (1.19) includes unclosed dissipation, transport, and pressure-strain terms, the modeled equation given by (1.28) and (1.29) – with appropriately chosen transport equations for the turbulence kinetic energy $k$ and its dissipation rate $\epsilon$ – allows closure of (1.2)-(1.4).

In principle, the set of partial differential equations given by (1.28) and (1.29) contains all of the relevant dynamics that determines the evolution of $a_{ij}$. In practice however, the representations for $\epsilon_{ij}$ and $\Pi_{ij}$ in (1.20) and (1.25) can become inaccurate in even basic flow problems. For example, in the near-wall region of wall bounded flows the local Reynolds number can become quite small, and the high-Reynolds number isotropic representation for $\epsilon_{ij}$ in (1.20) becomes inaccurate. Moreover, the neglect of nonlocality in obtaining the purely local representation for $\Pi_{ij}$ in (1.25) poses problems in strongly inhomogeneous regions such as those found, once again, in the near-wall region of wall bounded flows, where flow properties vary rapidly in the wall-normal direction.

Perhaps more so than these physical inaccuracies however, the greatest impediment to the widespread adoption of Reynolds stress transport models has been the challenge of integrating the six coupled partial differential equations given by (1.28) – in addition to the two transport equations required for the variables $k$ and $\epsilon$ – in simulations of complex problems. Numerical integration of this set of eight equations increases the computational requirements and introduces stability issues associated with solving (1.2)-(1.4), often to such an extent that Reynolds stress transport models can be prohibitive for many practical applications.

### 1.3.2 Two-Equation Equilibrium Closure Models

By contrast to Reynolds stress transport models, the most widely used anisotropy models are obtained by assuming convective equilibrium on the left-hand side of (1.28), namely $Da_{ij}/Dt \approx 0$, as originally suggested by Pope [77] and Rodi [83]. Further neglecting the transport term $D_{ij}$, this allows the anisotropy to be obtained from (1.28) as

$$a_{ij} = \frac{\alpha_2}{\alpha_1}\frac{k}{\epsilon}\overline{S}_{ij} + \frac{\alpha_3}{\alpha_1}\frac{k}{\epsilon}(a_{il}\overline{S}_{lj} + \overline{S}_{il}a_{lj} - \frac{2}{3}a_{nl}\overline{S}_{nl}\delta_{ij}) - \frac{\alpha_4}{\alpha_1}\frac{k}{\epsilon}\left(a_{il}\overline{W}_{lj} - \overline{W}_{il}a_{lj}\right), \quad (1.30)$$

where $\alpha_1$ depends on $a_{ij}$ through $P/\epsilon$ in (1.29). As a result, (1.30) is an *implicit* algebraic expression for the anisotropy.

In both nonlinear and linear two equation eddy viscosity models, $a_{ij}$ is given by an *explicit* algebraic formulation based on (1.30). The closure is completed by specifying two additional modeled transport equations for $k$ and $\epsilon$, usually written as

$$\frac{Dk}{Dt} = P - \epsilon + \frac{\partial}{\partial x_j}\left[\left(\nu + \frac{\nu_T}{\sigma_k}\right)\frac{\partial k}{\partial x_j}\right], \quad (1.31)$$

$$\frac{D\epsilon}{Dt} = C_{\epsilon 1}P\frac{\epsilon}{k} - C_{\epsilon 2}\frac{\epsilon^2}{k} + \frac{\partial}{\partial x_j}\left[\left(\nu + \frac{\nu_T}{\sigma_\epsilon}\right)\frac{\partial \epsilon}{\partial x_j}\right], \quad (1.32)$$

where the kinetic energy production rate $P$ is given by (1.18). There have been a number of proposals for the values of the constants in (1.31) and (1.32), however standard values [52] are

$$C_{\epsilon 1} = 1.44, \quad C_{\epsilon 2} = 1.92, \quad \sigma_k = 1.0, \quad \sigma_\epsilon = 1.3. \quad (1.33)$$

It is possible (e.g. Wilcox [108]) to replace $\epsilon$ in (1.30) with the variable $\omega \sim \epsilon/k$, resulting in what are commonly known as two-equation $k$-$\omega$ models. However this modification does not introduce any additional physics in the specific closure representation for the anisotropy, and as a result this dissertation will focus primarily on the variables $k$ and $\epsilon$, with the understanding that all model developments can be readily implemented in $k$-$\omega$ frameworks.

### 1.3.2.1 Nonlinear Eddy Viscosity Models

Nonlinear eddy viscosity models seek to obtain an explicit representation for $a_{ij}$ from (1.30) while retaining much of the nonlinearity in the anisotropy evolution. As originally shown by Pope [77], if the anisotropy is written as a general nonlinear expansion in terms of $\overline{S}_{ij}$ and $\overline{W}_{ij}$ and substituted into (1.30), then it is possible to obtain an explicit closure for the anisotropy of the form

$$a_{ij} = G_1\frac{k}{\epsilon}\overline{S}_{ij} + G_2\left(\frac{k}{\epsilon}\right)^2\left[\overline{S}_{il}\overline{S}_{lj} - \frac{\delta_{ij}}{3}\overline{S}_{kl}\overline{S}_{kl}\right] + G_3\left[\overline{S}_{il}\overline{W}_{lj} - \overline{W}_{il}\overline{S}_{lj}\right], \quad (1.34)$$

where the $G_i$ coefficients are related to the $\alpha_i$ in (1.30) and typically depend on invariants of $\overline{S}_{ij}$ and $\overline{W}_{ij}$. The resulting nonlinear form in (1.34) is termed an *explicit algebraic stress model*, and is closely connected through (1.30) to the modeled transport equation for $a_{ij}$ in (1.28) and (1.29). Perhaps the most notable examples of models based on (1.34) have been obtained by Gatski and Speziale [24], Girimaji [27], and Wallin and Johansson [107], all of whom derived explicit algebraic stress models using various equilibrium assumptions.

While such nonlinear models seek to remain closely connected to the transport equation in (1.28) by relating the $G_i$ to the $\alpha_i$ coefficients, various nonlinear closures based on expansion methods and physical considerations have also been proposed. In these models no rigorous connection to the implicit equation in (1.30) or the transport equation in (1.28) is attempted, and the anisotropy is simply represented as a tensorial expansion in powers of $\overline{S}_{ij}$ and $\overline{W}_{ij}$. The expansion coefficients are then determined by physical considerations or other means, often through comparison with experimental and DNS data. Yoshizawa [112], Speziale [95], Rubinstein and Barton [88], Taulbee [102], and Yakhot, Orszag and coworkers [111] have derived nonlinear models based on various expansion methods, and the resulting models are distinct from explicit algebraic stress models due to their disconnect from the anisotropy transport equation given exactly by (1.19), or in modeled form by (1.28).

Regardless of the derivation method however, essentially all nonlinear eddy viscosity models express the anisotropy in terms of the *local instantaneous* mean strain and rotation rate tensors only, and thus are fundamentally equilibrium closure representations. Moreover, these models do not account for nonlocal effects in the pressure-strain correlation that arise due to spatial variations in the mean velocity gradient field. Thus, while nonlinear models hold the promise of providing physically accurate predictions for $a_{ij}$ in a relatively simple computational framework, they are primarily aimed at capturing the nonlinearity in (1.28) and (1.30), and do not account for nonlocal or nonequilibrium effects on the anisotropy. In addition, there has been a proliferation of nonlinear closure models over the last several decades (perhaps more so than any other general class of closure approach), and the "best" nonlinear model for any particular problem remains unclear. This has, in general, lead to the widespread avoidance of nonlinear eddy viscosity models in engineering practice.

#### 1.3.2.2 Linear Eddy Viscosity Models

From the implicit algebraic formulation for $a_{ij}$ in (1.30), a linear equilibrium closure is obtained by neglecting all terms involving higher-order combinations $\overline{S}_{ij}$ and $\overline{W}_{ij}$ on the right-hand side. The resulting closure, which is identical to the classical Boussinesq hypothesis first introduced in 1877, fundamentally assumes the anisotropy to be directly proportional to the *local instantaneous* mean strain rate tensor $\overline{S}_{ij}$. The corresponding model for $a_{ij}$ is then given by

$$a_{ij} = -2\frac{\nu_T}{k}\overline{S}_{ij}\,, \tag{1.35}$$

where $\nu_T$ is an eddy viscosity that is rigorously defined from (1.30) as

$$\nu_T \equiv C_\mu \frac{k^2}{\epsilon}\,, \tag{1.36}$$

with the eddy viscosity coefficient $C_\mu$ given in terms of the $\alpha_i$ in (1.29) as

$$C_\mu \equiv -\frac{\alpha_2}{2\alpha_1}\,. \tag{1.37}$$

When the equilibrium closure in (1.35) is used for the anisotropy with the eddy viscosity in (1.36), the resulting equilibrium $k$-$\epsilon$ model represents the anisotropy as

$$a_{ij} = -2C_\mu \frac{k}{\epsilon}\overline{S}_{ij} = -2C_\mu \left(\frac{Sk}{\epsilon}\right)\frac{\overline{S}_{ij}}{S}\,, \tag{1.38}$$

where $S \equiv \left(2\overline{S}_{ij}\overline{S}_{ji}\right)^{1/2}$ characterizes the mean strain rate magnitude. Closure is then achieved through solution of the transport equations for $k$ and $\epsilon$ in (1.31) and (1.32), respectively.

While $C_\mu$ defined in (1.37) is rigorously connected to the modeled transport equation for $a_{ij}$ through the $\alpha_i$ coefficients, the dependence on $\alpha_1$, and hence $P/\epsilon$ via (1.29), has posed particular challenges when using the equilibrium closure given by (1.38). It has been common [52] to write $C_\mu$ using the constant value

$$C_\mu = 0.09\,, \tag{1.39}$$

and with (1.38) this gives the standard $k$-$\epsilon$ (SKE) linear eddy viscosity model. The SKE model is relatively successful in turbulent flows where the non-dimensional shear parameter $Sk/\epsilon$ and Lagrangian derivatives of flow properties like $k$ and $\epsilon$ are sufficiently small, such as in channel flow or other thin shear flows. In regions where $Sk/\epsilon$ becomes large however, the neglect of the dependence on $P/\epsilon$ in obtaining (1.39) from (1.37) becomes problematic. In reality, when $P/\epsilon$ and the closely connected variable $Sk/\epsilon$ become large, $C_\mu$ should decrease due to its dependence on $1/\alpha_1 \sim (P/\epsilon)^{-1}$. Rodi [83] was the first to note the relation between $C_\mu$ and $P/\epsilon$, and several approaches for reducing $C_\mu$ when $P/\epsilon$ – and hence $Sk/\epsilon$ – becomes large have been proposed. Perhaps the simplest approach, which was originally proposed as a realizable form for $C_\mu$, is the Bradshaw hypothesis where $C_\mu$ is given as

$$C_\mu = \begin{cases} 0.09 & \text{for} \quad (Sk/\epsilon) \leq 3.4 \\ 0.31(Sk/\epsilon)^{-1} & \text{for} \quad (Sk/\epsilon) > 3.4 \end{cases}\,. \tag{1.40}$$

With (1.38), the formulation for $C_\mu$ in (1.40) gives the partially realizable $k$-$\epsilon$ (RKE) model. Substitution of (1.40) into (1.38) results in an anisotropy magnitude that is independent of $Sk/\epsilon$, resulting in improved predictions of the anisotropy for large values of $Sk/\epsilon$.

While a number of representations for $\nu_T$ – and $C_\mu$ in particular – have been proposed, all models based on the equilibrium closure in (1.35) fundamentally assume that the anisotropy is proportional to the *local instantaneous* mean strain rate tensor $\overline{S}_{ij}$. However, such a representation fares poorly when nonequilibrium or nonlocal effects are significant, namely when there are large temporal or spatial variations in the mean strain rate tensor. Despite these shortcomings, two-equation linear eddy viscosity models based on (1.35) are overwhelmingly the most popular models for the anisotropy used in common engineering practice, due primarily to their computational simplicity and stability.

### 1.3.3 Performance of Prior Closures in Inhomogeneous Flows

The equilibrium SKE and RKE closures have been applied to a wide-range of turbulent flow problems, often with a surprising level of success. Indeed, Figure 1.1 shows close agreement between DNS results [39] and the SKE model in fully-developed turbulent channel flow for $y^+ > 60$, where $y^+ \equiv y u_\tau / \nu$ and $u_\tau$ is the wall friction velocity. For $y^+ < 60$ however, the SKE model predicts an increase in the anisotropy magnitude, which is in poor agreement with DNS results.

The disagreement between the SKE and DNS results in the near-wall region is due in part to the linear dependence of the SKE model on the parameter $Sk/\epsilon$ in (1.38). As shown in Figure 1.2, the SKE model agrees closely with the DNS results [39] for small values of $Sk/\epsilon$, but in the near-wall region where $Sk/\epsilon$ becomes large the SKE model over-predicts the anisotropy magnitude due to its linear dependence on $Sk/\epsilon$. Somewhat better agreement is obtained by the RKE model with $C_\mu$ from (1.40), where the anisotropy magnitude is independent of $Sk/\epsilon$ in the near-wall region. However, even the RKE model is unable to capture the decrease in the anisotropy magnitude as the wall is approached, as shown in Figure 1.1, and the non-trivial relation between $a_{12}$ and $Sk/\epsilon$ shown in Figure 1.2 is not accurately predicted.

While the RKE model has certainly captured some additional physics in the near-wall region by limiting $C_\mu$ for large $Sk/\epsilon$, in order to obtain better agreement with the DNS results nonlocal effects due to the strong near-wall variations in $\overline{S}_{12}$ must also be accounted for. The local equilibrium closure in (1.35), which forms the basis of both the SKE and RKE models, is fundamentally obtained by assuming that the mean velocity gradient field in the rapid pressure-strain correlation is homogeneous. The good agreement between the SKE and RKE models with DNS for $y^+ > 60$ suggests that this may be an adequate approximation near the center of the channel, but as the wall is approached this approximation becomes invalid. In reality, the near-wall spatial variations in $\overline{S}_{12}$ introduce nonlocal effects which must be accurately predicted by the anisotropy closure model to obtain good agreement with DNS all of the way to the wall.

In the past it has been common to account for these nonlocal effects (as well as other effects due to the low-Reynolds number and two dimensionality of the flow in the near-wall

region) through the use of wall damping functions $f_\mu$. These functions modify the eddy viscosity in (1.36) as

$$\nu_T = f_\mu C_\mu \frac{k^2}{\epsilon}, \tag{1.41}$$

where $C_\mu$ is still given by (1.39) or (1.40). A wide variety of forms for $f_\mu$ have been suggested (the review by Speziale and So [99] provides an extensive account of many such formulations), and Figures 1.1 and 1.2 show that using the van Driest [19] function

$$f_\mu = 1 - \exp\left(-\frac{y^+}{A^+}\right) \tag{1.42}$$

in (1.41), with $A^+ = 26$ and $C_\mu$ given by the realizable form in (1.40), gives significantly improved agreement with DNS results in the near-wall region. However, while wall-damping approaches clearly yield improved predictions in certain flows, they are distinctly *ad hoc* and suffer from a lack of universality that makes their use problematic in more complex flows, particularly in the presence of separated flow regions.

### 1.3.4   Performance of Prior Closures in Nonequilibrium Flows

Figures 1.3 and 1.4 show the performance of the equilibrium anisotropy closure from (1.35) in the SKE and RKE models for the case of initially-isotropic homogeneous turbulence with $k = k_0$ and $\epsilon = \epsilon_0$ at $t = 0$ that is suddenly subjected for $t > 0$ to homogeneous mean shear with relative magnitude $Sk_0/\epsilon_0 = 3.4$. The anisotropy created by the impulsive shear $\overline{S}_{12}(t)$ leads to changes in $k(t)$, $\epsilon(t)$ and $a_{ij}(t)$. The resulting $k(t)$ from the equilibrium closure in the SKE and RKE models is compared in Figure 1.3 with results from the LRR Reynolds stress transport model [51] in (1.28) using the constants in (1.26) and LES [3] for this case. At relative times $(S \cdot t) \gg 1$, all models and the LES show an increase in $k$ with time. However, until $(S \cdot t) \approx 2$ there are significant differences between the various results. In particular, LES and the LRR model show that the initial response of the turbulence to the impulsively applied shear is a decrease in $k(t)$, while the equilibrium closure in the SKE and RKE models causes the turbulence kinetic energy to instead immediately increase with time. Similarly, the SKE, RKE, and LRR models all predict an approach to an asymptotically unchanging shear anisotropy $a_{12}$ for large times, as shown in Figure 1.4, but the LRR model predicts a relatively gradual increase in the anisotropy magnitude. The differences between the equilibrium SKE and RKE models and the LRR model are due to nonequilibrium effects in the anisotropy response, as given by the $Da_{ij}/Dt$ on the left-hand side of (1.28), which are not correctly represented by the equilibrium closure in (1.35).

Figure 1.5 shows the evolution of the shear anisotropy $a_{12}$ for initially-isotropic periodically sheared homogeneous turbulence at three different relative shearing frequencies. In this case, the turbulence is suddenly subjected at $t = 0$ to the periodic shearing $\overline{S}_{12}(t) = (S/2)\sin(\omega t)$, where the initial shearing magnitude is $Sk_0/\epsilon_0 = 3.3$ and $\omega/S$

14

is the relative shearing frequency. Figure 1.5 compares results from the SKE, RKE, and LRR models with DNS results obtained by Yu and Girimaji [115]. It is clear that for all shearing frequencies there are substantial amplitude and phase disagreements between the SKE and RKE models and DNS results. In particular, the equilibrium closure in (1.35), which is used in both the SKE and RKE models, predicts a frequency-independent phase shift $\phi = \pi$ between $a_{12}$ and $\overline{S}_{12}$, whereas the DNS shows that $\phi \to \pi$ for small $\omega/S$ and $\phi \to \pi/2$ for large $\omega/S$. There is also a substantial amplitude disagreement between the SKE and DNS results, particularly for large values of $\omega/S$. The amplitude agreement is somewhat improved for small and moderate shearing frequencies using the RKE model, but Figure 1.5(c) shows that for the largest frequencies both the SKE and RKE models fail to predict the large decrease in the anisotropy amplitude. As with the impulsively-sheared case, these discrepancies are caused by the neglect of nonequilibrium effects in (1.35), and the generally good agreement between the LRR model and DNS results in Figure 1.5 is due to the retention of the nonequilibrium $Da_{ij}/Dt$ term in the closure.

In general, nonequilibrium effects in turbulent flows will arise whenever Lagrangian time variations in the strain rate $\overline{S}_{ij}(t)$, as well as corresponding variations of $k$ and $\epsilon$, are sufficiently large that the finite time-response of the turbulence prevents the anisotropy from reaching equilibrium with the strain rate (as assumed by the closure in (1.35)). As will be seen in Chapter III, such nonequilibrium in the turbulence response can also occur where rotation effects along the mean-flow streamlines are sufficiently large, and even when cross-stream spatial inhomogeneities in the strain and rotation rates are sufficiently large. Since these features commonly arise in practical engineering turbulent flow problems, at least some of the shortcomings of traditional equilibrium turbulence models based on (1.35) may be addressed by properly incorporating nonequilibrium effects into the closure scheme.

## 1.4   Present Study

The present study outlines the formulation of a new computationally-efficient closure for the anisotropy that provides more accurate predictions of nonlocal and nonequilibrium effects in turbulent flows than closure approaches based on the equilibrium implicit algebraic relation for $a_{ij}$ in (1.30). Fundamentally, the new closure attempts to remain closely connected to the physics underlying the anisotropy evolution in complex turbulent flows, most notably by developing – and then solving – a physically-accurate nonlocal transport equation for the anisotropy. In the following the general "philosophy" of the present approach is outlined, and an attempt is made to place the present study within the field of current research on turbulence modeling.

### 1.4.1 Philosophy of the Present Approach

As noted in Section 1.3, progress in developing turbulence anisotropy closures has been made over the last several decades by firmly rooting all closure approaches for (1.2)-(1.4) in the exact transport equation for the anisotropy given by (1.19). Certainly, Reynolds stress transport models based on (1.28) have long attempted to remain faithful to the exact anisotropy equation, but it has become increasingly common to connect algebraic closure approaches with this exact equation as well, as in (1.30). In general, there has been a marked movement in recent years away from developing new closures on an *ad hoc* or heuristic basis. This shift is perhaps most clearly demonstrated by the equilibrium closure given in (1.35)-(1.37); the general form of this closure was originally proposed by Boussinesq in 1877 from gradient transport arguments, but has been shown more recently to have a direct relation to the exact and modeled transport equations for $a_{ij}$ in (1.19) and (1.28), respectively.

As a result of the increased emphasis on physical rigor in recent years, it is reasonable to divide current research on turbulence anisotropy closure modeling into two separate areas. First, there is the issue of how the anisotropy evolution in turbulent flows can be understood and represented from a fundamental physical standpoint. As shown in Section 1.2, the exact transport equation for the anisotropy is known, but there is still substantial uncertainty as to how the pressure-strain correlation, dissipation, and transport terms in this equation should be represented in complex flows. The quantity of research on models for the pressure-strain correlation has been overwhelmingly greater than on the dissipation and transport terms, but still a closed representation that provides accurate predictions for a wide-range of flows has yet to be developed. In particular, while significant progress has been made in developing pressure-strain correlation models for homogeneous flows, such as the representation for $\Pi_{ij}$ in (1.25), inhomogeneous flows remain a challenge for nearly all approaches.

The second important area of research of anisotropy closures concerns the issue of how, once a modeled anisotropy transport equation such as that in (1.28) is obtained, this equation can best be solved. Here "best" refers not just to the physical accuracy of the solution, but also to its computational complexity. The relatively modest computing resources available to the typical engineer rules out, in most cases, the use of DNS or LES for practical flow problems, and even second-order Reynolds stress transport models can be problematic in terms of the computational resources required (not to mention their sometimes unfavorable convergence and stability properties). As a result, approaches based on algebraic stress models and the linear equilibrium closure in (1.35) remain overwhelmingly popular because they are currently the "best" available solution methods, in terms of both accuracy and efficiency, for the typical engineer.

Ultimately, the objective of this dissertation is to make fundamental contributions to both the research areas noted above. An attempt is made to improve upon the existing anisotropy transport equation in (1.28) by obtaining a new nonlocal representation for the

rapid pressure-strain correlation $\Pi_{ij}^{(r)}$. Despite the inherently nonlocal nature of $\Pi_{ij}^{(r)}$, which is given exactly as an integral over the entire flow, previous models for the correlation are incorrectly expressed in terms of local flow variables only, as in (1.24). This approximation is based on the assumption of a spatially invariant mean velocity gradient tensor in the integral for $\Pi_{ij}^{(r)}$, which is not accurate in strongly inhomogeneous flows. The new nonlocal rapid pressure-strain correlation developed herein reconsiders this fundamental assumption, and the resulting nonlocal anisotropy transport equation extends the accuracy of even Reynolds stress transport models without significantly increasing the computational complexity of existing approaches.

This nonlocal anisotropy transport equation is then solved through a linearization of the anisotropy dynamics, where the primary nonequilibrium dynamics neglected in obtaining prior linear and nonlinear eddy viscosity approaches from (1.30) are now retained. The resulting closure accounts for both nonlocal and nonequilibrium effects on the turbulence anisotropy, but does so within a relatively simple formulation that allows straightforward implementation in existing two equation frameworks for solving (1.2)-(1.4). This closure approach is specifically developed with a view towards maintaining high physical accuracy within a computationally-efficient framework, and thus addresses the second challenge of current research on turbulence anisotropy closures noted above.

Finally, as a general principal it may be claimed that reductions in computational complexity without large sacrifices in closure accuracy require new physical insights into the anisotropy evolution in real turbulent flows. In nearly all closure model approaches, computational complexity is reduced by neglecting certain aspects of the underlying physics (almost by definition), and this can only be accomplished in a rational manner through consideration of the most important physical effects on the anisotropy evolution in common problems. Moreover, when physical accuracy *is* lost it is important to understand the types of problems in which the resulting closure is less accurate. Once again, this can only be achieved by basing all closure assumptions in physical reasoning, where the limits of the closure become obvious. In the present work, new physical insights into the anisotropy evolution have been obtained through fundamental DNS studies of the vorticity alignment in turbulent flows. These studies suggest a substantial nonlocal, quasi-linear aspect to the anisotropy evolution, and this result has been used to motivate the quasi-linearization of the anisotropy dynamics noted above.

### 1.4.2 Organization of this Dissertation

In Chapter II the vorticity alignment in turbulent flows is examined using high-resolution DNS of homogeneous isotropic turbulence. It is shown that decomposition of the total strain rate tensor into its local and nonlocal constituents reveals a substantial nonlocal and quasi-linear aspect to the vorticity dynamics. The anomalous alignment of the vorticity with the eigenvector of the strain rate tensor corresponding to the intermediate eigenvalue is

also partially resolved, and it is shown for the first time that the vorticity aligns with the most extensional eigenvector of the nonlocal background strain rate tensor. An expansion solution for the background strain rate is also derived in terms of Laplacians of the total strain rate. Certain aspects of Chapter II can be found in Refs. [33, 34].

Using insights from the vorticity alignment studies in Chapter II, Chapter III outlines the derivation of a physics-based anisotropy closure for nonlocal and nonequilibrium effects in turbulent flows. Through reexamination of the homogeneity approximation typically used to model the rapid pressure-strain correlation $\Pi_{ij}^{(r)}$, a new nonlocal representation for $\Pi_{ij}^{(r)}$ is obtained. The nonlocal formulation is derived by Taylor-expanding the mean velocity gradient appearing in the exact integral for $\Pi_{ij}^{(r)}$, and closely mirrors the derivation of the expansion for the background strain rate tensor in Chapter II. The new correlation is expressed in terms of Laplacians of the mean strain rate tensor and thereby accounts for nonlocal effects due to spatial variations in the mean strain field. When used in the exact anisotropy transport equation, this nonlocal rapid pressure-strain correlation gives a new nonlocal anisotropy transport equation. Motivated by the quasi-linearity suggested by the alignment studies in Chapter II, higher-order nonlinear terms in this equation are neglected, resulting in a nonlocal quasi-linear equation for the anisotropy evolution. It is then shown that this equation permits a relatively simple convolution integral solution for the anisotropy. In particular, a history-dependent nonlocal effective strain rate tensor replaces the traditional mean strain rate tensor in the classical local equilibrium closure in (1.35), resulting in a relatively simple formulation of nonlocal and nonequilibrium effects in turbulent flows. This new closure is closely related to the nonequilibrium closure outlined in Ref. [31], but now additionally accounts for nonlocal effects on the anisotropy evolution. It is further shown that the nonlocal effective strain rate can be written in simple time-local form for implementation in existing computational frameworks for solving (1.2)-(1.4). In such frameworks only local instantaneous variables are typically available, and the time-local formulation of the nonlocal effective strain rate avoids the need to explicitly calculate the history-dependent convolution integral.

Chapters IV and V then present nonequilibrium and nonlocal tests, respectively, of the present closure. In Chapter IV the new closure is examined in nonequilibrium homogeneous flows, for which the nonlocal behavior of the new closure is unimportant. It is shown that the new closure gives significantly improved results over various prior approaches for a wide range of nonequilibrium test cases. Six cases are examined in total: ($i$) impulsively sheared turbulence, ($ii$) impulsive axisymmetric contraction, ($iii$) decaying anisotropic turbulence, ($iv$) turbulence that is strained, relaxed, and destrained, ($v$) periodically sheared turbulence, and ($vi$) the interaction of turbulence with a normal shock. For the periodically sheared case a rigorous parametric frequency analysis of the anisotropy dynamics is conducted, and the new closure is used to develop analytical scalings for many key quantities. Additional details of this frequency response analysis can be found in Ref. [32].

In Chapter V the new closure is tested in fully-developed turbulent channel flow and the zero pressure gradient turbulent boundary layer. In both flows nonequilibrium effects are small, and it is shown that by addressing nonlocal effects the present closure approach gives substantially improved agreement with computational and experimental results compared to prior closures based on the local equilibrium hypothesis in (1.35). For the fully-developed channel flow, direct comparisons are made with results from DNS of eight different Reynolds numbers cases. These channel flow tests allow the nonlocal behavior of the new closure to be directly examined, since $\overline{S}_{ij}$, $k$, and $\epsilon$ are all taken directly from the DNS databases. It is shown that the new closure gives good agreement with DNS results down to $y^+ \approx 16$, and a blended model is formulated to further allow integration to $y^+ = 0$. This blended model is then applied within a full computational fluid dynamics (CFD) code for the zero pressure gradient boundary layer, demonstrating not only the practical utility of the present closure for computational simulations of real turbulent flow problems, but also the accuracy of the closure in predicting nonlocal effects on the anisotropy.

Finally, conclusions and an outline of future research are provided in Chapter VI. Appendix 6.2 addresses nonlinear effects in turbulent flows through the formulation of a nonlinear representation for $C_\mu$ appearing in the standard definition of the eddy viscosity in (1.36). When implemented in the present closure approach, the nonlinear $C_\mu$ gives a closure that accounts for nonlinear, nonlocal, and nonequilibrium effects on the anisotropy.
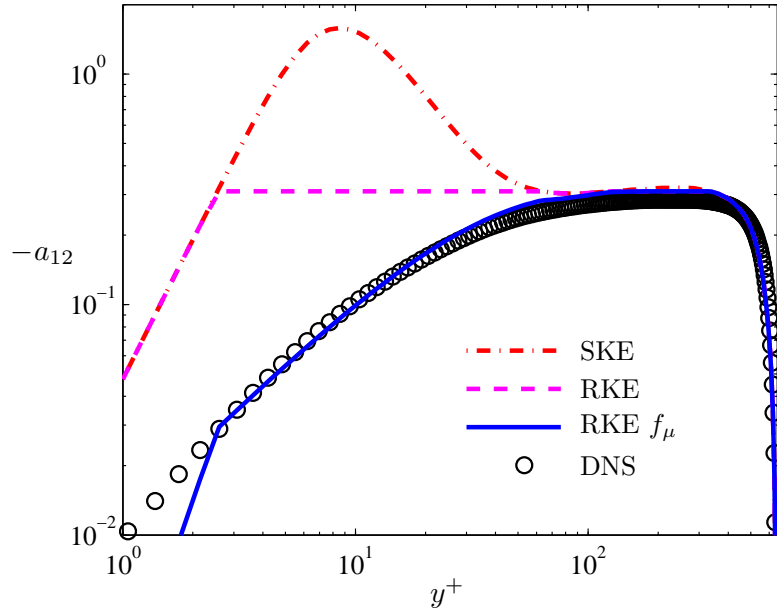
Figure 1.1: Variation of anisotropy $-a_{12}$ with $y^+$ in turbulent channel flow, showing good agreement of linear form from equilibrium $k$-$\epsilon$ models (SKE and RKE) in (1.38) with DNS results of Iwamoto *et al.* [39] for $y^+ > 60$. Better agreement is obtained with DNS results using the wall damping function $f_\mu$ in (1.42).
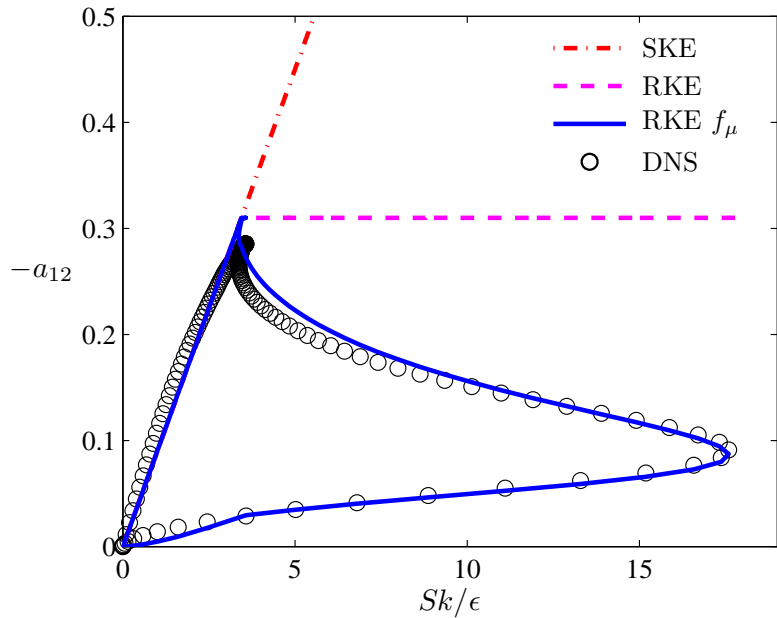


Figure 1.2: Variation of anisotropy component $-a_{12}$ with $Sk/\epsilon$ in turbulent channel flow, showing good agreement of linear form from equilibrium $k$-$\epsilon$ models (SKE and RKE) in (1.38) with DNS results of Iwamoto *et al.* [39] for $Sk/\epsilon$ values outside the near-wall region. Once again, better agreement with DNS results is obtained using $f_\mu$ in (1.42).
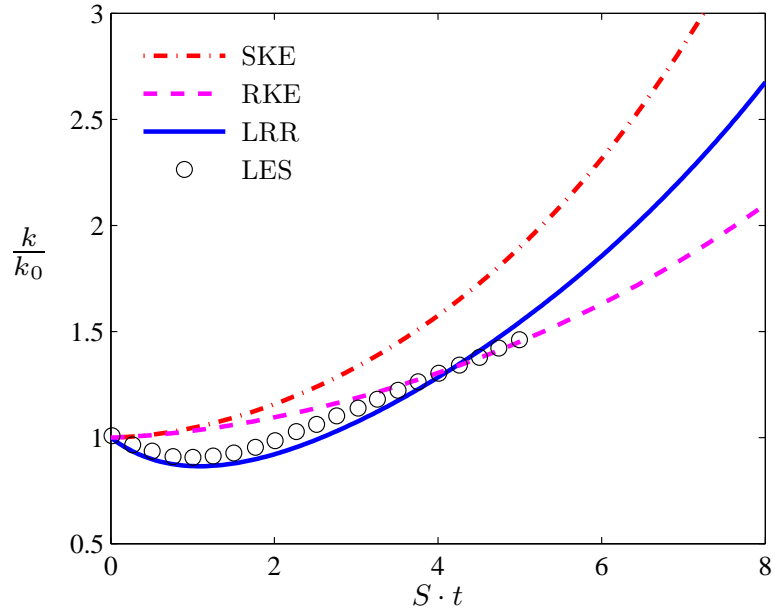
Figure 1.3: Evolution of turbulence kinetic energy $k(t)$ for initially isotropic impulsively sheared homogeneous turbulence with $Sk_0/\epsilon_0 = 3.4$, showing failure of equilibrium $k$-$\epsilon$ (SKE and RKE) models to predict initial nonequilibrium response in $k(t)$ from LES results of Bardina *et al.* [3]. Results from the LRR model [51] from (1.28) with the constants in (1.26) are also shown.
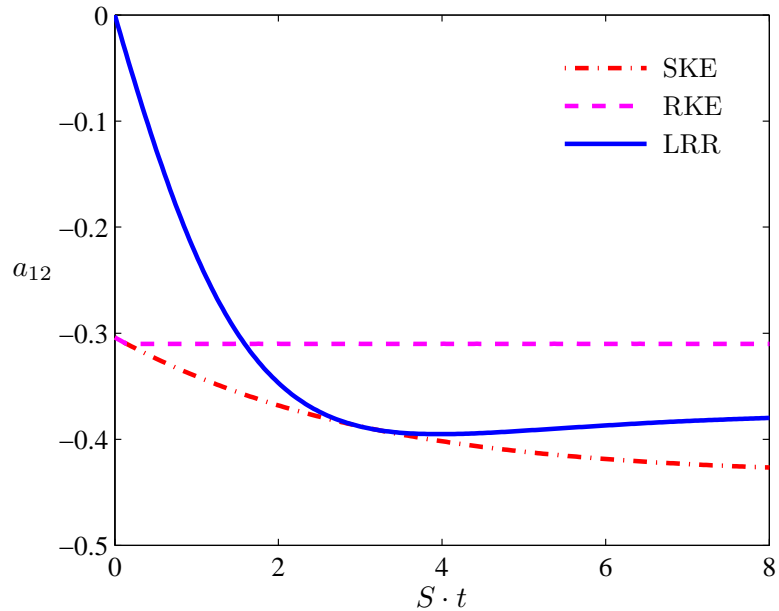


Figure 1.4: Evolution of shear anisotropy $a_{12}$ for initially-isotropic impulsively-sheared homogeneous turbulence with $Sk_0/\epsilon_0 = 3.4$, showing results from $k$-$\epsilon$ (SKE and RKE) models and the LRR model [51] given by (1.28) with the constants in (1.26).

21
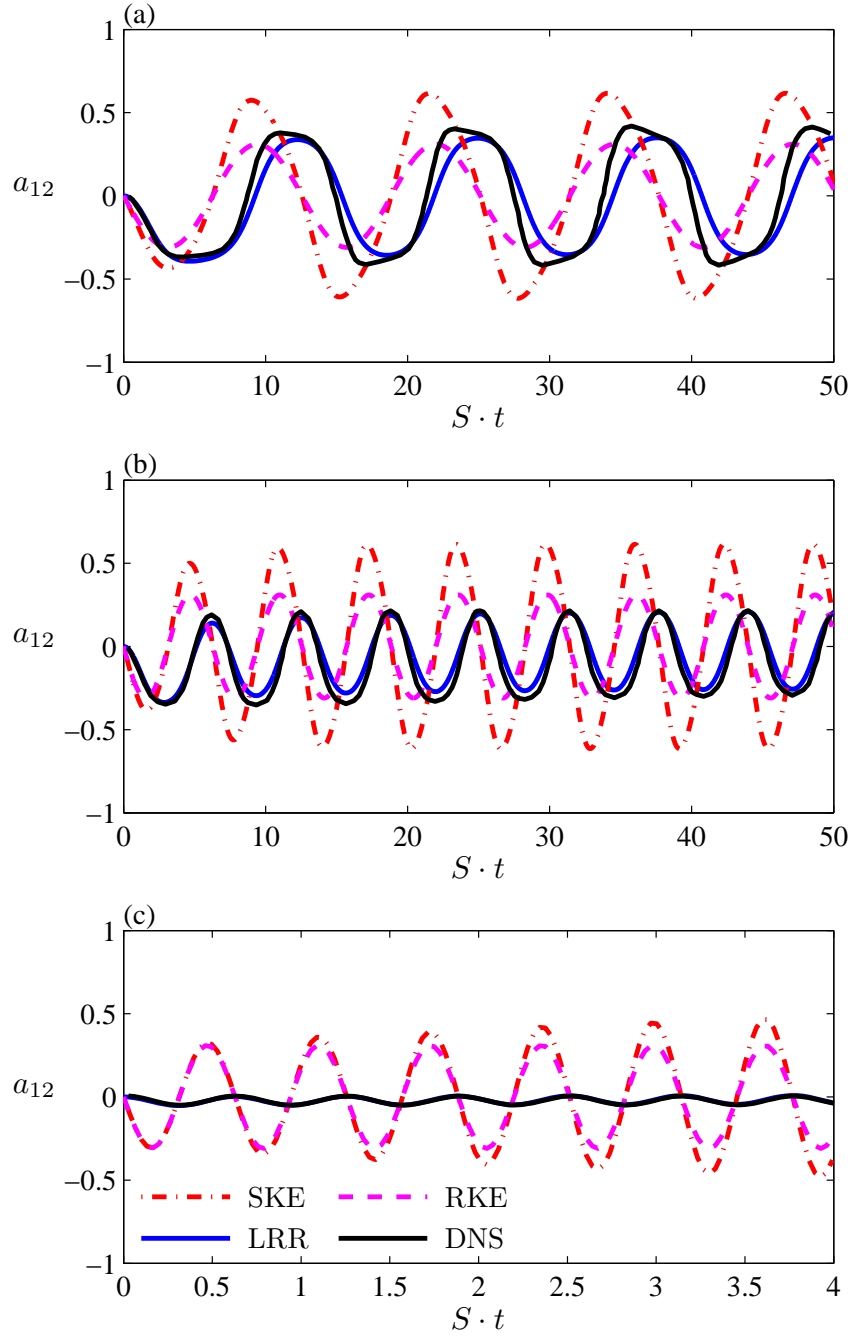
Figure 1.5: Evolution of anisotropy $a_{12}$ for initially-isotropic periodically-sheared homogeneous turbulence with $Sk_0/\epsilon_0 = 3.3$ for $\omega/S = 0.5$ (a), $\omega/S = 1.0$ (b), and $\omega/S = 10$ (c). Results from the SKE and RKE models fail to predict frequency dependent phase shift and amplitude seen in the DNS by Yu and Girimaji [115]. Results from the LRR model [51] given by (1.28) with the constants in (1.26) are also shown.

# CHAPTER II

# Vorticity Alignment Physics and Relation to Turbulence Anisotropy

There has been little prior work on the connection between vorticity alignment in turbulent flows and the evolution of the Reynolds stress anisotropy $a_{ij}$, despite substantial research on each area individually. This is due in large part to the fact that vorticity alignment has primarily been studied in homogeneous isotropic turbulence, and similar fundamental studies of anisotropic flows have been relatively uncommon. However, a formal relationship between the vorticity and the anisotropy can be established via the Biot-Savart integral for the fluctuating velocity $u_i'(\mathbf{x}, t)$, namely

$$u_i'(\mathbf{x}, t) = \frac{1}{4\pi} \int_{\hat{\mathbf{R}}} \boldsymbol{\omega}'(\hat{\mathbf{x}}, t) \times \frac{(\mathbf{x} - \hat{\mathbf{x}})}{|\mathbf{x} - \hat{\mathbf{x}}|^3} \, d\hat{\mathbf{x}} \,, \tag{2.1}$$

where $\boldsymbol{\omega}' \equiv \nabla \times \mathbf{u}'$ is the fluctuating vorticity and the integration is carried out over the entire spatial domain, denoted by $\hat{\mathbf{R}}$. From (2.1), the single-point velocity fluctuation correlation can be written exactly in terms of the two-point vorticity fluctuation correlation via a double Biot-Savart integral as

$$\overline{u_i' u_j'}(\mathbf{x}, t) = \frac{1}{4\pi} \int_{\hat{\mathbf{R}}} \frac{1}{4\pi} \int_{\check{\mathbf{R}}} \epsilon_{ikl} \epsilon_{jmn} \overline{\omega_k'(\check{\mathbf{x}}, t) \omega_m'(\hat{\mathbf{x}}, t)} \frac{(x_l - \check{x}_l)}{|\mathbf{x} - \check{\mathbf{x}}|^3} \frac{(x_n - \hat{x}_n)}{|\mathbf{x} - \hat{\mathbf{x}}|^3} \, d\check{\mathbf{x}} \, d\hat{\mathbf{x}} \,, \tag{2.2}$$

where we have used the definition $\boldsymbol{\omega}' \times \mathbf{x} \equiv \epsilon_{ikl} \, \omega_k' \, x_l$ and $\epsilon_{ikl}$ is the cyclic permutation tensor. It is apparent from (2.2) that the two-point vorticity fluctuation correlation determines the Reynolds stresses, and thus the anisotropy $a_{ij}$. The vorticity fluctuation correlation, being a small-scale quantity, is in turn fundamentally determined by the relative alignment of the vorticity field $\omega_i(\mathbf{x}, t)$ at relatively closely-spaced points, and thus a rigorous connection between vorticity alignment and the anisotropy is established.

In the following, fundamental studies of the vorticity alignment in homogeneous isotropic turbulence are used to gain insights into the physics underlying the anisotropy evolution in turbulent flows. These studies also provide new insights into the mechanisms by which the vorticity aligns with the intermediate strain rate eigenvector. This has generally been

regarded as a somewhat surprising result, and reflects fundamental physical aspects of the structure and dynamics of turbulent flows. Through decomposition of the total strain rate tensor into its local and nonlocal constituents, this "anomalous" alignment is partly resolved and it is shown that there is a substantial nonlocal, quasi-linear aspect to the vorticity dynamics. This last result provides physical motivation for the new anisotropy closure for nonlocal and nonequilibrium effects in turbulent flows that will be developed in Chapter III.

## 2.1 Prior Approaches for Understanding Vorticity Dynamics

The alignment of the vorticity vector $\boldsymbol{\omega} \equiv \nabla \times \mathbf{u}$ with the eigenvectors of the strain rate tensor $S_{ij}$ in turbulent flows has been a subject of considerable interest over the past two decades. The vorticity alignment is ultimately responsible for the transfer of kinetic energy between scales in three-dimensional incompressible turbulent flows, as well as for the nonlinearity in the dynamics of the underlying vorticity field [4, 9, 58, 59, 103]. The evolution of the vorticity is given by the transport equation [78]

$$\frac{D\omega_i}{Dt} = S_{ij}\omega_j + \nu\nabla^2\omega_i \,, \tag{2.3}$$

where the strain rate tensor $S_{ij}$ is defined as the symmetric part of the velocity gradient tensor, namely

$$S_{ij} \equiv \frac{1}{2}\left(\frac{\partial u_i}{\partial x_j} + \frac{\partial u_j}{\partial x_i}\right) \,. \tag{2.4}$$

On the right side of (2.3) the magnitude of the nonlinear stretching term

$$|S_{ij}\omega_j| \equiv \omega[s_i^2 \left(\mathbf{e}_i \cdot \mathbf{e}_\omega\right)^2]^{1/2} \tag{2.5}$$

depends on the strain rate eigenvalues $s_i$ and the vorticity magnitude $\omega \equiv (\omega_i\omega_i)^{1/2}$, and also on the alignment cosines $(\mathbf{e}_i \cdot \mathbf{e}_\omega)$ between the vorticity unit vector $\mathbf{e}_\omega$ and the strain rate eigenvectors $\mathbf{e}_i$. For perfectly aligned vectors $(\mathbf{e}_i \cdot \mathbf{e}_\omega) = 1$, whereas for completely misaligned – or perpendicular – vectors $(\mathbf{e}_i \cdot \mathbf{e}_\omega) = 0$. The strain rate eigenvalues $s_i$ can be ordered as $s_1 \geq s_2 \geq s_3$ so that incompressibility $(s_1 + s_2 + s_3 \equiv 0)$ requires $s_1 \geq 0$ and $s_3 \leq 0$. The positivity of $s_1$ and the negativity of $s_3$ correspond, respectively, to extensional and compressional straining along the $\mathbf{e}_1$ and $\mathbf{e}_3$ directions. While the intermediate eigenvalue $s_2$ is on average weakly positive in turbulent flows, the instantaneous $s_2$ can take on large positive or negative values [2, 101, 103] bounded only by the $s_1$ and $s_3$ values. The alignment between the vorticity and the strain rate eigenvectors similarly determines the production rate

$$\omega_i S_{ij}\omega_j \equiv \omega^2 s_i \left(\mathbf{e}_i \cdot \mathbf{e}_\omega\right)^2 \,, \tag{2.6}$$

for the enstrophy $\frac{1}{2} (\boldsymbol{\omega} \cdot \boldsymbol{\omega})$. The three alignment cosines $(\mathbf{e}_i \cdot \mathbf{e}_\omega)$ thus play an essential role in the structure and dynamics of turbulent flows.

Despite its importance, the mechanism by which the vorticity aligns with the strain rate eigenvectors $\mathbf{e}_i$ is still not well understood. In particular, the maximality and positivity of $s_1$ might suggest that the vorticity in (2.3) would show preferred alignment with the most extensional eigenvector $\mathbf{e}_1$. However, since $S_{ij}$ on the right side of (2.3) is coupled back to $\omega_i$, the resulting nonlinearity complicates any such simple alignment. Indeed, DNS (e.g. [2, 70, 92]) and experimental studies (e.g. [8, 68, 101, 104, 116]) of the fine-scale structure of turbulence have revealed a somewhat unexpected preferred alignment with the intermediate eigenvector $\mathbf{e}_2$ of the strain rate tensor.

This can be seen, for example, in Figure 2.1, where distributions of the three alignment cosines $|\mathbf{e}_i \cdot \mathbf{e}_\omega|$ are shown from a recent highly-resolved, three-dimensional, $2048^3$ DNS generated by Schumacher *et al.* [90, 91] of statistically stationary, forced, homogeneous, isotropic turbulence at Taylor-scale Reynolds number $Re_\lambda = 107$. The DNS was done using a pseudospectral method with a spectral resolution that exceeds the standard value by a factor of eight. As a result the highest wavenumber corresponds to $k_{max}\eta_K = 10$, and the Kolmogorov lengthscale $\eta_K \equiv (\nu^3/\epsilon)^{1/4}$ is resolved with three grid spacings. Figure 2.2 gives a representative sample of the DNS data, where the instantaneous shear component $S_{12}(\mathbf{x})$ is shown in a typical two-dimensional intersection through the $2048^3$ cube. Using these simulations, the resulting alignment distributions in Figure 2.1 agree with those from lower-resolution DNS studies as well as from laboratory measurements [68, 101, 104]. In particular, the vorticity tends to point away from the most compressive eigenvector $\mathbf{e}_3$, namely $|\mathbf{e}_3 \cdot \mathbf{e}_\omega| \to 0$, and there is essentially no tendency for any preferred alignment relative to the most extensional strain rate eigenvector $\mathbf{e}_1$, since $P(|\mathbf{e}_1 \cdot \mathbf{e}_\omega|) \approx 1$. However, the vorticity shows a strong tendency toward alignment with the intermediate strain rate eigenvector $\mathbf{e}_2$, namely $|\mathbf{e}_2 \cdot \mathbf{e}_\omega| \to 1$.

There have been numerous studies seeking to understand the reasons for this result, and various theoretical approaches have been proposed to explain the failure of the vorticity to align with the most extensional strain rate eigenvector. Previous explanations have tended to focus on the vorticity-strain coupling in the evolution equation for the strain rate tensor, namely [70, 103]

$$\frac{DS_{ij}}{Dt} = -S_{ik}S_{kj} - \frac{1}{4}(\omega_i\omega_j - \omega_k\omega_k\delta_{ij}) - \frac{1}{\rho}\frac{\partial^2 p}{\partial x_i \partial x_j} + \nu\nabla^2 S_{ij}. \tag{2.7}$$

The nonlinear coupling between the strain rate and the vorticity is apparent in (2.3) and (2.7), where the nonlocality of the vorticity and strain rate co-evolution arises from the pressure Hessian, which can be written in terms of isotropic and anisotropic parts as [70, 72]

$$\frac{\partial^2 p}{\partial x_i \partial x_j} = \frac{\omega_l\omega_l - 2S_{ln}S_{ln}}{6}\delta_{ij} + \left(\frac{\partial^2 p}{\partial x_i \partial x_j}\right)_{aniso}, \tag{2.8}$$

where $\left(\partial^2 p/\partial x_i \partial x_j\right)_{aniso}$ is the anisotropic contribution. The isotropic part is clearly expressed in terms of local variables, while the anisotropic part accounts for the remaining nonlocal contribution to the pressure Hessian in the flow.

Some progress has been made in understanding the alignments in Figure 2.1 via the restricted Euler (RE) equations, which are obtained by neglecting the anisotropic (nonlocal) contribution to the pressure Hessian in (2.8), and writing (2.3) and (2.7) in inviscid principal strain coordinates (e.g. [10, 70, 105]). While nonlocal effects are neglected entirely in the RE equations, these equations result in alignment of the vorticity with $\mathbf{e}_2$, as shown by the maximality of $\omega_2$ in Figure 2.3. However, it is also clear from the evolution of $\omega_i$ and $s_i$ in Figures 2.3 and 2.4, respectively, that there is a finite-time singularity in the RE dynamics due to the neglect [12] of viscous and nonlocal effects in the RE equations. While various approaches have been outlined for modeling these additional terms (e.g. Girimaji and Pope [29], Martin *et al.* [64], Naso and Pumir [69], and Chevillard and Meneveau [12]), the analysis of vorticity alignment in real turbulent flows using (2.7) is generally complicated by the challenge of addressing nonlocal effects due to the anisotropic part of the pressure-Hessian in (2.8). This is true even in inviscid flows for which the viscous diffusion terms in (2.3) and (2.7) can be neglected. As a result, a complete picture of vorticity alignment that clearly accounts for nonlinear and nonlocal contributions to the coupled vorticity-strain dynamics – without resorting to substantial simplifications of (2.7) and (2.8) or models for the unclosed terms – has remained largely elusive.

## 2.2 Present Study of Local and Nonlocal Effects on Vorticity Alignment

In the following, the anomalous alignment of the vorticity in Figure 2.1 is examined through decomposition of the total strain rate tensor into its local and nonlocal constituents. It is shown that vorticity does tend toward alignment with the most extensional eigenvector of the *nonlocal* (background) strain, namely the strain field induced in the immediate region around any vortical structure by the surrounding vorticity outside this region. The anomalous alignment occurs with the eigenvectors of the *combined* strain rate in (2.4), namely the sum of this nonlocal background strain and the *local* strain induced in the region by the vorticity within it.

In contrast to analyses based on the RE equations, here we forego the use of (2.7) in representing the strain rate appearing in (2.3) and instead use an integral representation for the strain rate. This integral relation can then be used to gain insights into the effects of nonlocality and nonlinearity on the vorticity alignment. Compared to working with (2.7), this approach has the advantage of addressing nonlocal effects on the coupled vorticity-strain dynamics directly, without the need to neglect or model the anisotropic pressure-Hessian term in (2.8).

To obtain an integral relation for $\overline{S}_{ij}$ we first note that the velocity $\mathbf{u}$ at any point $\mathbf{x}$ induced by the vorticity field $\boldsymbol{\omega}(\mathbf{x})$ is given by the Biot-Savart integral, which is written in

index notation as

$$u_i(\mathbf{x}) = \frac{1}{4\pi} \int_{\mathbf{R}} \epsilon_{ilk}\omega_l(\hat{\mathbf{x}}) \frac{(x_k - \hat{x}_k)}{|\mathbf{x} - \hat{\mathbf{x}}|^3} d\hat{\mathbf{x}}, \tag{2.9}$$

where the integration is carried out over the entire spatial domain, denoted by $\mathbf{R}$. The derivative with respect to $x_j$ then gives the velocity gradient tensor

$$\frac{\partial}{\partial x_j} u_i(\mathbf{x}) = \frac{1}{4\pi} \int_{\mathbf{R}} \epsilon_{ilk}\omega_l(\hat{\mathbf{x}}) \left[ \frac{\delta_{kj}}{r^3} - 3\frac{r_k r_j}{r^5} \right] d\hat{\mathbf{x}}, \tag{2.10}$$

where $r \equiv |\mathbf{x} - \hat{\mathbf{x}}|$ and $r_m \equiv x_m - \hat{x}_m$. From (2.4) and (2.10), $S_{ij}(\mathbf{x})$ can be expressed [71] as an integral over the vorticity field as

$$S_{ij}(\mathbf{x}) = \frac{3}{8\pi} \int_{\mathbf{R}} (\epsilon_{ikl}r_j + r_i\epsilon_{jkl}) \frac{r_k}{r^5} \omega_l(\hat{\mathbf{x}}) d\hat{\mathbf{x}}. \tag{2.11}$$

Substituting (2.11) in (2.3) then gives a direct nonlocal integro-differential equation for the vorticity evolution as

$$\frac{D\omega_i}{Dt} = \frac{3}{8\pi} \int_{\mathbf{R}} (\epsilon_{ikl}r_j + r_i\epsilon_{jkl}) \frac{r_k}{r^5} [\omega_j(\mathbf{x})\omega_l(\hat{\mathbf{x}})] d\hat{\mathbf{x}} + \nu\nabla^2\omega_i, \tag{2.12}$$

which depends only on the vorticity field itself.

### 2.2.1 Background Strain Rate Decomposition

In (2.11) and (2.12) the local and nonlocal contributions to the strain rate and vorticity dynamics can be understood by separating the integration domain into a *local* spherical region of radius $r \leq R$ centered on $\mathbf{x}$, and a *nonlocal* region that accounts for the rest of the domain [92]. The strain rate in (2.11) then is the sum

$$S_{ij}(\mathbf{x}) = S_{ij}^R(\mathbf{x}) + S_{ij}^B(\mathbf{x}) \tag{2.13}$$

of the local strain rate $S_{ij}^R(\mathbf{x})$ induced at $\mathbf{x}$ by the vorticity within $R$, and the nonlocal (background) strain rate $S_{ij}^B(\mathbf{x})$ induced at $\mathbf{x}$ by all the vorticity outside $R$. From (2.13), the strain rate tensor in (2.11) thus becomes

$$S_{ij}(\mathbf{x}) = \underbrace{\frac{3}{8\pi} \int_{r \leq R} [\cdots] d\hat{\mathbf{x}}}_{\equiv\, S_{ij}^R(\mathbf{x})} + \underbrace{\frac{3}{8\pi} \int_{r > R} [\cdots] d\hat{\mathbf{x}}}_{\equiv\, S_{ij}^B(\mathbf{x})}, \tag{2.14}$$

where $[\cdots]$ denotes the integrand in (2.11), and the nonlocal background strain is then given by

$$S_{ij}^B(\mathbf{x}) = S_{ij}(\mathbf{x}) - S_{ij}^R(\mathbf{x}). \tag{2.15}$$

27

The total strain tensor $S_{ij}(\mathbf{x})$ in (2.15) is readily evaluated via (2.4) from derivatives of the velocity field at point $\mathbf{x}$. Thus all that is required to obtain the background strain rate tensor $S_{ij}^B(\mathbf{x})$ via (2.15) is an evaluation of the local strain integral $S_{ij}^R(\mathbf{x})$ in (2.14) produced by the vorticity field $\omega_l(\hat{\mathbf{x}})$ within $r \leq R$.

As a practical matter, an appropriate value for $R$ is required to calculate $S_{ij}^R(\mathbf{x})$ from (2.14) and thus obtain $S_{ij}^B(\mathbf{x})$. From a physical standpoint, the background strain field $S_{ij}^B(\mathbf{x})$ in the vicinity of any local vortical structure in the turbulence is that induced by all the *other* vortical structures. Thus, the proper physical value for $R$ used to obtain $S_{ij}^B(\mathbf{x})$ should exclude from (2.11) essentially all the vorticity associated with any local vortical structure. Prior studies (e.g. [41, 45]) have shown that the characteristic radius of intense vortical structures in turbulence is in the range $r/\eta_K \approx 4 - 10$, where $\eta_K$ is the Kolmogorov length scale. This is consistent with the two-point vorticity correlation from the present DNS of homogeneous isotropic turbulence, which is found to decrease to 20% of its maximum value at $r \approx 12\eta_K$ as shown in Figure 2.6. This gives a physically appropriate cutoff radius, since beyond this the vorticity becomes essentially uncorrelated with itself. Thus, $R = 12\eta_K$ as used herein excludes essentially all the local vorticity for most structures, and thereby allows the self-induced strain field in the vicinity of typical vortical structures to be separated from the background strain field in which the structures reside.

With this choice of $R$, the local strain rate $S_{ij}^R(\mathbf{x})$ in (2.15) can then be obtained by directly integrating (2.11) over the domain $R$ centered on $\mathbf{x}$. As shown schematically in Figure 2.5, at any point $\mathbf{x}$ in the $2048^3$ cubic simulation domain, a smaller cubic subdomain with side length $2R$ is taken to define the local region around $\mathbf{x}$. The local strain rate $S_{ij}^R(\mathbf{x})$ is obtained by numerically integrating (2.11) over this subdomain. We then determine the nonlocal strain rate from (2.15) and examine the alignment of the vorticity $\boldsymbol{\omega}(\mathbf{x})$ with each of these strain rates to understand how the alignment in Figure 2.1 arises.

As a test of the analysis procedure, Figure 2.7 shows that for an axisymmetric Burgers vortex with vorticity field given by

$$\boldsymbol{\omega}(\mathbf{x}) = \omega_z(r)\hat{\mathbf{z}} = \frac{\alpha}{\pi} \frac{\Gamma}{\lambda_\nu^2} \exp\left(-\alpha\eta^2\right) \hat{\mathbf{z}}, \tag{2.16}$$

the local straining induced by the vortex is increasingly removed as the cutoff radius $R$ increases, resulting in convergence to the expected result $S_{12}^B(\mathbf{x}) = 0$. In (2.16), $\Gamma$ is the circulation, $\lambda_\nu$ is the viscous lengthscale that characterizes the diameter of the vortex, $\eta \equiv r/\lambda_\nu$ is the radial similarity coordinate, and the constant $\alpha$ reflects the chosen definition of $\lambda_\nu$. The Burgers vortex test case will be examined in more detail in Section 2.4, but here Figure 2.7 suffices to demonstrate the accuracy of the direct procedure for separating the local and nonlocal strain rates.

### 2.2.2 Vorticity Alignment in Turbulent Flows

For the high resolution DNS of Schumacher *et al.* [90, 91], Figures 2.8 and 2.9 show an example of the resulting decomposition of the shear strain rate field $S_{12}(\mathbf{x})$ (shown in Figure 2.8) into its background and local fields, $S_{12}^B(\mathbf{x})$ (Figure 2.9(a)) and $S_{12}^R(\mathbf{x})$ (Figure 2.9(b)). Similar local-nonlocal decompositions are obtained for the other strain rate components, and the eigenvalues and eigenvectors of the resulting background and local strain rate tensor fields are then computed. At every point $\mathbf{x}$, the alignment cosines $|\mathbf{e}_i \cdot \mathbf{e}_\omega|$ of the vorticity with the background and local strain rate eigenvectors, denoted $\mathbf{e}_i^B$ and $\mathbf{e}_i^R$ respectively, can then be evaluated.

The resulting vorticity alignment distributions $P\left(|\mathbf{e}_i^B \cdot \mathbf{e}_\omega|\right)$ and $P\left(|\mathbf{e}_i^R \cdot \mathbf{e}_\omega|\right)$ are shown, respectively, in Figures 2.10 and 2.11. From the *background* strain alignments in Figure 2.10 it is apparent that the vorticity is preferentially aligned with the most *extensional* background strain rate eigenvector $\mathbf{e}_1^B$, namely $|\mathbf{e}_1^B \cdot \mathbf{e}_\omega| \to 1$. There is essentially no preferred alignment of the vorticity relative to the intermediate background eigenvector $\mathbf{e}_2^B$, since $P\left(|\mathbf{e}_2^B \cdot \mathbf{e}_\omega|\right) \approx 1$, while the vorticity tends to point preferentially away from the most compressive background eigenvector $\mathbf{e}_3^B$, namely $|\mathbf{e}_3^B \cdot \mathbf{e}_\omega| \to 0$. Note that Figure 2.12 shows the background strain alignment as a function of $R$, and it is clear that $R = 12\eta_K$ as used herein is sufficient to fully reveal the alignment of the vorticity with the background strain rate tensor. As shown in Figure 2.12, larger values of $R$ result in only small changes in the observed distributions.

The alignments in Figure 2.10 with the background strain rate are precisely as would be expected when the strain rate evolution is decoupled from that of the vorticity, as is essentially the case for the background strain. From (2.3) with (2.13), the inviscid dynamics of the vorticity satisfies

$$\frac{D\omega_i}{Dt} = S_{ij}^B \omega_j + S_{ij}^R \omega_j . \tag{2.17}$$

By definition, the background strain rate $S_{ij}^B$ in (2.17) is independent of the vorticity at $\mathbf{x}$, and thus its effect on the dynamics of the vorticity $\omega_i(\mathbf{x})$ is essentially linear. Since $s_1^B \geq 0$ and $s_3^B \leq 0$, and since $s_2^B \leq s_1^B$, the effect is to cause $\boldsymbol{\omega}$ to rotate toward alignment with the most extensional eigenvector $\mathbf{e}_1^B$ of $S_{ij}^B$. The fact that such alignment of the vorticity is seen in Figure 2.10 suggests that the quasi-linear dynamics from the first term on the right in (2.17) plays at least a significant role in the overall evolution of the vorticity field in turbulent flows. In the terminology of She *et al.* [92], this would be referred to as *kinematic nonlocality*, as distinguished from the *dynamic locality* that was the focus of their study.

From the vorticity alignments in Figure 2.11 with the *local* strain rate field induced in $R$ by the local vorticity, $\boldsymbol{\omega}$ shows substantial and essentially equal preference for pointing largely perpendicular to the most extensional and compressional eigenvectors $\mathbf{e}_1^R$ and $\mathbf{e}_3^R$ of the local strain rate $S_{ij}^R$, namely $|\mathbf{e}_1^R \cdot \mathbf{e}_\omega| \to 0$ and $|\mathbf{e}_3^R \cdot \mathbf{e}_\omega| \to 0$. This is consistent with the fact that much of the vorticity in turbulent flows concentrates into relatively compact

line-like and sheet-like structures formed by locally axisymmetric and planar background strain rate fields [8, 40]. In the former case, the axisymmetric Burgers vortex is often used as an idealized representation of such structures, while in the latter case the planar Burgers vortex sheet provides a similar idealized representation. In both cases, the two-dimensional *local* strain field induced by the vortical structure has large extensional and compressional eigenvalues with eigenvectors that are necessarily perpendicular to the vorticity, due to the geometry of the structures. The remaining eigenvalue is zero for perfectly two-dimensional structures, and will be nonzero only due to small departures from strict two-dimensionality of the structures. Its small magnitude is thus nearly always between the other two eigenvalues, and will therefore be the intermediate eigenvalue. Its eigenvector must necessarily be perpendicular to the other two, and so will necessarily be closely aligned with the vorticity itself.

This is precisely the alignment seen with $\mathbf{e}_2^R$ in Figure 2.11, where the vorticity points strongly along the direction of the intermediate eigenvector, namely $|\mathbf{e}_2^R \cdot \mathbf{e}_\omega| \to 1$. Note that this 'preferred' alignment of the vorticity with the intermediate local strain eigenvector in Figure 2.11 is not a result of the nonlinear dynamics from the second term on the right side in (2.17), but rather is a simple geometric consequence of the largely sheet-like and line-like structures into which the vorticity is formed [40].

The alignments in Figures 2.10 and 2.11 allow the relative contributions from the two terms on the right side of the inviscid vorticity dynamics in (2.17) to be understood. In particular, Figure 2.13 shows the distribution of the ratio of background and local vortex stretching rates, which is given from (2.5) as

$$\frac{|S_{ij}^B \omega_j|}{|S_{ij}^R \omega_j|} \equiv \left[ \frac{(s_i^B)^2 \left(\mathbf{e}_i^B \cdot \mathbf{e}_\omega\right)^2}{(s_j^R)^2 \left(\mathbf{e}_j^R \cdot \mathbf{e}_\omega\right)^2} \right]^{1/2} \tag{2.18}$$

It is apparent that in much of the flow this stretching ratio exceeds one, meaning that the linear stretching dynamics produced by the background (nonlocal) strain field $S_{ij}^B$ in (2.17) exceeds the nonlinear stretching dynamics from the local strain field $S_{ij}^R$. Thus, despite the overall nonlinear dynamics governing the vorticity evolution in (2.3), a substantial part of the underlying dynamics is linear and nonlocal.

This is consistent with the alignment in Figure 2.11 of the vorticity with the intermediate eigenvector of the local strain rate $S_{ij}^R$, for which the associated eigenvalue $s_2^R$ has the smallest magnitude among the three local strain eigenvalues, and thus the associated stretching is not necessarily large. By contrast, Figure 2.10 shows that the vorticity aligns with the most extensional eigenvector of the background strain rate $S_{ij}^B$, and thus is stretched by the largest of its three eigenvalues. As a result, even when $|S_{ij}^B|$ is smaller than $|S_{ij}^R|$, the background stretching may be larger than the local stretching. This is a consequence of the fact that in (2.17) vortex stretching by the local strain rate is generally not favored from

the standpoint of geometrical alignment. It is remarkable that the linear stretching dynamics from this background (nonlocal) strain field is comparable to the nonlinear stretching dynamics from the local strain field.

Further insights into the background and local dynamics may be gained by conditioning the vortex stretching ratio on the vorticity magnitude $\omega$, as shown in Figure 2.14. While there is a tendency towards smaller vortex stretching ratios for large vorticity magnitudes in Figure 2.14, the observed dependence is relatively weak. This is due to the competition between increased local strain rate magnitude (which favors local stretching) and the correspondence with nearly two-dimensional intense vortical structures (which favors background stretching) for large values of $\omega$. Unraveling the contributions of these two effects to the distribution in Figure 2.14 is an important direction for future research.

## 2.3   Exact Series Expansion for Background Strain Rate

In the preceding sections, the strain rate was decomposed into its local and nonlocal constituents through direct numerical integration of (2.11) over a cubic subdomain of length $2R$, as shown in Figure 2.5. However, such an integration is generally impractical if the background strain tensor is ever to be connected to existing computational frameworks for solving (1.2)-(1.4). In such frameworks, only local instantaneous variables at location $\mathbf{x}$ and time $t$ are typically available. As a result of this restriction, a systematic expansion of the total strain rate field $S_{ij}(\mathbf{x})$ is derived in the following, allowing the background strain rate field $S_{ij}^B(\mathbf{x})$ to be extracted in any flow. This approach is based on an expansion of the vorticity over a local spherical region of radius $R$ centered at any point $\mathbf{x}$. This leads to an exact operator that provides direct access to the background strain rate field. The operator is tested for the case of a Burgers vortex, where it is shown that the local self-induced strain field produced by the vortex can be successfully removed, and the underlying background strain field can be increasingly recovered as higher order terms are retained in the expansion. The anomalous alignment of the vorticity with respect to the eigenvectors of the total strain field is shown in that case to follow from a local switching of the principal strain axes when the vortex becomes sufficiently strong relative to the background strain. Finally, the operator is applied to obtain insights into the vorticity alignment with the background strain in DNS of homogeneous isotropic turbulence. The resulting alignment distributions are shown to be consistent with those obtained from the full numerical integration procedure outlined in the previous section.

### 2.3.1 Evaluating the Background Strain Rate Tensor

Considering the strain integrals in (2.11) and (2.14), the vorticity field within the sphere of radius $R$ can be represented by its Taylor expansion about the center point $\mathbf{x}$ as

$$\omega_l(\hat{\mathbf{x}})|_{r \leq R} = \omega_l(\mathbf{x}) + (\hat{x}_m - x_m) \left.\frac{\partial \omega_l}{\partial x_m}\right|_{\mathbf{x}} + \frac{1}{2}(\hat{x}_m - x_m)(\hat{x}_n - x_n) \left.\frac{\partial^2 \omega_l}{\partial x_m \partial x_n}\right|_{\mathbf{x}} + \cdots . \quad (2.19)$$

Recalling that $x_m - \hat{x}_m \equiv r_m$ and using $a_l, b_{lm}, c_{lmn}, \ldots$ to abbreviate the vorticity and its derivatives at $\mathbf{x}$, we can write (2.19) as

$$\omega_l(\hat{\mathbf{x}})|_{r \leq R} \equiv a_l - r_m b_{lm} + \frac{1}{2} r_m r_n c_{lmn} - \cdots . \quad (2.20)$$

Substituting (2.20) into the $S_{ij}^R$ integral in (2.14) and changing the integration variable to $\mathbf{r} = \mathbf{x} - \hat{\mathbf{x}}$, the strain tensor at $\mathbf{x}$ produced by the vorticity in $R$ is

$$S_{ij}^R(\mathbf{x}) = \frac{3}{8\pi} \int_{r \leq R} (\epsilon_{ikl} r_j + r_i \epsilon_{jkl}) \frac{r_k}{r^5} \left[ a_l - r_m b_{lm} + \frac{r_m r_n}{2} c_{lmn} - \cdots \right] d\mathbf{r} . \quad (2.21)$$

This integral can be solved in spherical coordinates centered on $\mathbf{x}$, with $r_1 = r \sin\theta \cos\phi$, $r_2 = r \sin\theta \sin\phi$, and $r_3 = r \cos\theta$ for $r \in [0, R]$, $\theta \in [0, \pi]$, and $\phi \in [0, 2\pi)$. To integrate (2.21) note that

$$\int_{r \leq R} \frac{r_k r_j}{r^5} d\mathbf{r} = \frac{4\pi}{3} \delta_{jk} \int_0^R \frac{1}{r} dr , \quad (2.22a)$$

$$\int_{r \leq R} \frac{r_k r_j r_m}{r^5} d\mathbf{r} = 0 , \quad (2.22b)$$

$$\int_{r \leq R} \frac{r_k r_j r_m r_n}{r^5} d\mathbf{r} = \frac{2\pi}{15} R^2 \left( \delta_{mn}\delta_{jk} + \delta_{mj}\delta_{kn} + \delta_{mk}\delta_{jn} \right) . \quad (2.22c)$$

The resulting local strain rate tensor at $\mathbf{x}$ is then

$$S_{ij}^R(\mathbf{x}) = \frac{R^2}{40} c_{lmn} \left( \epsilon_{ijl}\delta_{mn} + \epsilon_{jil}\delta_{mn} + \epsilon_{inl}\delta_{mj} + \epsilon_{jnl}\delta_{mi} + \epsilon_{iml}\delta_{nj} + \epsilon_{jml}\delta_{ni} \right) + O(R^4) , \quad (2.23)$$

where the contribution from the $a_l$ term in (2.21) is zero since $\epsilon_{ijl} = -\epsilon_{jil}$. For the same reason the first two terms in (2.23) also cancel, giving

$$S_{ij}^R(\mathbf{x}) = \frac{R^2}{40} c_{lmn} \left( \epsilon_{inl}\delta_{mj} + \epsilon_{jnl}\delta_{mi} + \epsilon_{iml}\delta_{nj} + \epsilon_{jml}\delta_{ni} \right) + O(R^4) . \quad (2.24)$$

Recalling that $c_{lmn} = c_{lnm} \equiv \partial^2 \omega_l / \partial x_m \partial x_n$, and contracting with the $\delta$ and $\epsilon$ in (2.24), gives

$$S_{ij}^R(\mathbf{x}) = \frac{R^2}{20} \left[ \frac{\partial}{\partial x_j} \left( \epsilon_{iml} \frac{\partial \omega_l}{\partial x_m} \right) + \frac{\partial}{\partial x_i} \left( \epsilon_{jml} \frac{\partial \omega_l}{\partial x_m} \right) \right] + O(R^4) . \quad (2.25)$$

Note that $\epsilon_{iml} \partial \omega_l / \partial x_m \equiv (\nabla \times \boldsymbol{\omega})_i$ and

$$\nabla \times \boldsymbol{\omega} = \nabla \times (\nabla \times \mathbf{u}) = \nabla (\nabla \cdot \mathbf{u}) - \nabla^2 \mathbf{u} \,, \tag{2.26}$$

so for an incompressible flow $(\nabla \cdot \mathbf{u} \equiv 0)$ the local strain rate tensor at $\mathbf{x}$ becomes

$$S_{ij}^R(\mathbf{x}) = -\frac{R^2}{20} \nabla^2 \left( \frac{\partial u_i}{\partial x_j} + \frac{\partial u_j}{\partial x_i} \right) + O(R^4) \,. \tag{2.27}$$

From (2.15), with $S_{ij}^R$ from (2.27) we obtain the background strain tensor as

$$S_{ij}^B(\mathbf{x}) = S_{ij}(\mathbf{x}) + \frac{R^2}{10} \nabla^2 S_{ij}(\mathbf{x}) + O(R^4) \,. \tag{2.28}$$

The remaining terms in (2.28) result from the higher-order terms in (2.20). These terms are readily obtained by rewriting (2.21) as a series expansion for the local strain rate $S_{ij}^R$, namely

$$S_{ij}^R(\mathbf{x}) = \sum_{n=0}^{\infty} \frac{3(-1)^n}{8\pi n!} \left[ \frac{\partial^n \omega_l}{\partial x_m \partial x_p \dots} \right] \int_{r \leq R} \left( \epsilon_{ikl} \frac{r_j}{r} + \epsilon_{jkl} \frac{r_i}{r} \right) \frac{r_k}{r} r^{n-3} \left[ \frac{r_m r_p \cdots}{r^n} \right] d\mathbf{r} \,. \tag{2.29}$$

Writing the differential in spherical coordinates as $d\mathbf{r} = r^2 dr d\Omega$, where $d\Omega = \sin \theta d\phi d\theta$, we obtain

$$S_{ij}^R(\mathbf{x}) = \sum_{n=0}^{\infty} \frac{3(-1)^n}{8\pi n!} \left[ \frac{\partial^n \omega_l}{\partial x_m \partial x_p \dots} \right] \int_0^R r^{n-1} dr \int_\Omega \left( \epsilon_{ikl} \frac{r_j}{r} + \epsilon_{jkl} \frac{r_i}{r} \right) \left[ \frac{r_k r_m r_p \cdots}{r^{n+1}} \right] d\Omega \,. \tag{2.30}$$

In order to solve the integrals in (2.29) we note the general integral relations

$$\int_\Omega \frac{r_m r_p r_q r_s \cdots}{r^n} d\Omega = 0 \,, \quad n = \text{odd} \tag{2.31a}$$

$$\int_\Omega \frac{r_m r_p r_q r_s \cdots}{r^n} d\Omega = \frac{4\pi}{(n+1)!!} \left[ \delta_{mp} \delta_{qs} \dots + \delta_{mq} \delta_{rs} \dots + \cdots \right] \,, \quad n = \text{even} \tag{2.31b}$$

where the terms in the brackets on the right-hand side of (2.31b) represent all possible combinations of delta functions for the indices $(m, p, q, s, \dots)$. For any $n$, there are $(n-1)!!$ delta function terms, and each term consists of $n/2$ delta functions. The double factorial !! in (2.31b) is defined as

$$n!! \equiv n(n-2)(n-4) \cdots \,, \tag{2.32}$$

with the definitions $0!! \equiv 1$ and $(-1)!! \equiv 1$.

Using (2.31a) it can be shown that all odd order terms in (2.30) are zero. Considering

the $n = 0$ term in (2.30), the integral over $d\Omega$ is solved using (2.31) as

$$\int_\Omega \left( \epsilon_{ikl} \frac{r_j r_k}{r^2} + \epsilon_{jkl} \frac{r_i r_k}{r^2} \right) d\Omega = \frac{4\pi}{3} \left( \epsilon_{ijl} + \epsilon_{jil} \right) . \qquad (2.33)$$

However, $\epsilon_{ijl} = -\epsilon_{jil}$ and thus the entire $n = 0$ term in (2.30) is zero. With this result we obtain nonzero terms only for $n \geq 2$, and the integral over $dr$ in (2.30) is solved as

$$\int_0^R r^{n-1} dr = \frac{R^n}{n} . \qquad (2.34)$$

We can then write (2.30) as

$$S_{ij}^R(\mathbf{x}) = \sum_{n=2,even}^\infty \frac{3R^n}{8\pi n! \cdot n} \left[ \frac{\partial^n \omega_l}{\partial x_m \partial x_p \ldots} \right] \int_\Omega \left( \epsilon_{ikl} \frac{r_j}{r} + \epsilon_{jkl} \frac{r_i}{r} \right) \left[ \frac{r_k r_m r_p \cdots}{r^{n+1}} \right] d\Omega , \qquad (2.35)$$

where once again we note that only the $n = even$ terms are nonzero, and since $n = even$ we have $(-1)^n = 1$ always. For the remaining integrals over $d\Omega$, from (2.31b) we obtain

$$\epsilon_{ikl} \int_\Omega \frac{r_j r_k r_m r_p \cdots}{r^{n+2}} d\Omega = \frac{4\pi}{(n+3)!!} \epsilon_{ikl} \left[ \delta_{jk} \delta_{mp} \ldots + \delta_{jm} \delta_{kp} \ldots + \cdots \right] , \qquad (2.36)$$

where there are now $(n+1)!!$ terms in the square brackets. Note however, that the terms involving $\delta_{jk}$ in (2.36) yield terms involving $\epsilon_{ijl}$ when contracted with $\epsilon_{ikl}$. These terms exactly cancel the corresponding $\epsilon_{jil}$ terms from the solution to the integral of $[r_i r_k r_m \ldots]/r^{n+2}$, similar to the reasoning used to obtain the result in (2.33). Thus, the $(n-1)!!$ terms involving $\delta_{jk}$ in (2.36) can all be neglected, leaving $[(n+1)!! - (n-1)!!]$ terms in the square brackets on the right-hand side. When contracted with the derivatives of $\omega_l$ in (2.35), it can be shown that *all* of the remaining terms in (2.36) are given by

$$\frac{4\pi \epsilon_{ikl}}{(n+3)!!} \left[ \delta_{jm} \delta_{kp} \delta_{qs} \ldots \right] \left[ \frac{\partial^n \omega_l}{\partial x_m \partial x_p \partial x_q \partial x_s \ldots} \right] = \frac{4\pi}{(n+3)!!} (\nabla^2)^{n/2-1} \frac{\partial}{\partial x_j} \left[ \epsilon_{ipl} \frac{\partial \omega_l}{\partial x_p} \right] . \qquad (2.37)$$

Note that there are $[(n+1)!! - (n-1)!!]$ remaining terms in (2.36), and all yield the result in (2.37) due to the invariance of the left-hand side of (2.37) to the order of $(m, n, p, q \ldots)$.

Substituting (2.37) into (2.35) then gives

$$S_{ij}^R(\mathbf{x}) = \sum_{n=2,even}^\infty \frac{3R^n \left[ (n+1)!! - (n-1)!! \right]}{2n!(n+3)!! n} (\nabla^2)^{n/2-1} \left[ \frac{\partial}{\partial x_j} \left( \epsilon_{ipl} \frac{\partial \omega_l}{\partial x_p} \right) + \frac{\partial}{\partial x_i} \left( \epsilon_{jpl} \frac{\partial \omega_l}{\partial x_p} \right) \right] . \qquad (2.38)$$

However, we note that by definition

$$\epsilon_{ipl} \frac{\partial \omega_l}{\partial x_p} \equiv (\nabla \times \boldsymbol{\omega})_i , \qquad (2.39)$$

and from the kinematic relation in (2.26) we obtain

$$\epsilon_{ipl} \frac{\partial \omega_l}{\partial x_p} = -\nabla^2 u_i \tag{2.40}$$

for incompressible flows, where $\nabla \cdot \mathbf{u} = 0$. Substitution of (2.40) into (2.38) then yields

$$S_{ij}^R(\mathbf{x}) = -\sum_{n=2,even}^{\infty} \frac{3\ R^n\ [(n+1)!! - (n-1)!!]}{2n!(n+3)!!n} \left(\nabla^2\right)^{n/2} \left(\frac{\partial u_i}{\partial x_j} + \frac{\partial u_j}{\partial x_i}\right). \tag{2.41}$$

From the definition of the strain rate $S_{ij}$ in (2.4) we can write

$$S_{ij}^R(\mathbf{x}) = -\sum_{n=2,even}^{\infty} \frac{3R^n\ [(n+1)!! - (n-1)!!]}{n!(n+3)!!n} \left(\nabla^2\right)^{n/2} S_{ij}, \tag{2.42}$$

and simplification of the double factorial terms yields

$$S_{ij}^R(\mathbf{x}) = -\sum_{n=2,even}^{\infty} \frac{3R^n}{n!(n+3)(n+1)} \left(\nabla^2\right)^{n/2} S_{ij}. \tag{2.43}$$

From (2.15) we then obtain the background strain rate $S_{ij}^B(\mathbf{x})$ as

$$S_{ij}^B(\mathbf{x}) = \sum_{n=0,even}^{\infty} \frac{3R^n}{n!(n+3)(n+1)} \left(\nabla^2\right)^{n/2} S_{ij}, \tag{2.44}$$

where we note that the $n = 0$ term in (2.44) yields simply $S_{ij}$. In order to obtain the final result, we can change the variable $n$ to $(2n-2)$ and carry out the summation over $n = 1, 2, 3, \ldots$, which finally gives

$$S_{ij}^B(\mathbf{x}) = \sum_{n=1}^{\infty} \frac{3R^{2n-2}}{(2n-2)!(4n^2-1)} \left(\nabla^2\right)^{n-1} S_{ij}. \tag{2.45}$$

The final result in (2.45) is an operator that extracts the nonlocal background strain rate tensor $S_{ij}^B$ at any point $\mathbf{x}$ from the total strain rate tensor $S_{ij}$. For the Taylor expansion in (2.19), this operator involves Laplacians of the total strain rate field $S_{ij}(\mathbf{x})$.

### 2.3.2 Practical Implementation

When using (2.45) to examine the local alignment of any concentrated vortical structure with the principal axes of the background strain rate field $S_{ij}^B(\mathbf{x})$ in which it resides, the radius $R$ must be taken sufficiently large that the spherical region $|\mathbf{x}' - \mathbf{x}| \leq R$ encloses essentially all the vorticity associated with the structure, so that its local induced strain rate field is fully accounted for. Generally, as $R$ increases it is necessary in (2.45) to retain terms of increasingly higher order $n$ to maintain a sufficient representation of $\boldsymbol{\omega}(\mathbf{x}')$

over the spherical region. Thus for any vortical structure having a characteristic gradient lengthscale $\lambda_\nu$, it can be expected that $R$ must be of the order of $\lambda_\nu$, and $n$ will then need to be sufficiently large to adequately represent the vorticity field within this sphere. However, since the local gradient lengthscale in the vorticity field in a turbulent flow is determined by an equilibrium between strain and diffusion, the vorticity field over the lengthscale $\lambda_\nu$ will be relatively smooth, and thus relatively low values of $n$ may suffice to give a usable representation of $\boldsymbol{\omega}(\mathbf{x}')$. This is examined in the following section.

## 2.4   Background Strain Expansion Test Case: Burgers Vortex

The equilibrium Burgers vortex [8, 9, 25, 58] is formed from vorticity in a fluid with viscosity $\nu$ by a spatially uniform, irrotational, axisymmetric background strain rate field $S_{ij}^B$ that has a single extensional principal strain rate $S_{zz}$ directed along the $z$ axis, as shown in Fig. 2.15. This simple flow, often regarded as an idealized model of the most concentrated vortical structures in turbulent flows, provides a test case for the result in (2.45). The combined strain rate field $S_{ij}(\mathbf{x})$ produced by the vortex and the background strain flow should, when applied in (2.45), produce the underlying background strain field $(S_{rr}^B, S_{\theta\theta}^B, S_{zz}^B) = (-\frac{1}{2}, -\frac{1}{2}, 1)S_{zz}$ at all $\mathbf{x}$ when $R \to \infty$ and all orders $n$ are retained. For finite $R$ and $n$, the resulting $S_{ij}^B(\mathbf{x})$ will reflect the convergence properties of (2.45).

### 2.4.1   Strain Rate Tensor

The equilibrium Burgers vortex aligned with the extensional principal axis of the background strain rate field has a vorticity field given by (2.16). Following [8], $\lambda_\nu$ is taken as the full width of the vortical structure at which $\omega_z$ has decreased to one-fifth of its peak value, for which $\alpha = 4\ln 5$. When diffusion of the vorticity is in equilibrium [8] with the background strain, then

$$\lambda_\nu = \sqrt{8\alpha} \left(\frac{\nu}{S_{zz}}\right)^{1/2}. \tag{2.46}$$

The combined velocity field $\mathbf{u}(\mathbf{x})$ produced by the vortex and the irrotational background strain is given by the cylindrical components

$$u_r(r, \theta, z) = -\frac{S_{zz}}{2}r, \tag{2.47a}$$

$$u_\theta(r, \theta, z) = \frac{\Gamma}{2\pi\lambda_\nu}\frac{1}{\eta}\left[1 - \exp\left(-\alpha\eta^2\right)\right], \tag{2.47b}$$

$$u_z(r, \theta, z) = S_{zz}z. \tag{2.47c}$$

The combined strain rate tensor for such a Burgers vortex is thus

$$S_{ij}(\mathbf{x}) = \begin{bmatrix} -S_{zz}/2 & S_{r\theta}^v & 0 \\ S_{r\theta}^v & -S_{zz}/2 & 0 \\ 0 & 0 & S_{zz} \end{bmatrix} , \qquad (2.48)$$

where $S_{r\theta}^v$ is the shear strain rate induced by the vortex, given by

$$S_{r\theta}^v(\mathbf{x}) = \frac{\Gamma}{\pi \lambda_\nu^2} \left[ \left( \alpha + \frac{1}{\eta^2} \right) \exp\left( -\alpha \eta^2 \right) - \frac{1}{\eta^2} \right] . \qquad (2.49)$$

From (2.48), $S_{ij}(\mathbf{x})$ has one extensional principal strain rate equal to $S_{zz}$ along the $\hat{\mathbf{z}}$ axis, with the remaining two principal strain axes lying in the $r$-$\theta$ plane and corresponding to the principal strain rates

$$s = -\frac{1}{2} S_{zz} \pm |S_{r\theta}^v| . \qquad (2.50)$$

As long as the largest $s$ in (2.50) is smaller than $S_{zz}$, the most extensional principal strain rate $s_1$ of $S_{ij}$ will be $S_{zz}$, and the corresponding principal strain axis will point in the $\hat{\mathbf{z}}$ direction. The vorticity is then aligned with the most extensional eigenvector of $S_{ij}$. This remains the case until the vortex becomes sufficiently strong relative to the background strain rate that $s > S_{zz}$, namely

$$|S_{r\theta}^v| \geq \frac{3}{2} S_{zz} , \qquad (2.51)$$

which from (2.49) occurs wherever

$$\left( \alpha + \frac{1}{\eta^2} \right) \exp(-\alpha \eta^2) - \frac{1}{\eta^2} \geq \frac{3\pi}{2} \left( \frac{\Gamma/\lambda_\nu^2}{S_{zz}} \right)^{-1} . \qquad (2.52)$$

At any $\eta$ for which (2.52) is satisfied, the most extensional principal axis of the combined strain rate tensor $S_{ij}(\mathbf{x})$ will switch from the $\hat{\mathbf{z}}$ direction to instead lie in the $r$-$\theta$ plane. Since the vorticity vector everywhere points in the $\hat{\mathbf{z}}$ direction, wherever (2.52) is satisfied the principal axis of $S_{ij}$ that is aligned with the vorticity will switch from the most extensional eigenvector to the intermediate eigenvector. This alignment switching is purely a result of the induced strain field $S_{ij}^v(\mathbf{x})$ locally dominating the background strain field $S_{ij}^B(\mathbf{x})$.

The dimensionless vortex strength parameter

$$\Omega \equiv \left[ \frac{\Gamma/\lambda_\nu^2}{S_{zz}} \right] = \frac{\pi}{\alpha} \frac{\omega_{max}}{S_{zz}} \qquad (2.53)$$

on the right-hand side of (2.52) characterizes the relative strength of the background strain and the induced strain from the vortical structure, where $\omega_{max}$ is obtained from (2.16) at $\eta = 0$. For

$$\Omega < \Omega^* \approx 2.45 , \qquad (2.54)$$

the background strain rate $S_{zz}$ is everywhere larger than the largest $s$ in (2.50), and thus no alignment switching occurs at any $\eta$. For $\Omega > \Omega^*$, alignment switching will occur over the limited range of $\eta$ values that satisfy (2.52). With increasing values of $\Omega$, more of the vorticity field will be aligned with the intermediate principal axis of the *combined* strain rate tensor, even though all of the vorticity field remains aligned with the most extensional principal axis of the *background* strain rate tensor.

Figure 2.16 shows the vorticity $\omega_z$ and the induced shear strain component $-S_{r\theta}^v$ as a function of $\eta$. The horizontal dashed lines correspond to three different values of $\Omega$, and indicate the range of $\eta$ values where the alignment switching in (2.52) occurs for each $\Omega$. Wherever $-S_{r\theta}^v$ is above the dashed line for a given $\Omega$, the vorticity will be aligned with the local intermediate principal axis of the combined strain rate field.

In principle, regardless of the vortex strength parameter $\Omega$, at any $\eta$ the result in (2.45) can reveal the alignment of the vorticity with the most extensional principal axis of the background strain field $S_{ij}^B$. However, this requires $R$ to be sufficiently large that a sphere with diameter $2R$, centered at the largest $\eta$ for which $-S_{r\theta}^v$ in Figure 2.16 is still above the horizontal dashed line, will enclose essentially all of the vorticity associated with the vortical structure. As $\Omega$ increases, the required $R$ will increase accordingly as dictated by (2.52), and as $R$ is increased the required $n$ in (2.45) also increases.

Irrespective of the value of $\Omega$, when (2.45) is applied to the combined strain rate field $S_{ij}(\mathbf{x})$ in (2.48) and (2.49), if $\tilde{R} \equiv (R/\lambda_\nu) \to \infty$ and all orders $n$ are retained then the resulting $S_{ij}^B(\mathbf{x})$ should recover the background strain field, namely

$$S_{r\theta}^B \to 0 \tag{2.55}$$

for all $\mathbf{x}$, and the vorticity should show alignment with the most extensional principal axis of $S_{ij}^B$. For finite $R/\lambda_\nu$ and various orders $n$, the convergence of $S_{ij}^B$ from (2.45) to this background strain field is examined below.

### 2.4.2 Convergence of the Background Strain

The accuracy with which (2.45) can recover the background strain field $S_{ij}^B(\mathbf{x})$ that acts on a concentrated vortical structure depends on how well the expansion in (2.19) represents the vorticity field within the local spherical neighborhood $R$. Figure 2.17 shows the results of a local sixth-order Taylor series approximation for the vorticity in (2.16) at various radial locations across the Burgers vortex. In each panel, the blue square marks the location $\mathbf{x}$ at which the sphere is centered, and the red dashed curve shows the resulting Taylor series approximation for the vorticity. On the axis of the vortex, the approximated vorticity field correctly accounts for most of the circulation in the vortex, and thus the induced strain field from the vortex will be reasonably approximated. Off the axis, the approximation becomes increasingly poorer, but the $1/r^2$ decrease in the Biot-Savart kernel in (2.11) nevertheless

renders it adequate to account for most of the vortex-induced strain rate field. At the largest radial location, corresponding to the bottom right panel of Figure 2.17, the approximation becomes relatively poor, however at large $\eta$ values the vortex-induced strain is sufficiently small that it is unlikely to lead to alignment switching for typical $\Omega$ values.

Figures 2.18-2.20 show the shear component $S_{r\theta}^B(\eta)$ of the background strain rate tensor obtained via (2.45) for various $n$ and $\tilde{R}$ as a function of $\eta$. In each Figure, the black curve shows the total strain rate $S_{r\theta}(\eta)$ and the colored curves show the background strain rate $S_{r\theta}^B(\eta)$ from (2.45) for the $(n, \tilde{R})$ combinations listed. The horizontal dashed line corresponding to $\Omega = (3/2)\Omega^*$ reflects the relative vortex strength, and shows the range of $\eta$ where the anomalous alignment switching occurs due to the vortex-induced strain field. Wherever the $-S_{r\theta}^B$ curves are above this line, the vorticity there will be aligned with the intermediate principal axis of the *combined* strain rate tensor $S_{ij}$. Figure 2.18 examines the effect of increasing the radius $\tilde{R}$ of the spherical region for fixed order $n = 6$. It is apparent that with increasing $\tilde{R}$ the resulting $-S_{r\theta}^B$ converges toward the correct background strain field in (2.55). For the value of $\Omega$ shown, it can be seen that for $R \gtrsim 0.5\lambda_\nu$ the resulting $S_{r\theta}^B$ is everywhere below the horizontal dashed line, indicating that the vorticity everywhere is aligned with the most extensional principal axis of the resulting background strain rate tensor $S_{ij}^B(\mathbf{x})$ from (2.45).

In Figure 2.19 similar results are shown for the effect of increasing the order $n$ of the expansion for the vorticity field for fixed $\tilde{R} = 0.65$. It is apparent that the effect of $n$ is somewhat smaller than for $\tilde{R}$ in Figure 2.18. Moreover, the results suggest that the series in (2.45) alternates with increasing order $n$. For this $\Omega$ and $\tilde{R}$, even $n = 3$ is seen to be sufficient to remove most of the vortex-induced shear strain, and thus reduce $S_{r\theta}^B(\mathbf{x})$ below the horizontal dashed line. For these parameters, the $S_{r\theta}^B$ field from (2.45) would thus reveal alignment of the vorticity with the most extensional principal axis of the background strain tensor throughout the entire field.

Figure 2.20 shows the combined effects of increasing both $\tilde{R}$ and $n$, in accordance with the expectation that larger $\tilde{R}$ should require a higher order $n$ to adequately represent the vorticity field within the spherical region. The shear strain rate field shows convergence to the correct background strain field in (2.55). The convergence of the shear strain rate $S_{r\theta}^B(\mathbf{x})$ to zero in the vicinity of the vortex core is of particular importance. The systematic reduction in the peak remaining shear stress indicates that, even for increasingly stronger vortices or increasingly weaker background strain fields as measured by $\Omega$, the resulting $S_{r\theta}^B(\mathbf{x})$ from (2.45) will reveal the alignment of all the vorticity in such a structure with the most extensional principal strain axis of the background strain field.

## 2.5   Vorticity Alignment Using Background Strain Expansion

Having seen in the previous Section how (2.45) is able to reveal the expected alignment of vortical structures with the most extensional eigenvector of the *background* strain rate in

which they reside, in this Section we apply it to obtain insights into the vorticity alignment in turbulent flows. In particular, we examine the alignment at every point $\mathbf{x}$ of the vorticity $\boldsymbol{\omega}$ relative to the eigenvectors of the total strain rate tensor field $S_{ij}(\mathbf{x})$ and those of the background strain field data $S_{ij}^B(\mathbf{x})$. This analysis uses data from the same highly-resolved, three-dimensional DNS of statistically stationary, forced, homogeneous, isotropic turbulence [90, 91] described in Section 2.2. The superfine resolution of this DNS makes it possible to apply the result in (2.45) for relatively high orders $n$, which require accurate evaluation of high-order derivatives of the DNS data. In Schumacher $et\ al.$ [91] it was demonstrated that derivatives up to order six are statistically converged. More details on the numerical simulations are given in Refs. [90, 91].

The background strain rate tensor field $S_{ij}^B(\mathbf{x})$ is first extracted via (2.45) from $S_{ij}(\mathbf{x})$ for $n = 3$ and various $(R/\eta_K)$. Higher-order evaluation of the background strain rate is not feasible, as the results in Ref. [91] show that only spatial derivatives of the velocity field up to order six can be accurately obtained from these high-resolution DNS data. For $n = 4$, the expansion in (2.45) involves seventh-order derivatives of the velocity field, and the background strain evaluation becomes limited due to the grid resolution. The results are shown and compared in Figure 2.21, where the shear component $S_{12}$ of the full strain rate tensor is shown at the top, and the corresponding nonlocal (background) component $S_{12}^B$ and local component $S_{12}^R$ are shown, respectively, in the left and right columns for $(R/\eta_K) = 2.5$ ($top\ row$), 3.5 ($middle\ row$), and 4.5 ($bottom\ row$). Consistent with the results from the Burgers vortex in Figure 2.18-2.20, as $(R/\eta_K)$ increases the magnitude of the extracted local strain rate in the right column increases. However, for the largest $(R/\eta_K) = 4.5$ case, $n = 3$ appears to be too small to adequately represent the local vorticity field. This leads to truncation errors which are manifested as strong ripples in the background and local strain fields (see panels (f) and (g)).

The results in Figure 2.21 thus indicate that radii up to $(R/\eta_K) = 3.5$ in combination with $n = 3$ can be used to assess alignment of the vorticity vector with the eigenvectors of the background strain rate field. Figure 2.22 shows the probability densities of the alignment cosines for the vorticity vector with the total strain rate tensor and with the background strain rate tensors from (2.45). We compare $S_{ij}$ (Figure 2.22a) with $S_{ij}^B$ for $(R/\eta_K) = 2.5, n = 3$ (Figure 2.22b) and $S_{ij}^B$ for $(R/\eta_K) = 3.5, n = 3$ (Figure 2.22c). The results for alignment with the total strain rate tensor are identical to those in Figure 2.1, and are shown in Figure 2.22a for comparison with the background alignments in Figures 2.22b and c.

Consistent with Figure (2.10), the results in Figure 2.22 (b) and (c) obtained for the alignment cosines of the vorticity vector with the $background$ strain rate tensor $S_{ij}^B$ from (2.45) show a significant decrease in alignment with the intermediate eigenvector, and an increase in alignment with the most extensional eigenvector. While data in panel (b) show only a slight change compared to those in (a), the results in panel (c) demonstrate that the

decomposition can indeed diminish the anomalous alignment significantly. This is consistent with the results in Section 2.2 and with the hypothesis that the alignment switching mechanism due to the local contribution $S_{ij}^R$ to the total strain rate tensor is the primary reason for the anomalous alignment seen in earlier studies. While a more detailed study is needed to examine possible nonequilibrium contributions to the alignment distributions associated with eigenvector rotations of the background strain field, as well as to definitively determine the $R$ and $n$ convergence of the background strain rate tensor in Figure 2.21, the present findings support both the validity of the result in (2.45) for extracting the background strain rate tensor field $S_{ij}^B(\mathbf{x})$ from the total strain rate tensor field $S_{ij}(\mathbf{x})$, and the hypothesis that at least much of the anomalous alignment of vorticity in turbulent flows is due to the differences between the total and background strain rate tensors and the resulting alignment switching noted herein.

## 2.6    Connection Between Vorticity Alignment and Anisotropy Evolution

At the beginning of this chapter, it was noted that the anisotropy tensor $a_{ij}$ is rigorously connected to the vorticity alignment through the double Biot-Savart integral relation in (2.2). Since the two-point vorticity fluctuation appearing in this relation is a small-scale quantity that depends on the vorticity alignment, there exists a connection between vorticity alignment and the anisotropy in turbulent flows. While establishing a more rigorous connection requires additional insights into how the two-point vorticity fluctuation correlation is exactly related to the vorticity alignment, certain heuristic conclusions concerning the anisotropy evolution can be obtained from the studies outlined herein.

Most significantly, the vorticity alignment studies in this chapter have revealed a substantial nonlocal, quasi-linear aspect to the vorticity dynamics in turbulent flows. The alignment of the vorticity with the most extensional eigenvector of the background strain rate tensor suggests that the turbulence responds in a linear fashion to at least *some* nonlocal measure of the strain rate. With respect to vorticity alignment, this nonlocal tensor is the background strain rate tensor defined in (2.15) and (2.45). In the next chapter, the evolution of the anisotropy is shown to depend on a nonlocal measure of the strain that is qualitatively similar to (2.45), where the principal nonlocality affecting the anisotropy has its origins in the exact integral relation for the pressure-strain correlation $\Pi_{ij}$.

With respect to the quasi-linearity of the vorticity dynamics, it can be seen that the time dynamics of $\overline{u_i' u_j'}$ from (2.2) are completely determined by the time-dynamics of the two-point vorticity fluctuation correlation. Thus, if this fluctuation correlation behaves in a quasi-linear fashion over a significant fraction of the flow, as would seem reasonable given the quasi-linearity of the vorticity dynamics, then it is reasonable to expect that the Reynolds stresses, and hence the anisotropy, may also behave in a similar quasi-linear manner. In the next chapter it is shown that quasi-linearization of the anisotropy dynamics, which is loosely motivated by the quasi-linearity of the vorticity dynamics noted herein, is

sufficient to obtain the principal nonequilibrium response of the anisotropy in real turbulent flows. Additional details of the connection between vorticity alignment and the anisotropy evolution are outlined in the next chapter.
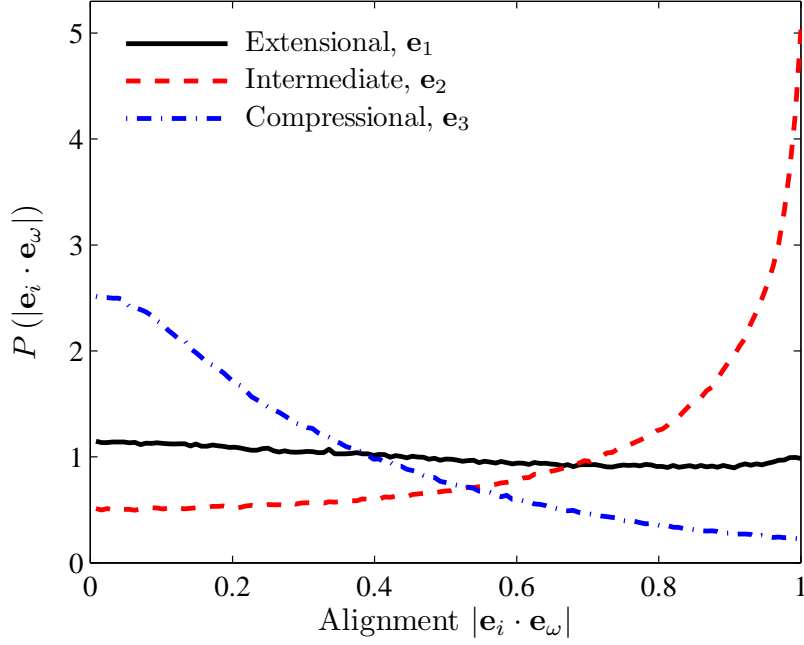
Figure 2.1: Distributions of alignment cosines $|\mathbf{e}_i \cdot \mathbf{e}_\omega|$ between the vorticity vector and eigenvectors of the total strain rate $S_{ij}$ using high-resolution $Re_\lambda = 107$ DNS of homogeneous, isotropic turbulence [90, 91].
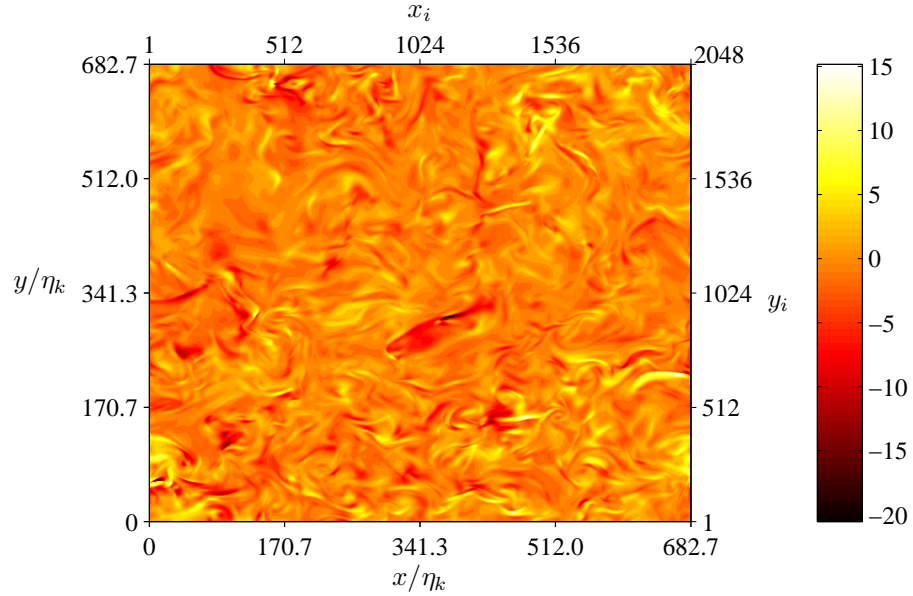


Figure 2.2: Instantaneous snapshot of total strain rate component field $S_{12}(\mathbf{x})$ in a two-dimensional slice through a highly-resolved three-dimensional ($2048^3$) DNS of homogeneous, isotropic turbulence [90, 91]. Axes are given both in grid coordinates ($i = 1 \dots 2048$) and normalized by the Kolmogorov length $\eta_K$.
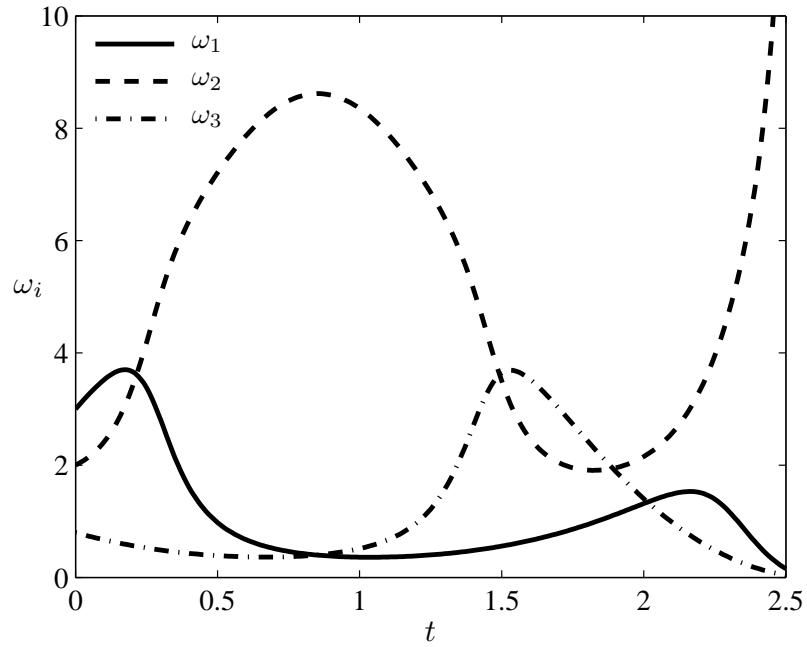
Figure 2.3: Evolution of vorticity vector in principal strain coordinates for the restricted Euler equations (e.g. Ref. [70]). The initial conditions are taken from Nomura and Post [70] and are $\omega_i(0) = [3.0, 2.0, 0.8]$ and $s_i(0) = [2.4, 0.2, -2.6]$.
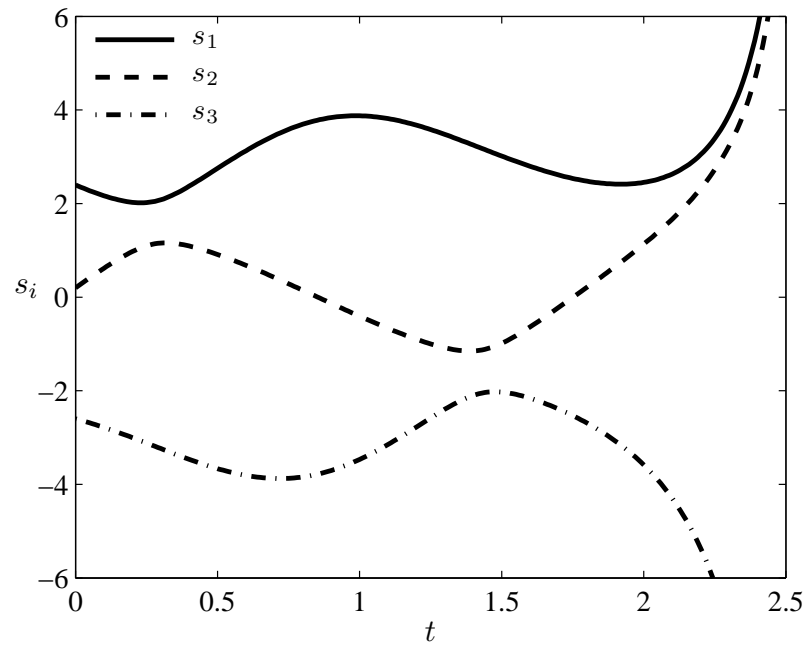


Figure 2.4: Evolution of strain eigenvalues for the restricted Euler equations (e.g. Ref. [70]). The initial conditions are taken the same as in Figure 2.3.
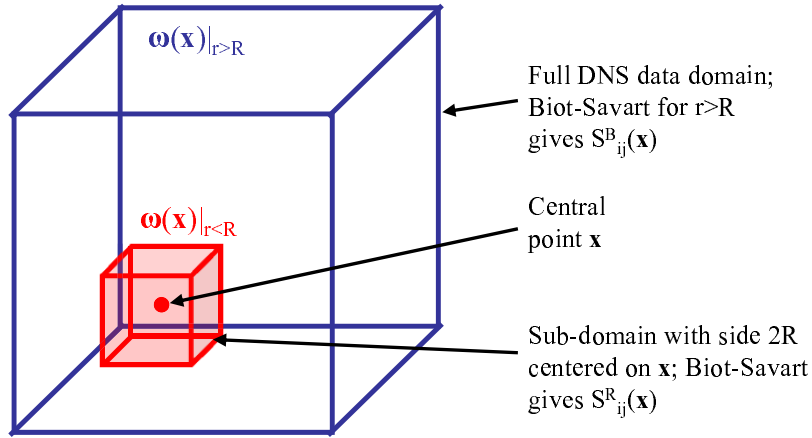
Figure 2.5: Schematic of the decomposition of the vorticity field in the vicinity of any point **x** into local and nonlocal parts; the Biot-Savart integral in (2.14) over each part gives the local and nonlocal (background) contributions to the total strain rate tensor $S_{ij}$ at **x**.
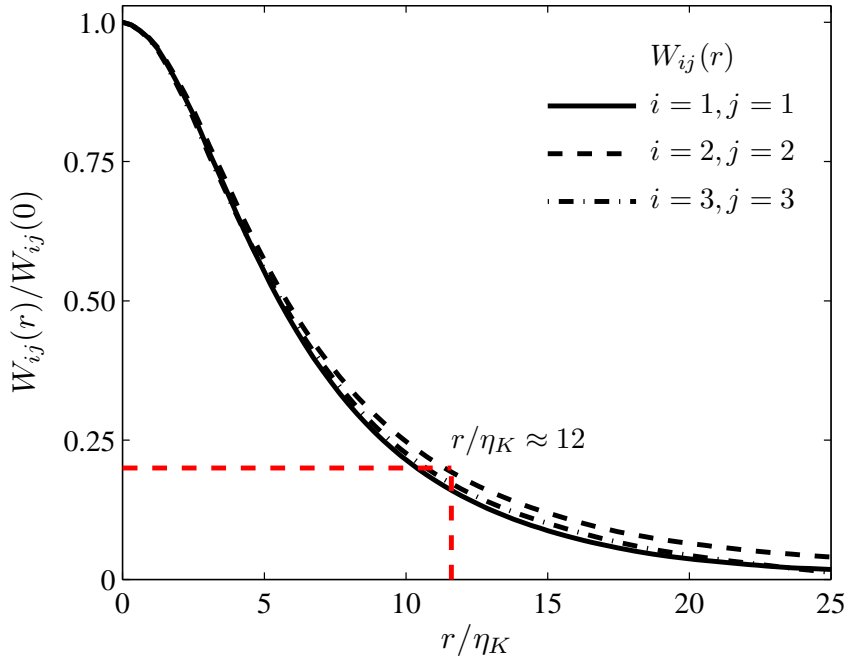


Figure 2.6: Two-point vorticity correlation for DNS of homogeneous, isotropic turbulence [90, 91] where $W_{ij}(r) \equiv \omega_i(\mathbf{x} + \mathbf{r})\omega_j(\mathbf{x})$ and $r = |\mathbf{r}|$. The red dashed lines show that the longitudinal correlations decay to 20% of their maximum values at $R \approx 12\eta_K$.
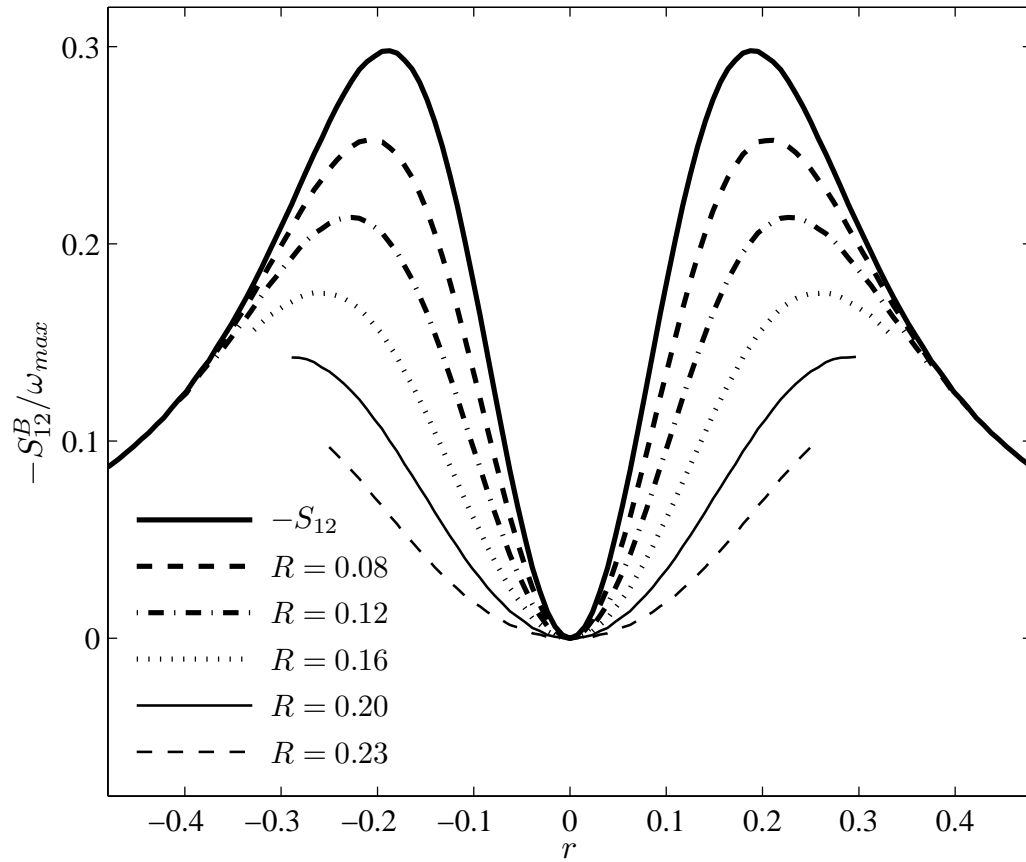
Figure 2.7: Convergence of background strain rate $S_{12}^B(r)$ to zero for all $r$ in the Burgers vortex test case by calculating (2.11) using direct numerical integration for increasing cutoff radius $R$.
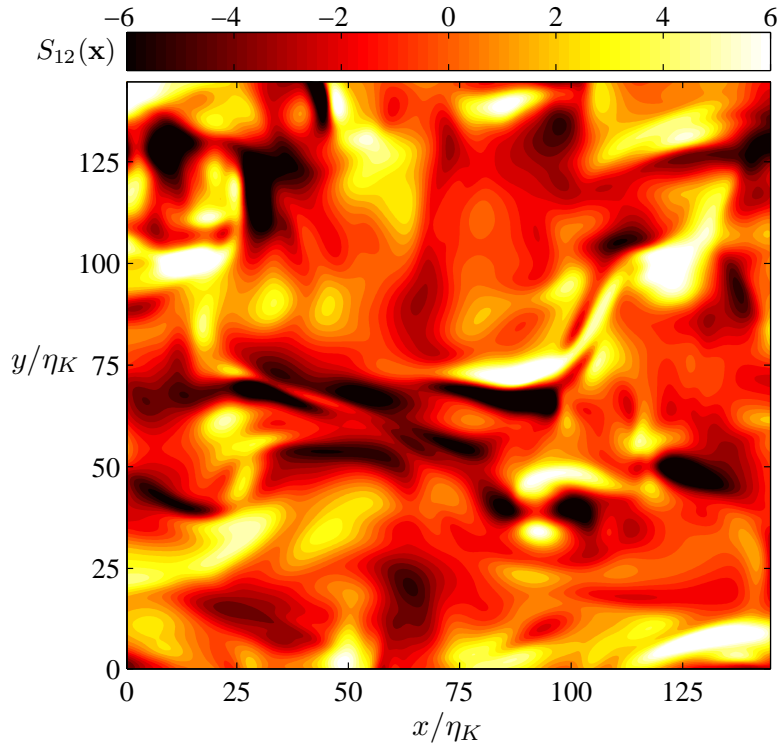
Figure 2.8: Total strain rate field $S_{12}(\mathbf{x})$ from high-resolution DNS of homogeneous isotropic turbulence [90, 91].
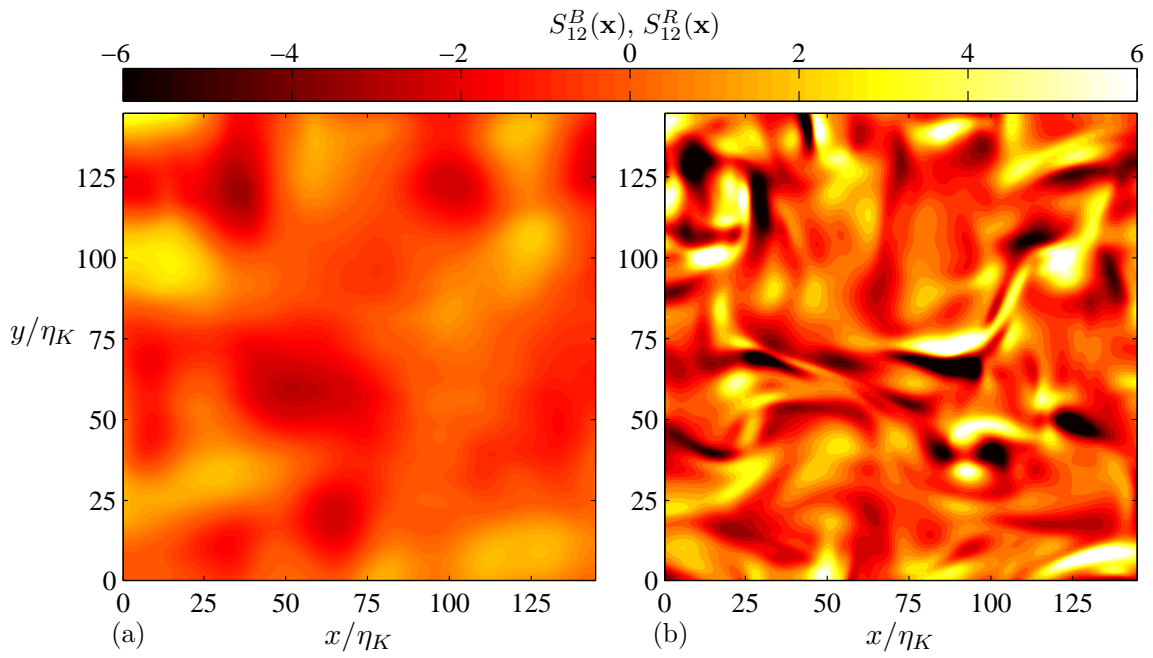


Figure 2.9: Background strain rate field $S_{12}^B(\mathbf{x})$ (a) and local strain rate field $S_{12}^R(\mathbf{x})$ (b) obtained from decomposition of the total strain field in Figure 2.8.
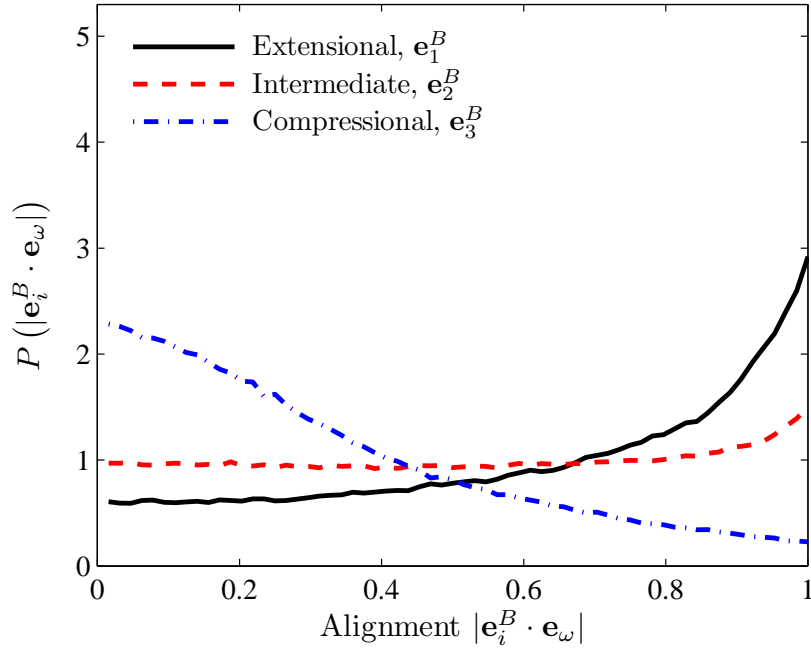
Figure 2.10: Distributions of alignment cosines $|\mathbf{e}_i^B \cdot \mathbf{e}_\omega|$ between the vorticity vector and eigenvectors of the background strain rate $S_{ij}^B$ using high-resolution $Re_\lambda = 107$ DNS of homogeneous, isotropic turbulence [90, 91].
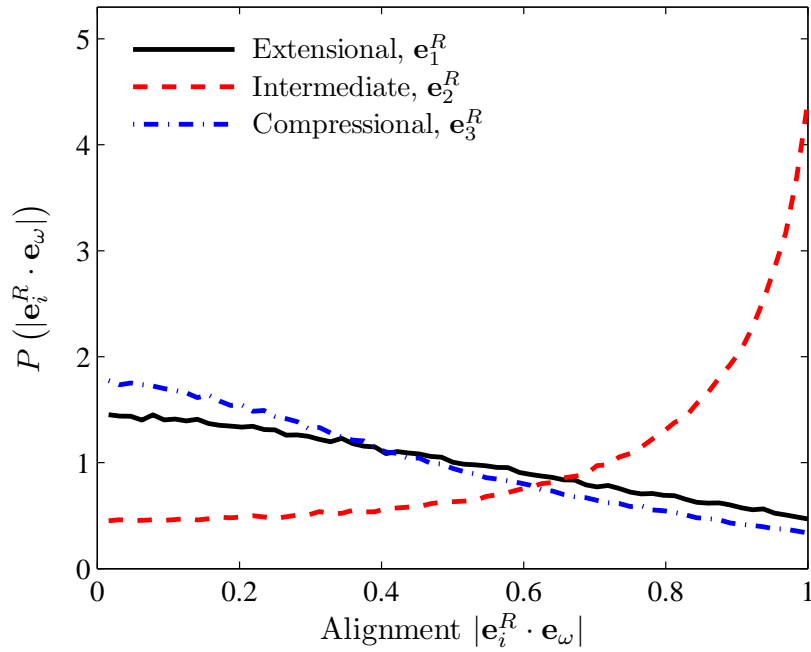


Figure 2.11: Distributions of alignment cosines $|\mathbf{e}_i^R \cdot \mathbf{e}_\omega|$ between the vorticity vector and eigenvectors of the local strain rate $S_{ij}^R$ using high-resolution $Re_\lambda = 107$ DNS of homogeneous, isotropic turbulence [90, 91].
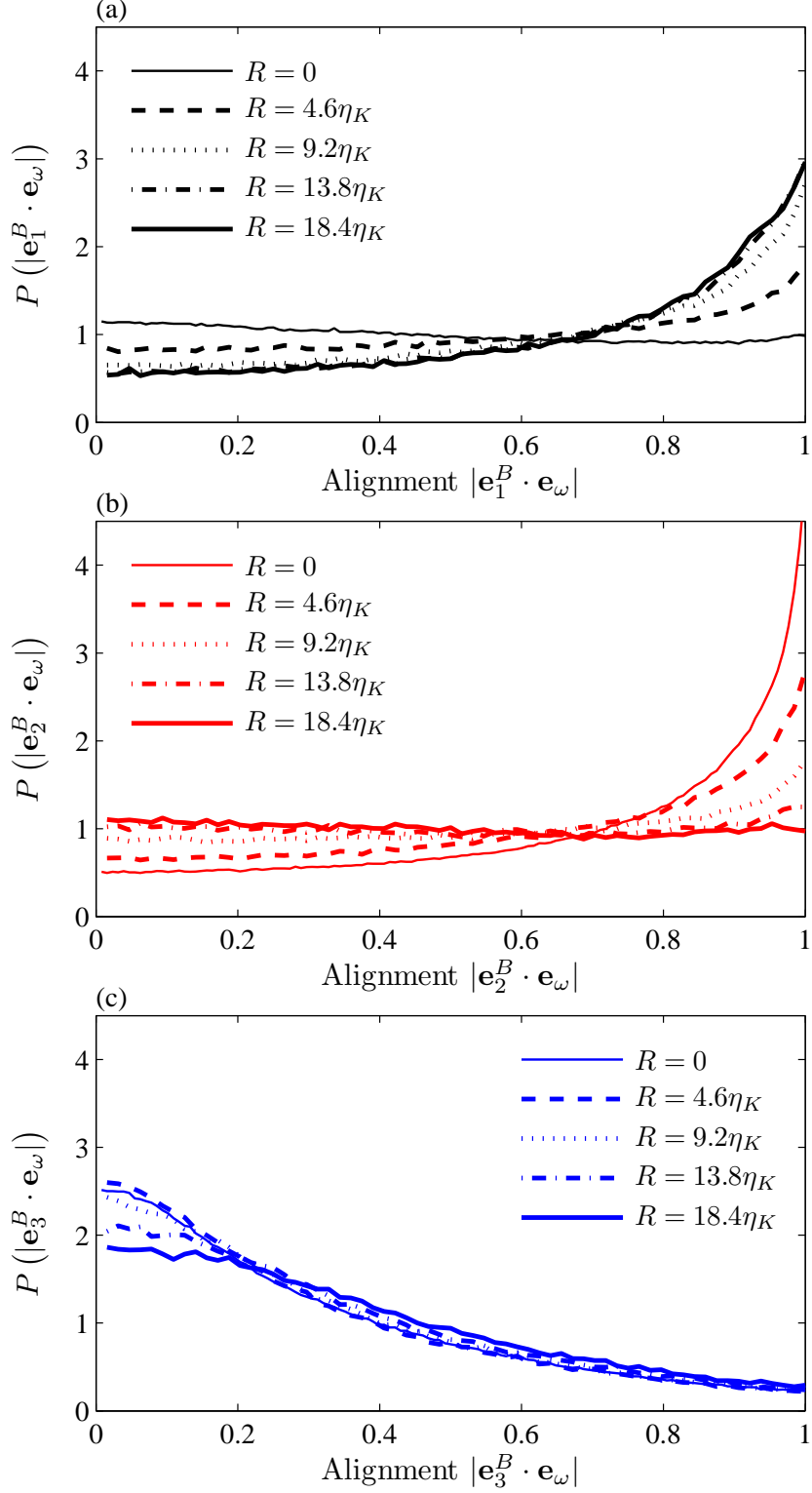
Figure 2.12: Distributions of alignment cosines $|\mathbf{e}_i^B \cdot \mathbf{e}_\omega|$ between the vorticity vector and eigenvectors of the background strain rate $S_{ij}^B$ as function of cutoff radius $R$. Alignments are shown for extensional (a), intermediate (b), and compressional (c) background strain eigenvectors.

49
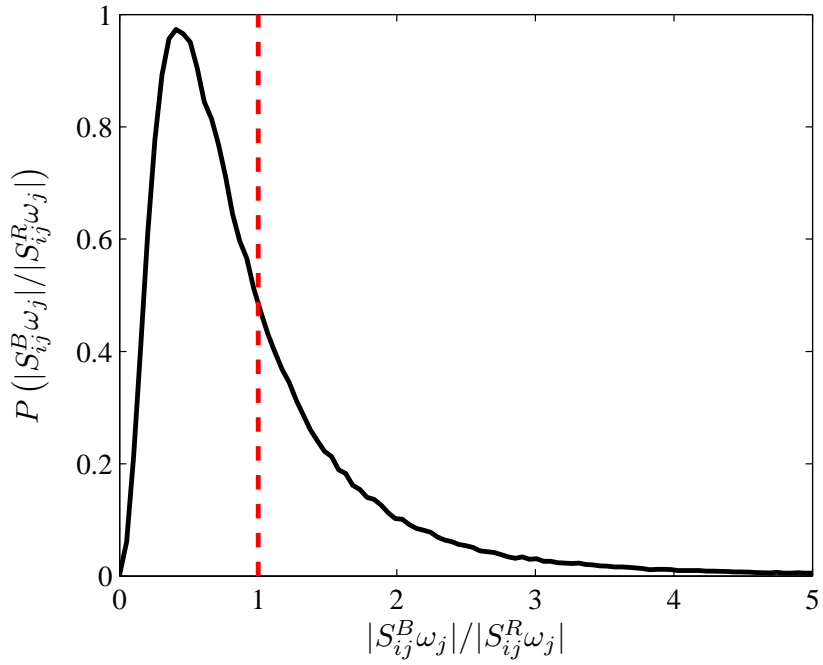
Figure 2.13: Distribution of background (linear) to local (nonlinear) vortex stretching ratio in (2.18) for high-resolution DNS of homogeneous isotropic turbulence [90, 91].
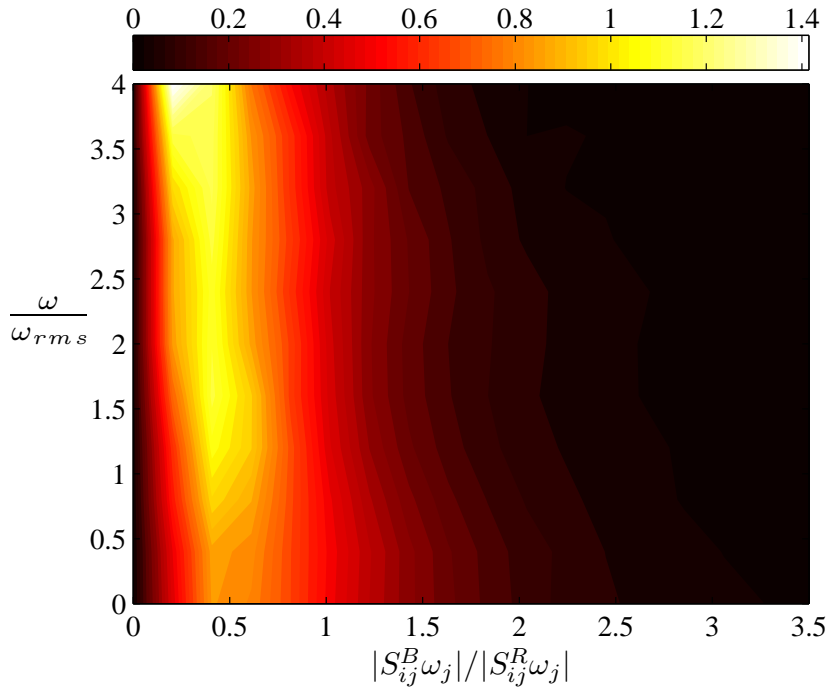


Figure 2.14: Distribution of background to local vortex stretching ratio from Figure 2.13 conditioned on vorticity magnitude $\omega/\omega_{rms}$.
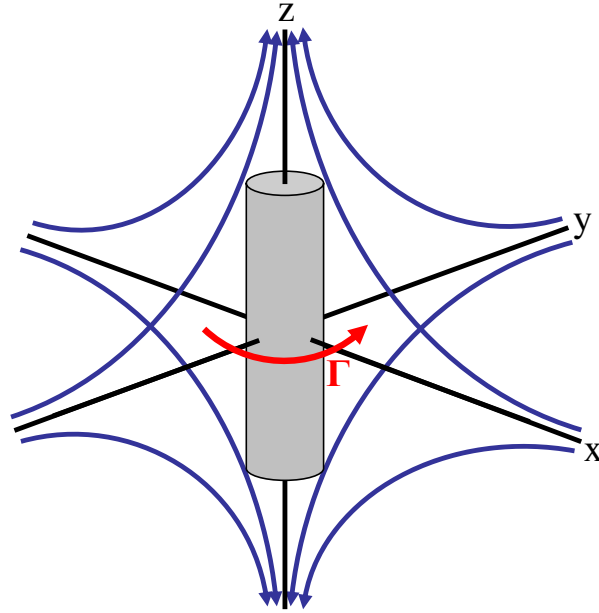
Figure 2.15: Equilibrium Burgers vortex with circulation $\Gamma$ and strain-limited viscous diffusion lengthscale $\lambda_\nu$ in a uniform, irrotational, axisymmetric background strain rate field $S_{ij}^B(\mathbf{x})$.
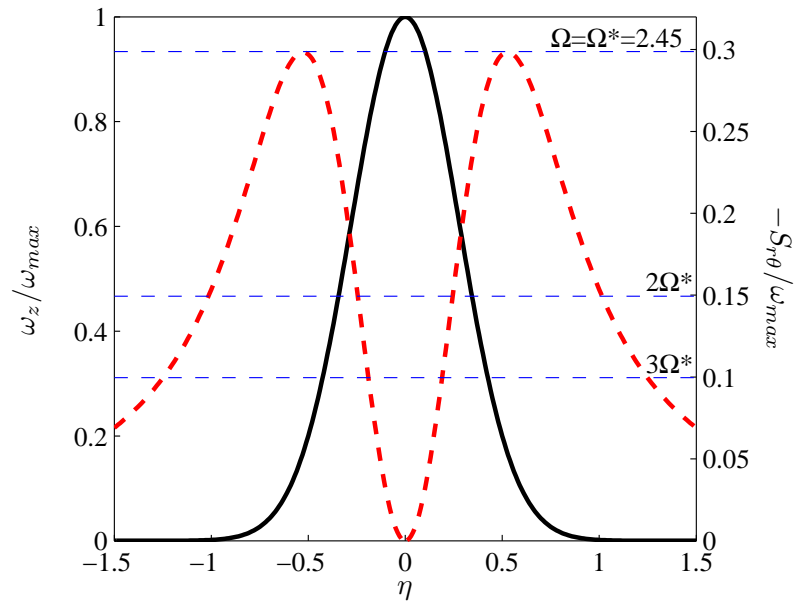


Figure 2.16: Similarity profiles of $\omega_z(\eta)$ and $S_{r\theta}(\eta)$ for any equilibrium Burgers vortex; wherever $-S_{r\theta}$ exceeds the line determined by the vortex strength parameter $\Omega$ in (2.53) the most extensional principal axis of the total strain rate $S_{ij}(\mathbf{x})$ switches from the $\hat{\mathbf{z}}$-axis to lie in the $r$-$\theta$ plane.

51
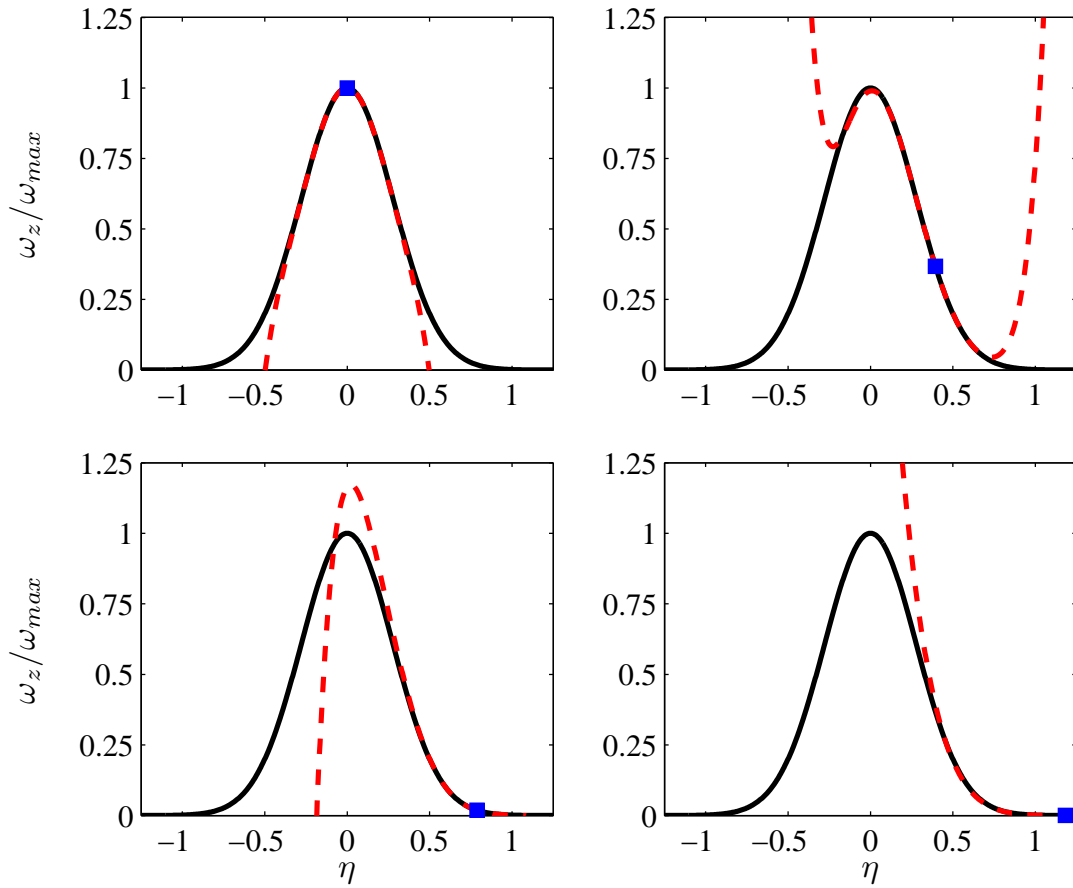
Figure 2.17: Accuracy of the Taylor expansion for the vorticity in (2.19) for a Burgers vortex, showing results for 6th order approximation. In each panel, solid black curve shows actual vorticity profile, and red dashed curve gives approximated vorticity from derivatives at location marked by square.
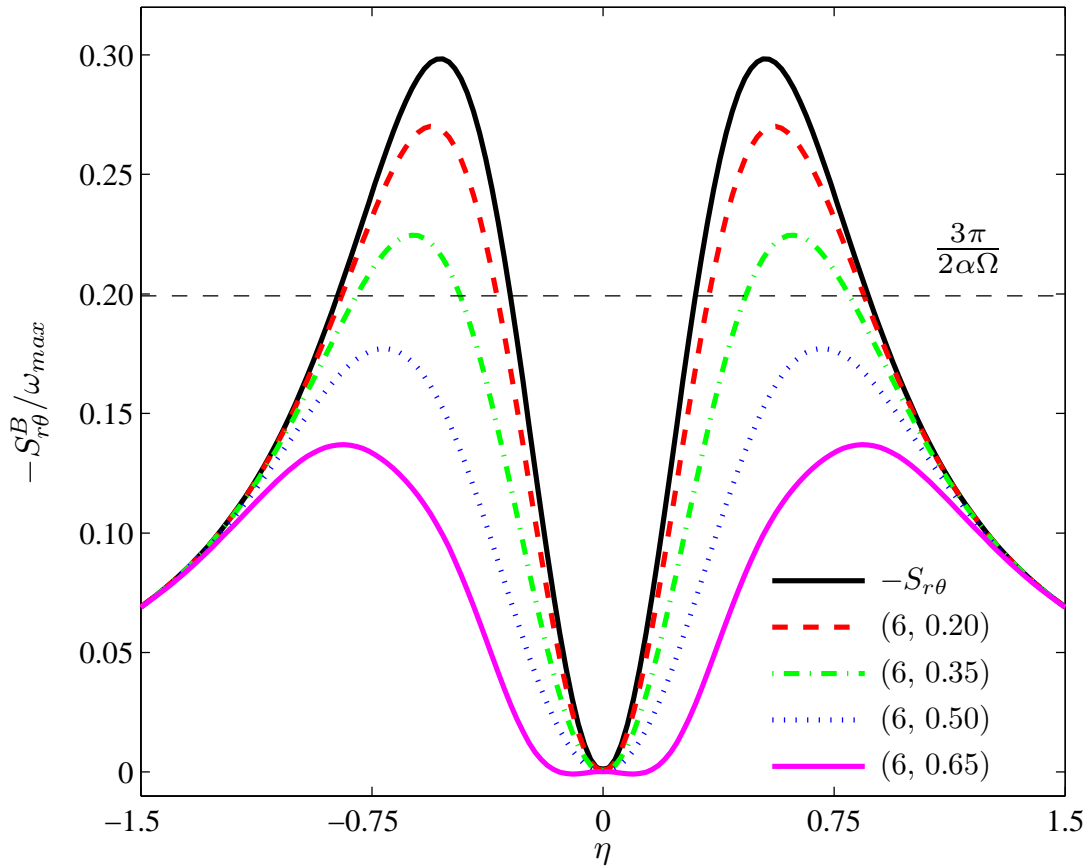
Figure 2.18: Convergence of background strain rate field $S_{ij}^B(\mathbf{x})$ to zero for all $\eta$ in a Burgers vortex, obtained from total strain rate field $S_{ij}(\mathbf{x})$ using (2.45) for various $(n, \tilde{R})$ combinations, where $\tilde{R} \equiv R/\lambda_\nu$. Shown are effects of increasing $\tilde{R}$ for fixed $n = 6$. The dashed horizontal lines follow from (2.51) and (2.53).
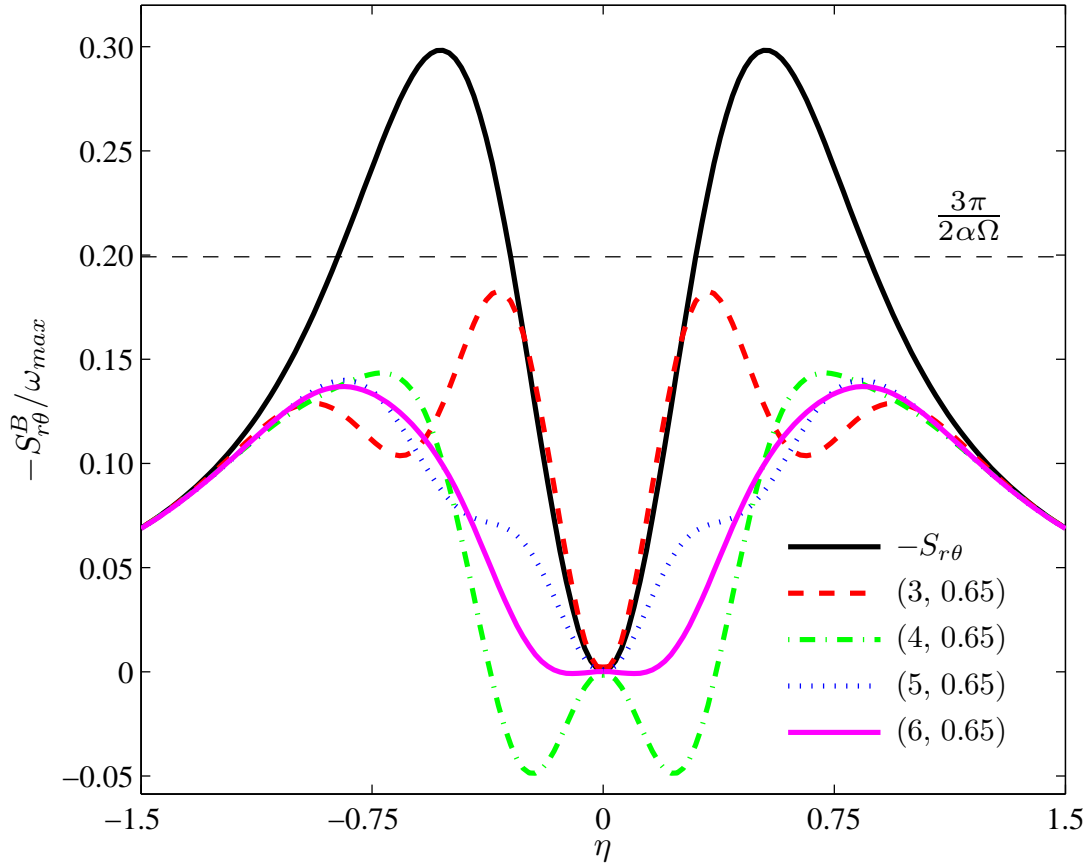
Figure 2.19: Convergence of background strain rate field $S_{ij}^B(\mathbf{x})$ to zero for all $\eta$ in a Burgers vortex, obtained from total strain rate field $S_{ij}(\mathbf{x})$ using (2.45) for various $(n, \tilde{R})$ combinations, where $\tilde{R} \equiv R/\lambda_\nu$. Shown are effects of increasing $n$ for fixed $\tilde{R} = 0.65$. The dashed horizontal lines follow from (2.51) and (2.53).
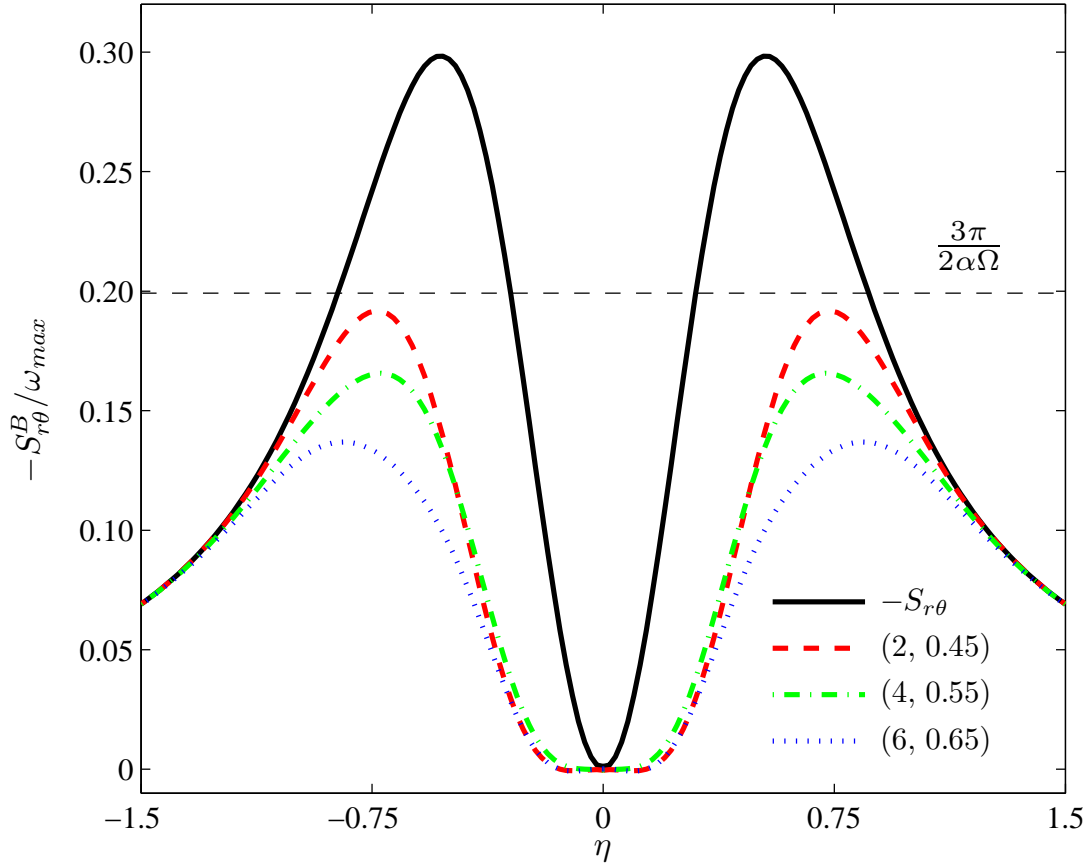
Figure 2.20: Convergence of background strain $S_{ij}^B(\mathbf{x})$ to zero for all $\eta$ in a Burgers vortex, obtained from total field $S_{ij}(\mathbf{x})$ using (2.45) for various $(n, \tilde{R})$ combinations, where $\tilde{R} \equiv R/\lambda_\nu$. Shown are effects of increasing $n$ and $\tilde{R}$ simultaneously. The dashed horizontal lines follow from (2.51) and (2.53).

(a)

$S_{12}(\mathbf{x})$

$S_{12}^B(\mathbf{x})$

$S_{12}^R(\mathbf{x})$

(b)

(c)

(d)

(e)

(f)

(g)

$S_{12}(\mathbf{x}),\ S_{12}^B(\mathbf{x}),\ S_{12}^R(\mathbf{x})$
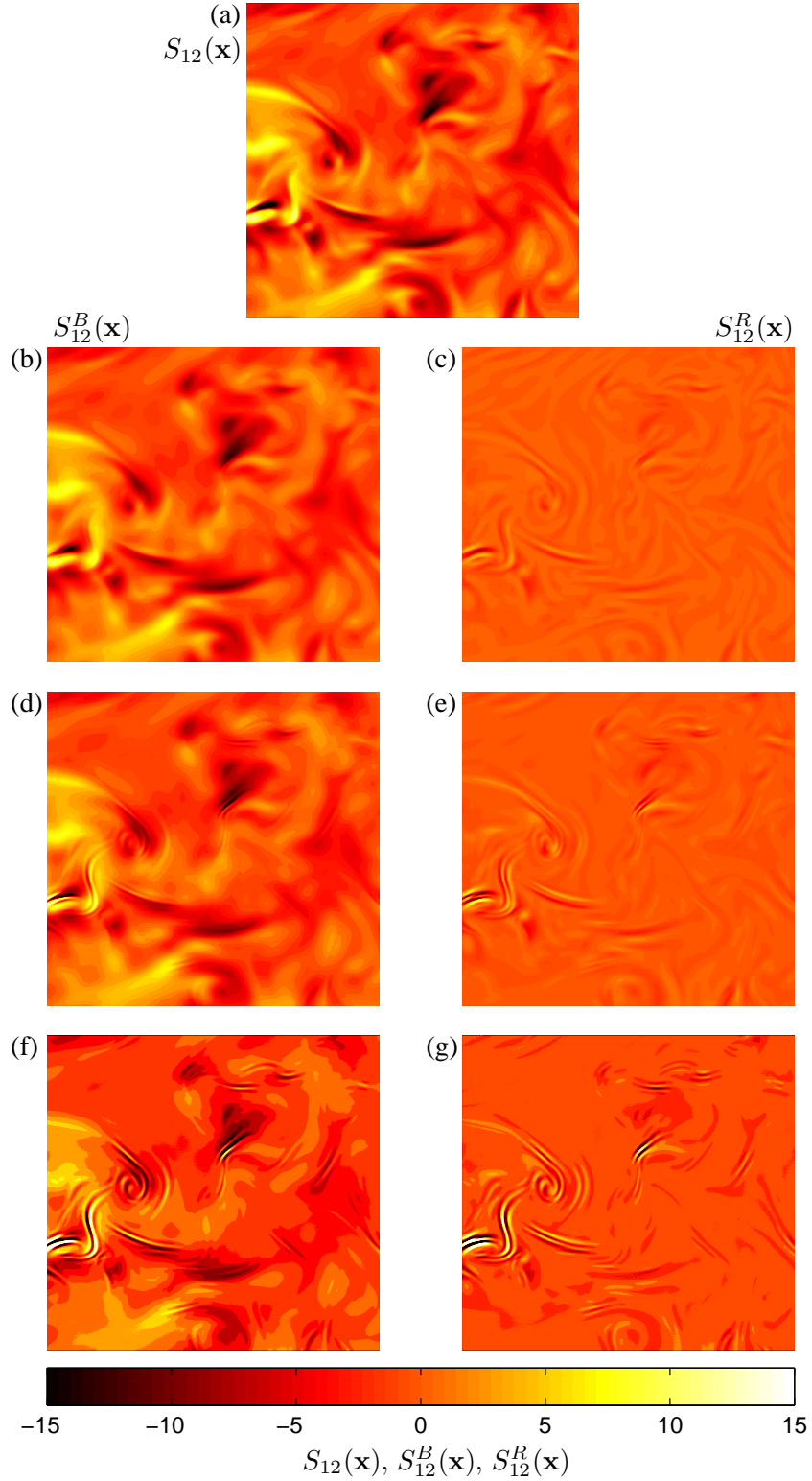
Figure 2.21: Total strain rate component field $S_{12}(\mathbf{x})$ (a), with corresponding results from (2.45) for nonlocal (background) field $S_{12}^B(\mathbf{x})$ (*left*) and local field $S_{12}^R(\mathbf{x})$ (*right*) for $(R/\eta_K) = 2.5$ (b, c), $(R/\eta_K) = 3.5$ (d, e), and $(R/\eta_K) = 4.5$ (f, g), all with $n = 3$.
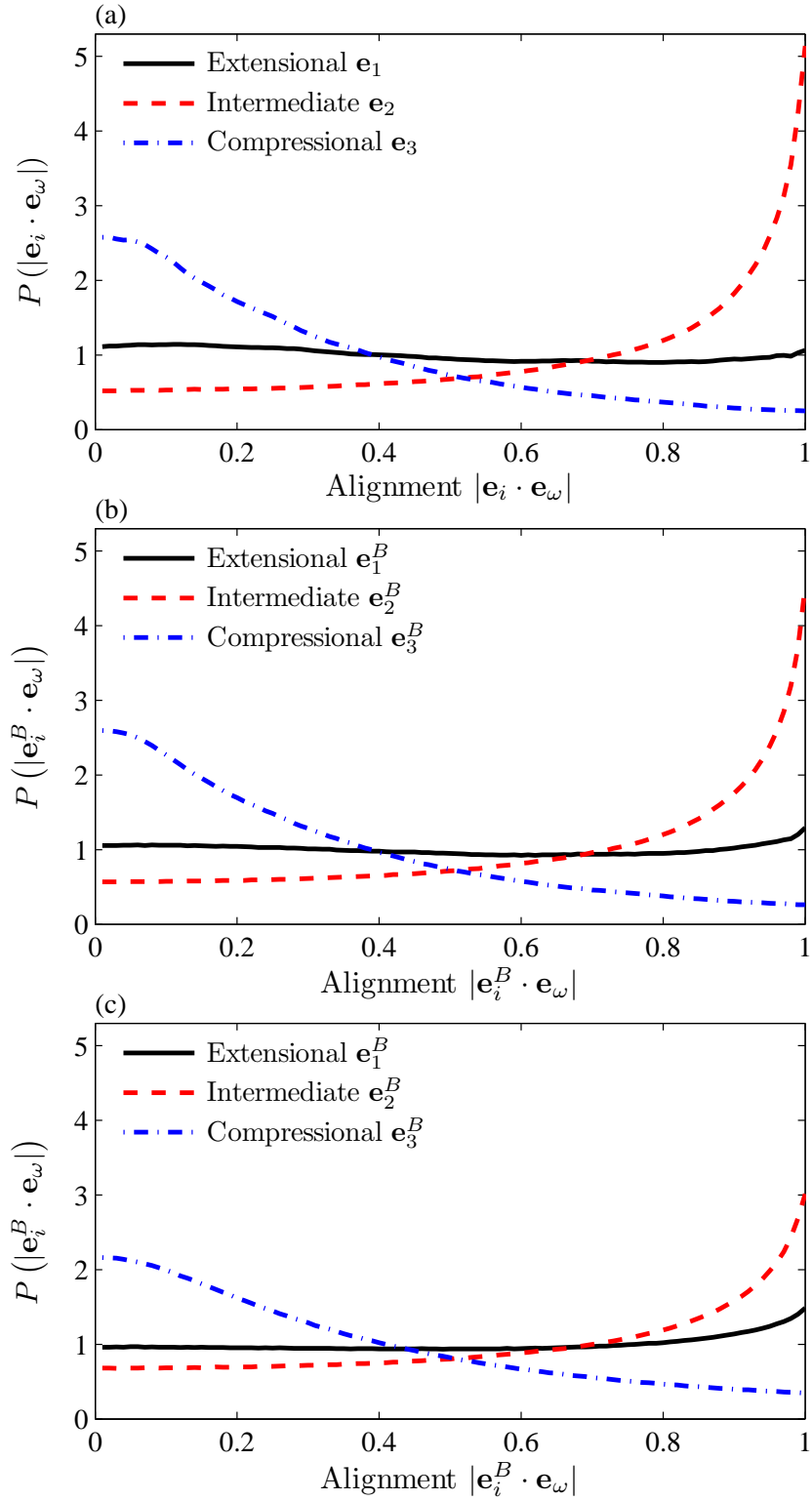
Figure 2.22: Probability densities of alignment cosines for the vorticity with the eigenvectors of the strain rate tensor, showing results for $S_{ij}$ (a) and for $S_{ij}^B$ using $(R/\eta_K) = 2.5$ with $n = 3$ (b) and $(R/\eta_K) = 3.5$ with $n = 3$ (c).

# CHAPTER III

# Present Anisotropy Closure for Nonlocal and Nonequilibrium Effects in Turbulent Flows

The fundamental studies of vorticity alignment in the previous Chapter have revealed a substantial nonlocal, quasi-linear aspect to the vorticity dynamics in turbulent flows. The relation in (2.2) establishes a rigorous connection between the two-point vorticity fluctuation correlation and the Reynolds stress anisotropy $a_{ij}$, and through this relation the dynamics of the vorticity are closely linked to those of the anisotropy.

The relation in (2.2) is written as a double Biot-Savart integral over the entire spatial domain, and thus explicitly accounts for nonlocal effects on the anisotropy evolution. Nonlocal effects are also present in the exact transport equation for the anisotropy in (1.19) via the pressure-strain correlation $\Pi_{ij}$, which is itself exactly expressed as an integral over the entire spatial domain. Despite the obvious importance of nonlocal effects on the anisotropy however, nearly all existing closures represent the anisotropy in terms of local variables only, as outlined in Chapter I. Nonlocal effects are particularly important in flows where the mean velocity gradient field is strongly varying, for example in wall-bounded flows, and must be accurately accounted for in order to obtain reliable predictions of the anisotropy in nearly all practical problems.

With respect to the Lagrangian evolution of the anisotropy (that is, temporal and convective changes in $a_{ij}$), the relation in (2.2) is a purely spatial integral and the dynamics of the anisotropy are completely determined by the dynamics of the two-point vorticity fluctuation correlation. The fundamental studies of vorticity alignment in the previous Chapter have revealed a substantial quasi-linear aspect to the vorticity dynamics in turbulent flows, and through (2.2) this thus suggests that the anisotropy dynamics can also be understood as a quasi-linear system. In this system, the anisotropy has a finite-time response to Lagrangian variations in flow properties, and $a_{ij}$ at any point depends on the prior history of the anisotropy experienced by fluid elements in the flow. Such history effects are particularly important in strongly nonequilibrium turbulent flows where the mean strain may be large and rapidly varying.

In the following, a new anisotropy closure that addresses both nonlocal and nonequilib-

rium effects in turbulent flows is formulated. The new closure seeks to include the principal nonequilibrium dynamics of $a_{ij}$ contained in full Reynolds stress transport models, while also accounting for nonlocal effects due to spatial variations in the mean strain rate tensor. This is accomplished by formulating a new nonlocal representation for the rapid pressure-strain rate correlation $\Pi_{ij}^{(r)}$, resulting in a nonlocal transport equation for the anisotropy that improves upon the conventional purely local model equation in (1.28). Based on the vorticity alignment studies in Chapter II, this nonlocal equation is linearized and then solved in order to replace the *local instantaneous* mean strain rate $\overline{S}_{ij}$ appearing in the classical equilibrium closure in (1.35) with a *nonlocal, nonequilibrium effective* strain rate $\widetilde{S}_{ij}$. This new tensor accounts for both the spatial structure of the mean strain rate as well as the straining history of the flow, but does so within a relatively simple approach that allows straightforward implementation in existing two-equation frameworks for solving (1.2)-(1.4).

## 3.1  Physical Basis of Turbulence Anisotropy

As noted in Chapter II, the relation in (2.2) establishes a rigorous connection between the two-point vorticity fluctuation correlation and the anisotropy in turbulent flows. Fundamentally, the two-point fluctuation correlation depends on the small-scale structure and vorticity alignment in the flow, and thus an informal connection between vorticity alignment and the anisotropy evolution is established.

In order to understand the effect of the strain rate $S_{ij}$ on the alignment of the vorticity and the resulting anisotropy from a heuristic standpoint, we can consider a small material element containing a segment of a typical vortical structure into which the vorticity is naturally concentrated at large Reynolds numbers by the competing effects of the stretching and diffusion terms in (2.3). As shown in (2.13) and (2.14), the strain rate field within such an element can be separated into a local part $S_{ij}^R$ induced within the element by the local vorticity inside the element, and a background part $S_{ij}^B$ induced within the element by all the remaining (nonlocal) vorticity outside the element. The background strain $S_{ij}^B$ reflects the largely linear influence of all the surrounding vorticity on the element; this provides only a relatively weak and indirect nonlinear coupling due to the effect of the local vorticity on the nonlocal vorticity. The direct nonlinearity in the vorticity dynamics is due to the local strain $S_{ij}^R$, through which the structure acts on itself. As described in Chapter II, the instantaneous vorticity vector naturally rotates toward alignment with the most extensional eigenvector of $S_{ij}^B$, while $S_{ij}^R$ induced by any vortical structure has almost no component along the vorticity vector direction. It is primarily through local curvature in the vortical structure that the effect of the local strain on the local vorticity becomes significant. Indeed, for axisymmetric (line-like) and planar (sheet-like) vortical structures [8] the local strain $S_{ij}^R$ may be large but has no component that interacts with the local vorticity.

This suggests that the local dynamics of the vorticity field may be represented in many regions of the flow as a linear inviscid process governed by the imposed nonlocal background

strain $S_{ij}^B(\mathbf{x}, t)$, namely

$$\frac{D\omega_i}{Dt} \approx \omega_j S_{ij}^B. \tag{3.1}$$

Key features of the nonequilibrium vorticity alignment dynamics in turbulence can be seen in (3.1). For slowly varying $S_{ij}^B(\mathbf{x}, t)$, the vorticity vector will rotate toward alignment with the most extensional principal axis of the *background* strain rate tensor – this is typically the intermediate principal axis of the *combined* strain rate tensor $S_{ij}$. So long as $S_{ij}^B(\mathbf{x}, t)$ varies sufficiently slowly, the vorticity will remain in this equilibrium alignment with the background strain rate tensor. However, when the background strain rate $S_{ij}^B(\mathbf{x}, t)$ changes rapidly, then in a frame aligned with the new eigenvectors of $S_{ij}^B$ the short-time dynamics in (3.1) leads to an exponential reorientation of the vorticity, on the reorientation time scale $1/S^B$ where $S^B \equiv \left(2 S_{ij}^B S_{ij}^B\right)^{1/2}$, toward the new most extensional principal axis of $S_{ij}^B$.

From this quasi-linearized model of the local vorticity orientation dynamics in a small material element, we now consider a Lagrangian element that is large enough to contain many such concentrated vortical structures, and thereby allows a spatial average within it to define the anisotropy tensor $a_{ij}(t)$ as well as the kinetic energy $k(t)$ and dissipation rate $\epsilon(t)$. In the absence of any preferred direction imposed by the strain rate tensor $S_{ij}^B$ acting on the element, the self-induced and mutual straining of the vortical structures produces a characteristic local strain rate $\epsilon/k$ that leads to randomization of the vorticity vector orientations within the element, and thus $a_{ij} = 0$. We then examine the impulse response of the anisotropy in this element by imposing a large background strain, specifically $(S^B k/\epsilon) \to \infty$, over a short duration. Since $S^B \gg \epsilon/k$ during the impulse, the vortical structures must all align on the time scale $1/S^B$ with the most extensional principal axis of $S_{ij}^B$. For the resulting completely aligned vorticity field, the anisotropy $a_{ij}$ then attains its maximum value. Once the imposed strain is relaxed, the self-induced and mutual straining of the vortical structures gradually returns the random orientations of the vorticity vectors within the element on the timescale $k/\epsilon$, so that $a_{ij} \to 0$. This impulse response of the vorticity alignment in the turbulence suggests a linearized description of turbulence anisotropy dynamics for an arbitrary imposed strain rate $S_{ij}^B$.

To formalize this, we return to the original small material element, where the dynamics are essentially linear due to (3.1), but rather than examining a single element we now consider the ensemble of elements – one from each realization of the flow for the same nominal initial and boundary conditions – that arrive at location $\mathbf{x}$ at time $t$, as indicated in Figure 3.1. Each element arrives along a different pathline, and thus has been subjected to a different straining history $S_{ij}^B(\tau)$, where the time $\tau$ identifies the position along the pathline. The ensemble average over all elements at time $t$ now defines the anisotropy tensor, and from the above considerations it is apparent that the resulting $a_{ij}(\mathbf{x}, t)$ will not be proportional to the *local instantaneous* ensemble average of $S_{ij}^B$ at location $\mathbf{x}$ and time $t$. Rather, if we seek an *effective* strain rate $\widetilde{S}_{ij}$ so that $a_{ij} \sim \widetilde{S}_{ij}$, then motivated by

the above considerations of the impulse response in the vorticity alignment we can regard the vorticity dynamics and associated turbulence anisotropy as a linear system, having the ensemble average of the straining history, denoted $\langle S_{ij}^B(\tau) \rangle$, as its input, $h(t - \tau)$ as its impulse response, and $a_{ij}$ – or equivalently $\widetilde{S}_{ij}$ – as its output. From linear system theory, the output will be a convolution of the input $\langle S_{ij}^B(\tau) \rangle$ with the impulse response $h(t - \tau)$, and thus the effective strain rate will be of the form

$$\widetilde{S}_{ij}(\mathbf{x}, t) = \int_{-\infty}^{t} \langle S_{ij}^B(\tau) \rangle_{R(\tau)} h(t - \tau) D\tau. \tag{3.2}$$

Here $\langle S_{ij}^B(\tau) \rangle_{R(\tau)}$ is the ensemble average over all elements at time $\tau$ along their individual pathlines, as indicated in Figure 3.1.

Note that as the material elements in Figure 3.1 translate, they also rotate with the local average rotation rate tensor

$$-\overline{\Omega}_{ij} \equiv \frac{1}{2} \left( \frac{\partial \overline{u}_i}{\partial x_j} - \frac{\partial \overline{u}_j}{\partial x_i} \right), \tag{3.3}$$

the elements of which are the components of the average vorticity vector within the element. The vortical structures within the element rotate with this mean rotation tensor $\overline{\Omega}_{ij}$, and thus at earlier times $\tau$ in Figure 3.1 the orientation of the vortical structures differs from that at time $\tau = t$. The rate of change in the anisotropy is determined by the relative alignment of these structures with the background strain rate tensor $S_{ij}^B$. As a consequence, in (3.2) the components of the background strain rate tensor $\langle S_{ij}^B(\tau) \rangle_{R(\tau)}$ must be given in the coordinate frame of the element at time $\tau$.

In the following sections, the heuristic result in (3.2) is derived more formally from a new nonlocal transport equation for $a_{ij}$. The linearization of the $a_{ij}$ dynamics, while historically done for other reasons, is here motivated by the quasi-linearized vorticity dynamics in (3.1), and will be seen to produce a closure for the anisotropy analogous to (3.2).

## 3.2    Nonlocal Formulation for the Pressure-Strain Correlation

The anisotropy closure for nonlocal and nonequilibrium effects in turbulent flows is fundamentally obtained as a quasi-linear solution to a new nonlocal anisotropy transport equation. This equation is based on a nonlocal formulation for the pressure-strain correlation $\Pi_{ij}$, and allows more accurate predictions of the anisotropy in flows with strong spatial variations in the mean velocity gradient field.

The challenge in representing $\Pi_{ij}$ stems in large part from the inherently nonlocal nature of the pressure-strain correlation, since the local pressure $p'$ in the definition for $\Pi_{ij}$ in (1.10) depends on an integral over the entire spatial domain of the flow. Some progress has been made by splitting $\Pi_{ij}$ into the sum of "slow" and "rapid" parts [14] as noted in Chapter I, where the rapid part $\Pi_{ij}^{(r)}$ is so named due to its direct dependence on the mean-flow velocity

gradients $\partial \overline{u}_i / \partial x_j$, variations in which have an immediate effect on $Da_{ij}/Dt$. Typically, the slow part $\Pi_{ij}^{(s)}$ is represented in terms of the local values of $a_{ij}$ and $\epsilon$, as in (1.22). For the rapid part, it has been common (*e.g.,* [14, 16, 86]) to take the mean velocity gradients as being essentially homogeneous, thus allowing them to be brought outside the integral. Under certain conditions [16] the remaining integral can then be solved for the local part of $\Pi_{ij}^{(r)}$. This is then typically combined with additional *ad hoc* terms involving $a_{ij}$ to model the rapid part solely in terms of local flow variables (e.g. Eq. (1.24)). Together with the assumed local representation for the slow part, this yields the purely local formulation for $\Pi_{ij}$ given by (1.25) that allows the exact anisotropy transport equation in (1.19) to be solved, but that neglects all nonlocal effects in the evolution of the anisotropy.

Such purely local models for $\Pi_{ij}$ have allowed relatively accurate simulations of homogeneous turbulent flows, where by construction there are no spatial variations in $\partial \overline{u}_i / \partial x_j$ and thereby all nonlocal effects vanish. However most practical situations involve strongly inhomogeneous flows, where large-scale structure and other manifestations of spatial variations in the mean-flow velocity gradients can produce significant nonlocal effects in the turbulence, the neglect of which in $\Pi_{ij}$ can lead to substantial inaccuracies in the resulting anisotropy. Such nonlocal effects are significant even in free shear flows such as jets, wakes, and mixing layers, and can become especially important in near-wall flows, where flow properties vary rapidly in the wall-normal direction. Improving the fidelity of turbulent flow simulations requires a fundamentally-based formulation for nonlocal effects in $\Pi_{ij}^{(r)}$ to account for spatial variations of velocity gradients in the ensemble-averaged flow.

Various methods for addressing such spatial variations have been proposed, however nearly all suffer from a lack of systematic physical and mathematical justification. For near-wall flows, by far the most common yet also least satisfying approach is the use of empirical wall damping functions, as discussed in Section 1.3.3. Although such functions are relatively straightforward to implement, they are also distinctly *ad hoc* and as a consequence do not perform well across a wide range of flows. Moreover, wall functions typically conflate the treatment of a number of near-wall effects that in fact originate from distinctly different physical mechanisms, including low Reynolds number effects, large strain effects, and wall-induced kinematic effects, and are not formulated to specifically account for nonlocality due to spatial variations in the mean flow gradients.

In the following we depart from these prior approaches by systematically deriving a new nonlocal formulation for the rapid pressure-strain correlation from the exact integral relation for the rapid part of $\Pi_{ij}$. Specifically, nonlocal effects due to mean-flow velocity gradients are accounted for through Taylor expansion of $\partial \overline{u}_k / \partial x_l$ in the rapid pressure-strain integral. The resulting nonlocal form of the rapid pressure-strain correlation $\Pi_{ij}^{(r)}$ appears as a series of Laplacians of the mean strain rate tensor. The only approximation involved – beyond the central hypothesis on which the present formulation is based – is an explicit form for the longitudinal correlation function $f(r)$, though the effect of this is only to determine specific

values of the coefficients in an otherwise fundamental result for the nonlocal effects in $\Pi_{ij}^{(r)}$. The coefficients are obtained here for the exponential form of $f(r)$ appropriate for high Reynolds numbers, and for the exact Gaussian $f(r)$ that applies at low Reynolds numbers. The resulting formulation for the rapid part of $\Pi_{ij}$ then provides a new nonlocal anisotropy transport equation that can be used with any number of closure approaches for representing $a_{ij}$, including Reynolds stress transport models as well as explicit stress models suitable for two-equation closures.

### 3.2.1 Exact Integral Expressions for $\Pi_{ij}^{(s)}$ and $\Pi_{ij}^{(r)}$

The starting point for developing a fundamentally-based representation for $\Pi_{ij}$ is the exact Poisson equation for the pressure fluctuations $p'$ appearing in (1.10), namely

$$\frac{1}{\rho}\nabla^2 p' = -2\frac{\partial\overline{u}_k}{\partial x_l}\frac{\partial u'_l}{\partial x_k} - \frac{\partial^2}{\partial x_k \partial x_l}\left(u'_k u'_l - \overline{u'_k u'_l}\right) \tag{3.4}$$

(*e.g.*, [78]). Beginning with Chou [14], it has been common to write $p'$ in terms of rapid, slow, and wall parts as

$$p' \equiv p'^{(r)} + p'^{(s)} + p'^{(w)}, \tag{3.5}$$

defined by their respective Poisson equations from (3.4) as

$$\frac{1}{\rho}\nabla^2 p'^{(r)} = -2\frac{\partial\overline{u}_k}{\partial x_l}\frac{\partial u'_l}{\partial x_k}, \tag{3.6}$$

$$\frac{1}{\rho}\nabla^2 p'^{(s)} = -\frac{\partial^2}{\partial x_k \partial x_l}\left(u'_k u'_l - \overline{u'_k u'_l}\right), \tag{3.7}$$

$$\frac{1}{\rho}\nabla^2 p'^{(w)} = 0. \tag{3.8}$$

The effect of $p'^{(w)}$ is significant in (1.15) only in the extreme near-wall region of wall-bounded flows [63, 78]. The remaining rapid and slow parts produce corresponding rapid and slow contributions to the pressure-strain correlation $\Pi_{ij}$ in (1.10), with Green's function solutions [78] of (3.6) and (3.7) giving these as

$$\Pi_{ij}^{(r)}(\mathbf{x}) = \frac{1}{\pi}\int_{\mathbf{R}} \frac{\partial\overline{u}_k(\hat{\mathbf{x}})}{\partial\hat{x}_l}\overline{\frac{\partial u'_l(\hat{\mathbf{x}})}{\partial\hat{x}_k}S'_{ij}(\mathbf{x})}\frac{d\hat{\mathbf{x}}}{|\mathbf{x}-\hat{\mathbf{x}}|} \tag{3.9}$$

$$\Pi_{ij}^{(s)}(\mathbf{x}) = \frac{1}{2\pi}\int_{\mathbf{R}} \overline{\frac{\partial^2\left(u'_k u'_l\right)_{\hat{\mathbf{x}}}}{\partial\hat{x}_k \partial\hat{x}_l}S'_{ij}(\mathbf{x})}\frac{d\hat{\mathbf{x}}}{|\mathbf{x}-\hat{\mathbf{x}}|}, \tag{3.10}$$

where the integration spans the entire flow domain $\mathbf{R}$.

The slow part $\Pi_{ij}^{(s)}$ is typically not treated in a systematic fashion via integration of (3.10). Instead, nearly all existing representations for $\Pi_{ij}^{(s)}$ are based on insights obtained from the return to isotropy of various forms of initially-strained grid turbulence, resulting

in the widely-used purely local formulation for $\Pi_{ij}^{(s)}$ given by (1.22). By contrast to the slow correlation, $\Pi_{ij}^{(r)}$ has received substantially greater attention. The direct effect of the mean velocity gradients $\partial \overline{u}_k / \partial x_l$ on this rapid part of the pressure-strain correlation is apparent in (3.9). In the following sections, we use the integral in (3.9) to develop a fundamentally-based representation for $\Pi_{ij}^{(r)}$ that accounts for nonlocal effects resulting from spatial nonuniformities in the mean velocity gradients.

### 3.2.2  Prior Local Formulation for $\Pi_{ij}^{(r)}$

Chou [14] first suggested the notion of using the integral form in (3.9) to obtain a representation for the rapid pressure-strain correlation. Subsequently, Rotta [86] and then Crow [16] used that approach to rigorously derive the purely local part of $\Pi_{ij}^{(r)}$, by assuming the mean velocity gradients in (3.9) to vary slowly enough that they could be taken as constant over the length scale on which the two-point correlation $\overline{[\partial u_k'(\hat{\mathbf{x}})/\partial \hat{x}_l]\, S_{ij}'(\mathbf{x})}$ in (3.9) is nonzero. Under such conditions, the mean velocity gradient in (3.9) can be brought through the integral, and $\Pi_{ij}^{(r)}$ then becomes

$$\Pi_{ij}^{(r)}(\mathbf{x}) \approx \frac{\partial \overline{u}_k(\mathbf{x})}{\partial x_l} \cdot \frac{1}{\pi} \int_{\mathbf{R}} \overline{\frac{\partial u_l'(\hat{\mathbf{x}})}{\partial \hat{x}_k} S_{ij}'(\mathbf{x})} \frac{d\hat{\mathbf{x}}}{|\mathbf{x} - \hat{\mathbf{x}}|}\ . \tag{3.11}$$

With $S_{ij}'(\mathbf{x})$ in (1.10), the integrand in (3.11) involves two-point correlations among velocity gradients of the form

$$\overline{\frac{\partial u_i'(\mathbf{x})}{\partial x_j} \frac{\partial u_l'(\hat{\mathbf{x}})}{\partial \hat{x}_k}} = -\frac{\partial^2 R_{il}(\mathbf{r})}{\partial r_j \partial r_k}\ , \tag{3.12}$$

where $R_{il}(\mathbf{r})$ denotes the velocity fluctuation correlation

$$R_{il}(\mathbf{r}) \equiv \overline{u_i'(\mathbf{x}) u_l'(\mathbf{r} + \mathbf{x})} \tag{3.13}$$

with $\mathbf{r} \equiv \hat{\mathbf{x}} - \mathbf{x}$. Defining [14, 16, 86]

$$M_{iljk} \equiv -\frac{1}{2\pi} \int_{\mathbf{R}} \frac{\partial^2 R_{il}(\mathbf{r})}{\partial r_j \partial r_k} \frac{d\mathbf{r}}{r}\ , \tag{3.14}$$

the rapid pressure-strain correlation in (3.11) can then be expressed as

$$\Pi_{ij}^{(r)}(\mathbf{x}) \approx \frac{\partial \overline{u}_k(\mathbf{x})}{\partial x_l} \left[ M_{iljk} + M_{jlik} \right]\ . \tag{3.15}$$

Using the homogeneous isotropic form of $R_{il}(\mathbf{r})$, namely

$$R_{il}(r) = \frac{2}{3} k \left[ f(r)\delta_{il} + \frac{r}{2} \frac{df}{dr} \left( \delta_{il} - \frac{r_i r_l}{r^2} \right) \right] \tag{3.16}$$

64

with

$$f(r) \equiv \frac{3}{2} \frac{\overline{u'(\mathbf{x} + \mathbf{r})u'(\mathbf{x})}}{k} , \tag{3.17}$$

where $k$ is the turbulence kinetic energy, it can be shown [16] that $M_{iljk}$ in (3.14) becomes

$$M_{iljk} = \frac{2}{15} k \left( 4\delta_{jk}\delta_{il} - \delta_{ij}\delta_{kl} - \delta_{jl}\delta_{ki} \right) , \tag{3.18}$$

where the leading $k$ again denotes the turbulence kinetic energy. Note that in (3.17), $r \equiv |\mathbf{r}|$, $u'$ is the velocity component along the direction of the separation vector $\mathbf{r}$, and we have used the isotropic relation $\overline{u'^2} = \frac{2}{3}k$. Using (3.18) in (3.15) then gives the rapid pressure-strain correlation as

$$\frac{1}{k} \Pi_{ij}^{(r)} \approx \frac{4}{5} \overline{S}_{ij} , \tag{3.19}$$

where $\overline{S}_{ij}$ is the local mean-flow strain rate tensor

$$\overline{S}_{ij} \equiv \frac{1}{2} \left( \frac{\partial \overline{u}_i}{\partial x_j} + \frac{\partial \overline{u}_j}{\partial x_i} \right) . \tag{3.20}$$

Typically, (3.19) is used as the leading-order isotropic term in tensorial expansions for the rapid pressure-strain correlation $\Pi_{ij}^{(r)}(\mathbf{x})$, where the remaining terms are expressed in terms of the local anisotropy $a_{ij}$ and the local mean velocity gradient tensor as in (1.24). Note however that such representations are still purely local, since in going from (3.9) to (3.11) all spatial variations in the mean velocity gradients $\partial \overline{u}_k/\partial x_l$ over the length scale on which the two-point correlations $\overline{\left[\partial u'_k(\hat{\mathbf{x}})/\partial \hat{x}_l\right] S'_{ij}(\mathbf{x})}$ are nonzero were ignored. The resulting neglect of nonlocal contributions to $\Pi_{ij}^{(r)}$ from that approximation can lead to substantial inaccuracies in many turbulent flows, including free shear flows and wall-bounded flows as noted in Section 1.3.3. In mitigation, it is usually claimed [16, 48] that $\partial \overline{u}_k/\partial x_l$ only has to be approximately homogeneous over the domain for which $R_{il}(\mathbf{r})$ is nonzero, which is typically much less than $(-\infty, \infty)$. However, Bradshaw *et al.* [7] showed using DNS of fully-developed turbulent channel flow [46] that the homogeneity approximation used to obtain (3.15) is invalid for $y^+ \leq 30$. Figure 3.2 further shows that the dominant component $\overline{S}_{12}$ of the mean strain begins to vary dramatically at locations as far from the wall as $y^+ \approx 60$. Comparable variations in mean velocity gradients are also found in turbulent jets, wakes, and mixing layers, where there are substantial spatial variations in $\overline{S}_{12}$ across the flow. Indeed in most turbulent flows of practical interest, there are significant variations in the mean flow velocity gradients that will produce nonlocal contributions to the rapid pressure-strain correlation via (3.9). In such situations, it may be essential to account for these nonlocal effects in $\Pi_{ij}^{(r)}$ to obtain accurate results from any closures based on the exact anisotropy equation in (1.19).

65

### 3.2.3 Present Nonlocal Formulation for $\Pi_{ij}^{(r)}$

In the following, nonlocal effects due to spatial variations in the mean flow are accounted for in $\Pi_{ij}^{(r)}$ through Taylor expansion of the mean velocity gradients appearing in (3.9). The central hypothesis in the approach developed here is that the nonlocality in $\Pi_{ij}^{(r)}$ is substantially due to spatial variations in $\partial \overline{u}_k / \partial x_l$ in (3.9), and that in order to address this effect all other factors in (3.9) can be adequately represented by their homogeneous isotropic forms. This allows a formulation of the rapid pressure-strain correlation analogous to that in (3.19), but goes beyond a purely local formulation to take into account the effects of spatial variations in the mean flow gradients.

We begin by defining the ensemble-averaged velocity gradients

$$A_{kl} \equiv \partial \overline{u}_k / \partial x_l \,, \tag{3.21}$$

and account for spatial variations in $A_{kl}(\hat{\mathbf{x}})$ in (3.9) via its local Taylor expansion about the point $\mathbf{x}$ as

$$A_{kl}(\hat{\mathbf{x}}) = A_{kl}(\mathbf{x}) + r_m \frac{\partial A_{kl}}{\partial x_m} + \frac{r_m r_p}{2} \frac{\partial^2 A_{kl}}{\partial x_m \partial x_p} + \cdots + \frac{1}{n!} \left( r_m r_p \ldots \right) \frac{\partial^n A_{kl}}{\partial x_m \partial x_p \ldots} \,, \tag{3.22}$$

where $\mathbf{r} \equiv \hat{\mathbf{x}} - \mathbf{x}$ and all derivatives of $A_{kl}$ are evaluated at $\mathbf{x}$, and where $n$ is the order of the expansion. As $n \to \infty$, the expansion provides an exact representation of all spatial variations in $A_{kl}(\mathbf{r} + \mathbf{x})$ from purely local information at $\mathbf{x}$. Substituting (3.22) into (3.9) then gives

$$\Pi_{ij}^{(r)}(\mathbf{x}) = \sum_{n=0}^{\infty} \frac{\partial^n A_{kl}(\mathbf{x})}{\partial x_m \partial x_p \ldots} \left[ {}_{(mp\ldots)} M_{iljk}^{(n)} + {}_{(mp\ldots)} M_{jlik}^{(n)} \right] \,, \tag{3.23}$$

where

$$_{(mp\ldots)} M_{iljk}^{(n)} \equiv -\frac{1}{2\pi n!} \int_{\mathbf{R}} \left[ \frac{r_m r_p \ldots}{r^n} \right] r^{n-1} \frac{\partial^2 R_{il}(\mathbf{r})}{\partial r_j r_k} d\mathbf{r} \,. \tag{3.24}$$

The $n$th-order term in (3.23) involves $n$ derivatives of $A_{kl}$ as well as $n$ total indices $(mp\ldots)$ in $_{(mp\ldots)} M_{iljk}^{(n)}$.

From the central hypothesis on which the present treatment of nonlocal effects in $\Pi_{ij}^{(r)}$ is based, we represent $R_{il}(\mathbf{r})$ in (3.24) by the form in (3.16). With the relations

$$\frac{\partial r}{\partial r_j} = \frac{r_j}{r}, \quad \frac{\partial r_i}{\partial r_j} = \delta_{ij} \,, \tag{3.25}$$

the double derivative of $R_{il}(\mathbf{r})$ in (3.24) is then given by

$$\frac{\partial^2 R_{il}(\mathbf{r})}{\partial r_j \partial r_k} = \frac{k}{3} \left[ a_{ijkl} \frac{1}{r} \frac{df}{dr} + b_{ijkl} \frac{d^2 f}{dr^2} + c_{ijkl} r \frac{d^3 f}{dr^3} \right] \,, \tag{3.26}$$

where we have introduced the compact notation

$$a_{ijkl} \equiv 3\delta_{jk}\delta_{il} - \delta_{ij}\delta_{kl} - \delta_{jl}\delta_{ki} - 3\alpha_{jk}\delta_{il} + \delta_{ij}\alpha_{lk} + \delta_{jl}\alpha_{ik} + \delta_{ik}\alpha_{lj} + \delta_{kl}\alpha_{ij} + \delta_{kj}\alpha_{il} - 3\beta_{iljk},$$
$$(3.27a)$$

$$b_{ijkl} \equiv \delta_{il}\delta_{jk} + 3\alpha_{jk}\delta_{il} - \delta_{ij}\alpha_{lk} - \delta_{lj}\alpha_{ik} - \delta_{ik}\alpha_{lj} - \delta_{kl}\alpha_{ij} - \delta_{kj}\alpha_{il} + 3\beta_{iljk}, \qquad (3.27b)$$

$$c_{ijkl} \equiv \delta_{il}\alpha_{jk} - \beta_{iljk}, \qquad (3.27c)$$

with

$$\alpha_{ij} \equiv \frac{r_i r_j}{r^2}, \qquad \beta_{ijkl} \equiv \frac{r_i r_j r_k r_l}{r^4}. \qquad (3.28)$$

Using (3.26)-(3.28), the integral in (3.24) can then be written as

$$_{(mp...)}M^{(n)}_{iljk} = -\frac{k}{6\pi n!} \int_{-\infty}^{\infty} \left[\frac{r_m r_p \cdots}{r^n}\right] \left[a_{ijkl} r^{n-2}\frac{df}{dr} + b_{ijkl} r^{n-1}\frac{d^2 f}{dr^2} + c_{ijkl} r^n \frac{d^3 f}{dr^3}\right] d\mathbf{r}. \qquad (3.29)$$

Writing the differential in (3.29) in spherical coordinates as $d\mathbf{r} = r^2 dr \, d\Omega$, where $d\Omega = \sin\theta \, d\theta \, d\phi$ and $r = [0, \infty)$, $\theta = [0, \pi]$, and $\phi = [0, 2\pi)$, since $f(r)$ has no dependence on $\theta$ or $\phi$ and since $a_{ijkl}$, $b_{ijkl}$, and $c_{ijkl}$ in (3.27) have no dependence on $r$, the integrals over these terms in (3.29) can be considered separately. Using (3.26), the integral in (3.29) can then be written as

$$_{(mp...)}M^{(n)}_{iljk} = -\frac{k}{6\pi n!}\left[\int_0^{\infty} r^n \frac{df}{dr} dr \int_\Omega a_{ijkl}\frac{r_m r_p \cdots}{r^n} \, d\Omega \qquad (3.30)\right.$$

$$\left. + \int_0^{\infty} r^{n+1}\frac{d^2 f}{dr^2} dr \int_\Omega b_{ijkl}\frac{r_m r_p \cdots}{r^n} \, d\Omega + \int_0^{\infty} r^{n+2}\frac{d^3 f}{dr^3} dr \int_\Omega c_{ijkl}\frac{r_m r_p \cdots}{r^n} \, d\Omega\right],$$

where $k$ in the leading factor is the turbulence kinetic energy. With the corresponding expression for $_{(mp...)}M^{(n)}_{jlik}$, (3.23) and (3.30) provide a nonlocal form for the rapid pressure-strain rate correlation $\Pi^{(r)}_{ij}$ in terms of the longitudinal correlation $f(r)$.

### 3.2.4 Representing the Longitudinal Correlation $f(r)$

As will be seen later, in (3.30) the integrals over $d\Omega$ can be readily evaluated. Moreover, for $n = 0$ the integrals over $dr$ are independent of $f(r)$, and thus $M^{(0)}_{iljk}$ can be obtained from the general properties

$$\Lambda = \int_0^{\infty} f(r)dr, \quad f(0) = 1, \quad f(\infty) = 0. \qquad (3.31)$$

However for $n > 0$, evaluating the integrals over $dr$ to obtain $_{(mp...)}M^{(n)}_{jlik}$ requires an explicit form for the longitudinal correlation function $f(r)$. We can anticipate, however, that the precise form may not be of central importance to our eventual result for $\Pi^{(r)}_{ij}$, since the only role of $f(r)$ is to weight the contributions from velocity gradients $A_{kl}(\mathbf{x} + \mathbf{r})$ around the local point $\mathbf{x}$. It is thus likely that the integral scale $\Lambda$ in (3.31) plays the most essential

role, since it determines the size of the region around $\mathbf{x}$ from which nonlocal contributions to the integral for $\Pi_{ij}^{(r)}$ will be significant. When $r$ is scaled by $\Lambda$, the precise form of $f(r/\Lambda)$ is likely to be far less important for most reasonable forms that satisfy the constraints in (3.31).

Despite its fundamental significance in turbulence theory, the form of $f(r)$ for any $r$ and all Reynolds numbers has yet to be determined even for homogeneous isotropic turbulence. Perhaps the most widely-accepted representation for $f(r)$ comes from Kolmogorov's 1941 universal equilibrium hypotheses. For large values of $Re_\Lambda \equiv k^{1/2}\Lambda/\nu$ and inertial range separations $\lambda_\nu \ll r \ll \Lambda$, where $\lambda_\nu \sim (\nu^3/\epsilon)^{1/4}$ is the viscous diffusion scale and $\Lambda$ is the integral length scale in (3.31), the mean-square velocity difference is taken to depend solely on $r$ and the turbulent dissipation rate $\epsilon$, and thus on dimensional grounds must scale as

$$\overline{[u'(\mathbf{x}+\mathbf{r})-u'(\mathbf{x})]^2} \sim \epsilon^{2/3}r^{2/3} . \tag{3.32}$$

Expanding the left-hand side of (3.32) and using (3.17) gives

$$\frac{4}{3}k\left[1-f(r)\right] \sim \epsilon^{2/3}r^{2/3} . \tag{3.33}$$

Defining the proportionality constant in (3.33) as $C_f$ and rearranging gives the inertial range form of $f(r)$ as

$$f(r) = 1 - \frac{3}{4}C_f\left[\frac{r}{k^{3/2}/\epsilon}\right]^{2/3} . \tag{3.34}$$

From Hinze [36], a value for $C_f$ can be obtained in terms of the Kolmogorov constant $K \equiv (8/9\alpha)^{2/3} \approx 1.7$, where $\alpha \approx 0.405$, as

$$C_f = \frac{81}{55}\,\Gamma(4/3)K \approx 2.24 , \tag{3.35}$$

where we have used $\Gamma(4/3) \approx 0.893$. Expressing $\Lambda$ in terms of $k$ and $\epsilon$ on dimensional grounds as

$$\Lambda = C_\lambda\frac{k^{3/2}}{\epsilon} , \tag{3.36}$$

where $C_\lambda$ is a presumably universal constant, then allows the inertial-range form of $f(r)$ in (3.34) to be given as

$$f(r/\Lambda) = 1 - \frac{3}{4}C_f C_\lambda^{2/3}\left(\frac{r}{\Lambda}\right)^{2/3} . \tag{3.37}$$

However the form for $f(r)$ in (3.37) is valid only for inertial-range $r$ values, namely $\lambda_\nu \ll r \ll \Lambda$ and thus for $Re_\Lambda^{-3/4} \ll (r/\Lambda) \ll 1$. As a consequence, this form cannot be used directly to evaluate the $r$-integrals in (3.30). However, experimental data from a wide range of turbulent free shear flows (*e.g.*, [109, 110]) and direct numerical simulation results for wall-bounded turbulent flows (*e.g.*, [39, 46]) show that $f(r)$ can be reasonably

represented by the exponential form

$$f(r/\Lambda) = e^{-r/\Lambda} \, , \tag{3.38}$$

as can be seen in Figures 3.3(a)-(c). Moreover, $C_\lambda$ in (3.36) can be chosen to closely match $f(r)$ in (3.38) with the fundamentally-rooted inertial-range form in (3.37). Indeed, Figure 3.4 shows that with

$$C_\lambda \approx 0.23 \tag{3.39}$$

the exponential form in (3.38) gives reasonable agreement with the inertial-range form in (3.37) up to $r/\Lambda \approx 1$. This exponential form is thus here taken to represent $f(r)$ in high-$Re_\Lambda$ turbulent flows, and will be used in (3.30) to obtain an explicit form for the nonlocal rapid pressure-strain correlation. Since (3.23) with (3.30) is a rigorous formulation for $\Pi_{ij}^{(r)}$ within the central hypothesis on which the present approach is based, the exponential representation for $f(r)$ is the principal additional approximation that will be used below in deriving the present result for the rapid pressure-strain correlation.

While the exponential $f(r)$ appears appropriate for high $Re_\Lambda$, in the $Re_\Lambda \to 0$ limit the Kármán-Haworth equation [106] allows a solution for $f(r)$. Batchelor and Townsend [5] showed that for small $Re_\Lambda$ when inertial effects can be neglected, this equation can be solved exactly, giving a Gaussian form for $f(r)$ as

$$f(r/\Lambda) = \exp\left[-\frac{4}{\pi}\left(\frac{r}{\Lambda}\right)^2\right] . \tag{3.40}$$

Ristorcelli [81] has proposed a blended form for $f(r)$ that satisfies various conditions placed on $f(r)$, including those in (3.31), while recovering the Gaussian $f(r)$ in (3.40) as $Re_\Lambda \to 0$ and the exponential $f(r)$ in (3.38) as $Re_\Lambda \to \infty$. It should be possible to use such blended forms for $f(r)$ to obtain a nonlocal pressure-strain correlation valid for all Reynolds numbers, following the procedure developed herein. In the following we obtain the nonlocal pressure-strain correlation using the high-Reynolds number exponential form in (3.38), which should be accurate for the vast majority of turbulent flow problems, and then show how this result can be extended to the low-Reynolds number limit using (3.40).

### 3.2.5 The Nonlocal Rapid Pressure-Strain Rate Correlation

Using (3.38), it can be shown that solution of the integrals over $dr$ in (3.29) gives

$$\int_0^\infty r^{n-2}\frac{df}{dr}r^2 dr = \int_0^\infty r^n\frac{df}{dr}dr = -n!\Lambda^n \, , \tag{3.41a}$$

$$\int_0^\infty r^{n-1}\frac{d^2f}{dr^2}r^2 dr = -(n+1)\int_0^\infty r^n\frac{df}{dr}dr = (n+1)!\Lambda^n \, , \tag{3.41b}$$

$$\int_0^\infty r^n \frac{d^3 f}{dr^3} r^2 dr = (n+2)(n+1) \int_0^\infty r^n \frac{df}{dr} dr = -(n+2)!\Lambda^n. \tag{3.41c}$$

With these results, (3.29) is then given by

$$_{(mp\dots)} M_{iljk}^{(n)} = \frac{k\Lambda^n}{6\pi} \int_\Omega \left[\frac{r_m r_p \dots}{r^n}\right] [a_{ijkl} - (n+1)b_{ijkl} + (n+2)(n+1)c_{ijkl}] \, d\Omega. \tag{3.42}$$

The remaining integrals over $d\Omega$ are all of the form $(r_m r_p \dots)/r^n$ and can be solved using the identities in (2.31).

For $n = 0$, it can be shown using (2.31b) that $M_{iljk}^{(0)}$ is given from (3.42) as

$$M_{iljk}^{(0)} = \frac{2k}{15} \left[4\delta_{il}\delta_{jk} - \delta_{ij}\delta_{kl} - \delta_{jl}\delta_{ki}\right]. \tag{3.43}$$

There is no contribution from the $n = 1$ term $M_{iljk}^{(1)}$ due to (2.31a), and for $n = 2$, from (2.31b), $_{mp} M_{iljk}^{(2)}$ is given by

$$_{mp} M_{iljk}^{(2)} = \frac{2k\Lambda^2}{315} [4\delta_{jk}\delta_{il}\delta_{mp} - 3\left(\delta_{ij}\delta_{kl}\delta_{mp} + \delta_{jl}\delta_{ik}\delta_{mp}\right) - 24\left(\delta_{il}\delta_{jm}\delta_{kp} + \delta_{il}\delta_{km}\delta_{jp}\right) \tag{3.44}$$
$$+ 4\left(\delta_{ij}\delta_{lm}\delta_{kp} + \delta_{ij}\delta_{km}\delta_{lp} + \delta_{jl}\delta_{im}\delta_{kp} + \delta_{jl}\delta_{km}\delta_{ip} + \delta_{ik}\delta_{lm}\delta_{jp}\right.$$
$$\left. + \delta_{ik}\delta_{jm}\delta_{lp} + \delta_{kl}\delta_{im}\delta_{jp} + \delta_{kl}\delta_{jm}\delta_{ip} + \delta_{jk}\delta_{im}\delta_{pl} + \delta_{jk}\delta_{lm}\delta_{ip}\right)].$$

Contracting (3.43) and (3.44) with $A_{kl}$ and its derivatives as in (3.23) then gives

$$A_{kl} \left[M_{iljk}^{(0)} + M_{jlik}^{(0)}\right] = \frac{4}{5} k\overline{S}_{ij}, \tag{3.45}$$

and

$$\frac{\partial^2 A_{kl}}{\partial x_m \partial x_n} \left[_{mp} M_{iljk}^{(2)} +_{mp} M_{jlik}^{(2)}\right] = \frac{68}{315} k\Lambda^2 \nabla^2 \overline{S}_{ij}, \tag{3.46}$$

where we have used $A_{kk} \equiv 0$ and the commutativity of the derivatives of $A_{kl}$, namely

$$\frac{\partial^2 A_{im}}{\partial x_m \partial x_j} = \frac{\partial^3 \overline{u}_i}{\partial x_m \partial x_m \partial x_j} = \nabla^2 A_{ij}. \tag{3.47}$$

From (3.45) and (3.46), the first two terms in the present formulation for the rapid pressure-strain correlation in (3.23) are thus given by

$$\frac{1}{k} \Pi_{ij}^{(r)}(\mathbf{x}) = \frac{4}{5}\overline{S}_{ij} + \frac{68}{315}\Lambda^2 \nabla^2 \overline{S}_{ij} + \cdots. \tag{3.48}$$

The first term on the right in (3.48) is the same as that in (3.19) obtained by Crow [16] assuming spatially uniform mean velocity gradients. Thus the second term in (3.48) is the first-order nonlocal correction accounting for spatial variations in the mean velocity gradient field.

To obtain the remaining higher-order nonlocal corrections in (3.48), it is helpful to

contract (3.42) with the derivatives of $A_{kl}$ and again use $A_{kk} \equiv 0$. It is then readily shown that all terms involving $\delta_{kl}$, $\delta_{km}$, $\delta_{kp}$, ... from the integral over $d\Omega$ are zero when contracted with the derivatives of $A_{kl}$, and as a result the coefficients in (3.27) can be simplified as

$$a_{ijkl} = 4\delta_{jk}\delta_{il} - \delta_{jl}\delta_{ki} - b_{ijkl} \,, \tag{3.49a}$$

$$b_{ijkl} = \delta_{il}\delta_{jk} + b^*_{ijkl} \,, \tag{3.49b}$$

$$b^*_{ijkl} = 3\alpha_{jk}\delta_{il} - \delta_{lj}\alpha_{ik} - \delta_{ik}\alpha_{lj} - \delta_{kj}\alpha_{il} + 3\beta_{iljk} \,, \tag{3.49c}$$

$$c_{ijkl} = \delta_{il}\alpha_{jk} - \beta_{iljk} \,, \tag{3.49d}$$

where $b^*_{ijkl}$ has been introduced to simplify the notation. Using (3.49) and contracting (3.42) with the derivatives of $A_{kl}$ we thus obtain

$$\frac{\partial^n A_{kl}}{\partial x_m \partial x_p \dots} \left[ _{(mp\dots)} M^{(n)}_{iljk} \right] = k\Lambda^n \frac{1}{6\pi} \left[ \frac{\partial^n A_{kl}}{\partial x_m \partial x_p \dots} \right] \int_\Omega \left[ \frac{r_m r_p r_q \dots}{r^n} \right]$$
$$\times [(2 - n)\,\delta_{il}\delta_{jk} - \delta_{ik}\delta_{jl} - (n + 2)\,b^*_{ijkl} + (n + 2)(n + 1)c_{ijkl}]d\Omega \,. \tag{3.50}$$

From (2.31a) all odd-$n$ terms in (3.50) are zero. For even-$n$, the integrals over $d\Omega$ are readily evaluated using (2.31b), and it can be shown that

$$\frac{\partial^n A_{kl}}{\partial x_m \partial x_p \dots} \int_\Omega \left[ \frac{r_m r_p r_q \dots}{r^n} \right] \delta_{jk}\delta_{il}d\Omega = \frac{4\pi(n - 1)!!}{(n + 1)!!} \left( \nabla^2 \right)^{n/2} A_{ji} \,, \tag{3.51}$$

where the invariance of the integral to the order of $(m, n, p, \dots)$ has been used in the result. We can then write (3.50) as

$$\frac{\partial^n A_{kl}}{\partial x_m \partial x_p \dots} \left[ _{(mp\dots)} M^{(n)}_{iljk} \right] = \frac{2k\Lambda^n}{3(n + 1)} \left( \nabla^2 \right)^{n/2} [(2 - n)\,A_{ji} - A_{ij}] \tag{3.52}$$
$$- \frac{k\Lambda^n (n + 2)}{6\pi} \left[ \frac{\partial^n A_{kl}}{\partial x_m \partial x_p \dots} \right] \int_\Omega \left[ \frac{r_m r_p r_q \dots}{r^n} \right] \left[ b^*_{ijkl} - (n + 1)c_{ijkl} \right] d\Omega \,,$$

where we have used $(n - 1)!!/(n + 1)!! = 1/(n + 1)$, and upon switching the $i$ and $j$ indices (3.51) also provides the solution for the integral involving $\delta_{jl}\delta_{ki}$ in (3.50). To solve the last integral in (3.52), from (3.49) we can write

$$b^*_{ijkl} - (n + 1)c_{ijkl} = (2 - n)\,\delta_{il}\alpha_{jk} - \delta_{lj}\alpha_{ik} - \delta_{ik}\alpha_{lj} - \delta_{kj}\alpha_{il} + (n + 4)\,\beta_{iljk} \,. \tag{3.53}$$

Considering the first term involving $\delta_{il}\alpha_{jk}$, we obtain

$$\left[ \frac{\partial^n A_{ki}}{\partial x_m \partial x_p \dots} \right] \int_\Omega \left[ \frac{r_j r_k r_m r_p r_q \dots}{r^{n+2}} \right] d\Omega = \frac{4\pi(n - 1)!!}{(n + 3)!!} \left( \nabla^2 \right)^{n/2} A_{ji} \,. \tag{3.54}$$

The $(n - 1)!!$ term in the numerator results from the fact that there are $(n + 1)!!$ total delta product terms in the solution to (3.54), but by incompressibility only those terms involving

$\delta_{jk}$ are nonzero. This leaves $(n-1)!!$ nonzero terms, all of which yield $\left(\nabla^2\right)^{n/2} A_{ji}$ when contracted with the derivatives of $A_{kl}$. The integral of the $\delta_{lj}\alpha_{ik}$ term in (3.52) gives a similar result to that in (3.38), except that the $i$ and $j$ indices are once again switched. We can thus rewrite (3.52) using (3.53) and (3.54) as

$$\frac{\partial^n A_{kl}}{\partial x_m \partial x_p \dots} \left[_{(mp\dots)} M_{iljk}^{(n)}\right] = \frac{2k\Lambda^n}{3(n+1)} \left(\nabla^2\right)^{n/2} \left[(2-n)\, A_{ji} - A_{ij}\right] \tag{3.55}$$

$$- \frac{2k\Lambda^n (n+2)(n-1)!!}{3(n+3)!!} \left(\nabla^2\right)^{n/2} \left[(2-n) A_{ji} - A_{ij}\right]$$

$$+ \frac{k\Lambda^n(n+2)}{6\pi} \left[\frac{\partial^n A_{kl}}{\partial x_m \partial x_p \dots}\right] \int_\Omega \left[\frac{r_m r_p r_q \dots}{r^n}\right] \left[\delta_{ik}\alpha_{lj} + \delta_{kj}\alpha_{il} - (n+4)\,\beta_{iljk}\right] d\Omega \, .$$

Now considering the integral involving the $\delta_{ik}\alpha_{lj}$ term we obtain

$$\frac{\partial^n A_{il}}{\partial x_m \partial x_p \dots} \int_\Omega \left[\frac{r_m r_p r_q \dots}{r^n}\right] \alpha_{lj} d\Omega = \frac{\partial^n A_{il}}{\partial x_m \partial x_p \dots} \int_\Omega \frac{r_l r_j r_m r_p r_q \dots}{r^{n+2}} d\Omega \, , \tag{3.56}$$

and using (2.31b) this is solved as

$$\frac{\partial^n A_{il}}{\partial x_m \partial x_p \dots} \int_\Omega \frac{r_l r_j r_m r_p r_q \dots}{r^{n+2}} d\Omega = \frac{\partial^n A_{il}}{\partial x_m \partial x_p \dots} \frac{4\pi}{(n+3)!!} \left[\delta_{lj}\delta_{mp} \dots + \delta_{lm}\delta_{jp} \dots + \dots\right] \, . \tag{3.57}$$

However, since $A_{kl} = \partial \overline{u}_k / \partial x_l$, the order of the indices $(l, m, p, \dots)$ on the right-hand side of (3.57) is irrelevant, and each term gives the same result, namely

$$\frac{\partial^n A_{il}}{\partial x_m \partial x_p \dots} \left[\delta_{lj}\delta_{mp} \dots\right] = \left(\nabla^2\right)^{n/2} A_{ij} \, . \tag{3.58}$$

Since there are $(n+1)!!$ such terms in (3.57) we obtain

$$\frac{\partial^n A_{il}}{\partial x_m \partial x_p \dots} \int_\Omega \frac{r_l r_j r_m r_p r_q \dots}{r^{n+2}} d\Omega = \frac{4\pi(n+1)!!}{(n+3)!!} \left(\nabla^2\right)^{n/2} A_{ij} \, . \tag{3.59}$$

A similar result is obtained for the $\delta_{kj}\alpha_{il}$ term in (3.55), again where the $i$ and $j$ indices are switched, so (3.55) can be written as

$$\frac{\partial^n A_{kl}}{\partial x_m \partial x_p \dots} \left[_{(mp\dots)} M_{iljk}^{(n)}\right] = \frac{2k\Lambda^n}{3(n+1)} \left(\nabla^2\right)^{n/2} \left[(2-n)\, A_{ji} - A_{ij}\right] \tag{3.60}$$

$$- \frac{2k\Lambda^n(n+2)(n-1)!!}{3(n+3)!!} \left(\nabla^2\right)^{n/2} \left[(2-n) A_{ji} - A_{ij}\right]$$

$$+ \frac{2k\Lambda^n(n+2)(n+1)!!}{3(n+3)!!} \left(\nabla^2\right)^{n/2} \left[A_{ji} + A_{ij}\right]$$

$$- \frac{k\Lambda^n(n+2)(n+4)}{6\pi} \left[\frac{\partial^n A_{kl}}{\partial x_m \partial x_p \dots}\right] \int_\Omega \left[\frac{r_m r_p r_q \dots}{r^n}\right] \beta_{iljk} d\Omega \, .$$

Now for the last integral we can write

$$\frac{\partial^n A_{kl}}{\partial x_m \partial x_p \ldots} \int_\Omega \left[ \frac{r_m r_p r_q \cdots}{r^n} \right] \beta_{iljk} d\Omega = \frac{\partial^n A_{kl}}{\partial x_m \partial x_p \ldots} \int_\Omega \frac{r_i r_j r_k r_l r_m r_p r_q \cdots}{r^{n+4}} d\Omega . \qquad (3.61)$$

We again note that by incompressibility, all terms involving $\delta_{kl}$, $\delta_{km}$, $\delta_{kp}$, etc. in the solution to (3.61) are zero. Thus we only obtain nonzero contributions to the result from the $\delta_{ik}$ and $\delta_{kj}$ terms. Following the same reasoning used to obtain the result in (3.59), we can solve (3.61) as

$$\frac{\partial^n A_{kl}}{\partial x_m \partial x_p \ldots} \int_\Omega \left[ \frac{r_m r_p r_q \cdots}{r^n} \right] \beta_{iljk} d\Omega = \frac{4\pi (n+1)!!}{(n+5)!!} \left( \nabla^2 \right)^{n/2} [A_{ji} + A_{ij}] . \qquad (3.62)$$

Note that here we have used the fact that of the $(n+3)!!$ delta function terms in the solution to (3.61), only the $(n+1)!!$ terms involving $\delta_{ik}$ and the $(n+1)!!$ terms involving $\delta_{jk}$ give a nonzero result when contracted with the derivatives of $A_{kl}$. As in (3.58), the resulting contracted terms are all equal, and switching $i$ and $j$ indices yields the final solution in (3.62). Substituting (3.62) into (3.60) then yields

$$\frac{\partial^n A_{kl}}{\partial x_m \partial x_p \ldots} \left[ _{(mp\ldots)} M_{iljk}^{(n)} \right] = \frac{2k\Lambda^n}{3(n+1)} \left( \nabla^2 \right)^{n/2} [(2-n) A_{ji} - A_{ij}] \qquad (3.63)$$
$$- \frac{2k\Lambda^n (n+2)(n-1)!!}{3(n+3)!!} \left( \nabla^2 \right)^{n/2} [(2-n) A_{ji} - A_{ij}]$$
$$+ \frac{2k\Lambda^n (n+2)(n+1)!!}{3(n+3)!!} \left( \nabla^2 \right)^{n/2} [A_{ji} + A_{ij}]$$
$$- \frac{2k\Lambda^n (n+2)(n+4)(n+1)!!}{3(n+5)!!} \left( \nabla^2 \right)^{n/2} [A_{ji} + A_{ij}] .$$

Adding the corresponding result for $M_{jlik}^{(n)}$ to (3.63) then gives $\Pi_{ij}^{(r)}$ in (3.23) as

$$\frac{1}{k} \Pi_{ij}^{(r)} = \sum_{n=0,even}^{\infty} \left[ C_2^{(n)} \Lambda^n \left( \nabla^2 \right)^{n/2} \overline{S}_{ij} \right] , \qquad (3.64)$$

where the coefficients are

$$C_2^{(n)} \equiv \frac{4(n^2 + 2n + 9)}{3(n+5)(n+3)(n+1)} . \qquad (3.65)$$

Since the indices in (3.65) and (3.64) are required to be even, we can change the index $n$ to $(2n-2)$, where then $n = 1, 2, 3, \ldots$. This gives the final result for the nonlocal rapid pressure-strain correlation from the present approach as

$$\frac{1}{k} \Pi_{ij}^{(r)} = C_2^{(1)} \overline{S}_{ij} + \sum_{n=2}^{\infty} \left[ C_2^{(n)} \Lambda^{2n-2} \left( \nabla^2 \right)^{n-1} \overline{S}_{ij} \right] \qquad (3.66)$$

73

with

$$C_2^{(n)} \equiv \frac{16n^2 - 16n + 36}{3(2n+3)(4n^2-1)}, \tag{3.67}$$

where $\Lambda$ in (3.66) is from (3.36) and (3.39). In (3.67) it may be readily verified that $C_2^{(1)} = 4/5$ and $C_2^{(2)} = 68/315$, consistent with (3.48) and (3.19). The first term on the right in (3.66) accounts for purely local effects on $\Pi_{ij}^{(r)}$, while the series term accounts for nonlocal effects.

The result in (3.66) and (3.67) is the first rigorous formulation for the rapid pressure-strain correlation $\Pi_{ij}^{(r)}$ that accounts for nonlocal effects due to spatial variations in the mean velocity gradients. Within the central hypothesis on which the present approach is based, the principal approximation used in deriving (3.66) and (3.67) is the exponential form of $f(r)$ in (3.38) for high-$Re_\Lambda$ turbulent flows. However, the only effect of this choice of $f(r)$ is in the resulting coefficients $C_2^{(n)}$ in (3.67). All other aspects of (3.66) are unaffected by the particular form of $f(r)$, and instead result directly from the fundamental approach taken here in solving (3.9) via Taylor expansion of the mean velocity gradients $\partial \overline{u}_k / \partial x_l$ to account for nonlocal effects in $\Pi_{ij}^{(r)}$.

The coefficients $C_2^{(n)}$ in (3.67) from the exponential representation of $f(r)$ are shown in Figure 3.5 and listed in Table 3.1 up to $n = 8$ for high-$Re_\Lambda$ flows. It is apparent that the $n = 1$ term in (3.66), which accounts for the purely local contribution to $\Pi_{ij}^{(r)}$ as verified in (3.48), is by far the dominant coefficient. The remaining coefficients for $n = 2, 3, 4, \ldots$ correspond to the nonlocal contributions to $\Pi_{ij}^{(r)}$, and can be seen in Figure 3.5 to decrease only slowly with increasing order $n$. However, while $C_2^{(1)}$ is clearly the dominant coefficient, in (3.66) the remaining coefficients are multiplied by successively higher-order Laplacians of the mean strain rate field, and thus may produce net contributions to $\Pi_{ij}^{(r)}$ that are comparable to, or possibly even larger than, the local term due to $n = 1$.

### 3.2.6 Corresponding Coefficients for $Re_\Lambda \to 0$

While the coefficients in (3.67) are appropriate for $Re_\Lambda \gg 1$, in this section we use the exact Gaussian form for $f(r)$ in (3.40) that applies in the $Re_\Lambda \to 0$ limit to obtain the result for $\Pi_{ij}^{(r)}$ applicable to low-$Re_\Lambda$ flows, as may occur in the near-wall region of wall-bounded turbulent flows. Using this expression for $f(r)$, the integrals in (3.41) can be calculated for low-$Re_\Lambda$ as

$$\int_0^\infty r^{n-2} \frac{df}{dr} r^2 dr = \int_0^\infty r^n \frac{df}{dr} dr = -n! \Lambda^n \left[ \frac{(n/2)!}{n!} \left( \frac{2}{\sqrt{\pi}} \right)^n \right], \tag{3.68a}$$

$$\int_0^\infty r^{n-1} \frac{d^2 f}{dr^2} r^2 dr = -(n+1) \int_0^\infty r^n \frac{df}{dr} dr = (n+1)! \Lambda^n \left[ \frac{(n/2)!}{n!} \left( \frac{2}{\sqrt{\pi}} \right)^n \right], \tag{3.68b}$$

$$\int_0^\infty r^n \frac{d^3 f}{dr^3} r^2 dr = (n+2)(n+1) \int_0^\infty r^n \frac{df}{dr} dr = -(n+2)! \Lambda^n \left[ \frac{(n/2)!}{n!} \left( \frac{2}{\sqrt{\pi}} \right)^n \right]. \tag{3.68c}$$

74

The result for $M_{iljk}^{(0)}$ in (3.43) is independent of the form of $f(r)$ and thus is unchanged in this limit, but now $_{mp}M_{iljk}^{(2)}$ in (3.44) is reduced by the factor $2/\pi$ to give

$$_{mp}M_{iljk}^{(2)} = \frac{4k\Lambda^2}{315\pi}[4\delta_{jk}\delta_{il}\delta_{mp} - 3\left(\delta_{ij}\delta_{kl}\delta_{mp} + \delta_{jl}\delta_{ik}\delta_{mp}\right) - 24\left(\delta_{il}\delta_{jm}\delta_{kp} + \delta_{il}\delta_{km}\delta_{jp}\right) \quad (3.69)$$
$$+4\left(\delta_{ij}\delta_{lm}\delta_{kp} + \delta_{ij}\delta_{km}\delta_{lp} + \delta_{jl}\delta_{im}\delta_{kp} + \delta_{jl}\delta_{km}\delta_{ip} + \delta_{ik}\delta_{lm}\delta_{jp}\right.$$
$$\left. +\delta_{ik}\delta_{jm}\delta_{lp} + \delta_{kl}\delta_{im}\delta_{jp} + \delta_{kl}\delta_{jm}\delta_{ip} + \delta_{jk}\delta_{im}\delta_{pl} + \delta_{jk}\delta_{lm}\delta_{ip}\right)].$$

With the remaining higher-order terms $_{(mp...)}M_{iljk}^{(n)}$, it may be readily verified that the result for $\Pi_{ij}^{(r)}$ in (3.66) is unchanged in this low-$Re_\Lambda$ limit, but the coefficients $C_2^{(n)}$ are now given by

$$C_2^{(n)} = \frac{16n^2 - 16n + 36}{3(2n+3)(4n^2-1)}\left[\frac{(n-1)!}{(2n-2)!}\left(\frac{4}{\pi}\right)^{n-1}\right], \quad (3.70)$$

where again $n = 1, 2, 3, \ldots$. The effect of the additional factor in (3.70) relative to (3.67) is to damp the higher-order terms in the $Re_\Lambda \gg 1$ coefficients, as shown in Figure 3.5. It is apparent that in this $Re_\Lambda \to 0$ limit, only the first nonlocal term ($n = 2$) in (3.66) is significant, with all higher-order coefficients being negligible. This may introduce significant simplifications in near-wall modeling, where this limit applies as $y^+ \to 0$.

### 3.2.7   Relation to Rotta

The present result in (3.66) with (3.67) for $Re_\Lambda \gg 1$ or (3.70) for $Re_\Lambda \to 0$ is the first nonlocal rapid pressure-strain correlation that rigorously accounts for the effect of spatial variations in the mean velocity gradients on the turbulence anisotropy. Previously, Rotta [86] derived some of the components of $M_{iljk}^{(0)}$ and $_{mp}M_{iljk}^{(2)}$, although not enough to construct the full series result for $\Pi_{ij}^{(r)}$ in (3.66). Using symmetry properties and isotropy arguments Rotta was able to deduce several components of $M_{iljk}^{(0)}$ as

$$M_{\alpha\alpha\alpha\alpha}^{(0)} = 0.4\overline{u'^2}, \quad M_{\alpha\alpha\beta\beta}^{(0)} = 0.8\overline{u'^2},$$

where summation over Greek indices is not assumed and $\alpha \neq \beta \neq \gamma$. The components of $M_{iljk}^{(0)}$ in (3.71) agree with the general expressions in (3.18) and (3.43) obtained by Crow [16] and the present approach, although it should be emphasized that Rotta was unable to obtain all components of the $M_{iljk}^{(0)}$ tensor. It is also emphasized that these results are independent of the specific representation for the correlation function $f(r)$, and thus are valid for all Reynolds numbers.

In agreement with the present study, Rotta showed that all components of $_mM_{iljk}^{(1)}$ are identically zero. Using an inertial-range form for $f(r)$ similar to (3.34), Rotta obtained

several components of $_{mp}M_{iljk}^{(2)}$ in the high Reynolds number limit as

$$_{\alpha\alpha}M_{\alpha\alpha\alpha\alpha}^{(2)} = -0.52\overline{u'^2}L^2\,, \quad _{\alpha\alpha}M_{\beta\beta\beta\beta}^{(2)} = -0.104\overline{u'^2}L^2\,, \tag{3.71}$$

$$_{\alpha\alpha}M_{\beta\beta\gamma\gamma}^{(2)} = 0.207\overline{u'^2}L^2\,, \quad _{\alpha\alpha}M_{\beta\beta\alpha\alpha}^{(2)} = -2.28\overline{u'^2}L^2\,, \quad _{\alpha\alpha}M_{\alpha\alpha\beta\beta}^{(2)} = 0.62\overline{u'^2}L^2\,,$$

while in the low-Reynolds number limit Rotta used the Gaussian representation for $f(r)$ in (3.40) to obtain

$$_{\alpha\alpha}M_{\alpha\alpha\alpha\alpha}^{(2)} = -0.243\overline{u'^2}L^2\,, \quad _{\alpha\alpha}M_{\beta\beta\beta\beta}^{(2)} = -0.049\overline{u'^2}L^2\,, \tag{3.72}$$

$$_{\alpha\alpha}M_{\beta\beta\gamma\gamma}^{(2)} = 0.097\overline{u'^2}L^2\,, \quad _{\alpha\alpha}M_{\beta\beta\alpha\alpha}^{(2)} = -1.07\overline{u'^2}L^2\,, \quad _{\alpha\alpha}M_{\alpha\alpha\beta\beta}^{(2)} = 0.292\overline{u'^2}L^2\,.$$

Note that rather than using the longitudinal integral scale $\Lambda$, Rotta expressed his results [86] in terms of the transverse integral scale $L$, defined as

$$L \equiv \int_0^\infty g(r)dr\,, \tag{3.73}$$

where $g(r)$ is the transverse correlation function. The two length scales are related by $L = 0.5\Lambda$ for incompressible flows, and this relation can be used directly in the $Re_\Lambda \to 0$ limit to verify that the present low-$Re_\Lambda$ result for $_{mp}M_{iljk}^{(2)}$ in (3.69) agrees with the components obtained by Rotta in (3.72).

For high Reynolds numbers, the inertial range representation for $f(r)$ used by Rotta is different than the exponential representation in (3.38), and subsequently the relation $L = 0.5\Lambda$ between the $L$ defined by Rotta and $\Lambda$ used herein does not hold in the high-Reynolds number limit. These differences can be addressed by considering that in both the present approach and the derivation by Rotta, the integral of $[r^2(df/dr)]$ from $r = 0$ to $r = \infty$ is critical for obtaining $_{mp}M_{iljk}^{(2)}$. This can be seen, for example, from the integrals in (3.41) for $n = 2$. By contrast to the present approach however, where this integral is solved in (3.41a) using the exponential $f(r)$ in (3.38), Rotta instead used the relation

$$\int_0^\infty r^2\frac{df}{dr}dr = -\frac{4}{\overline{u'^2}}\int_0^\infty \frac{F(\kappa)}{\kappa^2}d\kappa\,, \tag{3.74}$$

where $\kappa$ is the wavenumber. For high Reynolds numbers, the spectrum $F(\kappa)$ is given by

$$F(\kappa) \propto \begin{cases} \kappa^4 & \text{for small } \kappa \\ \kappa^{-5/3} & \text{for large } \kappa \end{cases}\,, \tag{3.75}$$

where the large-$\kappa$ result is obtained from inertial range scaling arguments and is analogous to the inertial range $f(r)$ in (3.34). Using (3.75), Rotta obtained [86]

$$\int_0^\infty \frac{F(\kappa)}{\kappa^2}d\kappa = 2.72\overline{u'^2}L^2\,. \tag{3.76}$$

and the integral in (3.74) can thus be solved as

$$\int_0^\infty r^2 \frac{df}{dr} dr = -10.88 L^2 \,. \tag{3.77}$$

Equating (3.77) with the present result in (3.41a) for $n = 2$ gives a relation between $\Lambda$ used herein and $L$ used by Rotta as

$$L = 0.43\Lambda \,. \tag{3.78}$$

Using this relation, the high-Reynolds number results obtained by Rotta in (3.71) can thus be written in terms of the present $\Lambda$ as

$$_{\alpha\alpha}M^{(2)}_{\alpha\alpha\alpha\alpha} = -0.064 k\Lambda^2 \,, \quad _{\alpha\alpha}M^{(2)}_{\beta\beta\beta\beta} = -0.013 k\Lambda^2 \,, \tag{3.79}$$

$$_{\alpha\alpha}M^{(2)}_{\beta\beta\gamma\gamma} = 0.025 k\Lambda^2 \,, \quad _{\alpha\alpha}M^{(2)}_{\beta\beta\alpha\alpha} = -0.28 k\Lambda^2 \,, \quad _{\alpha\alpha}M^{(2)}_{\alpha\alpha\beta\beta} = 0.076 k\Lambda^2 \,,$$

where we have used the relation $\overline{u'^2} = \frac{2}{3}k$ for isotropic turbulence to obtain the results. It is readily verified that the values in (3.79) agree with the corresponding tensor components from (3.44).

The agreement with those components of $_{mp}M^{(2)}_{iljk}$ reported by Rotta [86] provides partial validation of the present results. However, the present results go much further by addressing the complete components of $_{(mp...)}M^{(n)}_{iljk}$ for all $n$, thereby allowing the first complete formulation of nonlocal effects in the rapid pressure-strain correlation $\Pi^{(r)}_{ij}$ due to spatial variations in the mean-flow gradients $\partial\overline{u}_i/\partial x_j$.

### 3.2.8 Final Form of the Nonlocal Pressure-Strain Correlation

The present result for nonlocal effects in the rapid part $\Pi^{(r)}_{ij}$ of the pressure-strain correlation, given by (3.66) with the coefficients $C^{(n)}_2$ in (3.67) or (3.70) and with $\Lambda$ in (3.36) and (3.39), can be combined with (1.22) for the slow part $\Pi^{(s)}_{ij}$ to give $\Pi_{ij}$ in (1.15) as

$$\frac{1}{k}\Pi_{ij} = -C_1 \frac{\epsilon}{k} a_{ij} + C^{(1)}_2 \overline{S}_{ij} + \sum_{n=2}^\infty \left[ C^{(n)}_2 \Lambda^{2n-2} \left(\nabla^2\right)^{n-1} \overline{S}_{ij} \right] \,. \tag{3.80}$$

In homogeneous flows, for which prior purely local models for $\Pi_{ij}$ have been relatively successful, the Laplacians of $\overline{S}_{ij}$ in (3.80) vanish, and thus the present nonlocal pressure-strain formulation recovers the local form from (1.22) and (3.19), since $C^{(1)}_2 = 4/5$ in both (3.67) and (3.70).

Note that while the formulation for $\Pi_{ij}$ in (3.80) addresses nonlocal effects due to variations in the mean strain, it does not address nonlocal effects that may arise due to inhomogeneities in the turbulence. For many free-shear and wall bounded flows it is expected that in much of the flow the principal nonlocality in the anisotropy evolution will be captured

by (3.80). However, in certain situations nonlocal effects due to turbulence inhomogeneities may also be significant, and future work is required to address these effects. Nevertheless, it will be seen from the nonlocal tests in Chapter V that the new nonlocal, nonequilibrium anisotropy closure developed in the following, which is based on the nonlocal pressure-strain formulation in (3.80), is sufficient to give substantially improved predictions of the anisotropy in wall-bounded flows compared to prior purely local closure approaches.

## 3.3 The Nonlocal Anisotropy Transport Equation

When (3.80) is introduced in (1.15) it gives a new anisotropy transport equation that accounts for both local and nonlocal effects via the present fundamental treatment of spatial variations in the mean velocity gradients in (3.9). However, (3.80) does not account for possible additional anisotropic effects in $\Pi_{ij}^{(r)}$, since the present nonlocal pressure-strain result in (3.80) is based on the central hypothesis that $R_{il}(\mathbf{r})$ in (3.24) can be represented by its isotropic form in (3.16). Fundamentally-based approaches for any such remaining anisotropic effects in $\Pi_{ij}$ have yet to be rigorously formulated, however it has been argued (e.g., [51, 98]) that such additional anisotropy effects may be represented by higher-order tensorial combinations of $a_{ij}$, $\overline{S}_{ij}$, and $\overline{W}_{ij}$. The most general of such combinations that remains linear in $a_{ij}$ is

$$\frac{1}{k}\Pi_{ij}^{(aniso)} = C_3 \left( a_{il}\overline{S}_{lj} + \overline{S}_{il}a_{lj} - \frac{2}{3}a_{nl}\overline{S}_{nl}\delta_{ij} \right) + C_4 \left( a_{il}\overline{W}_{lj} - \overline{W}_{il}a_{lj} \right), \qquad (3.81)$$

where the constants $C_3$ and $C_4$ can be chosen to presumably account for such additional anisotropic effects. In general, choices for these coefficients vary widely from one model to another; a summary of various models is given in Ref. [99].

When (3.80) is combined with (3.81), it provides an anisotropy transport equation that accounts for both local and nonlocal effects, as well as possible additional anisotropic effects, in the pressure-strain correlation as

$$\frac{Da_{ij}}{Dt} = -\alpha_1 \frac{\epsilon}{k}a_{ij} + \alpha_2 \overline{S}_{ij} + \sum_{n=2}^{\infty} \left[ C_2^{(n)} \Lambda^{2n-2} \left( \nabla^2 \right)^{n-1} \overline{S}_{ij} \right] \qquad (3.82)$$

$$-\frac{1}{k} \left[ \epsilon_{ij} - \frac{2}{3}\epsilon\delta_{ij} \right] + \alpha_3 \left( a_{il}\overline{S}_{lj} + \overline{S}_{il}a_{lj} - \frac{2}{3}a_{nl}\overline{S}_{nl}\delta_{ij} \right)$$

$$-\alpha_4 \left( a_{il}\overline{W}_{lj} - \overline{W}_{il}a_{lj} \right) + \frac{1}{k} \left[ D_{ij} - \left( a_{ij} + \frac{2}{3}\delta_{ij} \right) D \right],$$

where the $C_2^{(n)}$ coefficients are given in (3.67) or (3.70), and the $\alpha_i$ are defined as

$$\alpha_1 = \frac{P}{\epsilon} - 1 + C_1, \quad \alpha_2 = C_2^{(1)} - \frac{4}{3}, \quad \alpha_3 = C_3 - 1, \quad \alpha_4 = C_4 - 1. \qquad (3.83)$$

Values for the constants $C_1$, $C_3$ and $C_4$ in (3.83) may be inferred from prior purely local

models, such as the LRR [51] or SSG [98] models in (1.26) and (1.27), respectively, which are all based on forms of (3.82) without the nonlocal effects given by the series term. However, optimal values for these constants may change in the presence of the nonlocal pressure-strain term in (3.83).

With respect to the remaining terms in (3.82), for high Reynolds numbers the dissipation tensor $\epsilon_{ij}$ is concentrated at the smallest scales of the flow, which are assumed to be isotropic. Thus, consistent with the central hypothesis on which the present result for the pressure-strain tensor is derived, the dissipation is commonly represented by its isotropic form in (1.20), with the result that the dissipation term in (3.82) vanishes entirely. The only remaining unclosed terms when (3.82) is used with the ensemble-averaged Navier-Stokes equations are the transport terms $D_{ij}$ and $D$, and these are typically represented using gradient-transport hypotheses, with several possible such formulations summarized in Ref. [99].

A number of different approaches can be taken for solving (3.82), many of which have been outlined in Section 1.3. First, (3.82) may be solved as a set of six coupled partial differential equations, together with the ensemble-averaged Navier-Stokes equations, to obtain a new nonlocal Reynolds stress transport closure that improves on existing approaches such as the LRR and SSG models in strongly inhomogeneous flows. Alternatively, equilibrium approximations may be used to neglect the $Da_{ij}/Dt$ and $D_{ij}$ terms in (3.82) to obtain a new explicit nonlocal equilibrium stress model for $a_{ij}$, analogous to the existing local models developed, for example, by Gatski and Speziale [24], Girimaji [27], and Wallin and Johannson [107] as discussed in Section 1.3.2.1. Perhaps preferably, a new explicit nonlocal, nonequilibrium stress model for $a_{ij}$ can be obtained from (3.82) following the approach in Ref. [31], by retaining $Da_{ij}/Dt$ and explicitly solving a quasi-linear form of (3.82).

## 3.4   New Nonlocal, Nonequilibrium Turbulence Anisotropy Closure

The new nonlocal, nonequilibrium anisotropy closure developed herein seeks to include the finite-time response of the turbulence anisotropy found in full Reynolds stress transport models, but will do so within a comparatively simple direct model for the anisotropy tensor $a_{ij}$. In the following, the new closure is rigorously derived from the nonlocal transport equation for the Reynolds stress anisotropy in (3.82).

### 3.4.1   Quasi-Linear Nonlocal Anisotropy Transport Equation

Motivated by the largely linear dynamics that govern the strain-vorticity alignment and thus the anisotropy, as discussed in Section 3.1, here we retain only the first three terms on the right-hand side of (3.82). This gives a nonlocal quasi-linearized dynamical equation for

the anisotropy evolution as

$$\frac{Da_{ij}}{Dt} = -\frac{1}{\Lambda_m}a_{ij} + \alpha_2\overline{S}_{ij} + \sum_{n=2}^{\infty}\left[C_2^{(n)}\Lambda^{2n-2}\left(\nabla^2\right)^{n-1}\overline{S}_{ij}\right] , \qquad (3.84)$$

where the $C_2^{(n)}$ coefficients are given in (3.67) or (3.70), $\alpha_2$ is given in (3.83), and we have denoted the resulting turbulence memory time scale $\Lambda_m$ as

$$\Lambda_m \equiv C_\Lambda\frac{k}{\epsilon} , \qquad (3.85)$$

with

$$C_\Lambda \equiv \frac{1}{\alpha_1} . \qquad (3.86)$$

Despite the dependence of $\alpha_1$ on $P/\epsilon$, as noted in (3.83), here we will determine a constant value for $C_\Lambda$ from the nonequilibrium test cases in Chapter IV. It should be noted that the quasi-linear equation in (3.84) is similar in some respects to the Maxwell model for linear viscoelastic fluids [6], where $\Lambda_m$ is the analogous relaxation time. This connection is not surprising, and Rivlin [82] and Crow [16] in particular have noted strong similarities between the dynamics of the stresses in turbulent and viscoelastic fluids.

While the nonlocal quasi-linear equation in (3.84) lacks many of the higher-order interactions between $a_{ij}$, $\overline{S}_{ij}$, and $\overline{W}_{ij}$ on the right-hand side of (3.82), it still contains the principal dynamics governing the evolution of the anisotropy in nonequilibrium turbulence, where the mean strain rate varies rapidly with respect to the turbulence response time scale $\Lambda_m$. The linearized anisotropy transport equation in (3.84) contains a "slow" $(-a_{ij}/\Lambda_m)$, a "fast" $(\alpha_2\overline{S}_{ij})$, and a nonlocal (via the Laplacians of $\overline{S}_{ij}$) contribution to the anisotropy evolution. The "fast" term accounts for the direct response of the turbulence to changes in the mean strain, and is often the leading term in rapid distortion analyses of the Reynolds stress anisotropy equation [78]. The "slow" term represents the vortex scrambling noted in Section 3.1 and thus accounts for the decreasing effect over time of the prior straining history on the local anisotropy. As a result, (3.84) addresses the two canonical limits of nonequilibrium turbulence, namely turbulence subjected to impulsively applied mean strain, where the "fast" term is dominant, and impulsively removed mean strain, where the "slow" term is dominant. Moreover, Figure 3.6 shows for various shearing frequencies in periodically-sheared homogeneous turbulence (in which the nonlocal terms can be neglected) that the evolution of $a_{12}$ predicted by (3.84) is in good agreement with results from the full $a_{ij}$ equation in (3.82) using the constants in (1.26), with only slight amplitude discrepancies at the maxima and minima of each cycle. The nonlocal term in (3.84) accounts for the effects of inhomogeneities in the mean strain rate on the anisotropy evolution, and has not been addressed by prior closure approaches. By contrast to the current nonlocal quasi-linear equation, a purely local form of (3.84) was originally proposed by Rotta [87],

and was used, for example, by Yakhot, Orszag and co-workers [111] as the basis for a simple "Reynolds stress transport model", where the six equations for $a_{ij}$ are solved together with the $k$ and $\epsilon$ equations.

### 3.4.2 The Nonlocal Effective Strain Rate Tensor

Here we will integrate (3.84) directly to obtain a relatively simple "direct Reynolds stress model" that can be readily implemented in conventional two-equation frameworks for closing the mean-flow equations in (1.2)-(1.4). Defining the nonlocal tensor $T_{ij}$ as

$$T_{ij} \equiv \overline{S}_{ij} + \sum_{n=2}^{\infty} \left[ \frac{C_2^{(n)}}{\alpha_2} \Lambda^{2n-2} \left( \nabla^2 \right)^{n-1} \overline{S}_{ij} \right] , \tag{3.87}$$

the nonlocal quasi-linear equation in (3.82) is written as

$$\frac{Da_{ij}}{Dt} = -\alpha_1 \frac{\epsilon}{k} a_{ij} + \alpha_2 T_{ij} . \tag{3.88}$$

This equation is solved exactly as

$$a_{ij}(t) = \int_{t_0}^{t} \alpha_2 T_{ij}(\tau) h(t-\tau) D\tau + a_{ij}(t_0) \exp \left[ -\int_{t_0}^{t} \frac{1}{\Lambda_m(t')} Dt' \right] , \tag{3.89}$$

where $t_0$ is the initial time and $h(t-\tau)$ is the impulse response function that represents the effective "memory" of the turbulence, namely

$$h(t-\tau) \equiv \exp \left[ -\int_{\tau}^{t} \left[ \Lambda_m(t') \right]^{-1} Dt' \right] . \tag{3.90}$$

The histories of both $T_{ij}$ and the time scale $\Lambda_m$ along a mean-flow pathline are accounted for in (3.89) and (3.90). Expanding the relaxation time scale $\Lambda_m(t')$ around the current time $t$ and integrating, (3.90) can be written as

$$h(t-\tau) = \exp \left[ -\frac{(t-\tau)}{\Lambda_m(t)} + \frac{1}{2}(t-\tau)^2 \frac{D\left(1/\Lambda_m\right)}{Dt} + \ldots \right] . \tag{3.91}$$

Here it is assumed that the derivative terms in (3.91) are negligible relative to the leading term, thus ignoring the explicit time history of $\Lambda_m$ in the $a_{ij}$ dynamics. However, the history of $\Lambda_m$ in (3.85) is still accounted for indirectly through the dynamical equations for $k$ and $\epsilon$ [e.g. (1.31) and (1.32)]. Thus the solution for $a_{ij}$ from (3.89) becomes a convolution integral of the form

$$a_{ij}(t) = \int_{-\infty}^{t} \alpha_2 T_{ij}(\tau) e^{-(t-\tau)/\Lambda_m(t)} D\tau , \tag{3.92}$$

where $t_0 \to -\infty$ and $a_{ij}(-\infty) \equiv 0$. It should be noted that the convolution integral in (3.92) is consistent with the heuristic result in (3.2) from Section 3.1. The present focus

on nonequilibrium effects due to the "fast" term in (3.84), as well as the emphasis on nonlocality, distinguishes the present approach from prior nonequilibrium eddy-viscosity models [73, 113, 114], which have emphasized purely local nonequilibrium effects related to the time variation of $k/\epsilon$ in the "slow" term and the associated time-varying eddy viscosity $\nu_T(t)$. The closure in (3.92) also provides a direct model for the anisotropy, whereas various prior nonequilibrium approaches [44, 100, 111] require the solution of more extensive sets of coupled differential equations.

By noting [24] that $C_\mu$ in (1.36) is related to the $\alpha_i$ as in (1.37), the convolution in (3.92) can be equivalently written, with (3.85) and (3.86), as

$$a_{ij}(t) = -2C_\mu \frac{k}{\epsilon} \frac{1}{\Lambda_m(t)} \int_{-\infty}^{t} T_{ij}(\tau) e^{-(t-\tau)/\Lambda_m(t)} D\tau \,. \tag{3.93}$$

Since $\Lambda_m(t)$ is a constant with respect to the integration variable $\tau$, the effective strain tensor $\widetilde{S}_{ij}$ can be defined as

$$\widetilde{S}_{ij}(t) = \int_{-\infty}^{t} T_{ij}(\tau) \frac{e^{-(t-\tau)/\Lambda_m(t)}}{\Lambda_m(t)} D\tau \,, \tag{3.94}$$

in terms of which the nonlocal, nonequilibrium anisotropy closure can be written in a form analogous to the traditional equilibrium closure in (1.38) as

$$a_{ij}(t) = -2C_\mu \frac{k}{\epsilon} \widetilde{S}_{ij}(t) \,. \tag{3.95}$$

From (3.87) and (3.94), the nonlocal effective strain rate $\widetilde{S}_{ij}$ is written in terms of $\overline{S}_{ij}$ only as

$$\widetilde{S}_{ij} = \int_{-\infty}^{t} \overline{S}_{ij}(\tau) \frac{e^{-(t-\tau)/\Lambda_m(t)}}{\Lambda_m(t)} D\tau + \sum_{n=2}^{\infty} \frac{C_2^{(n)}}{\alpha_2} \int_{-\infty}^{t} \left[\Lambda^{2n-2} \left(\nabla^2\right)^{n-1} \overline{S}_{ij}\right]_\tau \frac{e^{-(t-\tau)/\Lambda_m}}{\Lambda_m} D\tau \,. \tag{3.96}$$

The closure in (3.95) with (3.94) or (3.96) thus accounts for nonequilibrium effects via the history-dependent convolution integrals, as well as spatially nonlocal effects via the Laplacians of $\overline{S}_{ij}$. In homogeneous flows, all Laplacians of $\overline{S}_{ij}$ are zero and the second term on the right-hand side of (3.96) can be neglected. The resulting formulation for $\widetilde{S}_{ij}$ is then identical to the purely nonequilibrium form derived in Ref. [31].

### 3.4.3 The Nonlocal, Nonequilibrium Anisotropy Hypothesis

By accounting for nonlocal effects in the pressure-strain correlation and retaining nonequilibrium effects through solution of the quasi-linear transport equation in (3.84), a new anisotropy closure for nonlocal and nonequilibrium effects in turbulent flows can be obtained. The relation in (3.95) between the anisotropy $a_{ij}$ and the effective strain, together

with the definition of the eddy viscosity $\nu_T$ in (1.36), gives the final form

$$a_{ij} = -2\frac{\nu_T}{k}\widetilde{S}_{ij}\,. \tag{3.97}$$

The result in (3.97) is a general nonlocal, nonequilibrium anisotropy closure hypothesis that replaces the classical local equilibrium anisotropy closure in (1.35). Comparison with (1.35) shows that (3.97) is still an eddy viscosity formulation, and that it differs from the classical closure only in that the anisotropy tensor is proportional to the *nonlocal, nonequilibrium effective* strain rate tensor $\widetilde{S}_{ij}$ in (3.96), rather than to the *local instantaneous* mean strain rate tensor $\overline{S}_{ij}$. This new closure can thus be readily implemented in essentially any existing computational framework for solving (1.2)-(1.4) based on an eddy viscosity approach, and modeling of the eddy viscosity $\nu_T$ can be done by precisely the same methods as currently used for the local equilibrium closure in (1.35).

It should be noted that the underlying convolution for the anisotropy in (3.92) is similar in some respects to a constitutive equation proposed by Crow [16]. In the present approach, however, the vortex scrambling effect that leads to the memory function $h(\tau)$ in the convolution is arrived at in a more natural way from the simple formulation for the slow pressure-strain correlation in (1.22). The Crow model is often cited [98, 99, 111] for its prediction of $\alpha_2$ in the "fast" pressure-strain term in (3.84) (see for example equations (3.18) and (3.19)). Here however, we have used the more recent form in (1.22) for the pressure-strain correlation to additionally incorporate effects due to the "slow" vortex scrambling term in (3.84). Several other studies [30, 76] have also noted the importance of the accumulated strain $\int \overline{S}_{ij}(\tau)d\tau$ in the response of turbulence anisotropy subjected to rapidly varying mean strain. However, this accumulated strain is derived from (3.84) by retaining only the "fast" term ($\alpha_2\overline{S}_{ij}$), while the exponentially-decreasing "memory" effect in (3.94) arises from the "slow" term ($-a_{ij}/\Lambda_m$). It has been noted [115] that the "slow" term is necessary for correctly capturing the physics governing the anisotropy evolution in periodically-sheared turbulence, and it will be seen in the test cases in Chapter IV that the memory effect in (3.94) is an essential aspect of the nonequilibrium response of turbulence anisotropy. Fundamentally however, none of these prior approaches address nonlocal effects in the context of a nonequilibrium model, as is done here in (3.96) and (3.97).

The numerical value of the memory time scale coefficient $C_\Lambda$ in (3.86) can be anticipated from the $\alpha_1$ values in various prior models. In particular, the stress relaxation model of Yakhot *et al.* [111], the pressure-strain correlation models of Launder *et al.* [51] and Gibson and Launder [26], and the explicit algebraic Reynolds stress model of Gatski and Speziale [24] give corresponding values of $C_\Lambda$ from (3.86) shown in Table 3.2 (where $P/\epsilon \approx 1.9$ for homogeneous flows was used to calculate $\alpha_1$). These earlier models thus suggest $C_\Lambda \approx 0.3$, and it will be seen in Chapter IV that for the constants in (1.33) the value

$$C_\Lambda = 0.26 \tag{3.98}$$

yields good agreement between the present closure and validation data for various test cases. Modifications of the constants in (1.33) can lead to changes in (3.98), although $C_\Lambda$ remains close to 0.3 for most commonly used values of the constants.

With respect to the extent of nonequilibrium and nonlocal effects in turbulent flows, we can formulate single parameters that quantify the magnitude of both of these effects. Such parameterizations are important for determining situations in which nonlocal and nonequilibrium effects on the anisotropy are important, and for indicating flow conditions in which significant improvements from the nonlocal, nonequilibrium closure in (3.97) are expected compared to predictions from prior local equilibrium closures such as (1.35).

Nonequilibrium effects can be parameterized through consideration of the anisotropy dynamics from the quasi-linear transport equation in (3.88). Defining the anisotropy magnitude

$$a \equiv [a_{ij} a_{ij}]^{1/2} \, , \tag{3.99}$$

we can multiply (3.88) by $a_{ij}$ to obtain

$$\frac{1}{2} \frac{Da^2}{Dt} = -\alpha_1 \frac{\epsilon}{k} a^2 - |\alpha_2| T_{ij} \, a_{ij} \, , \tag{3.100}$$

where $\alpha_1 > 0$ and $\alpha_2 < 0$. On the right-hand side of (3.100) the first term is always negative, since $\epsilon$, $k$, and $a^2$ are strictly positive, and as a consequence this term always contributes to a *relaxation* toward isotropy. The second term on the right-hand side of (3.100) may be positive or negative depending on the sign of $T_{ij} \, a_{ij}$. The sum of these two terms may thus be positive, in which case the local rate-of-change $Da^2/Dt$ in the anisotropy magnitude is increasing, or may be negative, in which case the rate-of-change in the anisotropy magnitude is decreasing.

The two terms on the right-hand side of (3.100) allow a measure of the local extent of nonequilibrium effects in the flow. Since the first term reduces $Da^2/Dt$ by the "natural relaxation" of the turbulence toward isotropy, we can take the ratio of the two terms as

$$\frac{-|\alpha_2| T_{ij} \, a_{ij}}{\alpha_1 (\epsilon/k) a^2} = -\frac{|\alpha_2|}{\alpha_1} \frac{k}{\epsilon} \left[ \frac{T_{ij} \, a_{ij}}{a_{ij} \, a_{ij}} \right] \equiv \Omega \, . \tag{3.101}$$

Whenever $\Omega = 1$ we have $Da^2/Dt = 0$ in (3.100), corresponding to local *equilibrium* in the anisotropy dynamics. When $\Omega = 0$ the turbulence is locally undergoing only its *natural relaxation* toward isotropy due to the first term on the right-hand side of (3.100). When $0 \leq \Omega \leq 1$, the turbulence is locally undergoing *retarded relaxation*, since its relaxation is slower than the "natural rate" due to the first term on the right-hand side of (3.100). When $-\infty < \Omega < 0$, the turbulence is undergoing *accelerated relaxation* to isotropy, since now the natural relaxation due to the first term is aided by the effect from the second term. Similarly, when $\Omega > 1$ the right-hand side of (3.100) is positive, and thus we have locally increasing anisotropy.

84

With regard to equilibrium versus nonequilibrium dynamics in the turbulence anisotropy, whether $Da^2/Dt$ in (3.100) is positive or negative depends only on whether the local nonequilibrium effects drive the turbulence toward anisotropy or away from isotropy. By contrast, the degree of nonequilibrium is measured by $\Upsilon \equiv |\Omega - 1|$, with $\Upsilon = 0$ corresponding to equilibrium (i.e. $Da^2/Dt = 0$) and with increasing $\Upsilon$ corresponding to increasing degrees of nonequilibrium in the anisotropy dynamics, regardless of whether the dynamics are driving the turbulence toward larger or smaller anisotropy magnitudes. Note that $\Upsilon = 1$ corresponds to the natural relaxation of turbulence towards isotropy in the absence of an applied $T_{ij}$.

From the definition of $\Omega$ in (3.101), the nonequilibrium parameter $\Upsilon$ is given by

$$\Upsilon = \left| \frac{|\alpha_2|}{\alpha_1} \frac{k}{\epsilon} \frac{T_{ij}\,a_{ij}}{a_{ij}\,a_{ij}} + 1 \right| . \tag{3.102}$$

Using the present closure in (3.97) and the definition of $C_\mu$ in (1.37), we can write $\Omega$ in terms of $T_{ij}$ and $\widetilde{S}_{ij}$ as

$$\Omega = \frac{T_{ij}\widetilde{S}_{ij}}{\widetilde{S}_{ij}\widetilde{S}_{ij}} , \tag{3.103}$$

which then gives

$$\Upsilon \equiv \left| \frac{T_{ij}\widetilde{S}_{ij}}{\widetilde{S}_{ij}\widetilde{S}_{ij}} - 1 \right| . \tag{3.104}$$

Thus, for the equilibrium condition $\Upsilon = 0$ we obtain $T_{ij} = \widetilde{S}_{ij}$. Nonzero values of $\Upsilon$, corresponding to nonequilibrium turbulence, are obtained when $T_{ij}$ and $\widetilde{S}_{ij}$ are substantially different. The expression for $\Upsilon$ in (3.104) will play a key role in characterizing the degree of local nonequilibrium in the homogeneous test cases examined in Chapter IV.

A similar parameter characterizing the extent of nonlocal effects can be obtained from comparison of $T_{ij}$ and $\overline{S}_{ij}$. Following a similar approach to that used to obtain (3.104), we can define the nonlocal parameter $\Psi$ as

$$\Psi \equiv \left| \frac{T_{ij}\overline{S}_{ij}}{T_{ij}T_{ij}} - 1 \right| . \tag{3.105}$$

In purely local regions, such as might be found in homogeneous turbulence, $\Psi = 0$ since $T_{ij} = \overline{S}_{ij}$, whereas $\Psi > 0$ corresponds to increasing nonlocal effects on the anisotropy evolution. The magnitude of $\Psi$ in nonlocal inhomogeneous wall-bounded flows will be considered in Chapter V.

While the closure given by (3.96) and (3.97) accounts for nonlocal and nonequilibrium effects in turbulent flows, it neglects much of the nonlinear dynamics governing the evolution of the anisotropy. The vorticity alignment studies in Chapter II and the comparison of the truncated and full anisotropy transport equations for periodically-sheared turbulence in Figure 3.6 indicate that the quasi-linearization of the anisotropy dynamics used to obtain

the present closure is a reasonable approximation in many cases. However, in instances where nonlinear effects due to the higher-order terms on the right-hand side of (3.82) are significant, the present closure – which primarily addresses nonlocal and nonequilibrium effects on the anisotropy – will not be able to account for certain important aspects of the anisotropy dynamics. Similarly, the dependence of $C_\Lambda$ on $P/\epsilon$ and the time history of $\Lambda_m$ have been neglected in obtaining the closure in (3.96) and (3.97), with $C_\Lambda$ given by (3.98). Thus, in cases where either $\Lambda_m$ is rapidly varying or $P/\epsilon$ takes on extreme values (for example, $P/\epsilon = 0$), the assumptions used to obtain the present closure may become inaccurate. With respect to the neglect of the explicit dependence of $C_\Lambda$ on $P/\epsilon$, a similar linear approach is also typically used when formulating a representation for $C_\mu$, which rigorously depends on $P/\epsilon$ from (1.37). Nevertheless, it will be seen from the tests in Chapters IV and V that the neglect of certain nonlinear effects in the present closure does not significantly affect the accuracy of the anisotropy predictions for a wide range of problems. Furthermore, Appendix 6.2 gives insights into how nonlinear effects may be incorporated in the present approach in the future, resulting in a nonlinear, nonlocal, nonequilibrium closure for the anisotropy.

Finally, it should be noted that (3.94) bears a resemblance to the heuristically-motivated background effective strain rate in (3.2). While $T_{ij}$ is not identical to the ensemble-averaged $S_{ij}^B$ from (2.45), both are nonlocal tensors involving Laplacians of $\overline{S}_{ij}$. The key physical motivation for the convolution integral in (3.2) comes from the vorticity alignment studies in Chapter II. Namely, the alignment of the vorticity with the most extensional eigenvector of the background strain rate suggests that the anisotropy responds in a quasi-linear manner to a nonlocal measure of the strain rate. Based on the DNS studies in Chapter II and the discussion in Section 3.1, this nonlocal strain rate was assumed in (3.2) to be $\overline{S}_{ij}^B$. The rigorously-derived closure in (3.97) and (3.94) suggests that while this assumption does not seem to be quantitatively correct, it is at least qualitatively accurate. That is, the quasi-linear response of the anisotropy in turbulent flows is driven by the nonlocal tensor $T_{ij}$ in (3.87), as opposed to the local mean strain rate $\overline{S}_{ij}$ assumed by previous models.

## 3.5 Practical Implementation of Nonlocal, Nonequilibrium Closure

Nonequilibrium effects in the effective strain rate $\widetilde{S}_{ij}$ were introduced naturally in (3.94) and (3.96) in the form of convolution integrals. These integrals can be directly evaluated in homogeneous flows for given imposed strain rate histories $\overline{S}_{ij}(t)$, as in the homogeneous nonequilibrium tests that will be presented in Chapter IV. However, the convolution integral does not readily lend itself to implementation in most computational frameworks for solving (1.2)-(1.4), where only local instantaneous variables are typically available. The integral can, however, be written in an equivalent time-local form that allows $\widetilde{S}_{ij}$ to be readily evaluated in terms of an infinite series of material derivatives of $\overline{S}_{ij}$.

The resulting infinite series, together with the infinite series of Laplacians for nonlo-

cal effects in (3.96), introduces additional practical issues when using the present closure to solve (1.2)-(1.4). In particular, the computational complexity of the closure increases dramatically as higher-order terms are retained and as a result, practical implementation requires truncation of the series for nonequilibrium and nonlocal effects. This in turn requires special treatment of the integrals used to obtain (3.96) in order to avoid truncation errors.

### 3.5.1 Time-Local Implementation of Nonequilibrium Effects

The Lagrangian history term $T_{ij}(\tau)$ in the convolution integral in (3.94) can be expanded about the current time $t$ as

$$T_{ij}(\tau) = T_{ij} - \left.\frac{DT_{ij}}{Dt}\right|_t (t - \tau) + \frac{1}{2} \left.\frac{D^2 T_{ij}}{Dt^2}\right|_t (t - \tau)^2 + \cdots. \tag{3.106}$$

Substituting (3.106) in (3.94), the nonlocal effective strain rate can be written as

$$\widetilde{S}_{ij}(t) = \int_{-\infty}^{t} \frac{e^{-(t-\tau)/\Lambda_m}}{\Lambda_m} \left[ T_{ij} - \frac{DT_{ij}}{Dt}(t - \tau) + \frac{1}{2}\frac{D^2 T_{ij}}{Dt^2}(t - \tau)^2 + \cdots \right] D\tau, \tag{3.107}$$

where the derivatives of $T_{ij}$ are evaluated at time $t$. Since these derivatives do not depend on $\tau$, (3.107) can be written as

$$\widetilde{S}_{ij}(t) = \sum_{m=0}^{\infty} \frac{(-1)^m}{m!} \frac{D^m T_{ij}}{Dt^m} \int_{-\infty}^{t} (t - \tau)^m \frac{e^{-(t-\tau)/\Lambda_m}}{\Lambda_m} D\tau, \tag{3.108}$$

which then gives

$$\widetilde{S}_{ij}(t) = T_{ij}(t) + \sum_{m=1}^{\infty} (-\Lambda_m)^m \left.\frac{D^m T_{ij}}{Dt^m}\right|_t. \tag{3.109}$$

The form of the nonlocal effective strain rate tensor in (3.109) is equivalent to the convolution integral in (3.94), but allows a time-local evaluation of $\widetilde{S}_{ij}$. With the nonlocal, nonequilibrium anisotropy hypothesis in (3.97), the time-local form in (3.109) allows straightforward implementation of the present closure in a computational framework where only local instantaneous variables are available.

Writing (3.109) in terms of $\overline{S}_{ij}$ using the definition of $T_{ij}$ in (3.87) then gives

$$\widetilde{S}_{ij}(t) = \overline{S}_{ij}(t) + \sum_{m=1}^{\infty} (-\Lambda_m)^m \left.\frac{D^m \overline{S}_{ij}}{Dt^m}\right|_t + \sum_{n=2}^{\infty} \left[ \frac{C_2^{(n)}}{\alpha_2} \Lambda^{2n-2} \left(\nabla^2\right)^{n-1} \overline{S}_{ij} \right]_t \tag{3.110}$$

$$+ \sum_{n=2}^{\infty} \sum_{m=1}^{\infty} \frac{C_2^{(n)}}{\alpha_2} (-\Lambda_m)^m \frac{D^m}{Dt^m} \left[ \Lambda^{2n-2} \left(\nabla^2\right)^{n-1} \overline{S}_{ij} \right]_t,$$

The first term on the right-hand side of (3.110) is the equilibrium response of the anisotropy to the mean strain $\overline{S}_{ij}$ found in the local equilibrium closure in (1.35). The second term

on the right in (3.110) accounts for nonequilibrium effects in the flow, while the third term accounts for nonlocal effects due to spatial variations in the mean velocity gradient. The last term in (3.110) is a mixed term that addresses both nonequilibrium and nonlocal effects, and is only expected to be significant in flow regions that simultaneously exhibit both strong nonequilibrium and inhomogeneity. The form for $\widetilde{S}_{ij}$ in (3.110) is appropriate for implementation in existing computational frameworks for solving (1.2)-(1.4), where typically only local and instantaneous flow variables are available.

Note that using the time-local effective strain in (3.110) to account for nonlocal and nonequilibrium effects requires that the applied strain $\overline{S}_{ij}$ be both temporally and spatially differentiable. The differentiability of the applied strain is not expected to be an issue for most practical problems, but in the homogeneous nonequilibrium tests in Chapter IV the applied mean strain will be seen to vary discontinuously in several instances. For example, the applied strain in impulsively-sheared turbulence is non-differentiable at $t = 0$, and as a result the time-local effective strain in (3.110) will be unable to account for the isotropic state of the turbulence for $t < 0$. Similarly, the time-local form in (3.110) cannot account for relaxation effects in unstrained, initially anisotropic turbulence if the applied strain is assumed to have been impulsively removed. Such abrupt and discontinuous transitions are not expected for most realistic problems however, and even in cases when the applied strain varies rapidly (but still smoothly) the time-local effective strain from (3.110) will converge to the full convolution formulation in (3.96) as an increasing number of terms are retained in the series.

### 3.5.2   Truncated Form of Nonlocal, Nonequilibrium Anisotropy Closure

Implementation of the nonlocal, nonequilibrium closure in (3.97) with (3.110) requires the calculation of numerous higher-order material derivatives and Laplacians of $\overline{S}_{ij}$. However, these higher-order derivatives may lead to stability issues associated with solving (1.2)-(1.4) in engineering simulations, and will certainly increase the computational resources required for the simulation. Tests using DNS or experimental data will also be affected, since data from even highly-resolved DNS typically permits only six or seven derivatives of the velocity field (e.g. Schumacher *et al.* [91]). Since there are $(n - 1)$ Laplacians of $\overline{S}_{ij}$ for the $n$th term in (3.110), the expansion is therefore only well-resolved up to $n = 4$ for most DNS data. Consequently, in nearly all applications of the nonlocal, nonequilibrium closure in (3.97) with (3.110), it will be necessary to truncate the series expansions at finite $n$ and $m$ for which issues due to computational requirements and grid resolution are not expected to be prohibitive.

While the exact truncation order of the series in (3.110) is ultimately determined by the specific user, application, and available computing resources, truncation of (3.110) imposes restrictions on the limits of the $r$ integrals in (3.30) and the $\tau$ integrals in (3.107). The present closure approach accounts for nonlocal effects in the rapid pressure-strain correlation

through Taylor expansion of $A_{kl}(\hat{\mathbf{x}})$ about the point $\mathbf{x}$, which gives the series in (3.23) with the integral coefficients in (3.30). Similarly, the time-local nonequilibrium effects in (3.110) are obtained through Taylor expansion of $T_{ij}(\tau)$ in (3.94) about the current location and time $(\mathbf{x}, t)$, which gives the relation in (3.107) as shown in Section 3.5.1. However, truncating the infinite series in (3.110) is fundamentally equivalent to truncating the expansions for $A_{kl}(\hat{\mathbf{x}})$ and $T_{ij}(\tau)$ in (3.22) and (3.106), respectively, and this can result in errors for the representations of $A_{kl}(\hat{\mathbf{x}})$ and $T_{ij}(\tau)$ outside a certain region centered on $\mathbf{x}$ and $t$.

In order to avoid these errors, we can replace the infinite limits on the integrals in (3.30) and (3.107) with finite bounds related to the order of the expansions for $A_{kl}(\hat{\mathbf{x}})$ and $T_{ij}(\tau)$. For truncations of the expansion for $A_{kl}$ at order $N$, we integrate $r$ in (3.30) from 0 to the length scale $R$, and for truncations of the expansion for $T_{ij}$ at order $M$ we replace $-\infty$ in the lower integration bound of (3.107) with the parameter $\Gamma$. Both $R$ and $\Gamma$ are related to the orders $N$ and $M$ of the expansions, as well as to the degree of local variation in $A_{kl}$ and $T_{ij}$. In general, only for $N \to \infty$ and $M \to \infty$ can we set $R \to \infty$ and $\Gamma \to -\infty$.

Replacing the upper integration bound on the integrals over $r$ in (3.30) with $R$, integration using the exponential $f(r)$ in (3.38) gives

$$\int_0^R r^{n-2} \frac{df}{dr} r^2 dr = -n! \Lambda^n \left[ \gamma_1^{(n)} (R/\Lambda) \right], \tag{3.111a}$$

$$\int_0^R r^{n-1} \frac{d^2 f}{dr^2} r^2 dr = (n+1)! \Lambda^n \left[ \gamma_2^{(n)} (R/\Lambda) \right], \tag{3.111b}$$

$$\int_0^R r^n \frac{d^3 f}{dr^3} r^2 dr = -(n+2)! \Lambda^n \left[ \gamma_3^{(n)} (R/\Lambda) \right], \tag{3.111c}$$

where

$$\gamma_j^{(n)} (x) \equiv 1 - e^{-x} \sum_{i=1}^{n+j} \frac{x^{i-1}}{(i-1)!}. \tag{3.112}$$

As shown in Figure 3.7, for any $n$ the $\gamma_j^{(n)}$ coefficients are bounded by 0 and 1, and thus behave as damping functions in (3.111). In the limit $R/\Lambda \to \infty$, (3.112) gives simply $\gamma_j^{(n)} = 1$ and we obtain the results in (3.41). It should be noted that as the order $n$ increases, the $\gamma_j^{(n)}$ coefficients in Figure 3.7 decrease for any particular value of $R/\Lambda$. As a result, for any finite $R/\Lambda$ the higher-order $n$ terms in (3.29) make a relatively smaller contribution to the final result.

With (3.111) and (3.112), we can then write (3.42) as

$$_{(mp\ldots)} M_{iljk}^{(n)} = \frac{k \Lambda^n}{6\pi} \int_\Omega \left[ \frac{r_m r_p \cdots}{r^n} \right] \left[ \gamma_1^{(n)} a_{ijkl} - (n+1) \gamma_2^{(n)} b_{ijkl} \right. \tag{3.113}$$

$$\left. + (n+2)(n+1) \gamma_3^{(n)} c_{ijkl} \right] d\Omega.$$

Following the same approach used to obtain (3.43) and (3.44), it can be shown that $M_{iljk}^{(0)}$

and $_{mp}M_{iljk}^{(2)}$ are given from (3.113) as

$$M_{iljk}^{(0)} = \frac{2k}{45}\left[\left(32\gamma_1^{(0)} - 28\gamma_2^{(0)} + 8\gamma_3^{(0)}\right)\delta_{il}\delta_{jk} - \left(8\gamma_1^{(0)} - 7\gamma_2^{(0)} + 2\gamma_3^{(0)}\right)(\delta_{ij}\delta_{kl} + \delta_{jl}\delta_{ki})\right],$$

(3.114)

$$\begin{aligned}
_{mp}M_{iljk}^{(2)} = {} & \frac{2k\Lambda^2}{315}\Big[\left(88\gamma_1^{(2)} - 156\gamma_2^{(2)} + 72\gamma_3^{(2)}\right)\delta_{jk}\delta_{il}\delta_{mp} \\
& - \left(24\gamma_1^{(2)} - 33\gamma_2^{(2)} + 12\gamma_3^{(2)}\right)(\delta_{ij}\delta_{kl}\delta_{mp} + \delta_{jl}\delta_{ik}\delta_{mp}) \\
& - \left(24\gamma_1^{(2)} + 72\gamma_2^{(2)} - 72\gamma_3^{(2)}\right)(\delta_{il}\delta_{jm}\delta_{kp} + \delta_{il}\delta_{km}\delta_{jp}) \\
& + \left(4\gamma_1^{(2)} + 12\gamma_2^{(2)} - 12\gamma_3^{(2)}\right)(\delta_{ij}\delta_{lm}\delta_{kp} + \delta_{ij}\delta_{km}\delta_{lp} + \delta_{jl}\delta_{im}\delta_{kp} + \delta_{jl}\delta_{km}\delta_{ip} \\
& + \delta_{ik}\delta_{lm}\delta_{jp} + \delta_{ik}\delta_{jm}\delta_{lp} + \delta_{kl}\delta_{im}\delta_{jp} + \delta_{kl}\delta_{jm}\delta_{ip} + \delta_{jk}\delta_{im}\delta_{pl} + \delta_{jk}\delta_{lm}\delta_{ip})\Big].
\end{aligned}$$

(3.115)

Contracting (3.114) and (3.115) with the derivatives of $A_{kl}$ and then gives the first two terms of $\Pi_{ij}^{(r)}$ as

$$\Pi_{ij}^{(r)}(\mathbf{x}) = \frac{4k}{15}\left(8\gamma_1^{(0)} - 7\gamma_2^{(0)} + 2\gamma_3^{(0)}\right)\overline{S}_{ij} + \frac{4k\Lambda^2}{315}\left(80\gamma_1^{(0)} - 75\gamma_2^{(0)} + 12\gamma_3^{(0)}\right)\nabla^2\overline{S}_{ij} + \cdots,$$

(3.116)

where $A_{kk} \equiv 0$. Following a derivation similar to that in Section 3.2.3 it can be shown that the general higher-order representation for $\Pi_{ij}^{(r)}$ – which now accounts for the finite convergence radius $R$ – is given by

$$\Pi_{ij}^{(r)} = k\sum_{n=1}^{N} C_2^{(n)}\Lambda^{2n-2}\left(\nabla^2\right)^{n-1}\overline{S}_{ij},$$

(3.117)

where $N$ denotes the order of the truncation, and the coefficients $C_2^{(n)}$ are written as

$$C_2^{(n)} = \frac{32n}{3(2n+3)(2n-1)}\gamma_1^{(2n-2)} + \frac{4(2n-9)}{3(2n+3)}\gamma_2^{(2n-2)} - \frac{8n(2n-5)}{3(2n+3)(2n+1)}\gamma_3^{(2n-2)}.$$ (3.118)

For convenience, Table 3.1 lists values of $C_2^{(n)}$ up to $n = 8$, corresponding to seven Laplacians of $\overline{S}_{ij}$ in (3.117). Note that the general form of the nonlocal, nonequilibrium anisotropy closure in (3.110) and (3.97) is essentially unchanged by the finite-$R$ formulation; the primary difference between the two formulations are the new $C_2^{(n)}$ coefficients in (3.118).

With respect to the nonequilibrium terms, for truncation at highest order $M$ the integration limits in (3.107) become $\tau = \Gamma$ to $\tau = t$, and the expansion in (3.107) can be written as

$$\widetilde{S}_{ij}(t) = \sum_{m=0}^{M}\frac{(-1)^m}{m!}\frac{D^m T_{ij}}{Dt^m}\int_{\Gamma}^{t}(t-\tau)^m\frac{e^{-(t-\tau)/\Lambda_m}}{\Lambda_m}D\tau.$$

(3.119)

It can be shown that solution of the integrals in (3.119) gives

$$\widetilde{S}_{ij}(t) = \sum_{m=0}^{M} (-\Lambda_m)^m \frac{D^m T_{ij}}{Dt^m} \left[ \gamma_1^{(m)} \left( \frac{t-\Gamma}{\Lambda_m} \right) \right] , \qquad (3.120)$$

where the damping function $\gamma_1^{(m)}$ is defined in (3.112). Once again, for $\Gamma \to -\infty$ we obtain $\gamma_1^{(m)} \to 1$, and the result in (3.110) is recovered. By analogy with the coefficients $C_2^{(n)}$ in (3.117), we can define

$$B^{(m)} \equiv \gamma_1^{(m)} \left( \frac{t-\Gamma}{\Lambda_m} \right) , \qquad (3.121)$$

which from (3.120) gives

$$\widetilde{S}_{ij}(t) = B^{(0)} \left[ T_{ij} + \sum_{m=1}^{M} \frac{B^{(m)}}{B^{(0)}} (-\Lambda_m)^m \frac{D^m T_{ij}}{Dt^m} \right] . \qquad (3.122)$$

With (3.117) and (3.122), the final truncated time-local representation for $\widetilde{S}_{ij}$ in (3.110) can be written as

$$\widetilde{S}_{ij}(t) = \overline{S}_{ij}(t) + \sum_{m=1}^{M} \frac{B^{(m)}}{B^{(0)}} (-\Lambda_m)^m \left. \frac{D^m \overline{S}_{ij}}{Dt^m} \right|_t + \sum_{n=2}^{N} \left[ \frac{C_2^{(n)}}{\alpha_2} \Lambda^{2n-2} \left( \nabla^2 \right)^{n-1} \overline{S}_{ij} \right]_t \qquad (3.123)$$

$$+ \sum_{n=2}^{N} \sum_{m=1}^{M} \frac{C_2^{(n)}}{\alpha_2} \frac{B^{(m)}}{B^{(0)}} (-\Lambda_m)^m \frac{D^m}{Dt^m} \left[ \Lambda^{2n-2} \left( \nabla^2 \right)^{n-1} \overline{S}_{ij} \right]_t ,$$

where the $C_2^{(n)}$ are defined in (3.118) and the $B^{(m)}$ are defined in (3.121). With (3.123) the anisotropy closure is still given by (3.97), but now the eddy viscosity, previously defined in (1.36) with $C_\mu$ given by (1.37), is written as

$$\nu_T = -\frac{B^{(0)} \left[ C_2^{(1)} - 4/3 \right]}{2\alpha_1} \frac{k^2}{\epsilon} . \qquad (3.124)$$

In contrast to most prior approaches there is a damping effect due to the $B^{(0)}$ and $C_2^{(1)}$ coefficients. For $R \to \infty$ and $\Gamma \to -\infty$, $C_2^{(1)}$ attains the standard value $4/5$ and $B^{(0)} = 1$, but it is clear from (3.124) that the finite-$R$ and finite-$\Gamma$ formulations in the present approach introduce a dependence on $R/\Lambda$ and $(t-\Gamma)/\Lambda_m$ in $\nu_T$. Coupled with the dependence of $\alpha_1$ on $P/\epsilon$, the formulation for the eddy viscosity from (3.124) is substantially different than the classical form in (1.36) with the constant $C_\mu$ in (1.39). Since nearly all practical implementations of (3.97) with (3.123) will require relatively small $N$ and $M$, the finite $R$ and $\Gamma$ effects in $\nu_T$ may become important, particularly in regions with strong inhomogeneities or nonequilibrium effects. While this may introduce a connection between the present approach and prior *ad hoc* damping functions for the eddy viscosity, this connection will not be explored in more detail here. For the tests in Chapters V and IV, we will continue to

use standard forms for $\nu_T$, such as that in (1.36) with $C_\mu$ given by (1.39) or the realizable form in (1.40).

### 3.5.3    Representation for Radius of Convergence $R$

Closure of the anisotropy using (3.97) with (3.123) requires formulations for $R$ appearing in the $C_2^{(n)}$ coefficients given by (3.118), and for $\Gamma$ appearing in the $B^{(m)}$ coefficients given by (3.121). While the parameter $\Gamma$ is important in nonequilibrium turbulent flows, here we focus specifically on the representation for $R$, since the $N = 2$ truncated form for $\widetilde{S}_{ij}$ from (3.123) will be used for the wall bounded nonlocal tests in Chapter V.

As noted in Section 3.5.2, $R$ is fundamentally determined by competition between two opposing effects, one physical and the other practical. From a physical standpoint, $R$ should be as large as possible in order to obtain good agreement between the result in (3.117) with (3.118) and the full integral solution for $\Pi_{ij}^{(r)}$ in (3.9), which is strictly defined as an integral over $(-\infty, \infty)$. This would suggest that good agreement requires $R \to \infty$, or at the very least $R \gg \Lambda$. At the same time however, the largest allowable value of $R$ is practically limited by the size of the region in which truncations of (3.22) are good approximations to the exact $A_{kl}(\mathbf{x} + \mathbf{r})$. Fundamentally, the accuracy of the approximation at any point is determined by both the order $N$ and the smoothness of $A_{kl}$ near the point of interest. In general, the allowable $R$ increases as $N$ increases, or the local inhomogeneity in $A_{kl}$ decreases. Conversely, for small $N$ or rapidly varying $A_{kl}$ the allowable $R$ will generally become relatively small. Only in the limit $N \to \infty$ does the allowable radius $R$ go to $\infty$.

Thus, we can make the following exact statement: $R$ *is strictly defined as the radius of the largest spherical region centered on* $\boldsymbol{x}$ *in which the $N$th-order truncation of (3.22) is in good agreement with the exact value of $A_{kl}(\boldsymbol{x} + \boldsymbol{r})$ within the region.* To obtain good agreement with the integral in (3.9), $R$ should ideally be greater than $\Lambda$, although this condition may be impractical for the relatively small $N$ permitted by the available computational resources as well as issues of numerical stability. As a result, a good approximation to the full integral for $\Pi_{ij}^{(r)}$ in (3.9) may be obtained for values of $R$ near $\Lambda$. In the following we will let $R \propto \Lambda$, and consequently the ratio $R/\Lambda$ appearing in the $\gamma_j^{(n)}$ damping coefficients in (3.112) is constant everywhere in the flow. It will be seen from comparisons with DNS of fully-developed turbulent channel flow and experiments of the zero pressure gradient turbulent boundary layer that for truncation at $N = 2$ in (3.123), the value

$$\frac{R}{\Lambda} \approx 0.9\,, \tag{3.125}$$

is sufficient to give good agreement with DNS and experimental results well into the near-wall region of both flows.

## 3.6  Relation to Prior Anisotropy Closure Models

The present closure given by (3.97) with the effective strain in (3.96), (3.110), or (3.123) is the first anisotropy closure that seeks to rigorously capture both nonlocal and nonequilibrium effects in turbulent flows within a relatively simple closure framework. However, there have been several prior attempts to predict either nonlocal or nonequilibrium effects within existing closure approaches for the anisotropy, and the strengths and weaknesses of each approach can be better understood in light of the developments used to obtain the present closure.

### 3.6.1  Relation to Prior Nonlocal Approaches

A number of approaches for addressing nonlocal effects in standard anisotropy closures have been proposed over the last several decades. Nearly all such approaches have been aimed at extending conventional closures, such as the classical local equilibrium closure in (1.35), into the near-wall region of wall-bounded flows where the mean shear becomes large and strongly inhomogeneous. As noted in Chapter I and Section 3.2, perhaps the most common method of addressing near-wall effects in standard models is to introduce an empirically-determined damping function $f_\mu$ in the eddy viscosity (e.g. Jones and Launder [43], Abid [1], and Rodi and Mansour [84]). These damping functions typically depend on the distance to the nearest viscous wall and are calibrated to give good agreement with experimental or computational data from either channel or boundary layer flows.

Fundamentally however, these approaches are simply *ad hoc* corrections to account for the omission of important physical effects in the derivation of simple closure approaches such as (1.35). Consequently, there has been substantial research on more rigorous approaches for predicting nonlocal effects due to nonuniformities in the mean velocity gradient, resulting in several notable prior approaches.

Launder and Tselepidakis [53, 54] have attempted to account for nonlocal effects in the pressure-strain correlation by replacing $\overline{S}_{ij}$ and $\overline{W}_{ij}$ in (1.25) with the effective mean velocity gradient tensor

$$\left.\frac{\partial \overline{u}_i}{\partial x_j}\right|_{eff} = \frac{\partial \overline{u}_i}{\partial x_j} + c_l l_n \frac{\partial l_n}{\partial x_k}\frac{\partial^2 \overline{u}_i}{\partial x_j \partial x_k}, \tag{3.126}$$

where $c_l = 0.3$, $l_n = (k/\epsilon)(\overline{u'_p u'_q}n_p n_q)$, and $\mathbf{n}$ is the outward unit vector normal to the wall. In contrast to the present approach, (3.126) attempts to simultaneously address inhomogeneities in both the turbulence length-scale $k^{3/2}/\epsilon$ (related to $l_n$) as well as the mean velocity gradient field. By addressing such inhomogeneities, improved predictions for the Reynolds stresses in the near-wall region of the turbulent channel flow were obtained [53]. However, the mathematical foundations of (3.126) remain unclear, and subsequent versions of the modification in (3.126) were proposed to remove the somewhat undesirable

dependence on the wall-normal unit vector $\mathbf{n}$ [50].

The fundamental difference between the approach by Launder and Tselepidakis and that proposed herein is tied to the homogeneous representation for the two-point turbulence correlation $R_{il}(\mathbf{r})$ in (3.16), which implicitly assumes $\partial l_n/\partial x_k = 0$. The present approach is based on the central hypothesis that nonlocal effects on the anisotropy in the near-wall region are substantially due to variations in the mean velocity gradient, and it will be seen from the channel flow and boundary layer tests in Chapter V that addressing these nonlocal effects gives good agreement with computational and experimental results well into the near-wall region of both flows. By contrast, the importance of nonlocal effects due to inhomogeneities in the turbulence, as addressed by (3.126), can be understood from an approach proposed by Manceau *et al.* [62], where the exponential correlation function $f(r)$ in (3.38) is reformulated to account for gradients in the turbulent length scale $\Lambda$ as

$$f(r) = \exp\left[-\frac{r}{\Lambda + r_m\partial\Lambda/\partial x_m}\right] .$$ 

(3.127)

Taylor expansion of (3.127) then results in

$$f(r) = e^{-r/\Lambda} + \frac{r^2}{\Lambda^2}\frac{r_m}{r}\frac{\partial\Lambda}{\partial x_m}e^{-r/\Lambda} ,$$ 

(3.128)

where higher order terms have been neglected. The first term in (3.128) is identical to (3.38) and thus gives the present result in (3.66) and (3.67), but the second term provides an additional nonlocal correction due to inhomogeneities in $\Lambda$. It can be shown that substitution of (3.128) in (3.30) introduces an additional factor of $r_m/r$ in the integrand, and as a result the $n =$ odd terms in the expansion for $\Pi_{ij}$ are nonzero. This is in contrast to the leading exponential term in (3.128), which has already been shown to yield nonzero integrals in (3.29) for $n =$ even only. The resulting odd-order terms from (3.128) introduce derivatives of $\overline{S}_{ij}$ combined with gradients of $\Lambda$, namely terms of the form $(\partial\Lambda^2/\partial x_m)(\partial\overline{S}_{ij}/\partial x_m)$, as in the Launder and Tselepidakis approach from (3.126). For fully-developed turbulent channel flow, this additional term reaches its maximum value at $y^+ \approx 8$, whereas the first-order Laplacian of $\overline{S}_{12}$ from the present result in (3.66) attains its maximum $y^+ \approx 14$, as shown qualitatively in Figure 3.8. Thus it is only very near the wall that inhomogeneities in $\Lambda$ may become important, and the present focus on nonlocal effects due to variations in $\overline{S}_{ij}$, as opposed to inhomogeneities in the turbulence considered in (3.126), will be seen in Chapter V to give substantially improved predictions of the anisotropy in the near-wall region of the channel and boundary layer flows.

Perhaps the most notable prior approach for addressing nonlocal effects on the anisotropy evolution is the elliptic relaxation method, first proposed by Durbin [20, 21], where $\Pi_{ij}$ is

obtained through solution of the additional equation

$$\phi_{ij} - L^2 \nabla^2 \phi_{ij} = \frac{1}{k} \Pi_{ij}^h \,, \tag{3.129}$$

where

$$\Pi_{ij} = k\phi_{ij} \,, \tag{3.130}$$

and $\Pi_{ij}^h$ is a homogeneous representation for the pressure-strain correlation as in (1.25). The length scale $L$ in (3.129) is given by

$$L = C_L \max \left[ \frac{k^{3/2}}{\epsilon}, \, C_\eta \eta_K \right] \,, \tag{3.131}$$

where [62] $C_L = 0.2$, $C_\eta = 80$, and $\eta_K$ is the Kolmogorov length scale. Physical justification for (3.129) is typically provided by noting that the Poisson equation in (3.4) can be rewritten as [78]

$$\frac{1}{\rho} \nabla^2 p'(\mathbf{x}) = F(\mathbf{x}) \,, \tag{3.132}$$

where $F(\mathbf{x})$ denotes the right-hand side of (3.4). The solution for the pressure-strain correlation $\Pi_{ij}$ in (1.10) is then given by

$$\Pi_{ij}(\mathbf{x}) \equiv \frac{2}{\rho} \overline{p'(\mathbf{x}) S'_{ij}(\mathbf{x})} = -\frac{1}{2\pi} \int_{-\infty}^{\infty} \overline{F(\mathbf{y}) S'_{ij}(\mathbf{x})} \frac{d\mathbf{y}}{|\mathbf{x} - \mathbf{y}|} \,. \tag{3.133}$$

The correlation $\overline{F(\mathbf{y}) S'_{ij}(\mathbf{x})}$ can be modeled using the approximate relation [78]

$$\overline{F(\mathbf{y}) S'_{ij}(\mathbf{x})} \approx \overline{F(\mathbf{y}) S'_{ij}(\mathbf{y})} e^{-|\mathbf{x}-\mathbf{y}|/L} \,, \tag{3.134}$$

which is then substituted into (3.133) to yield

$$\Pi_{ij}(\mathbf{x}) = 2 \int_{-\infty}^{\infty} \overline{F(\mathbf{y}) S'_{ij}(\mathbf{y})} \left[ -\frac{1}{4\pi} \frac{e^{-|\mathbf{x}-\mathbf{y}|/L}}{|\mathbf{x} - \mathbf{y}|} \right] d\mathbf{y} \,. \tag{3.135}$$

The physical argument is completed [78] by noting that, when multiplied by $L^2$, the term in square brackets in (3.135) is the Green's function for the operator $(I - L^2 \nabla^2)$ on the left-hand side of (3.129). The right-hand side of (3.129) is obtained by assuming $\Pi_{ij}^h(\mathbf{x}) = \overline{F(\mathbf{x}) S'_{ij}(\mathbf{x})}$. The accuracy of elliptic relaxation approaches thus depends in large part on the latter assumption as well as the validity of the approximation in (3.134), both of which are somewhat tenuous. Nevertheless, it has been shown that such approaches are relatively successful in a variety of flows [18, 21, 62]. The appearance of the Laplacian operator in both (3.129) and the present closure also suggests a connection between the two approaches which is undoubtedly due, at some fundamental level, to the functional similarity between the approximation in (3.134) and the exponential representation for

$f(r)$ used herein. However, there is still uncertainty as to the correct form for (3.129) in wall-bounded flows, and both the representation for the right-hand side of (3.129) and the approximation in (3.134) remain weaknesses in the physical justification for the approach (see Manceau *et al.* [61, 62] for a discussion of various possible modifications and their respective effects on the anisotropy in fully developed channel flow). Perhaps most telling, Durbin and Pettersson-Reif have noted [22] that while the elliptic relaxation method gives improved predictions of the pressure-strain correlation, it is not yet mathematically clear why this is the case. The present approach for addressing nonlocal effects may provide some clues as to the accuracy of the elliptic relaxation method, particularly with respect to the appearance of the Laplacian operator in both approaches, but this connection will not be explored in more detail here.

### 3.6.2 Relation to Prior Nonequilibrium Models

While the nonequilibrium effects in the anisotropy closure outlined herein enter naturally through the effective strain rate tensor $\widetilde{S}_{ij}$ in (3.97), there have been several prior approaches that have sought to introduce nonequilibrium effects within the traditional equilibrium closure via various modifications to the eddy viscosity $\nu_T$ in (1.35).

For example, Olsen and Coakley [73, 74] have developed a relatively straightforward nonequilibrium eddy viscosity model that takes into account nonequilibrium effects by solving an additional transport equation for the eddy viscosity as

$$\frac{D\nu_T}{Dt} = a_0 \frac{\epsilon}{k} \left( \nu_{Te} - \nu_T \right) , \qquad (3.136)$$

where $a_0 \approx 3.9$. The parameter $\nu_{Te}$ is the equilibrium eddy viscosity, given in (1.36) in the context of a $k$-$\epsilon$ implementation, and the transport equation for $\nu_T$ in (3.136) is then solved with the equations for $k$ and $\epsilon$ in (1.31) and (1.32). However, the equilibrium closure in (1.35) is still used to relate the Reynolds stresses to the eddy viscosity $\nu_T$ and the mean strain rate tensor $\overline{S}_{ij}$.

The Olsen and Coakley model shows modest improvements over standard equilibrium models for a range of flow problems. However, despite the inclusion of the additional transport equation for $\nu_T$, owing to the equilibrium relation between $a_{ij}(t)$ and $\overline{S}_{ij}(t)$ in (1.35) the model cannot predict the phase lag between the strain rate $\overline{S}_{ij}(t)$ and the resulting anisotropy $a_{ij}(t)$ in periodically-sheared turbulence, as shown in Figure 3.9. While the additional eddy-viscosity transport equation accounts for some nonequilibrium effects, the continued reliance on the instantaneous mean strain rate tensor in the equilibrium anisotropy closure inherently limits the model in accurately accounting for nonequilibrium effects.

In a somewhat similar approach, Yoshizawa and Nisizima [112, 113] have proposed a

lagged eddy viscosity having the basic form

$$\nu_T = \nu_{Te} - C\frac{k}{\epsilon}\frac{D\nu_{Te}}{Dt} , \qquad (3.137)$$

where $\nu_{Te}$ is the equilibrium eddy viscosity in (1.36). More recently Yoshizawa, Nisizima and co-workers [114] developed a modified version of the same basic model, in which (3.137) is replaced by

$$\nu_T = \begin{cases} \nu_{Te}\left[\Lambda_y + C_A\frac{1}{k}\frac{D}{Dt}\left(\frac{k^2}{\epsilon}\right)\right]^{-1} & \text{for} \quad \frac{D\nu_{Te}}{Dt} > 0 \\[2mm] \nu_{Te}\left[\frac{1}{\Lambda_y} - \frac{C_A}{\Lambda_y^2}\frac{1}{k}\frac{D}{Dt}\left(\frac{k^2}{\epsilon}\right)\right] & \text{for} \quad \frac{D\nu_{Te}}{Dt} < 0 \end{cases} \qquad (3.138)$$

where $\Lambda_y$ is a dimensionless parameter that depends on $Sk/\epsilon$ and $Wk/\epsilon$, with $W \equiv \left(2\overline{W}_{ij}\overline{W}_{ij}\right)^{1/2}$. However, this approach still uses the equilibrium closure in (1.35) to relate the anisotropy $a_{ij}(t)$ to the mean strain rate tensor $\overline{S}_{ij}(t)$. Thus, although this nonequilibrium eddy-viscosity model was seen, for example, to improve agreement with DNS results in homogeneous sheared turbulence [113, 114], the phase properties in the resulting anisotropy evolution for periodically sheared turbulence are not substantially different from those in Figure 3.9 using the Olsen and Coakley model.

Recently Revell *et al.* [80] proposed a novel nonequilibrium $k$-$\epsilon$-$C_{as}$ eddy-viscosity model in which an additional parameter

$$C_{as} = -\frac{a_{ij}\overline{S}_{ij}}{S} , \qquad (3.139)$$

is used to account for alignment between the Reynolds stress and mean strain rate tensors. In this case, the turbulence kinetic energy production is written as $P = C_{as}kS$, and an additional transport equation is solved to determine $C_{as}$. This additional equation can be incorporated into standard approaches such as the SKE model, in which case the eddy viscosity becomes

$$\nu_T = k\min\left[\frac{C_\mu k}{\epsilon}, \frac{C_{as}}{S}\right] , \qquad (3.140)$$

and the usual transport equations in (4.3) and (4.4) are solved for $k$ and $\epsilon$. However, as with the Olsen and Coakley and Yoshizawa and Nisizima models, the $k$-$\epsilon$-$C_{as}$ model fundamentally still employs the Boussinesq equilibrium closure between the anisotropy $a_{ij}(t)$ and the mean strain $\overline{S}_{ij}(t)$. Thus, while the $k$-$\epsilon$-$C_{as}$ model shows some improvement over the SKE model in predicting the evolution of periodically strained homogeneous turbulence [80], it still predicts zero anisotropy for zero applied strain, resulting in poor agreement with DNS for the periodically-sheared case when the applied shear is zero.

All of the prior nonequilibrium models noted above modify the eddy viscosity $\nu_T$ to account for nonequilibrium effects, but still use the equilibrium closure in (1.35) to relate the anisotropy $a_{ij}$ to the mean strain rate $\overline{S}_{ij}$. While such $\nu_T$ modifications allow some nonequilibrium effects to be addressed, it is clear that a general nonequilibrium Reynolds

stress closure cannot represent the anisotropy $a_{ij}$ as being directly proportional to $\overline{S}_{ij}$ as in (1.35), and must take into account the straining history of the turbulence via some method such as the effective strain rate $\widetilde{S}_{ij}$ in the present nonequilibrium closure.

### 3.6.3 Relation to Prior Nonlinear Models

In order to retain some dependence on the straining history, several prior anisotropy models [38, 95, 102, 112] have included various time derivatives of $\overline{S}_{ij}$ in nonlinear expansions of the anisotropy to obtain the most general closure possible. However, in contrast to the present closure the focus of most prior nonlinear models has not been explicitly on nonequilibrium effects due to Lagrangian variations in the mean strain rate, often to the detriment of the model accuracy in nonequilibrium flows.

For instance, using the most general nonlinear constitutive equation for the Reynolds stress tensor, Speziale [95] devised a nonlinear $k$-$\epsilon$ anisotropy closure of the form

$$a_{ij} = -2C_\mu \frac{k}{\epsilon} \overline{S}_{ij} - 4C_D C_\mu^2 \left(\frac{k}{\epsilon}\right)^2 \left(\overline{S}_{il}\overline{S}_{lj} - \frac{\delta_{ij}}{3}\overline{S}_{nl}\overline{S}_{nl}\right) \tag{3.141}$$
$$-4C_E C_\mu^2 \left(\frac{k}{\epsilon}\right)^2 \left(\frac{\mathcal{D}\overline{S}_{ij}}{\mathcal{D}t} - \frac{\delta_{ij}}{3}\frac{\mathcal{D}\overline{S}_{ll}}{\mathcal{D}t}\right),$$

where $C_D = C_E \approx 1.68$ and $\mathcal{D}/\mathcal{D}t$ denotes the Oldroyd derivative defined as

$$\frac{\mathcal{D}\overline{S}_{ij}}{\mathcal{D}t} = \frac{D\overline{S}_{ij}}{Dt} - \frac{\partial \overline{u}_i}{\partial x_l}\overline{S}_{lj} - \frac{\partial \overline{u}_j}{\partial x_l}\overline{S}_{li}. \tag{3.142}$$

The analogous memory time scale in the Speziale model is $\Lambda_m = 2C_E C_\mu (k/\epsilon)$, which comparing with (3.85) shows that $C_\Lambda = 2C_E C_\mu$. Typically, $C_\mu$ is given a value between 0.08 and 0.09, and for this range the Speziale model gives a memory time scale coefficient $C_\Lambda$ between 0.27 and 0.30, which is in good agreement with the value in (3.98) used for the preceding test cases.

However, in deriving the empirical constants $C_E$ and $C_D$, Speziale relied on fully developed turbulent channel flow data, for which the material derivative $D\overline{S}_{ij}/Dt$ is zero. This has significant consequences for application of the Speziale model to nonequilibrium flows, since the sign accompanying the $\mathcal{D}\overline{S}_{ij}/\mathcal{D}t$ term in (3.141) is opposite that accompanying the first-order $D\overline{S}_{ij}/Dt$ term in the present closure using (3.110). The discrepancy arises because the Oldroyd derivative was introduced in the Speziale model in an *ad hoc* manner to obtain the most general nonlinear expansion for the Reynolds stress anisotropy, with the coefficient $C_E$ determined from channel flow data where $D\overline{S}_{ij}/Dt = 0$. The Lagrangian derivatives of the mean strain in (3.110), on the other hand, are derived from the expansion of the effective strain rate in (3.107), which is itself directly linked to the physics underlying the evolution of the anisotropy, as embodied in (3.84).

The effects of the differing signs become especially apparent in periodically-sheared

turbulence. Using the Speziale model as in (3.141), Figure 3.10 shows that the phase of the resulting anisotropy is significantly different than in the DNS data. A similar Reynolds stress model by Huang and Ma [38] also includes a negatively-signed Oldroyd derivative term, as in (3.141), and is therefore expected to be comparably limited in simulating the anisotropy dynamics in periodically-sheared turbulence.

It should be noted that as an intermediate step in the derivation of a nonlinear Reynolds stress model, Taulbee [102] derived an expression for the anisotropy of the form

$$a_{ij} = -2C_\mu \frac{k}{\epsilon} \overline{S}_{ij} - 4\alpha_2 \left(\frac{k}{\epsilon}\right)^2 \left(\overline{S}_{il}\overline{W}_{lj} - \overline{W}_{il}\overline{S}_{lj}\right) \tag{3.143}$$

$$-4\alpha_3 \left(\frac{k}{\epsilon}\right)^2 \left(\overline{S}_{il}\overline{S}_{lj} - \frac{1}{3}\overline{S}_{nl}\overline{S}_{nl}\delta_{ij}\right) + 4C'_\mu \left(\frac{k}{\epsilon}\right)^2 \frac{D\overline{S}_{ij}}{Dt} + \dots,$$

where the only relevant constant for this discussion is $C'_\mu = \frac{1}{2}(0.35)C_\mu$, where $C_\mu \approx 0.09$ and we have taken $P/\epsilon \approx 1.9$. While the final nonlinear Reynolds stress model devised by Taulbee cannot capture certain nonequilibrium effects due to its dependence on the local and instantaneous values of $\overline{S}_{ij}$ and $\overline{W}_{ij}$, it can be seen that the sign accompanying the $D\overline{S}_{ij}/Dt$ term in the intermediate result in (3.143) is positive, in agreement with the present model in (3.97) using (3.110). When applied to periodically-sheared turbulence the closure in (3.143) gives the anisotropy evolution shown in Figure 3.11, which is clearly in better agreement with the DNS results than is the Speziale model, due to the correctly predicted sign accompanying the $D\overline{S}_{ij}/Dt$ term in (3.143).

Thus, in the form in (3.97) with (3.110) for the present nonequilibrium closure the time derivative of the strain rate results directly from the physics underlying nonequilibrium turbulence anisotropy, resulting in a model that reveals the correct dependence of the anisotropy on time variations in the mean strain rate tensor. Moreover, the coefficient $C_\Lambda$ associated with this term in (3.110) will be validated for a wide range of nonequilibrium flows in Chapter IV, resulting in increased accuracy over prior models that introduce nonequilibrium effects in an *ad hoc* manner.
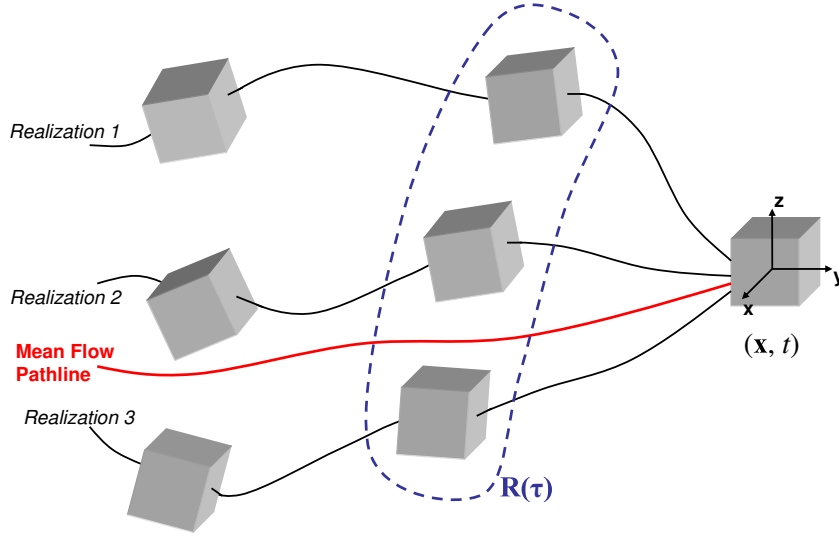
Figure 3.1: Schematic showing material elements arriving at $(\mathbf{x}, t)$ along different pathlines in three realizations of the same turbulent flow. Anisotropy $a_{ij}(\mathbf{x}, t)$ results from ensemble average over all elements at $(\mathbf{x}, t)$, and thus reflects vorticity alignments due to different straining histories along different pathlines. $R(\tau)$ shows representative ensemble of all elements at earlier time $\tau$, revealing effect of strain and rotation histories of mean-flow streamline on $a_{ij}(\mathbf{x}, t)$.
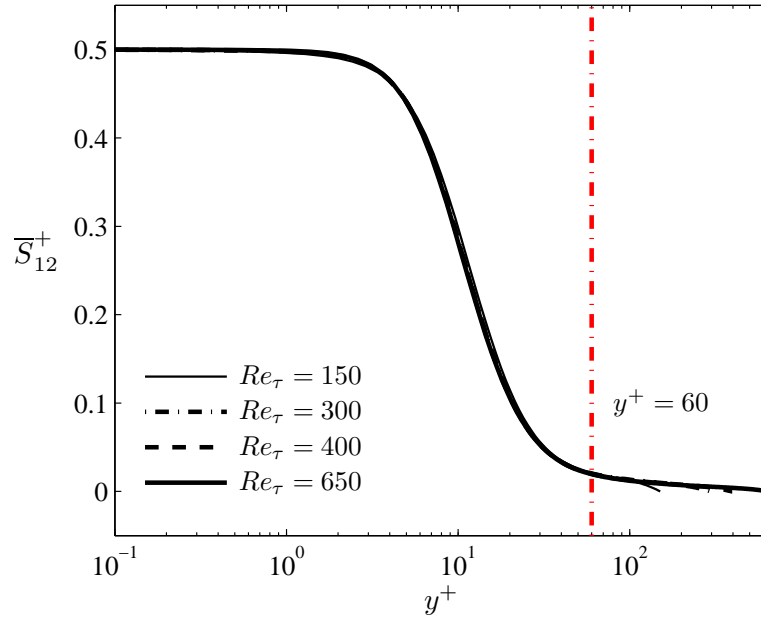


Figure 3.2: Mean shear $\overline{S}_{12}^+ \approx (1/2)\partial u^+/\partial y^+$ for a range of Reynolds numbers from the turbulent channel flow DNS of Iwamoto *et al.* [39]. Inhomogeneities in $\overline{S}_{12}^+$ become significant for $y^+ < 60$, as indicated by the vertical line.

100
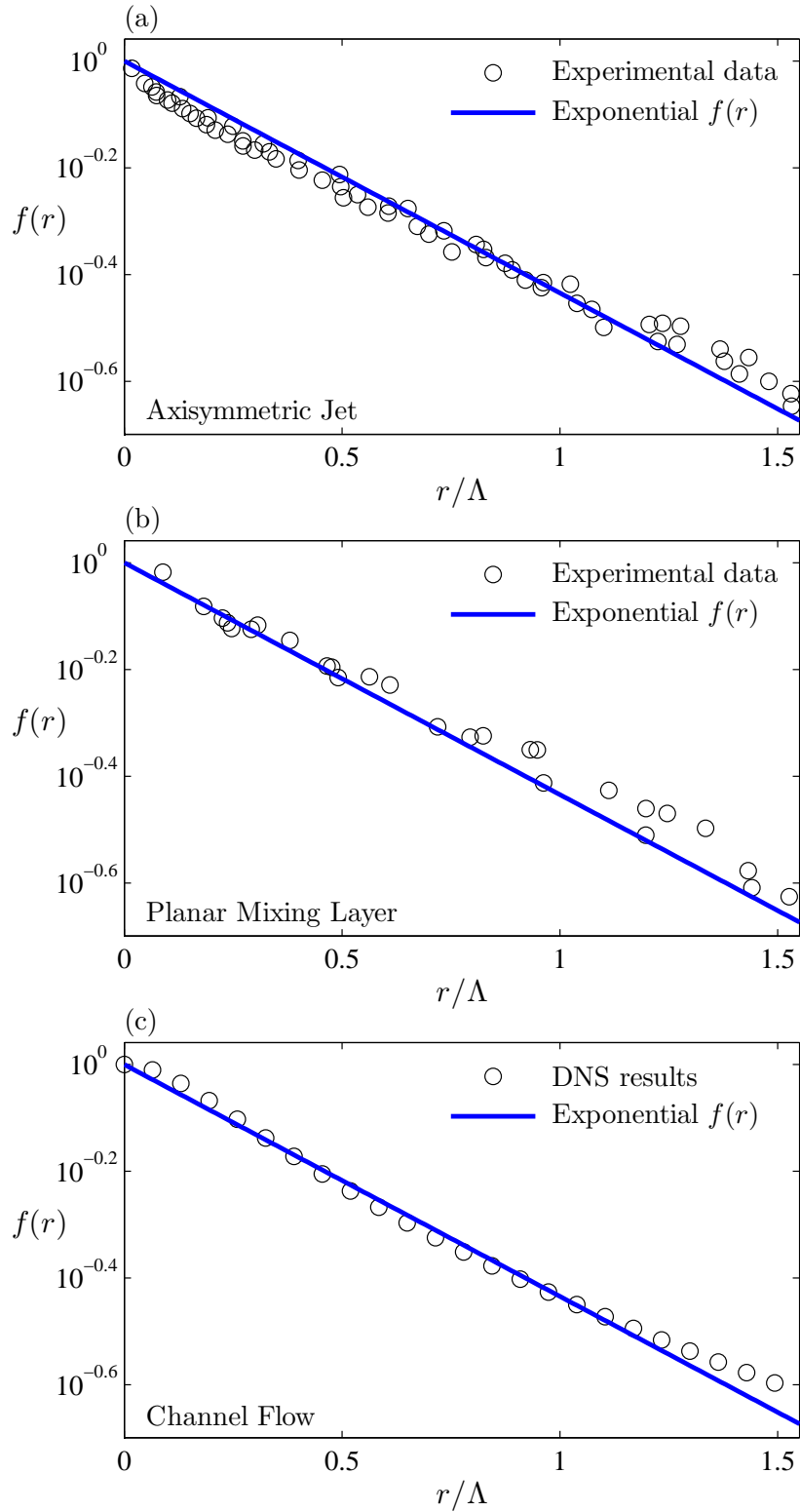
Figure 3.3: Comparison of exponential $f(r)$ in (3.38) with experimental data from axisymmetric turbulent jet [109] (a) and planar turbulent mixing layer [110] (b), and with DNS data from turbulent channel flow at $Re_\tau = 650$ [39] (c).
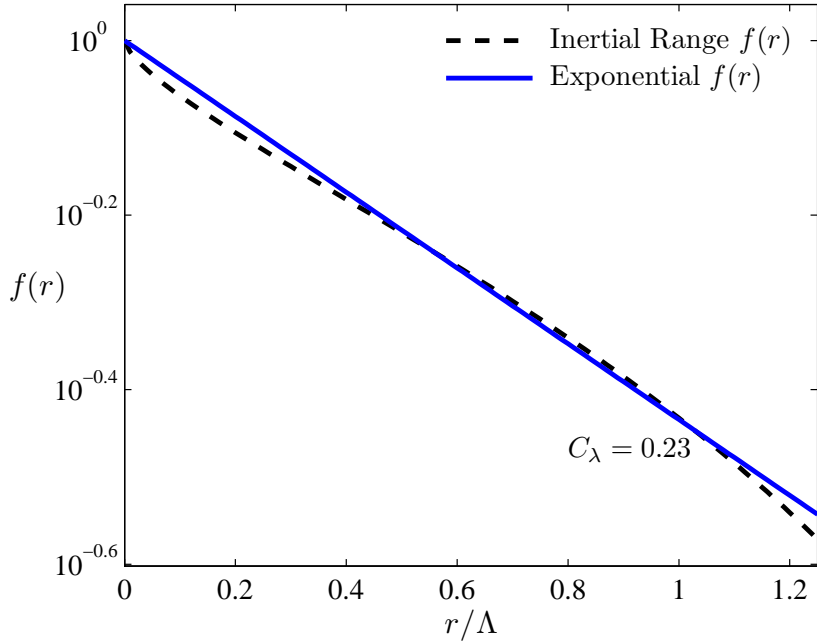
Figure 3.4: Comparison of inertial range and exponential forms for $f(r)$ from (3.34) and (3.38), respectively. In both cases, $f(r)$ is shown as a function of $r/\Lambda$ and $C_\lambda = 0.23$ in (3.39) gives good agreement between the two forms.
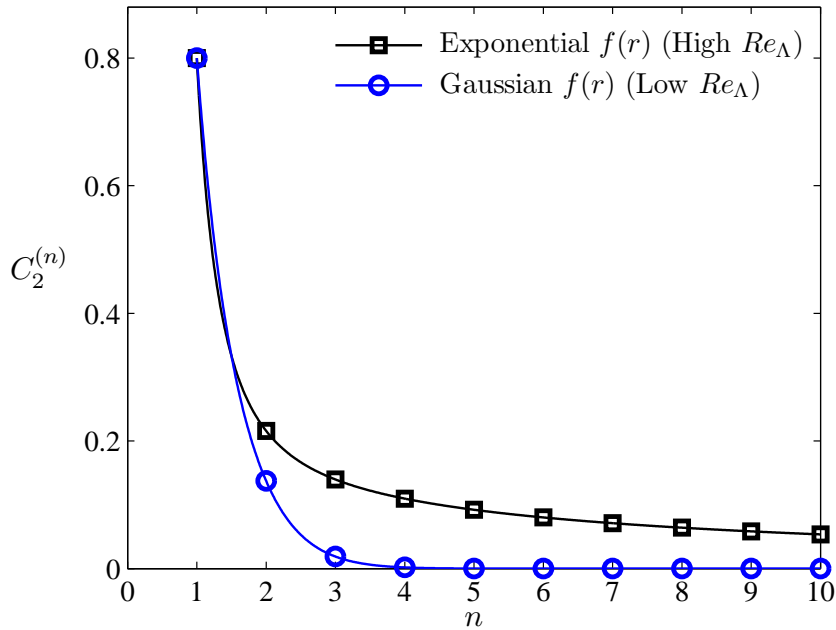


Figure 3.5: Comparison of rapid pressure-strain coefficients $C_2^{(n)}$ from (3.67) for the high-Reynolds number exponential $f(r)$ in (3.38), and from (3.70) for the low-Reynolds number Gaussian $f(r)$ in (3.40).
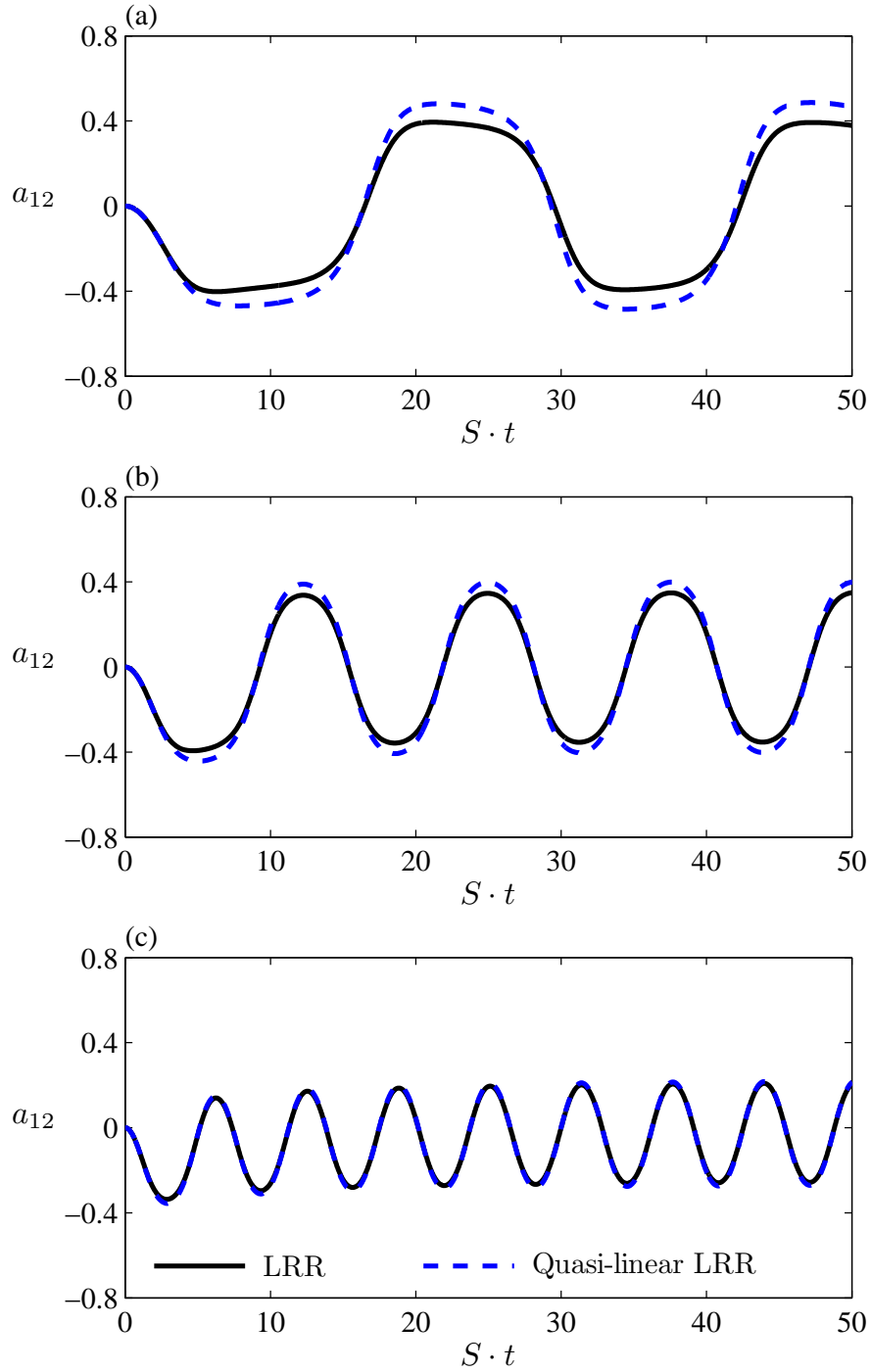
Figure 3.6: Comparison of anisotropy $a_{12}(t)$ from full $a_{ij}$ equation in (1.28) and truncated quasi-linear form in (3.84) for shearing frequencies $\omega/S = 0.25$ (a), $\omega/S = 0.5$ (b), and $\omega/S = 1.0$ (c); both curves are for LRR [51] constants in (1.26).
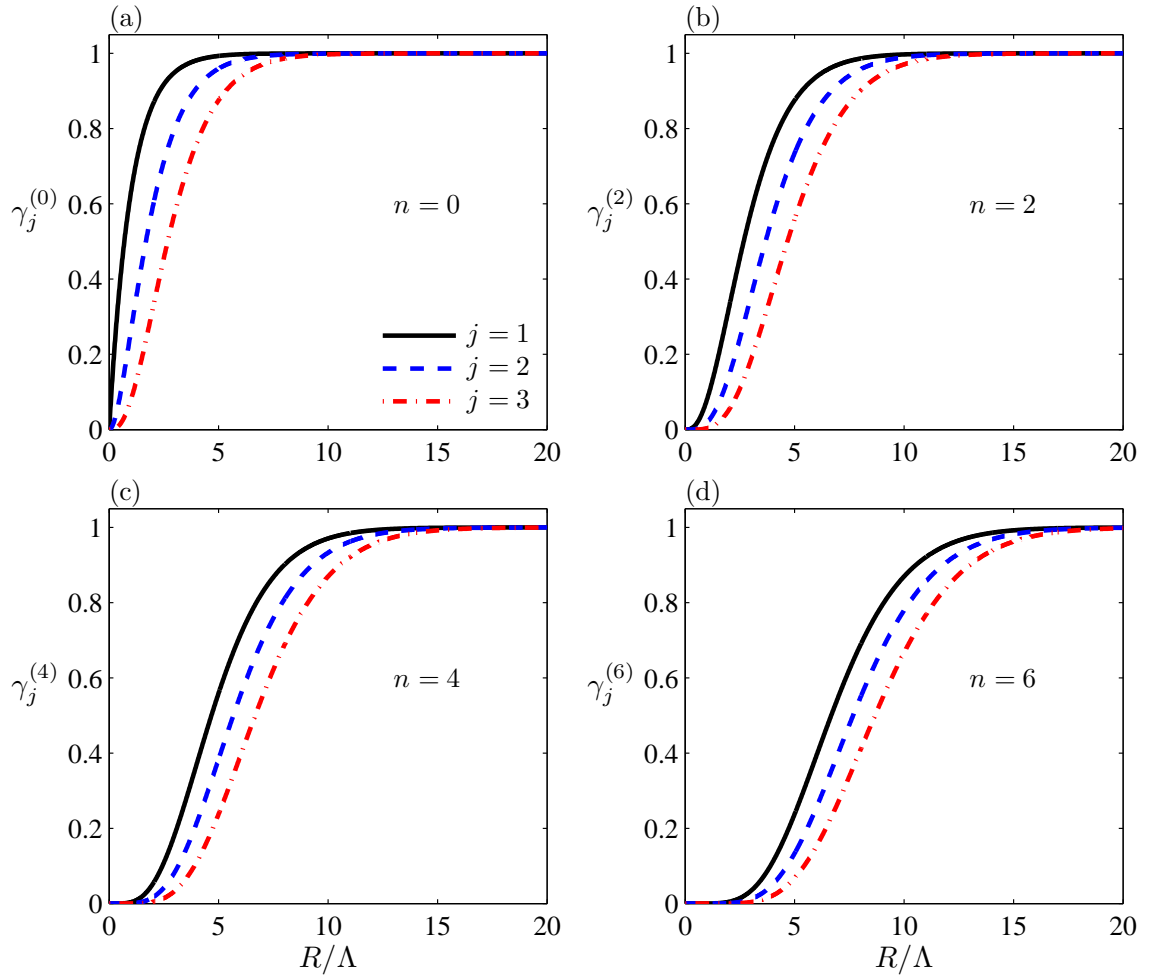
Figure 3.7: Parameter $\gamma_j^{(n)}$ from (3.112) as a function of $R/\Lambda$ for $n = 0$ (a), $n = 2$ (b), $n = 4$ (c), and $n = 6$ (d).
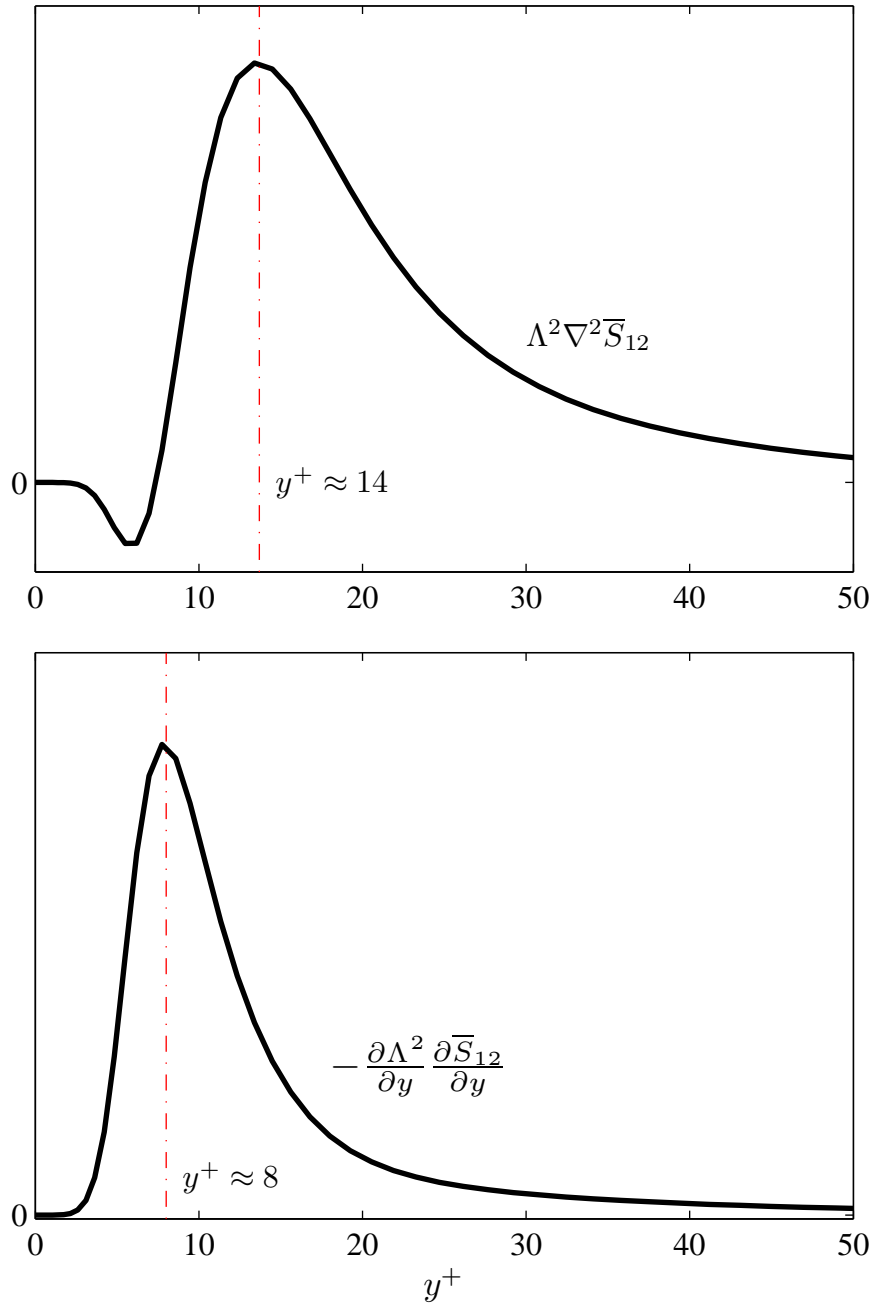
Figure 3.8: Magnitude of first nonlocal correction term due to inhomogeneities in the mean strain rate (top) and the length scale $\Lambda$ (bottom) for the $Re_\tau = 650$ fully-developed turbulent channel flow DNS of Iwamoto $et\ al.$ [39].
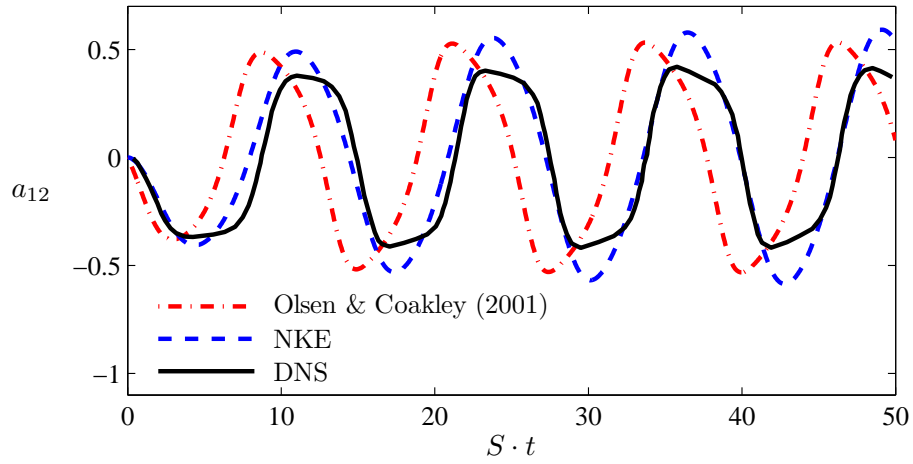
Figure 3.9: Comparison of anisotropy $a_{12}(t)$ in periodically-sheared turbulence at $\omega/S = 0.5$ from DNS of Yu and Girimaji [115] with corresponding results from nonequilibrium model of Olsen and Coakley [73, 74] and with results from the present closure (NKE), which are discussed in Section 4.5.
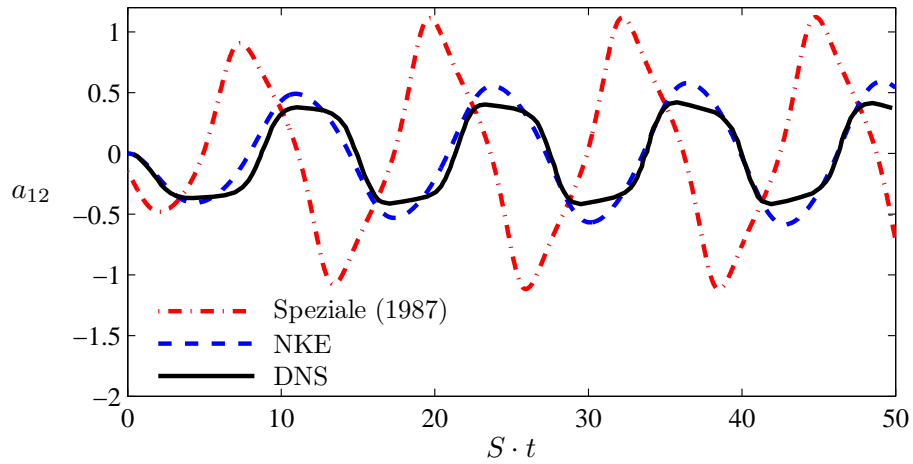


Figure 3.10: Comparison of anisotropy $a_{12}(t)$ in periodically-sheared turbulence at $\omega/S = 0.5$ from DNS of Yu and Girimaji [115] with corresponding results from Speziale [95] and with results from the present closure (NKE), which are discussed in Section 4.5.
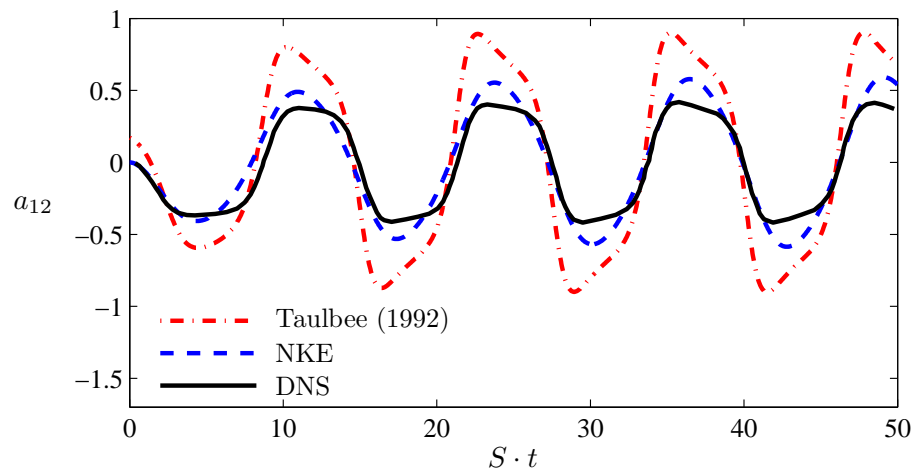
Figure 3.11: Comparison of anisotropy $a_{12}(t)$ in periodically-sheared turbulence at $\omega/S = 0.5$ from DNS of Yu and Girimaji [115] with corresponding results from Taulbee [102] and with results from the present closure (NKE), which are discussed in more detail in Section 4.5.

| $n$ | $C_2^{(n)}$ | Finite $R$ $C_2^{(n)}$ |
|---|---|---|
| 1 | 4/5 | $(32/15)\gamma_1^{(0)} - (28/15)\gamma_2^{(0)} + (8/15)\gamma_3^{(0)}$ |
| 2 | 68/315 | $(64/63)\gamma_1^{(2)} - (20/21)\gamma_2^{(2)} + (16/105)\gamma_3^{(2)}$ |
| 3 | 44/315 | $(32/45)\gamma_1^{(4)} - (4/9)\gamma_2^{(4)} - (8/63)\gamma_3^{(4)}$ |
| 4 | 76/693 | $(128/231)\gamma_1^{(6)} - (4/33)\gamma_2^{(6)} - (32/99)\gamma_3^{(6)}$ |
| 5 | 356/3861 | $(160/351)\gamma_1^{(8)} + (4/39)\gamma_2^{(8)} - (200/429)\gamma_3^{(8)}$ |
| 6 | 172/2145 | $(64/165)\gamma_1^{(10)} + (4/15)\gamma_2^{(10)} - (112/195)\gamma_3^{(10)}$ |
| 7 | 236/3315 | $(224/663)\gamma_1^{(12)} + (20/51)\gamma_2^{(12)} - (56/85)\gamma_3^{(12)}$ |
| 8 | 932/14535 | $(256/855)\gamma_1^{(14)} + (28/57)\gamma_2^{(14)} - (704/969)\gamma_3^{(14)}$ |

Table 3.1: Values of the coefficients $C_2^{(n)}$ for $n = [1, 8]$ from (3.67), and from (3.118) for the finite $R$ and $N$ truncated formulation of $\Pi_{ij}^{(r)}$ in (3.117).

|  | $\alpha_1$ | $C_\Lambda$ |
|---|---|---|
| Yakhot *et al.* [111] | 4.4 | 0.23 |
| Launder *et al.* [51] | 2.4 | 0.42 |
| Gibson and Launder [26] | 2.7 | 0.37 |
| Gatski and Speziale [24] | 4.3 | 0.23 |

Table 3.2: Recommended $\alpha_1$ values and corresponding $C_\Lambda$ values from various prior closure approaches.

# CHAPTER IV

# Nonequilibrium Tests of the Present Anisotropy Closure

In the following, the nonlocal, nonequilibrium closure in (3.97) with the corresponding convolution effective strain rate in (3.96) is examined for various homogeneous turbulence test cases. Such homogeneous flows play a key role in turbulence model development since they allow the underlying model physics to be probed directly. The resulting decoupling of the turbulence model from the mean flow equations allows the anisotropy evolution to be calculated by simple numerical integration of ordinary differential equations, without the need for a full computational framework that can often confuse numerical issues with the performance of the turbulence closure model. Nonequilibrium homogeneous flows are used in this section to conduct a detailed evaluation of turbulence model dynamics in the presence of time-varying imposed mean strain rates $\overline{S}_{ij}(t)$. Such direct assessments of nonequilibrium closure models can be difficult to conduct in the framework of a full computational simulation for various steady and equilibrium mean flow problems that are often used for turbulence model validation [76].

For homogeneous flows the closure in (3.96) and (3.97) can be substantially simplified. Nonlocal effects are not important in homogeneous flows and all Laplacians of the mean strain rate in (3.96) are zero. Consequently, a greatly simplified closure formulation is obtained, identical to that derived and validated in Ref. [31]. Moreover, by considering homogeneous tests for which the entire straining history $\overline{S}_{ij}(t)$ is known, the full convolution form of the effective strain in (3.96) can be used to obtain the anisotropy evolution. The homogeneous tests in this Chapter thus permit a full assessment of the nonequilibrium aspects of the new closure approach. In the next Section the model formulation for equilibrium flows is outlined in the context of a $k$-$\epsilon$ framework, where the evolution of $k$ and $\epsilon$ is given by the homogeneous forms of (1.31) and (1.32), respectively, and the eddy viscosity will be given in standard form by (1.36).

The closure given by (3.96) and (3.97) will be applied herein to six different homogeneous nonequilibrium test cases, namely ($i$) impulsively sheared turbulence, for which LES results are available for comparison from Bardina *et al.* [3], ($ii$) axisymmetrically contracted turbulence, which has been studied using DNS by Lee and Reynolds [55], ($iii$)

decaying anisotropic turbulence, for which experimental data are available from Choi and Lumley [13] and Le Penven *et al.* [75], (*iv*) strained, relaxed, and destrained turbulence, for which experimental data are available from Chen *et al.* [11], (*v*) periodically-sheared turbulence, for which computational data are available from Yu and Girimaji [115], and (*vi*) the interaction of initially-isotropic turbulence with a shock wave, for which DNS data are available from Lee *et al.* [56] and Mahesh *et al.* [60]. In each case, comparisons of the present closure in (3.97) are made with the equilibrium hypothesis in (1.35) via the SKE or RKE models outlined in Chapter I. For nearly all cases, comparisons are also made with the LRR [51] Reynolds stress transport model, where the anisotropy transport equation in (1.28) is solved directly using the model coefficients in (1.26). In all cases, the imposed mean strain rate $\overline{S}_{ij}(t)$ allows the effective strain rate $\widetilde{S}_{ij}(t)$ in (3.96) to be evaluated analytically.

With respect to the periodic-shearing case, the present closure will be used to conduct a detailed frequency response analysis of the anisotropy dynamics. This demonstrates the full analytical power of the new closure approach, and also yields valuable physical insights into the different frequency regimes of homogeneous turbulence. At the end of this Chapter, the time-local implementation of the new closure proposed in Section 3.5.1 is evaluated for periodically-sheared and Gaussian-strained turbulence.

## 4.1    Nonequilibrium Anisotropy Closure in Homogeneous Flows

In homogeneous turbulence, the Laplacians of $\overline{S}_{ij}$ in the definition of $\overline{T}_{ij}$ in (3.87) are zero, and we thus obtain $\overline{T}_{ij} = \overline{S}_{ij}$. As a result, the effective strain rate in (3.96) can be written for homogeneous turbulence as

$$\widetilde{S}_{ij} = \int_{-\infty}^{t} \overline{S}_{ij}(\tau) \frac{e^{-(t-\tau)/\Lambda_m(t)}}{\Lambda_m(t)} D\tau \, , \tag{4.1}$$

where the anisotropy is still given by (3.97) and $\Lambda_m$ is defined in (3.85) with $C_\Lambda$ given by (3.98). In the following, the eddy viscosity $\nu_T$ is given in standard $k$-$\epsilon$ form by (1.36), which then gives the anisotropy as

$$a_{ij} = -2C_\mu \frac{k}{\epsilon} \widetilde{S}_{ij} \, . \tag{4.2}$$

This formulation for the anisotropy is identical to the purely nonequilibrium closure that was derived and validated in Ref. [31].

Here, this model is applied to predict the turbulence response in a range of different nonequilibrium homogeneous turbulence test cases. These cases provide ideal tests for assessing the accuracy of new turbulence closure approaches, in large part because the $k$ and $\epsilon$ equations in (1.31) and (1.32) become substantially simpler in homogeneous flows. Since $\partial/\partial x_j \overline{()} \equiv 0$ in homogeneous turbulence, the time-evolution of the Reynolds stress tensor becomes decoupled from (1.2)-(1.4). For a given applied strain rate tensor $\overline{S}_{ij}(t)$,

the equations for $k(t)$ and $\epsilon(t)$ in (1.31) and (1.32) thus reduce to

$$\frac{dk}{dt} = -ka_{ij}\overline{S}_{ij} - \epsilon \,, \tag{4.3}$$

$$\frac{d\epsilon}{dt} = -C_{\epsilon 1}\epsilon\, a_{ij}\overline{S}_{ij} - C_{\epsilon 2}\frac{\epsilon^2}{k} \,. \tag{4.4}$$

For a given $\overline{S}_{ij}(t)$ the resulting $k(t)$ and $\epsilon(t)$ are found from (4.3) and (4.4), with the anisotropy $a_{ij}(t)$ given by (4.2).

Thus (4.3) and (4.4) with the standard model constants in (1.33) still determine the resulting $k(t)$ and $\epsilon(t)$, but the anisotropy $a_{ij}(t)$ in these equations is now obtained using the closure in (4.2) with (4.1), by contrast to the formulation for $a_{ij}(t)$ from the equilibrium closure in (1.35) used in the SKE and RKE models. The turbulence memory time scale $\Lambda_m$ is given by (3.85), and for all tests presented herein we use the value of $C_\Lambda$ given by (3.98). When implemented in this manner, the resulting nonequilibrium $k$-$\epsilon$ (NKE) model differs from the SKE and RKE models outlined in Chapter I solely due to this new nonequilibrium anisotropy relation for $a_{ij}$.

## 4.2   Impulsively-Strained Homogeneous Test Cases

For initially isotropic, impulsively-strained homogeneous turbulence the applied mean strain $\overline{S}_{ij}$ is zero for $t < 0$ and takes on a constant nonzero value for $t \geq 0$. The equilibrium closure in (1.35) with $\nu_T$ in (1.36) gives the corresponding anisotropy in the SKE model for $t \geq 0$ as

$$a_{ij}(t) = -2C_\mu \frac{k}{\epsilon}\overline{S}_{ij} \,, \tag{4.5}$$

which results in nonzero $a_{ij}$ at $t = 0$ – a result that is inconsistent with the isotropic initial condition. For the present nonequilibrium closure however, the effective strain rate $\widetilde{S}_{ij}(t)$ for $t \geq 0$ is obtained from (4.1) for all initially-isotropic impulsively-strained test cases as

$$\widetilde{S}_{ij}(t) = \overline{S}_{ij}\left[1 - e^{-t/\Lambda_m}\right] \,, \tag{4.6}$$

where $\overline{S}_{ij}$ used here is constant (time-independent) for $t \geq 0$, and the corresponding anisotropy from (4.2) is given by

$$a_{ij}(t) = -2C_\mu \frac{k}{\epsilon}\overline{S}_{ij}\left[1 - e^{-t/\Lambda_m}\right] \,. \tag{4.7}$$

It is clear that the form in (4.7) is zero at $t = 0$, consistent with the isotropic initial condition, and approaches the equilibrium result in (4.5) in a finite time given by the memory time scale $\Lambda_m$.

For these impulsively-strained flows, where the time rate of change of $\overline{S}_{ij}$ at $t = 0$ is infinite, the degree of nonequilibrium can be characterized by the non-dimensional initial

strain parameter $Sk_0/\epsilon_0$, where $S \equiv (2\widetilde{S}_{ij}\widetilde{S}_{ji})^{1/2}$. This can be seen by considering that the nonequilibrium parameter $\Upsilon$ defined in (3.104) is given using (4.6) as

$$\Upsilon = \left| \frac{1}{e^{(St)/(S\Lambda_m)} - 1} \right|. \tag{4.8}$$

Recall that $\Upsilon = 0$ in full equilibrium, whereas $\Upsilon > 0$ corresponds to nonequilibrium conditions. At $t = 0$ we obtain $\Upsilon = \infty$, consistent with the impulsive nature of the shearing. However, the rate at which the equilibrium condition $\Upsilon = 0$ is recovered is fundamentally determined by the magnitude of $S\Lambda_m = C_\Lambda(Sk/\epsilon)$. For large values of the initial strain parameter $Sk_0/\epsilon_0$, $S\Lambda_m$ is initially large and the equilibrium condition $\Upsilon = 0$ is approached only very slowly with increasing non-dimensional time $(St)$. As a result, the degree of nonequilibrium in the flow can remain substantial for relatively long times. For small values of $Sk_0/\epsilon_0$ however, $\Upsilon = 0$ can be quickly recovered even for small $(St)$, resulting in equilibrium flow conditions for essentially all $t > 0$. In such quasi-equilibrium flows there are thus only small differences between the anisotropy predicted by the equilibrium and nonequilibrium closures in (4.5) and (4.7), respectively. As will be seen herein however, for large $Sk_0/\epsilon_0$ there are substantial differences between results from the equilibrium and nonequilibrium closures due to the resulting large degree of nonequilibrium in the flow.

In the following, kinetic energy and anisotropy results from (4.7) are compared with results from (4.5) and the LRR model for impulsively-sheared turbulence [3] and turbulence subjected to an impulsive axisymmetric contraction [55]. In these cases $a_{ij}$ is initially zero, and the applied mean strain $\overline{S}_{ij}$ is constant for $t > 0$. The initial magnitude of the applied strain, characterized by $Sk_0/\epsilon_0$, is relatively large in both cases, resulting in substantial nonequilibrium effects on the anisotropy evolution. These effects, which can dominate the anisotropy dynamics for sufficiently large $Sk_0/\epsilon_0$, require the use of the nonequilibrium closure in (4.7) to give good agreement with validation results. By contrast, nonequilibrium effects do not have a dominant effect on the anisotropy in flows where $Sk_0/\epsilon_0$ is relatively small, and as a result such quasi-equilibrium flows are not considered herein.

### 4.2.1 Sheared Turbulence

For impulsively-sheared homogeneous turbulence the imposed mean strain rate is given for $t \geq 0$ as

$$\overline{S}_{ij} = \begin{bmatrix} 0 & S/2 & 0 \\ S/2 & 0 & 0 \\ 0 & 0 & 0 \end{bmatrix}, \tag{4.9}$$

For the particular case $(Sk_0/\epsilon_0) = 3.4$, for which Bardina *et al.* [3] give LES results, integration of (4.3) and (4.4) for $k(t)$ and $\epsilon(t)$ from the SKE and NKE models in (4.5) and (4.7), respectively, gives the kinetic energy evolution shown in Figure 4.1. The history effect in the nonequilibrium closure, and the consequent reduction in (4.7) of the anisotropy magnitude

relative to that in (4.5) from the equilibrium closure, lowers the initial kinetic energy production from the NKE model relative to the corresponding production from the equilibrium closure in the SKE model. This can be seen in Figure 4.1 to give an initial reduction in the kinetic energy $k(t)$ from the nonequilibrium closure, in good agreement with results from LES and the LRR model, while the equilibrium closure shows a strictly monotonic increase in $k(t)$. Figure 4.2 additionally shows that the NKE model in (4.7) predicts an evolution of $a_{12}$ that is in good agreement with LRR model results. While the SKE model predicts a nonzero value for $a_{12}$ at $t = 0$, both the NKE and LRR models predict a finite-time increase in $a_{12}$ from zero at $t = 0$. The SKE and NKE models show large discrepancies until $St \approx 3$, in agreement with the results for the evolution of $k$ in Figure 4.1.

Note that due to the initially lower kinetic energy production, $k(t)$ from the nonequilibrium closure in the NKE model is always below that from the equilibrium closure in the SKE model. For $t \gg \Lambda_m$, the nonequilibrium correction to the anisotropy in (4.7) becomes negligible, and the kinetic energy production in the NKE model can be seen in Figure 4.1 to become similar to that from the equilibrium closure in the SKE model. Thus the nonequilibrium effect that creates the initially lower kinetic energy production remains active only for a time of $O(\Lambda_m)$ after the turbulence is subjected to the change in shear. However, this temporary nonequilibrium effect produces a permanent lag in the turbulence response relative to that from the equilibrium closure. This nonequilibrium lag will be seen in the remaining test cases to be a key component of the turbulence response to changes in the mean shear, and cannot be accounted for by the classical local equilibrium closure in (1.35).

### 4.2.2 Axisymmetric Contraction

For initially isotropic turbulence subjected to an impulsively applied axisymmetric contraction at $t = 0$, the mean strain is given by

$$\overline{S}_{ij} = \begin{bmatrix} S & 0 & 0 \\ 0 & -S/2 & 0 \\ 0 & 0 & -S/2 \end{bmatrix}. \tag{4.10}$$

This case has been studied using DNS by Lee and Reynolds [55] for the initial strain parameter $Sk_0/\epsilon_0 = 5.59$.

Figure 4.3 shows large differences between the kinetic energy evolution predicted by the SKE model in (4.5) and the NKE model in (4.7). As with the impulsively-sheared case in Figure 4.1, the SKE model predicts a large growth rate of $k$ for small times, whereas the NKE and LRR models predict much more modest growth of $k$, in better agreement with DNS results. Similarly, results for $a_{ij}$ from the NKE model follow the LRR and DNS results much more closely than the SKE results, as shown in Figure 4.4. The substantial differences between the SKE and NKE results in Figures 4.3 and 4.4 for this case are due to the relatively large initial value of $Sk_0/\epsilon_0$. This results in a large degree of nonequilibrium

113

when the strain in (4.10) is applied at $t = 0$, and the anisotropy lag in (4.7) is required to obtain good agreement with the DNS results for small times.

Taken together, the impulsively-strained results in Figures 4.1-4.4 indicate that results from the NKE model in (4.7) generally show better agreement with LRR and computational results than results from the SKE model in (4.5). In particular, the NKE model predicts a finite-time increase in the anisotropy magnitude at $t = 0$ from the initially isotropic state, which results in a lag between the kinetic energy evolution predicted by the SKE and NKE models for all times. Moreover, the exact nature of the applied strain (e.g. sheared versus axisymmetric contraction) does not seem to affect the accuracy of the nonequilibrium closure. Note that the observed large differences between the SKE and NKE model results is not surprising, since the parameter $Sk_0/\epsilon_0$, which characterizes the degree of nonequilibrium in the flow as shown in (4.8), is relatively large for both impulsively-strained cases considered herein. As noted previously, for large values of $Sk_0/\epsilon_0$ the nonequilibrium correction in (4.7) – which is fundamentally obtained by retaining the $Da_{ij}/Dt$ term in (3.84) – is critical for accurately capturing the most important physics underlying the anisotropy evolution.

## 4.3 Decaying Anisotropic Turbulence

For the impulsively-strained test cases in the preceding section, the effect of the rapid straining term $\alpha_2 \overline{S}_{ij}$ in (3.84) generally dominates the slow turbulence relaxation term $a_{ij}/\Lambda_m$, particularly when the initial shearing parameter $Sk_0/\epsilon_0$ is large. However, in decaying initially anisotropic homogeneous turbulence there is no applied strain and the anisotropy evolution is completely determined by the slow relaxation term. As a result, the nonequilibrium parameter in (3.104) is given for this case as $\Upsilon = 1$ – reflecting the fact that the nonequilibrium in this flow (where in general $\Upsilon > 0$ reflects nonequilibrium flow conditions) is dominated by slow relaxation processes.

We here consider an arbitrary flow subjected to a constant applied strain $\overline{S}_{ij}$ for all $t < 0$, which is then impulsively removed at $t = 0$. For all $t \geq 0$, the equilibrium closure in (1.35) predicts $a_{ij}(t) = 0$. From (3.89) however, the nonequilibrium closure yields

$$a_{ij}(t) = a_{ij}(0)e^{-t/\Lambda_m} , \tag{4.11}$$

where we have used $t_0 = 0$ and higher-order derivatives of $1/\Lambda_m$ have been neglected as in (3.92). The nonequilibrium closure in (4.11) thus predicts a finite-time exponential decay of the initial anisotropy $a_{ij}(0)$. In decaying turbulence the anisotropy has no effect on the evolution of $k$ and $\epsilon$ since $P = 0$ due to $\overline{S}_{ij}(t) = 0$ for $t > 0$. Thus, from (4.3) and (4.4) we obtain the transport equation for $k/\epsilon$ as

$$\frac{d(k/\epsilon)}{dt} = (C_{\epsilon 2} - 1) , \tag{4.12}$$

114

which has the solution

$$\frac{(k/\epsilon)(\tau)}{(k_0/\epsilon_0)} = (C_{\epsilon 2} - 1)\,\tau + 1\,, \qquad (4.13)$$

where we have defined the dimensionless time $\tau \equiv t\epsilon_0/k_0$, and $k_0$ and $\epsilon_0$ denote the initial values $k$ and $\epsilon$ at $t = 0$. Substitution of (4.13) into (4.11) then gives

$$a_{ij}(\tau) = a_{ij}(0)\exp\left[-\frac{\tau}{C_\Lambda\,(C_{\epsilon 2} - 1)\,\tau + C_\Lambda}\right]\,. \qquad (4.14)$$

This expression describes the decay of the initial anisotropy $a_{ij}(0)$ in any unstrained flow using the nonequilibrium closure in (4.2).

Experimental results for decaying anisotropic turbulence have been obtained by Choi and Lumley [13] for initially plane-strained turbulence and by Le Penven *et al.* [75] for a plane contraction. Using the initial values of $a_{ij}(0)$ specified in these experiments, Figures 4.5 and 4.6 compare the anisotropy predicted by the NKE and LRR models with the available experimental data. Note that it can be anticipated for this case that the value of $C_\Lambda$ in (3.98) is too small to give good agreement with the experimental data. This can be seen from the definition of $C_\Lambda$ in (3.86), which gives $C_\Lambda = 1/(C_1 - 1)$ for unstrained turbulence where $P/\epsilon = 0$. Using the value for $C_1$ from the LRR model [51] in (1.26) then gives $C_\Lambda = 2$. With this value for $C_\Lambda$, Figures 4.5 and 4.6 show that results from the NKE model in (4.14) are in good agreement with the LRR and experimental results. In particular, the NKE model predicts a finite-time decay of the anisotropy magnitude that is in good agreement with the LRR and experimental results for both cases, whereas the SKE model predicts $a_{ij} = 0$ for all $\tau > 0$. The remaining discrepancies between the NKE and LRR models are due to the neglect of the higher-order derivatives of $1/\Lambda_m$ in obtaining (4.11) from (3.89).

While Figures 4.5 and 4.6 indicate that good agreement with LRR and experimental results for this case requires a modified value for $C_\Lambda$, it should be borne in mind that the constant value of $C_\Lambda$ given by (3.98) and used for the rest of the tests in this study is intended as a reasonable approximate value that gives good agreement with a wide-range of tests where $P/\epsilon$ is typically nonzero. Since $C_\Lambda$ is related to $P/\epsilon$ from (3.86) as $C_\Lambda = 1/(P/\epsilon - 1 + C_1)$, extreme values such as $P/\epsilon = 0$ are expected to affect the accuracy of the present closure. Nevertheless, for the preceding impulsively strained tests and the remaining more complex tests, it will be seen that the constant value of $C_\Lambda$ in (3.98) is sufficient to give substantially improved agreement with validation data when compared to the equilibrium closure in (1.35), due to the focus on nonequilibrium effects in the present approach.

## 4.4   Straining, Relaxation, and Destraining

An even more complex test of the nonequilibrium turbulence response to an imposed mean strain $\overline{S}_{ij}(t)$ is provided by recent experimental results of Chen *et al.* [11] for the

straining, relaxation, and destraining of initially-isotropic homogeneous turbulence. This test effectively combines the impulsive straining cases in Section 4.2 and the decaying case in Section 4.3, and thus allows a more sophisticated evaluation of the anisotropy predictions from the various models in a relatively complex flow.

In the experiment by Chen *et al.*, $\overline{S}_{22}(t) = -\overline{S}_{11}(t)$ and all other components of the imposed mean strain are zero. Their measured values for the imposed $\overline{S}_{11}(t)$ are given by the symbols in Figure 4.7, and this straining history can be analytically approximated by the piecewise linear form

$$
\overline{S}_{11}(t) = \begin{cases}
0 & \text{for} \quad 0 \leq t \leq t_1 \\
c_1(t - t_1) & \text{for} \quad t_1 < t \leq t_2 \\
-c_2(t - t_3) & \text{for} \quad t_2 < t \leq t_3 \\
0 & \text{for} \quad t_3 < t \leq t_4 \\
-c_3(t - t_4) & \text{for} \quad t_4 < t \leq t_5 \\
c_4(t - t_6) & \text{for} \quad t_5 < t \leq t_6
\end{cases} \tag{4.15}
$$

where $\overline{S}_{22}(t) = -\overline{S}_{11}(t)$. The $c_i$ have dimensions of $1/t^2$ and are chosen, along with the $t_i$, to give good agreement with the experimentally applied strain, as shown in Figure 4.7. The straining in (4.15) serves as the input for the various closures to generate their respective turbulence anisotropy responses $a_{ij}(t)$. The only nonzero components are $a_{11}(t)$ and $a_{22}(t)$, and for the traditional equilibrium closure in the SKE model the resulting anisotropy components are

$$
a_{11}(t) = -a_{22}(t) = -2C_\mu \frac{k}{\epsilon} \overline{S}_{11}(t) \,. \tag{4.16}
$$

For the proposed closure in the NKE model, the effective strain rate $\widetilde{S}_{11}(t)$ is obtained via (4.1) by integrating the piecewise linear analytical form of $\overline{S}_{11}(t)$ in (4.15), which yields

$$
\widetilde{S}_{11}(t) = \begin{cases}
\widetilde{S}_{11}^{(1)}(t) & \text{for} \quad 0 \leq t \leq t_1 \\
\widetilde{S}_{11}^{(2)}(t) & \text{for} \quad t_1 < t \leq t_2 \\
\widetilde{S}_{11}^{(3)}(t) & \text{for} \quad t_2 < t \leq t_3 \\
\widetilde{S}_{11}^{(4)}(t) & \text{for} \quad t_3 < t \leq t_4 \\
\widetilde{S}_{11}^{(5)}(t) & \text{for} \quad t_4 < t \leq t_5 \\
\widetilde{S}_{11}^{(6)}(t) & \text{for} \quad t_5 < t \leq t_6
\end{cases} \tag{4.17}
$$

where

$$
\widetilde{S}_{11}^{(1)}(t) = 0 \,, \tag{4.18a}
$$

$$
\widetilde{S}_{11}^{(2)}(t) = c_1 \left[ t - t_1 - \Lambda_m \left( 1 - e^{-(t-t_1)/\Lambda_m} \right) \right] \,, \tag{4.18b}
$$

$$\widetilde{S}_{11}^{(3)}(t) = c_1 \left[ \Lambda_m e^{-(t-t_1)/\Lambda_m} - (\Lambda_m + t_1 - t_2) e^{-(t-t_2)/\Lambda_m} \right] \qquad (4.18c)$$
$$+ c_2 \left[ \Lambda_m - t + t_3 - (\Lambda_m - t_2 + t_3) e^{-(t-t_2)/\Lambda_m} \right] ,$$

$$\widetilde{S}_{11}^{(4)}(t) = c_1 \left[ \Lambda_m e^{-(t-t_1)/\Lambda_m} - (\Lambda_m + t_1 - t_2) e^{-(t-t_2)/\Lambda_m} \right] \qquad (4.18d)$$
$$+ c_2 \left[ \Lambda_m e^{-(t-t_3)/\Lambda_m} - (\Lambda_m - t_2 + t_3) e^{-(t-t_2)/\Lambda_m} \right] ,$$

$$\widetilde{S}_{11}^{(5)}(t) = \widetilde{S}_{11}^{(4)}(t) + c_3 \left[ \Lambda_m - t + t_4 - \Lambda_m e^{-(t-t_4)/\Lambda_m} \right] , \qquad (4.18e)$$

$$\widetilde{S}_{11}^{(6)}(t) = \widetilde{S}_{11}^{(4)}(t) + c_3 \left[ (\Lambda_m + t_4 - t_5) e^{-(t-t_5)/\Lambda_m} - \Lambda_m e^{-(t-t_4)/\Lambda_m} \right] \qquad (4.18f)$$
$$+ c_4 \left[ t - t_6 - \Lambda_m + (\Lambda_m - t_5 + t_6) e^{-(t-t_5)/\Lambda_m} \right] .$$

The resulting anisotropy components are then

$$a_{11}(t) = -a_{22}(t) = -2C_\mu \frac{k}{\epsilon} \widetilde{S}_{11}(t) . \qquad (4.19)$$

For both (4.16) and (4.19), the respective $a_{ij}(t)$ allows the corresponding $k(t)$ and $\epsilon(t)$ to be obtained by integrating (4.3) and (4.4).

The results for $a_{11}(t)$ from the SKE, NKE, and LRR models are shown in Figure 4.8, with the measured anisotropy values from Chen *et al.* [11] shown by the symbols for comparison. The measured values were converted from the two-dimensional anisotropy reported by Chen *et al.* to the usual three-dimensional form via isotropy in the unstrained out-of-plane component. The large strain rate values in this test case require the weak realizability constraint in (1.40) to limit the $C_\mu$ value. Using the average strain rate magnitude in Figure 4.7, together with $S = 2|S_{11}|$, gives $C_\mu = 0.05$. This value is used in both the SKE and NKE models and reflects the fact that the present closure given by (3.97) with (3.96) addresses nonlocal and nonequilibrium effects on the anisotropy without specifying a representation for the eddy viscosity $\nu_T$. As a result, in many instances (including the nonlocal wall bounded tests in Chapter V) it may be necessary to specify a more appropriate representation for $\nu_T$ and $C_\mu$ than the standard representations in (1.36) and (1.39). A more sophisticated nonlinear representation for $C_\mu$ within the present nonlocal, nonequilibrium closure framework is provided in Appendix 6.2.

In any case, it is apparent in Figure 4.8 that even with the realizable value $C_\mu = 0.05$, the results from the classical equilibrium closure in the SKE model compare very poorly with the measured values from Chen *et al.* This is due to the fact that the equilibrium closure in (1.35) assumes the turbulence anisotropy to respond instantaneously to the imposed strain. Thus, for instance, the equilibrium closure predicts zero anisotropy during the relaxation phase. By contrast, over the entire straining, relaxation, and destraining

cycle in Figure 4.8 the results from the present closure in (4.2) can be seen to agree remarkably well with the measured anisotropy values from Chen *et al.* [11]. In particular, the present closure correctly predicts a more gradual increase in anisotropy magnitude during the straining phase, as opposed to the rapid increase predicted by the standard equilibrium closure. The nonequilibrium closure then predicts a slow decay of the anisotropy magnitude during the relaxation phase, and a gradual increase to positive anisotropy during the destraining phase. The timescales associated with these dynamics show good agreement with the measurements, and the anisotropy values from the NKE model are also in good agreement with the measurements.

Moreover, the results from the NKE model seem to agree better in many respects with the experimental results than do results from the LRR model. In particular, the LRR model predicts only a very slow decay of the anisotropy during the relaxation phase, whereas the more rapid decay predicted by the NKE model is in better agreement with the measurements. This is due to the choice of $C_\Lambda$ in (3.98) for the NKE model, which is substantially less than $C_\Lambda = 2$ given by the LRR model, as noted for the decaying anisotropic case in Section 4.3. For the present case, the more rapid decay from the NKE model during the relaxation phase gives better agreement with the experimental measurements. These results for straining, relaxation, and destraining of turbulence indicate that the effective strain rate $\widetilde{S}_{ij}(t)$ in (4.1) and the associated closure in (3.97) capture much of the nonequilibrium dynamics of turbulent flows, and thereby allow most of the advantages of a Reynolds stress transport model to be obtained within the computationally simpler framework of a direct model for the Reynolds stresses.

## 4.5   Periodically-Sheared Turbulence

Tests based on time-periodic shear applied to initially-isotropic homogeneous turbulence allow an examination of the nonequilibrium frequency response of turbulent flows. Yu and Girimaji [115] provide simulation results for applied mean shear of the form

$$\overline{S}_{12}(t) = \overline{S}_{21}(t) = \begin{cases} 0 & \text{for} \quad t < 0 \\ (S/2)\sin(\omega t) & \text{for} \quad t \geq 0 \end{cases}, \tag{4.20}$$

where $S$ is the shearing amplitude, $\omega$ is the shearing frequency, and all other components of the mean strain are zero. The equilibrium closure in (1.35) with $\nu_T$ in (1.36) gives the corresponding anisotropy in the SKE model as

$$a_{12}(t) = a_{21}(t) = -C_\mu \frac{Sk}{\epsilon}\sin(\omega t). \tag{4.21}$$

From (4.20) and (4.21), the equilibrium closure thus produces anisotropy that remains in phase with the imposed mean shear, and an anisotropy response amplitude that has no direct dependence on the shearing frequency $\omega$. For sufficiently large $\omega$ however, the time

scale on which the shear varies can become much faster than the turbulence response time scale, leading to substantial nonequilibrium between the turbulence and the applied shear. This gives rise to frequency-dependent phase and amplitude that the classical equilibrium closure in (1.35) cannot accurately account for, as shown in Figure 1.5 in Chapter I.

### 4.5.1 Anisotropy Evolution

For the nonequilibrium closure, the effective strain $\widetilde{S}_{ij}(t)$ from (4.1) and (4.20) for $t \geq 0$ is

$$\widetilde{S}_{12}(t) = \frac{S}{2} \left[ \frac{1}{1 + (\omega \Lambda_m)^2} \right] \left\{ \sin(\omega t) - (\omega \Lambda_m) \left[ \cos(\omega t) - e^{-t/\Lambda_m} \right] \right\}, \qquad (4.22)$$

where $\widetilde{S}_{21}(t) = \widetilde{S}_{12}(t)$, and the nonequilibrium anisotropy from (4.2) can then be written as

$$a_{12}(t) = -\frac{C_\mu}{C_\Lambda} \left( \frac{S}{\omega} \right) \left[ \frac{\omega \Lambda_m}{1 + (\omega \Lambda_m)^2} \right] \left\{ \sin(\omega t) - (\omega \Lambda_m) \left[ \cos(\omega t) - e^{-t/\Lambda_m} \right] \right\}. \qquad (4.23)$$

By contrast to the equilibrium response in (4.21), the response in (4.23) from the nonequilibrium closure predicts that as the relative shearing frequency increases and the nondimensional parameter $(\omega \Lambda_m)$ becomes large, there will be a decrease in the anisotropy amplitude and an increase in the phase difference between the imposed shear and the anisotropy. Additionally, the nonequilibrium closure also predicts a lag in the anisotropy response, analogous to the lag seen in the impulsively-strained cases in Section 4.2, but predicts that in this case the lag depends on $(\omega \Lambda_m)$. This frequency-dependent lag, as well as the frequency-dependent phase shift and response amplitude, are all missed by classical equilibrium closures based on (1.35).

For $(Sk_0/\epsilon_0) = 3.3$ and $(\omega/S) = 0.5$, 1.0, and 10, Yu and Girimaji [115] give simulation results for the anisotropy response $a_{12}(t)$ shown by the heavy lines in Figures 4.9(a)-(c). For the same conditions, the SKE, NKE, and LRR models yield the corresponding anisotropy evolution also shown in Figures 4.9(a)-(c). Comparisons of these results with the Yu and Girimaji simulations show that the present closure in the NKE model provides an anisotropy response that agrees far more closely with the simulations than does the equilibrium closure in the SKE model. In particular, as the shearing frequency $(\omega/S)$ increases, the direct decrease in anisotropy amplitude from the nonequilibrium closure, as well as the indirect effect from changes in $k$ and $\epsilon$ with straining frequency, are in overall good agreement with the simulation results. By contrast, the equilibrium closure shows only a far weaker indirect decrease in anisotropy amplitude via the changes in $k$ and $\epsilon$ with shearing frequency.

Moreover, for $\omega/S = 0.5$ in Figure 4.9(a) the LRR model shows significantly poorer phase agreement with the DNS results at large times than does the closure in (4.23), despite giving slightly better prediction of the anisotropy amplitude at this frequency. For the two higher shearing frequencies in Figures 4.9(b) and (c), the phase and amplitude from

the LRR model are only slightly better than those from (4.23), and both models are in generally good agreement with the DNS results. The result in (4.23) thus retains the most relevant dynamics governing the evolution of the anisotropy in periodically sheared turbulence, giving predictions of the shear anisotropy in Figure 4.9 that are of nearly comparable fidelity as the more computationally intensive LRR model.

### 4.5.2 Production to Dissipation Ratio

In periodically-sheared turbulence, the phase difference between the anisotropy $a_{12}(t)$ and the imposed mean shear $\overline{S}_{12}(t)$ is of additional interest, since any phase lag between the two corresponds to negative turbulence kinetic energy production over part of each period. It is qualitatively apparent in Figure 4.9 that the phase response from the nonequilibrium closure is in good agreement with the simulation results, while that from the equilibrium closure in the SKE model is in very poor agreement, particularly at the higher shearing frequencies in Figures 4.9(b) and 4.9(c). This poor phase agreement corresponds to poor predictions of the production-to-dissipation ratio $P/\epsilon$, as shown in Figure 4.10 for shearing frequencies $\omega/S = 0.5$ and 1.0, and in Figure 4.11 for $\omega/S = 10$. The production-to-dissipation ratio $P/\epsilon$ is given generally as

$$\frac{P}{\epsilon} = -\frac{k}{\epsilon} a_{ij} \overline{S}_{ij} \,, \tag{4.24}$$

and from (4.21) and (4.20) the equilibrium closure in the SKE model gives

$$\frac{P}{\epsilon} = C_\mu \left( \frac{Sk}{\epsilon} \right)^2 \sin^2(\omega t) \,. \tag{4.25}$$

It is clear from (4.25) and Figures 4.10 and 4.11 that the SKE model predicts strictly positive $P/\epsilon$ regardless of shearing frequency, in poor agreement with DNS results from Yu and Girimaji [115] where $P/\epsilon$ takes on both positive and negative values. From (4.24) and (4.23), $P/\epsilon$ from the present closure in (4.2) is given as

$$\frac{P}{\epsilon} = \frac{C_\mu}{C_\Lambda^2} \left( \frac{S}{\omega} \right)^2 \left[ \frac{(\omega \Lambda_m)^2}{1 + (\omega \Lambda_m)^2} \right] \left\{ \sin^2(\omega t) - (\omega \Lambda_m) \sin(\omega t) \left[ \cos(\omega t) - e^{-t/\Lambda_m} \right] \right\} \,. \tag{4.26}$$

The resulting evolution of $P/\epsilon$ from (4.26) is shown for shearing frequencies $(\omega/S) = 0.5$, 1.0, and 10 in Figures 4.10 and 4.11. The evolution of $P/\epsilon$ in (4.26) can be seen to agree better with the DNS results in many respects than do the results from the LRR model, though the asymmetry at the highest frequency is not captured. For all shearing frequencies, the SKE model shows very poor amplitude agreement with DNS results and the NKE and LRR models, and in particular for $(\omega/S) = 10$ in Figure 4.11 the amplitude predicted by the SKE model is much larger than that predicted by the other models. As noted earlier, the evolution of $P/\epsilon$ is closely connected to the frequency-dependent phase shift

120

between the anisotropy and the applied shear, and in the next section the frequency response of periodically-sheared turbulence will be examined in more detail using the new nonequilibrium closure.

## 4.6  Frequency Analysis of Periodically-Sheared Turbulence

The DNS study by Yu and Girimaji [115] of initially-isotropic homogeneous turbulence subjected to periodic shear has revealed some aspects of the frequency response produced by unsteady shearing of turbulent flows. In particular, the DNS results show a frequency-dependent phase lag between the applied shear $\overline{S}_{12}(t)$ and the resulting Reynolds shear stress anisotropy $a_{12}(t)$. The DNS results have also revealed a transition from asymptotic growth in $k(t)$ at low shearing frequencies to asymptotic decay above a critical frequency $\omega_{cr} \approx 0.5S$. Somewhat similar frequency-dependent nonequilibrium features have also been observed in turbulence subjected to time-varying plane strain [11, 30].

While the computational burden of DNS necessarily limits the extent of any detailed parametric study of periodically sheared turbulence dynamics, accurate second-order RANS closures such as the LRR model could in principle allow a more extensive parametric investigation. In general, however, the correct prediction of nonequilibrium dynamics in the anisotropy and energetics of turbulence poses a significant challenge for turbulence modeling. The widely used LRR [51] and SSG [98] models, for example, were found [115] to significantly underpredict the critical shearing frequency $\omega_{cr}$ observed in the DNS study of Yu and Girimaji. Rapid distortion theory (RDT) has also been used to investigate nonequilibrium effects, such as in homogeneous turbulence subjected to rotating shear [28]. However, for periodically sheared homogeneous turbulence as in (4.20), RDT cannot be used [115] due both to the reversibility properties of the RDT equations and the invalidity of the linearized Navier-Stokes equations when the applied mean strain $\overline{S}_{ij}(t)$ is near zero.

Using the nonequilibrium solution for the anisotropy in (4.23), the DNS study of Yu and Girimaji can be substantially extended to present a relatively complete parametric analysis for the frequency response of periodically sheared homogeneous turbulence. As shown in Figures 4.9 and 4.10, the solution in (4.23) yields good agreement with DNS, and will be used in the following to predict the frequency-dependent amplitude and phase lag between the anisotropy and the applied shear over a wide range of frequencies, from the full equilibrium limit through the saturated nonequilibrium regime. It will also used to obtain an analytical result for the critical shearing frequency $\omega_{cr}$. The new nonequilibrium approach furthermore gives analytical scalings for key dynamical quantities such as the anisotropy, the production-to-dissipation ratio, and the turbulence time scale in the full equilibrium limit as well as the quasi-equilibrium and saturated nonequilibrium regimes. The simplicity of the result in (4.23), combined with its accuracy in reproducing results from DNS, thus permits a detailed parametric frequency response analysis of the periodically sheared homogeneous turbulence case.

### 4.6.1  Anisotropy Phase Response

In the long-time limit, after initial transients have sufficiently decayed and thus $e^{-t/\Lambda_m} \to 0$, the anisotropy in (4.23) can be written as

$$a_{12}(t) = -C_\mu \alpha_1 \left(\frac{S}{\omega}\right) \left[\frac{\omega \Lambda_m}{1 + (\omega \Lambda_m)^2}\right] \left[\sin(\omega t) - (\omega \Lambda_m) \cos(\omega t)\right] . \tag{4.27}$$

Defining the phase difference $\phi$ as the lag between the zero-crossing times for the anisotropy $a_{12}(t)$ and the applied shear $\overline{S}_{12}(t)$ in the long-time limit $S \cdot t \to \infty$, this phase lag can be obtained analytically from (4.27) as

$$\phi = \pi - \tan^{-1}\left[\omega \Lambda_m(t_0)\right] , \tag{4.28}$$

where $t_0$ denotes the time at which $a_{12} = 0$.

Figure 4.12 shows that the analytical result for $\phi$ in (4.28) agrees well with the DNS results of Yu and Girimaji [115] over a wide range of shearing frequencies. For small values of $\omega/S$, corresponding to the quasi-equilibrium regime, the phase difference approaches $\pi$ in the full equilibrium limit $\omega/S \to 0$, where $a_{12}(t)$ responds instantly to changes in $\overline{S}_{12}(t)$. As $\omega/S$ increases, nonequilibrium effects become significant and $\phi$ smoothly approaches $\pi/2$ as shown in Figure 4.12. For values of $\omega$ above a critical frequency $\omega_{cr}$, the dynamics reach a saturated nonequilibrium regime for which the phase difference remains at the frequency-independent value $\pi/2$. From Figure 4.12 it is apparent that $\omega_{cr}/S \approx 0.5$, although a more precise value will be obtained analytically in Section 4.6.4.

By contrast to the NKE model results in Figure 4.12, the equilibrium SKE model in (4.21) incorrectly predicts $\phi = \pi$ for all shearing frequencies. Figure 4.12 also shows that the phase response from the LRR model agrees relatively poorly with the DNS results. In particular, the LRR model significantly underpredicts the critical frequency $\omega_{cr}$, in agreement with Figure 31 of Yu and Girimaji [115], leading to poorer phase agreement with the DNS results for $\omega < \omega_{cr}$. This in turn is the origin of the slight phase errors from the LRR model for $\omega/S = 0.5$ in Figure 4.9(a). While the LRR results might be improved by changing the model constants in (1.26), for periodically sheared homogeneous turbulence Figure 4.12 shows that the standard values of these constants do not give results for the phase response at $\omega < \omega_{cr}$ that are as accurate as the anisotropy in (4.28) from the present closure.

Before continuing, it should be noted that in Figure 4.12 the transition to $\phi \equiv \pi/2$ in the saturated nonequilibrium regime for the LRR model, the NKE model, and in the DNS results is remarkably abrupt. This is indicative of a bifurcation in the turbulence dynamics at the critical frequency $\omega_{cr}$. The result in (4.28) suggests that the observed $\phi = \pi/2$ for all $\omega > \omega_{cr}$ is a result of $(\omega \Lambda_m) \to \infty$ above the critical frequency. This in turn suggests that $\Lambda_m \to \infty$ in the long-time limit $S \cdot t \to \infty$, while for $\omega < \omega_{cr}$ the associated $\Lambda_m$ remains

finite for all time. The long-time limit of $\Lambda_m$ for $\omega > \omega_{cr}$ will be explored in more detail in Section 4.6.5, and it will be shown in Section 4.6.4 that $\omega_{cr}$ has a value that is determined by the model constants in (4.23) and the $k$ and $\epsilon$ equations in (4.3) and (4.4), respectively.

### 4.6.2   Anisotropy Limit Forms

From a physical standpoint, the parameter $(\omega\Lambda_m)$ characterizes how rapidly the applied shear varies with respect to the turbulence relaxation time scale $\Lambda_m$, and is thus the appropriate nonequilibrium parameter for periodically sheared turbulence. However, $\Lambda_m$ is itself part of the turbulence response to the applied shearing, and for this reason $\omega/S$ provides an alternative nonequilibrium parameter that involves only parameters associated with the applied periodic shear. It will be seen later that the cycle average of $(\omega\Lambda_m)$ increases monotonically with $\omega/S$, and thus either can be used as a nonequilibrium parameter. In this Section we consider the characteristics of the turbulence anisotropy in the full equilibrium limit $\omega/S \to 0$ where $(\omega\Lambda_m) \to 0$, in the quasi-equilibrium regime for small $\omega/S$ where $(\omega\Lambda_m) \ll 1$, and in the saturated nonequilibrium regime where $(\omega\Lambda_m) \to \infty$ for all $\omega > \omega_{cr}$.

For $\omega/S \to 0$ and $(\omega\Lambda_m) \to 0$, the turbulence responds more rapidly than the variations in the applied shear, allowing the turbulence anisotropy to remain in full equilibrium with the mean shear. Thus the resulting anisotropy in the long-time limit from (4.27) is

$$\lim_{(\omega\Lambda_m)\to 0} a_{12}(t) = -C_\mu \frac{Sk}{\epsilon} \sin\left(\omega t\right) , \tag{4.29}$$

which is identical to the result from the classical equilibrium Boussinesq closure in (4.21), where the anisotropy is assumed to be directly proportional to the instantaneous mean strain rate. The full equilibrium result in (4.29) for the anisotropy is consistent with the phase results in Figure 4.12, where the phase difference between the anisotropy and the shear approaches $\phi = \pi$ for small $\omega/S$, and hence small $(\omega\Lambda_m)$. However, it can be seen from (4.28) in Figure 4.12 that even for shearing frequencies as small as $\omega/S = 0.01$, the turbulence is still not fully in equilibrium with the applied shear. This result establishes the existence of a quasi-equilibrium regime for small but non-zero values of $\omega/S$ corresponding to $(\omega\Lambda_m) \ll 1$, where the anisotropy is given as

$$\lim_{(\omega\Lambda_m)\ll 1} a_{12}(t) = -C_\mu \frac{Sk}{\epsilon} \left[\sin\left(\omega t\right) - (\omega\Lambda_m)\cos(\omega t)\right] . \tag{4.30}$$

The full equilibrium result in (4.29) for $(\omega\Lambda_m) \to 0$ is only obtained as $\omega/S \to 0$.

In the saturated nonequilibrium regime where $(\omega\Lambda_m) \to \infty$ the turbulence response is far slower than the rate at which the mean shear varies. In this regime, the anisotropy from (4.27) is thus

$$\lim_{(\omega\Lambda_m)\to \infty} a_{12}(t) = \frac{C_\mu}{C_\Lambda} \left(\frac{S}{\omega}\right) \cos\left(\omega t\right) . \tag{4.31}$$

123

It is apparent in (4.31) that the amplitude of the anisotropy decreases with increasing shearing frequency as $\omega^{-1}$, and that the phase difference relative to $\overline{S}_{12}(t)$ in (4.20) is constant at $\phi = \pi/2$, independent of $\Lambda_m$ or $\omega$. The abrupt switch to $\phi = \pi/2$ at $\omega = \omega_{cr}$ in Figure 4.12 suggests that (4.31) describes the anisotropy for all $\omega > \omega_{cr}$.

The root mean square (rms) amplitude of the anisotropy gives additional insights into the turbulence response in the full equilibrium limit and the saturated nonequilibrium regime, and also into the abrupt transition in the dynamics at $\omega_{cr}$. We define

$$\langle f \rangle \equiv \lim_{t \to \infty} \frac{\omega}{2\pi} \int_{t-\pi/\omega}^{t+\pi/\omega} f(t')dt' , \tag{4.32}$$

as the long-time cycle average of any time-dependent quantity $f(t)$, and note that the rms amplitude of the anisotropy, here denoted $a'_{12}$, is defined as $(a'_{12})^2 \equiv \langle a_{12}^2 \rangle - \langle a_{12} \rangle^2$. From (4.27), it is apparent that in the long-time limit $\langle a_{12} \rangle \equiv 0$ for all shearing frequencies, giving

$$\lim_{(\omega\Lambda_m) \to 0} a'_{12} = \frac{C_\mu}{C_\Lambda} S \langle \Lambda_m^2 \sin^2(\omega t) \rangle^{1/2} , \tag{4.33}$$

in the full equilibrium limit. It will be seen later that the existence of a fixed point in the dynamics of $\langle \Lambda_m \rangle$ for $\omega < \omega_{cr}$ yields the relation

$$\lim_{(\omega\Lambda_m) \to 0} \langle \Lambda_m^2 \sin^2(\omega t) \rangle = \frac{C_\Lambda^2}{C_\mu S^2} \left[ \frac{C_{\epsilon 2} - 1}{C_{\epsilon 1} - 1} \right] , \tag{4.34}$$

which allows (4.33) to be written as

$$\lim_{(\omega\Lambda_m) \to 0} a'_{12} = \left[ \frac{C_\mu (C_{\epsilon 2} - 1)}{C_{\epsilon 1} - 1} \right]^{1/2} = 0.43 , \tag{4.35}$$

where values of the constants in (1.33) and (3.98) have been used to obtain the numerical result. The corresponding form of $a'_{12}$ in the saturated nonequilibrium regime where $(\omega\Lambda_m) \to \infty$ is given by

$$\lim_{(\omega\Lambda_m) \to \infty} a'_{12} = \frac{C_\mu}{\sqrt{2}C_\Lambda} \left( \frac{S}{\omega} \right) . \tag{4.36}$$

Figure 4.13 shows the resulting frequency dependence of $a'_{12}$ obtained from the long-time limit anisotropy in (4.27), and also shows the equilibrium and nonequilibrium limit forms given by (4.35) and (4.36), respectively. For small $\omega/S$, $a'_{12}$ approaches the full equilibrium result in (4.35), but even for $\omega/S = 0.01$ it is clear that the turbulence is not fully in equilibrium with the applied shear, consistent with the phase results in Figure 4.12. For all $\omega > \omega_{cr}$, $a'_{12}$ decreases as $(\omega/S)^{-1}$ in accordance with the saturated nonequilibrium result in (4.36). As with the phase results in Figure 4.12, Figure 4.13 shows that $a'_{12}$ transitions abruptly at $\omega_{cr}$ to the nonequilibrium form in (4.36), again reflecting the fact that $(\omega\Lambda_m) \to \infty$ in the saturated nonequilibrium regime for all $\omega > \omega_{cr}$.

Figures 4.12 and 4.13 thus indicate that the full equilibrium limit of periodically sheared turbulence is attained only at very small shearing frequencies as $\omega/S \to 0$. At slightly larger frequencies, the turbulence is in a quasi-equilibrium regime where $(\omega\Lambda_m) \ll 1$. As $\omega/S$ continues to increase, but remains below $\omega_{cr}/S$, the degree of nonequilibrium increases smoothly, as indicated by the gradual approach of the phase difference $\phi$ to $\pi/2$ in Figure 4.12. At the critical frequency $\omega_{cr}$, however, the turbulence abruptly transitions to the saturated nonequilibrium regime, where the phase difference remains constant at $\pi/2$ and the anisotropy amplitude begins to decrease as $\omega^{-1}$. It can be inferred from the abrupt transition at $\omega_{cr}$ to the saturated nonequilibrium regime that $(\omega\Lambda_m) \to \infty$ in the long-time limit for all $\omega > \omega_{cr}$, and this result will be explored in more detail in Sections 4.6.4 and 4.6.5.

### 4.6.3  Production-to-Dissipation Limit Forms

In the long-time limit $S \cdot t \to \infty$, where initial transients have fully decayed, $P/\epsilon$ from (4.26) is given as

$$\frac{P}{\epsilon} = \frac{C_\mu}{2C_\Lambda^2} \left(\frac{S}{\omega}\right)^2 \left[\frac{(\omega\Lambda_m)^2}{1 + (\omega\Lambda_m)^2}\right] \left[1 - \cos\left(2\omega t\right) - (\omega\Lambda_m)\sin\left(2\omega t\right)\right]. \tag{4.37}$$

For the full equilibrium limit where $(\omega\Lambda_m) \to 0$ the production-to-dissipation ratio from (4.37) becomes

$$\lim_{(\omega\Lambda_m)\to 0} \frac{P}{\epsilon} = C_\mu \left(\frac{Sk}{\epsilon}\right)^2 \sin^2(\omega t). \tag{4.38}$$

As with the anisotropy $a_{12}(t)$ in the full equilibrium limit in (4.29), this form, valid for $\omega/S \to 0$, is identical to the result in (4.25) obtained from the equilibrium Boussinesq closure. In the quasi-equilibrium regime for small but non-zero $\omega/S$, where $(\omega\Lambda_m) \ll 1$, $P/\epsilon$ is

$$\lim_{(\omega\Lambda_m)\ll 1} \frac{P}{\epsilon} = C_\mu \left(\frac{Sk}{\epsilon}\right)^2 \left[\sin^2(\omega t) - \frac{(\omega\Lambda_m)}{2}\sin(2\omega t)\right]. \tag{4.39}$$

In the saturated nonequilibrium regime where $(\omega\Lambda_m) \to \infty$ for all $\omega > \omega_{cr}$, $P/\epsilon$ from (4.37) becomes

$$\lim_{(\omega\Lambda_m)\to\infty} \frac{P}{\epsilon} = \frac{C_\mu}{2C_\Lambda^2} \left(\frac{S}{\omega}\right)^2 \left[1 - \cos(2\omega t) - (\omega\Lambda_m)\sin\left(2\omega t\right)\right], \tag{4.40}$$

and since $(\omega\Lambda_m)$ is large in this limit, the amplitude of the $P/\epsilon$ fluctuations become correspondingly large.

While (4.38)-(4.40) provide insights into the time dynamics of $P/\epsilon$ in the full equilibrium limit and the quasi-equilibrium and saturated nonequilibrium regimes, it is the cycle average

125

value of $P/\epsilon$ that determines the asymptotic behavior of the turbulence kinetic energy $k$ and the relaxation time scale $\Lambda_m$. Applying the definition of the cycle average from (4.32) to (4.37) gives the resulting frequency response of $\langle P/\epsilon \rangle$ shown in Figure 4.14, where frequency-independent scaling is observed for $\omega < \omega_{cr}$, and power-law scaling is observed in the saturated nonequilibrium regime for $\omega > \omega_{cr}$.

The low- and high-frequency scaling of $\langle P/\epsilon \rangle$ in Figure 4.14 can be understood analytically from the long-time limit forms of $\langle P/\epsilon \rangle$ obtained from (4.37). In the full equilibrium limit $(\omega \Lambda_m) \to 0$, the cycle average of (4.37) is given as

$$\lim_{(\omega \Lambda_m) \to 0} \left\langle \frac{P}{\epsilon} \right\rangle = \frac{C_\mu S^2}{C_\Lambda^2} \left\langle \Lambda_m^2 \sin^2(\omega t) \right\rangle , \qquad (4.41)$$

where there is no explicit dependence on the shearing frequency $\omega$. While $\langle \Lambda_m^2 \sin^2(\omega t) \rangle$ appearing in (4.41) does not appear at first to permit an analytical solution, it will be seen in Section 4.6.5 that the evolution of $\langle \Lambda_m \rangle$ depends on $\langle P/\epsilon \rangle$, and that there is a stable fixed point in the dynamics of $\langle \Lambda_m \rangle$ when

$$\left\langle \frac{P}{\epsilon} \right\rangle = \frac{C_{\epsilon 2} - 1}{C_{\epsilon 1} - 1} . \qquad (4.42)$$

Equating (4.41) and (4.42) thus provides the analytical expression for $\langle \Lambda_m^2 \sin^2(\omega t) \rangle$ in (4.34), and for the standard values of the constants in (1.33), (4.42) gives the classical value

$$\left\langle \frac{P}{\epsilon} \right\rangle = 2.09 \qquad (4.43)$$

indicated by the horizontal dashed line in Figure 4.14. The agreement between the low-frequency limit of $\langle P/\epsilon \rangle$ from (4.37) in Figure 4.14 and the result in (4.43) indicates that for $\omega < \omega_{cr}$, the long-time dynamics of $\langle \Lambda_m \rangle$ correspond to the fixed point and $\langle P/\epsilon \rangle$ thus attains the frequency-independent value in (4.43). In the saturated nonequilibrium regime $\omega > \omega_{cr}$ where $(\omega \Lambda_m) \to \infty$ and $\langle \Lambda \sin(2\omega t) \rangle$ is negligible, the cycle average of $\langle P/\epsilon \rangle$ from (4.37) becomes

$$\lim_{(\omega \Lambda_m) \to \infty} \left\langle \frac{P}{\epsilon} \right\rangle = \frac{C_\mu}{2 C_\Lambda^2} \left( \frac{S}{\omega} \right)^2 , \qquad (4.44)$$

and thus $\langle P/\epsilon \rangle$ decreases with increasing frequency as $(\omega/S)^{-2}$. The result in (4.44) agrees in Figure 4.14 with the frequency response of $\langle P/\epsilon \rangle$ from (4.37) for essentially all $\omega > \omega_{cr}$.

It is the decrease in $\langle P/\epsilon \rangle$ with increasing frequency in the saturated nonequilibrium regime that is responsible for the distinctly different turbulence response for shearing frequencies above and below $\omega_{cr}$. As the shearing frequency increases past $\omega_{cr}$, the cycle average of $\langle P/\epsilon \rangle$ drops below the value required to support turbulence kinetic energy growth, resulting in kinetic energy decay for all $\omega > \omega_{cr}$. The asymptotic frequency response of the turbulence kinetic energy $k(t)$ and the relaxation time scale $\Lambda_m(t)$ is examined in more

detail in Section 4.6.5.

### 4.6.4 Analytical Result for the Critical Frequency

Due to the abrupt transition in Figure 4.14 from the fixed point dynamics for $\omega < \omega_{cr}$ to the saturated nonequilibrium dynamics for $\omega > \omega_{cr}$, the corresponding limit forms of $\langle P/\epsilon \rangle$ in (4.42) and (4.44) can be used to determine an analytical result for the critical frequency $\omega_{cr}$. Equating (4.42) and (4.44) at $\omega = \omega_{cr}$ thus gives

$$\omega_{cr} = S \left[ \frac{C_\mu (C_{\epsilon 1} - 1)}{2 C_\Lambda^2 (C_{\epsilon 2} - 1)} \right]^{1/2} . \tag{4.45}$$

For the standard values of the constants in (1.33) and $C_\Lambda$ in (3.98), the resulting critical frequency is

$$\omega_{cr} = 0.55 S , \tag{4.46}$$

which is in good agreement with the approximate empirical value $\omega_{cr} \approx 0.5 S$ reported by Yu and Girimaji [115] from their DNS results.

The fact that the critical frequency in (4.46) depends only on model constants may provide guidance in determining more appropriate values of the constants in (1.26) and (1.27) for second-order closure models in unsteadily forced turbulent flows. Values for $C_\Lambda$ in such models can vary widely, as shown in Table 3.2 where $C_\Lambda = 0.42$ in the LRR model and $C_\Lambda = 0.23$ in the SSG model. In the present approach however, $C_\Lambda$ is dictated by $\omega_{cr}$ in (4.45). For the values of $C_\mu$, $C_{\epsilon 1}$, and $C_{\epsilon 2}$ in (1.33) we *must* have $C_\Lambda = 0.26$ in order to have $\omega_{cr} \approx 0.5 S$ as observed in the DNS data. As noted in Chapter III, the choice of $C_\Lambda$ depends on the values for $C_{\epsilon 1}$ and $C_{\epsilon 2}$, and if the common alternative value $C_{\epsilon 2} = 1.83$ is used then (4.45) indicates that $C_\Lambda = 0.28$ is required to give good agreement with $\omega_{cr} \approx 0.5 S$ from the DNS.

With respect to the DNS study by Yu and Girimaji [115], Figure 4.12 shows that the critical frequency $\omega_{cr}$ is more clearly defined in the NKE model than in the DNS results, thereby allowing the precise determination of $\omega_{cr}$ in (4.46). Whereas the NKE model transitions abruptly to the saturated nonequilibrium regime at $\omega_{cr}$, the DNS results indicate a more gradual approach to this regime. The slight differences between the NKE model and DNS results near $\omega_{cr}$ are most likely due, in part, to the physical approximations used in the formulation of the NKE model. At the same time however, owing to the substantial computational demands of the DNS approach used in the Yu and Girimaji [115] study, a precise determination of the critical frequency such as that provided in (4.46) was impractical. Only a limited number of frequencies could be simulated, as evident in Figure 4.12, and - even more importantly - for $\omega \approx \omega_{cr}$ the simulations would need to have run for impractically long times to accurately discern between the extremely slow average rates of growth and decay in the otherwise oscillatory $k(t)$ as $\omega_{cr}$ is crossed. Similarly, it will

be seen in Section 4.6.5 that as $\omega_{cr}$ is crossed, $\langle \Lambda \rangle$ grows only very slowly with increasing time $t$, thus requiring simulation times much greater than $S \cdot t = 50$ in order to obtain $\langle \Lambda \rangle \to \infty$ and the corresponding asymptotic phase shift $\phi = \pi/2$ from (4.28). It is thus likely that the small differences between the NKE model and DNS results near $\omega_{cr}$ are due to a combination of effects from the physical simplifications used to derive the NKE model, as well as the practical limitations of the DNS.

### 4.6.5 Turbulence Kinetic Energy and Relaxation Time

The turbulence kinetic energy $k(t)$ is determined by (4.3) and (4.4), with $\overline{S}_{12}(t)$ from (4.20) and $a_{12}(t)$ from (4.23). Results are shown for a range of shearing frequencies $\omega/S$ in Figure 4.15. It can be seen that the kinetic energy varies with a frequency twice that of the applied shear, consistent with the frequency doubling for $P/\epsilon$ seen in (4.37). Its cycle average value $\langle k \rangle$ can be seen in Figure 4.15 to grow for frequencies below the $\omega_{cr}/S = 0.55$ critical value, and decay for higher frequencies, in agreement with the findings of Yu and Girimaji [115]. As noted in Section 4.6.3, the decay in $k(t)$ for $\omega > \omega_{cr}$ in Figure 4.15 is due to the $(\omega/S)^{-2}$ decrease in the cycle average of $P/\epsilon$ in the saturated nonequilibrium regime.

From (4.3) and (4.4), the dynamical equation for the turbulence relaxation time scale $\Lambda_m(t)$ is

$$\frac{d\Lambda_m}{dt} = C_\Lambda \left(1 - C_{\epsilon 1}\right) \frac{P}{\epsilon} + C_\Lambda \left(C_{\epsilon 2} - 1\right) . \tag{4.47}$$

Figure 4.16 shows the evolution of $\Lambda_m(t)$ for various shearing frequencies, where the transition in the dynamics is apparent as the frequency increases past $\omega_{cr}$. The cycle average value $\langle \Lambda_m \rangle$ grows without bound for $\omega > \omega_{cr}$, while for $\omega < \omega_{cr}$ the resulting $\Lambda_m(t)$ oscillates around a mean that remains constant after the initial transient has decayed.

As with the production-to-dissipation ratio in the previous section, the cycle average $\langle \Lambda_m \rangle$ reveals the transition in the dynamics as $\omega$ increases above the critical value $\omega_{cr}$. From the equation for $\Lambda_m$ in (4.47), the corresponding equation for $\langle \Lambda_m \rangle$ is

$$\frac{d\langle \Lambda_m \rangle}{dt} = C_\Lambda \left(1 - C_{\epsilon 1}\right) \left\langle \frac{P}{\epsilon} \right\rangle + C_\Lambda \left(C_{\epsilon 2} - 1\right) . \tag{4.48}$$

The frequency response of $d\langle \Lambda_m \rangle/dt$ from (4.48) is shown in Figure 4.17, where $d\langle \Lambda_m \rangle/dt = 0$ for $\omega < \omega_{cr}$, and there is a clear power-law increase in $d\langle \Lambda_m \rangle/dt$ in the saturated nonequilibrium regime for $\omega > \omega_{cr}$.

The evolution of $\langle \Lambda_m \rangle$ from (4.48) can be understood analytically for all $\omega$ from the corresponding forms of $\langle P/\epsilon \rangle$ in (4.42) and (4.44). For $\omega < \omega_{cr}$ there is clearly a stable fixed point in the dynamics of $\langle \Lambda_m \rangle$, as indicated by the fluctuations of $\Lambda_m(t)$ about a steady mean value for $\omega/S = 0.125$ and $\omega/S = 0.25$ in Figure 4.16, and by the fact that $d\langle \Lambda_m \rangle/dt = 0$ for $\omega < \omega_{cr}$ in Figure 4.17. In Section 4.6.3, the existence of this fixed point

was used to obtain the value of $\langle P/\epsilon \rangle$ in (4.42). With this, the right hand side of (4.48) is thus zero, giving $\langle \Lambda_m \rangle$ as a time-independent value that depends on $\omega$ and $S$. Figure 4.18(a) shows $\langle \Lambda_m \rangle$ as a function of $\omega/S$, where $\langle \Lambda_m \rangle$ generally decreases with increasing $\omega/S$ for $\omega \ll \omega_{cr}$.

In the saturated nonequilibrium regime $\omega > \omega_{cr}$, $\langle P/\epsilon \rangle$ depends on $\omega/S$ as in (4.44), and thus the resulting dynamical equation for $\langle \Lambda_m \rangle$ is

$$\lim_{(\omega \Lambda_m) \to \infty} \frac{d\langle \Lambda_m \rangle}{dt} = (1 - C_{\epsilon 1}) \frac{C_\mu}{2C_\Lambda} \left( \frac{S}{\omega} \right)^2 + C_\Lambda \left( C_{\epsilon 2} - 1 \right) . \tag{4.49}$$

This form of $d\langle \Lambda_m \rangle/dt$ is seen to agree well with the result from (4.48) in Figure 4.17 for $\omega > \omega_{cr}$, and since none of the quantities on the right-hand side vary with time, in the saturated nonequilibrium regime the cycle average $\langle \Lambda_m \rangle$ increases linearly with $t$. This thus gives $\langle \Lambda_m \rangle \to \infty$ as $S \cdot t \to \infty$ in the saturated nonequilibrium regime for all $\omega > \omega_{cr}$, as shown in Figure 4.18(a).

Finally, Figure 4.16(b) shows the relationship between $\langle \omega \Lambda_m \rangle$ and $\omega/S$. The former is the proper nonequilibrium parameter, since it compares the shearing frequency with the turbulence relaxation time, but is not known *a priori* from the specified forcing parameters $\omega$ and $S$ for any given case. In contrast, $\omega/S$ can be determined directly from these parameters, and also provides an indirect indication of the degree of nonequilibrium. Figure 4.16 verifies that these two nonequilibrium parameters depend monotonically on one another, and thus either can be used to identify the extent of nonequilibrium in periodically sheared homogeneous turbulence. Consistent with the linear increase in $\langle \Lambda_m \rangle$ with time from (4.49), Figure 4.16(b) shows that $\langle \omega \Lambda_m \rangle \to \infty$ in the saturated nonequilibrium regime for all $\omega > \omega_{cr}$.

## 4.7 Shock-Turbulence Interaction

A final test case deals with homogeneous initially-isotropic turbulence passing through a shock wave – a highly nonequilibrium process that is known [94] to be very poorly predicted by equilibrium models. The interaction is typically represented as steady and one-dimensional, and following Sinha *et al.* [94] the dissipation $\epsilon$ is taken to have a negligible effect on the evolution of $k$ and $\epsilon$ across the shock. The resulting $k$ transport equation is therefore dominated by kinetic energy production, and thus in a Lagrangian frame becomes

$$\frac{dk}{dt} = -\overline{u'u'} \, \overline{S}_{11} . \tag{4.50}$$

The straining imposed as the turbulence passes through the normal shock can be represented by a top-hat function in terms of the pre- and post-shock speeds $\bar{u}_1$ and $\bar{u}_2$ and the shock width $\Delta$ as

$$\overline{S}_{11} = \lim_{\Delta \to 0} \frac{\bar{u}_2 - \bar{u}_1}{\Delta} , \tag{4.51}$$

where the straining begins at time $t_1$ and ends at $t_2 \to t_1$ as $\Delta \to 0$. For all other times $\overline{S}_{11} \equiv 0$. The effective strain rate for $t_1 \leq t \leq t_2$ is thus obtained using (4.1) as

$$\widetilde{S}_{11}(t) = \lim_{\Delta \to 0} \left( \frac{\overline{u}_2 - \overline{u}_1}{\Delta} \right) \left[ 1 - e^{-(t-t_1)/\Lambda_m} \right] . \tag{4.52}$$

With the general form of the anisotropy closure in (3.97) for a compressible flow, given as

$$a_{ij} = -2 \frac{\nu_T}{k} \left( \widetilde{S}_{ij} - \frac{1}{3} \widetilde{S}_{ll} \delta_{ij} \right) , \tag{4.53}$$

expansion of the exponential contribution to the effective strain rate in (4.52) in a Taylor series then allows (4.50) to be written as

$$\frac{1}{k} \frac{dk}{dt} = -\frac{2}{3} \left( \frac{\overline{u}_2 - \overline{u}_1}{\Delta} \right) + \frac{4}{3} \frac{C_\mu}{C_\Lambda} \left( \frac{\overline{u}_2 - \overline{u}_1}{\Delta} \right)^2 (t - t_1), \tag{4.54}$$

where $(t - t_1)/\Lambda_m \to 0$ within the shock removes higher-order terms in the Taylor expansion. Integrating with respect to $t$ and defining $\Delta \equiv U_s(t_2 - t_1)$, where $U_s \equiv \frac{1}{2}(\overline{u}_2 + \overline{u}_1)$ is the characteristic speed through the shock, the turbulence kinetic energy amplification from (4.54) then is

$$\frac{k_2}{k_1} = \exp \left[ -\frac{4}{3} \left( \frac{1 - \overline{u}_1/\overline{u}_2}{1 + \overline{u}_1/\overline{u}_2} \right) + \frac{8}{3} \frac{C_\mu}{C_\Lambda} \left( \frac{1 - \overline{u}_1/\overline{u}_2}{1 + \overline{u}_1/\overline{u}_2} \right)^2 \right] . \tag{4.55}$$

As shown in Figure 4.19, results from the present closure in (4.55) show closer agreement with the DNS data [56, 60] than do either the standard (SKE) or realizable (RKE) $k$-$\epsilon$ models. In particular, for small upstream Mach numbers Figure 4.19 shows that the present closure predicts significantly lower kinetic energy amplification across the shock than the SKE model. Moreover, Figure 4.19 indicates that the nonequilibrium closure in the NKE model better predicts the kinetic energy amplification $k_2/k_1$ across the shock at all Mach numbers than does the equilibrium closure in either the SKE and RKE models. For large values of the incoming Mach number $M_1$, *ad hoc* treatments specific to this problem that provide further reductions in the kinetic energy amplification, as in Sinha *et al.* [94], can be used to obtain even better agreement with the DNS data.

## 4.8   Accuracy of Time-Local Nonequilibrium Closure

Existing codes for solving (1.2)-(1.4) typically only store flow variables at the current time step, or at most one or two time steps in the past. While it may be possible to develop an entirely new computational approach that is specifically designed to handle the mean pathline convolution form of $\widetilde{S}_{ij}$ in (3.96), which requires knowledge of the past straining history of the flow, implementation of the present closure in standard codes requires the

time-local formulation for $\widetilde{S}_{ij}$ in (3.123), which is written for homogeneous flows as

$$\widetilde{S}_{ij}(t) = \overline{S}_{ij}(t) + \sum_{m=1}^{M} \frac{B^{(m)}}{B^{(0)}} (-\Lambda_m)^m \left. \frac{D^m \overline{S}_{ij}}{Dt^m} \right|_t , \qquad (4.56)$$

where the $B^{(m)}$ are defined in (3.121) with $\Gamma$ determined by the order of the expansion $M$ and the degree of variation in $\overline{S}_{ij}$. The representation in (4.56) is equivalent to the homogeneous convolution form for $\widetilde{S}_{ij}$ in (4.1) when $M \to \infty$ and $\Gamma \to -\infty$.

In order to avoid issues of numerical stability and computational complexity as an increasing number of terms are retained in (4.56) – as discussed in Section 3.5 – it is of interest to consider how truncations of (4.56) affect the agreement with results from the full convolution effective strain in (4.1). This analysis can be carried out through consideration of initially isotropic periodically-sheared homogeneous turbulence [115] with the shear given by (4.20), and turbulence that is subjected to a Gaussian strain, as in the straining phase in Figure 4.7 for the straining-relaxation-destraining case [11] in Section 4.4. These tests provide insights into the accuracy of (4.56) over a range of nonequilibrium flow conditions characterized by the magnitude of the shearing frequency $\omega/S$ in the periodic shear case, and the duration of the straining in the Gaussian case (as determined by the width of the Gaussian). Moreover, both these cases allow an analytical evaluation of the convergence of (4.56) to the convolution form in (4.1) as an increasing number of terms are retained in the expansion. For problems where the straining history is inherently non-differentiable, for instance the impulsive strain cases in Section 4.2, the time-local formulation for $\widetilde{S}_{ij}$ from (4.56) cannot be used to obtain reliable predictions of the anisotropy near the points of non-differentiability.

### 4.8.1 Periodically-Sheared Turbulence

From the convolution form of the present closure in (4.1) and (4.2), the shear anisotropy $a_{12}$ for the periodic shear in (4.20) is given in (4.23). Considering the time-local formulation of the anisotropy from (4.2) and (4.56) for the shearing in (4.20) we obtain

$$a_{12}(t) = -\frac{\nu_T}{k} S \left\{ 1 - (\omega \Lambda_m)^2 + (\omega \Lambda_m)^4 + \cdots \right\} [\sin(\omega t) - \omega \Lambda_m \cos(\omega t)] , \qquad (4.57)$$

where we have set $M \to \infty$ with $\Gamma \to -\infty$, and hence $B^{(m)} = 1$. The series in braces on the right-hand side of (4.57) is the Taylor expansion of the frequency-dependent amplitude $\left[1 + (\omega \Lambda_m)^2\right]^{-1}$ in (4.23). The frequency-dependent phase shift in (4.23) is thus almost entirely accounted for in (4.57) by the $[\omega \Lambda_m \cos(\omega t)]$ term, which appears for $M \geq 1$ with $M = \text{odd}$, and inclusion of higher-order terms serves primarily to yield better amplitude agreement with (4.23) via the expansion for $\left[1 + (\omega \Lambda_m)^2\right]^{-1}$. As a result, we may expect low order truncations of (4.56) to give reasonable predictions of the anisotropy for flows with moderately strong nonequilibrium effects, which are parameterized for the periodic

131

shear case by the magnitude of $\omega/S$.

The accuracy of truncations of (4.57) can be assessed by integrating the $k$ and $\epsilon$ equations in (4.3) and (4.4), with $\nu_T$ given by (1.36). The anisotropy $a_{12}$ is obtained from (3.97) using (4.56), where here we consider the $M = 1$ and $M = 3$ truncated forms for $a_{12}$, namely

$$a_{12}(t) = -\frac{\nu_T}{k} S \left[ \sin(\omega t) - \frac{B^{(1)}}{B^{(0)}} (\omega \Lambda_m) \cos(\omega t) \right] \tag{4.58}$$

for $M = 1$ and

$$a_{12}(t) = -\frac{\nu_T}{k} S \left\{ \left[ 1 - \frac{B^{(2)}}{B^{(0)}} (\omega \Lambda)^2 \right] \sin(\omega t) - \left[ \frac{B^{(1)}}{B^{(0)}} - \frac{B^{(3)}}{B^{(0)}} (\omega \Lambda)^2 \right] (\omega \Lambda_m) \cos(\omega t) \right\} \tag{4.59}$$

for $M = 3$, where the $B^{(m)}$ coefficients are defined in (3.121). Note that we do not consider the $M = 2$ expansion, since only odd order expansions of the effective strain in (4.56) yield the correct phase term $[(\omega \Lambda_m) \cos \omega t]$ in (4.57)-(4.59) for periodically-sheared turbulence.

Figure 4.20 shows for shearing frequencies $\omega/S = 0.125$, $\omega/S = 0.25$, and $\omega/S = 0.5$ that the anisotropy evolution predicted by (4.58) and (4.59) is generally in good agreement with the full convolution form for $a_{12}$ from (4.23). For the two lower shearing frequency cases in Figures 4.20(a) and (b), the relatively small $\omega/S$ allows the use of $\Gamma \to -\infty$, where $B^{(m)} = 1$ for all $m$. While both the $M = 1$ and $M = 3$ forms for $a_{12}$ in (4.58) and (4.59), respectively, closely agree with the full convolution form in (4.23) for these lower shearing frequencies, Figure 4.20(b) does show that the form in (4.59) is in slightly better agreement with (4.23) as a result of retaining terms up to $M = 3$ in the expansion.

For the higher shearing frequency case in Figure 4.20(c), the truncations of (4.56) used to obtain (4.58) and (4.59) lead to integration errors when calculating the temporal evolution of $a_{12}$ using $\Gamma \to -\infty$. In particular, the $M = 3$ form in (4.59) could not be stably integrated beyond $S \cdot t \approx 10$, and consequently results from (4.59) are not shown in Figure 4.20(c). Even the $M = 1$ form in (4.58) begins to show amplitude disagreements with the full convolution form in (4.23) for the higher shearing frequency in Figure 4.20(c), although the phase response of the anisotropy is still predicted relatively accurately.

As discussed in Section 3.5, these truncation errors can be avoided by using a finite value for $\Gamma$, resulting in values of the $B^{(m)}$ coefficients that are less than 1. Figure 4.21 shows predictions for $a_{12}$ from (4.58) and (4.59) using $(t - \Gamma)/\Lambda_m = 1.7$ for $\omega/S = 0.5$. It is clear that results from the truncated forms are in relatively good agreement with results from the convolution form in (4.23), and that the higher-order $M = 3$ expansion in (4.59) is in better agreement with (4.23) than the $M = 1$ expansion in (4.58). In general, as the shearing frequency $\omega/S$ is increased the value of $(t - \Gamma)/\Lambda_m$ must be decreased to avoid errors due to the truncation of (4.56).

With respect to the phase difference between $a_{12}$ and $\overline{S}_{12}$ considered in Figure 4.12,

Figure 4.22 shows that for $\Gamma \to -\infty$, where $B^{(m)} = 1$ for all $m$, both (4.58) and (4.59) reproduce the phase difference predicted by the full nonequilibrium model in (4.23) up to $\omega/S \approx 0.25$. The $M = 1$ model in (4.58) further predicts the same qualitative approach to $\phi = \pi/2$ for large $\omega/S$ seen in the DNS and full convolution results, although agreement in the intermediate frequency range is somewhat poor. Despite this disagreement however, the truncated forms are still in much better agreement with DNS results [115] than the equilibrium expression for $a_{12}$ in (4.21) over all shearing frequencies. While the $M = 3$ truncation of $a_{12}$ more closely matches the full convolution result for the available shearing frequencies, it is clear from (4.22) that the bulk of the phase response is correctly captured even by the lowest-order $M = 1$ truncation in (4.58). Note that integration of the $M = 3$ closure is stopped at $\omega/S = 0.25$ due to truncation errors introduced by the use of $\Gamma \to -\infty$, as discussed with respect to Figures 4.20(c) and 4.21.

Taken together, Figures 4.20-4.22 show that there is greater disagreement between the truncated and convolution results for higher relative shearing frequencies $\omega/S$, corresponding to stronger nonequilibrium in the flow. The relatively poorer agreement as the shearing frequency increases is due in large part to the neglect of the higher-order amplitude terms in obtaining (4.58) and (4.59) from (4.57), as well as errors due to the truncation of the expansion for $\widetilde{S}_{ij}$ in (4.56). This indicates that as the degree of nonequilibrium increases (as characterized by $\omega/S$ or $\omega\Lambda_m$ in periodically sheared turbulence), a greater number of terms in the time-local expansion in (4.56) must be retained to yield good agreement with the convolution form in (4.1). Nevertheless, Figures 4.20-4.22 do indicate that even the $M = 1$ truncated closure in (4.58) is sufficient to obtain significantly higher-fidelity results for periodically-sheared turbulence than the classical equilibrium closure in (1.35). This suggests that a truncated $M = 1$ form of the anisotropy closure in (4.56), where numerical difficulties are not expected to be prohibitive, is sufficient to give good results for practical nonequilibrium turbulent flow problems.

It should be noted before continuing that retention of terms up to $M = 3$ in (4.56) may give additional large improvements for strongly nonequilibrium test cases. While this higher level of closure may introduce additional numerical difficulties in computational implementations of the closure, the computational resources and complexity required to simulate practical flow problems using (3.97) with the $M = 3$ form of (4.56) are still expected to be substantially less than for full Reynolds stress transport closures such as the LRR model. Regardless of the order of expansion used for the effective strain rate however, it is important for practical implementation of the closure to limit the resulting nonequilibrium correction terms using the $B^{(m)}$ coefficients with finite $\Gamma$ in order to prevent errors for large degrees of nonequilibrium due to truncations of the time-local expansion in (4.56).

### 4.8.2 Gaussian-Strained Turbulence

For the straining-relaxation-destraining case examined experimentally by Chen *et al.* [11], Figure 4.8 shows that the full convolution results for the anisotropy from the NKE closure are in good agreement with experimental results, where the applied strain is approximated by the piecewise-linear profile in Figure 4.7. However, the "straining" phase of the straining cycle can also be represented by the Gaussian form

$$\overline{S}_{11}(t) = S_{max} \exp\left[-\frac{(t-t_0)^2}{\sigma_s^2}\right] \quad \text{for} \quad t \geq 0 \,, \tag{4.60}$$

where $\overline{S}_{11}(t) = 0$ for $t < 0$. In (4.60), $S_{max}$ is the amplitude of the applied strain, $t_0$ is the location of the maximum applied strain, and $\sigma_s$ is a measure of the duration of the straining. As with the periodically-sheared case, the Gaussian strain in (4.60) readily allows calculation of the higher-order strain derivatives in (4.56), and thus provides an ideal case for assessing the convergence of truncated time-local forms of (4.56) to the exact convolution result for $\widetilde{S}_{ij}$.

Using (4.60) in the convolution form for $\widetilde{S}_{ij}$ in (4.1), the anisotropy $a_{11}$ is given from the present closure in (4.2) as

$$a_{11}(t) = S_{max} \frac{\sigma_s \sqrt{\pi}}{2\Lambda_m} \exp\left[\frac{\sigma_s^2 + 4\Lambda_m(t_0 - t)}{4\Lambda_m^2}\right] \tag{4.61}$$

$$\times \left[\text{erf}\left(\frac{\sigma_s^2 + 2\Lambda_m t_0}{2\Lambda_m \sigma_s}\right) - \text{erf}\left(\frac{\sigma_s^2 + 2\Lambda_m(t_0 - t)}{2\Lambda_m \sigma_s}\right)\right] \,.$$

In order to use the time-local representation for $\widetilde{S}_{ij}$ in (4.56) for this case, several higher-order derivatives of $\overline{S}_{11}$ from (4.60) must be calculated. These are given up to $m = 3$ for $t \geq 0$ by

$$\frac{D\overline{S}_{11}}{Dt} = \frac{d\overline{S}_{11}}{dt} = -S_{max} \frac{2}{\sigma_s^2}(t - t_0) \exp\left[-\frac{(t-t_0)^2}{\sigma_s^2}\right] \,, \tag{4.62}$$

$$\frac{D^2\overline{S}_{11}}{Dt^2} = \frac{d^2\overline{S}_{11}}{dt^2} = S_{max}\left[\frac{4(t-t_0)^2}{\sigma_s^4} - \frac{2}{\sigma_s^2}\right]\exp\left[-\frac{(t-t_0)^2}{\sigma_s^2}\right] \,, \tag{4.63}$$

$$\frac{D^3\overline{S}_{11}}{Dt^3} = \frac{d^3\overline{S}_{11}}{dt^3} = S_{max}\left[\frac{12(t-t_0)}{\sigma_s^4} - \frac{8(t-t_0)^3}{\sigma_s^6}\right]\exp\left[-\frac{(t-t_0)^2}{\sigma_s^2}\right] \,, \tag{4.64}$$

and the corresponding time-local truncated anisotropy closures are given from (4.56) and (4.2) for $M = 1, 2, 3$ as

$$a_{11}^{(1)} = -2C_\mu \frac{k}{\epsilon}\left[\overline{S}_{11} - \frac{B^{(1)}}{B^{(0)}}\Lambda_m \frac{D\overline{S}_{11}}{Dt}\right] \,, \tag{4.65}$$

$$a_{11}^{(2)} = -2C_\mu \frac{k}{\epsilon} \left[ \overline{S}_{11} - \frac{B^{(1)}}{B^{(0)}} \Lambda_m \frac{D\overline{S}_{11}}{Dt} + \frac{B^{(2)}}{B^{(0)}} \Lambda_m^2 \frac{D^2\overline{S}_{11}}{Dt^2} \right], \tag{4.66}$$

$$a_{11}^{(3)} = -2C_\mu \frac{k}{\epsilon} \left[ \overline{S}_{11} - \frac{B^{(1)}}{B^{(0)}} \Lambda_m \frac{D\overline{S}_{11}}{Dt} + \frac{B^{(2)}}{B^{(0)}} \Lambda_m^2 \frac{D^2\overline{S}_{11}}{Dt^2} - \frac{B^{(3)}}{B^{(0)}} \Lambda_m^3 \frac{D^3\overline{S}_{11}}{Dt^3} \right]. \tag{4.67}$$

The $B^{(m)}$ coefficients are defined in (3.121) and require a formulation for the parameter $(t - \Gamma)/\Lambda_m$. As noted in Section 4.8.1, the value of this parameter generally decreases as the degree of nonequilibrium in the flow (in this case determined by $\sigma_s$) increases. At the same time however, larger values of $(t-\Gamma)/\Lambda_m$ are permitted as the order of the truncation of the effective strain in (4.56) increases. For the following tests of the time-local closures in (4.65)-(4.67), the dependence of $(t - \Gamma)/\Lambda_m$ on both the degree of nonequilibrium and the truncation order $M$ will be accounted for by increasing $(t - \Gamma)/\Lambda_m$ – which is taken to be independent of $t$ in the following – as $M$ and the parameter $\sigma_s$ increase.

For the large and rapid straining in the Chen *et al.* [11] experiment, where $\sigma_s\epsilon_0/k_0 \approx 0.09$ gives good agreement between (4.60) and the applied strain during the "straining" phase in Figure 4.7, it can be anticipated that a large number of terms in the time-local effective strain will be necessary to obtain good agreement with the full convolution result. Consequently, here we will follow a similar approach to that employed in the periodically-sheared case and consider the convergence of the time-local forms in (4.65)-(4.67) to (4.61) for more realistic degrees of nonequilibrium. Results for $a_{11}$ are shown in Figure 4.23 for the Gaussian applied strain in (4.60) with $\sigma_s\epsilon_0/k_0 = [1.0, 0.7, 0.4]$, where $S_{max}k_0/\epsilon_0 = 9.5$ for each case. The degree of nonequilibrium increases as the width of the applied Gaussian strain decreases, and as a result $\sigma_s\epsilon_0/k_0 = 0.4$ corresponds to the strongest degree of nonequilibrium for the three cases shown in Figure 4.23.

For $\sigma_s\epsilon_0/k_0 = 1.0$ in Figure 4.23(a), Figure 4.23(b) shows that the evolutions of $a_{11}$ predicted by the time-local closures in (4.65)-(4.67) are all in relatively good agreement with the exact convolution result, particularly for small times when the magnitude of the straining is increasing. This is in contrast to results from the SKE closure, which over-predicts the magnitude of the anisotropy as the strain increases, and under-predicts the decaying anisotropy magnitude as the strain is removed. Similarly good agreement between the time-local and full convolution results is seen in Figure 4.23(d) for the $\sigma_s\epsilon_0/k_0 = 0.7$ Gaussian strain in Figure 4.23(c). Once again, results from the time-local closures more closely follow the full convolution results, particularly as the strain increases for small times, whereas the SKE model over-predicts the peak anisotropy magnitude as well as the rate at which the anisotropy decays as the strain decreases. For both the Gaussian strain cases in Figures 4.23(b) and (d), it is clear that the $M = 3$ truncated closure in (4.67) generally shows the best agreement with the full convolution results, although even the lowest-order $M = 1$ closure provides significantly improved predictions of the anisotropy compared to the local equilibrium closure in the SKE model. Note also that the values of $(t - \Gamma)/\Lambda_m$

used in the truncated closures in Figures 4.23(b) and (d) are consistent with the value used for the $\omega/S = 0.5$ periodically-sheared case shown in Figure 4.21.

For the most rapidly strained case in Figure 4.23(e), where $\sigma_s \epsilon_0 / k_0 = 0.4$, Figure 4.23(f) shows that the truncated time-local closures are in somewhat poorer agreement with the full convolution closure than for the cases in Figures 4.23(a)-(d). Due to the relatively high degree of nonequilibrium in this case, the convergence of the time-local anisotropy formulations in (4.65)-(4.67) to the full convolution result is relatively slow with increasing $M$. Moreover, relatively small values of $(t - \Gamma)/\Lambda_m$ are required to avoid truncation errors. Nevertheless, Figure 4.23(f) does show that predictions from the time-local closures are still in better agreement with the full convolution NKE model results than results from the SKE model, and it is clear that the agreement improves as the truncation order $M$ increases. In particular, the peak anisotropy magnitude is seen to decrease as the truncation order $M$ increases, and the decay of the anisotropy as the strain is removed becomes less rapid.

Taken together, the results for the periodic-shear and Gaussian-strain cases show that for many practical flows where the degree of nonequilibrium is relatively moderate, low-order truncations of the time-local effective strain from (4.56) give good agreement with the full convolution formulation for $\widetilde{S}_{ij}$ in (4.1). As the degree of nonequilibrium increases however, an increasing number of time-local terms are required to give good agreement with predictions from the convolution form. Moreover, since the parameter $(t - \Gamma)/\Lambda_m$ must be decreased in order to avoid truncation errors for large degrees of nonequilibrium, resulting in reduced values of the $B^{(m)}$ coefficients, the convergence to the full convolution form can become relatively slow. This is evident, for example, from the convergence of (4.65)-(4.67) to (4.61) for the relatively strong nonequilibrium case in Figures 4.23(e) and (f). Nevertheless, the periodic-shear and Gaussian-strain time-local tests indicate that for the relatively moderate degree of nonequilibrium found in many practical problems, low-order truncations of (4.56) – where computational issues are not expected to be prohibitive – are sufficient to give significantly improved predictions of the anisotropy when compared to results from the local equilibrium closure in (1.35).
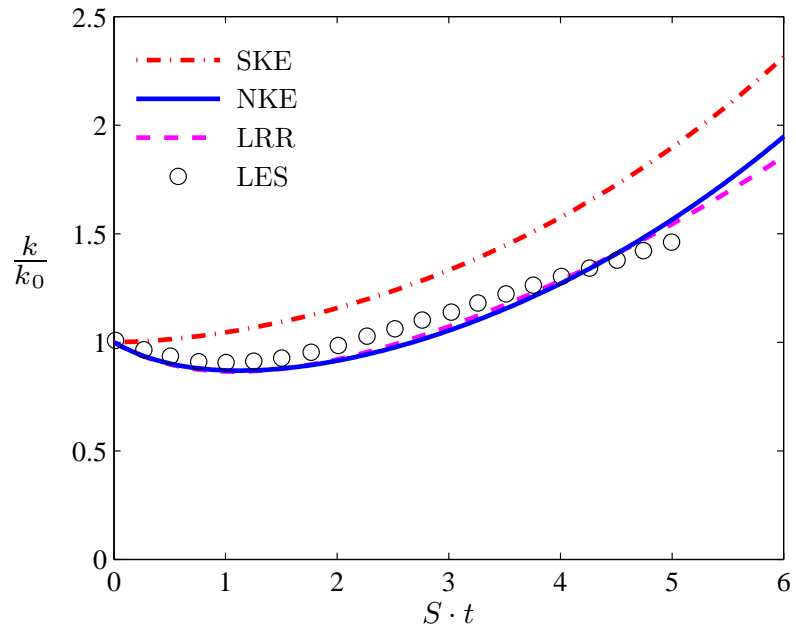
Figure 4.1: Turbulence kinetic energy $k(t)/k_0$ for initially-isotropic impulsively-sheared homogeneous turbulence in (4.9), where $Sk_0/\epsilon_0 = 3.4$. NKE model results are compared with results from the SKE and LRR [51] models, and the LES of Bardina *et al.* [3].
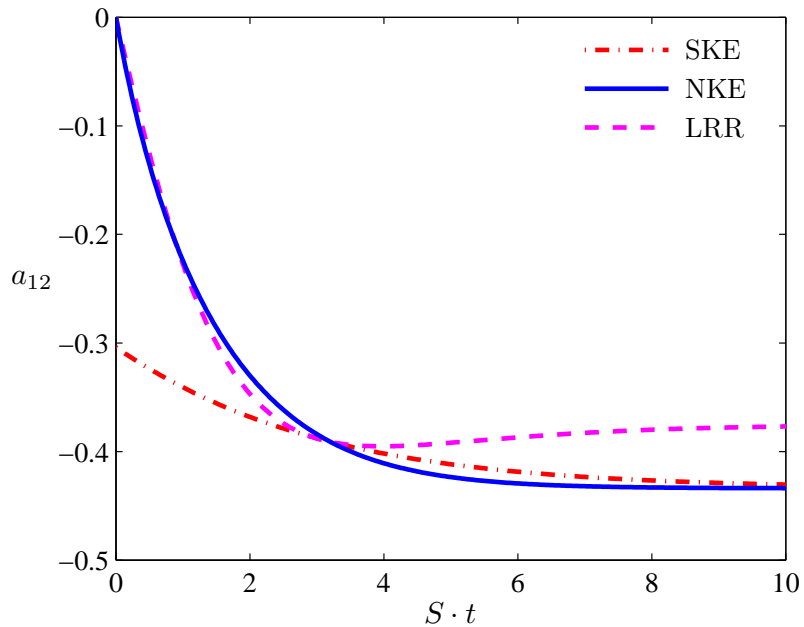


Figure 4.2: Anisotropy $a_{12}$ for initially-isotropic impulsively-sheared homogeneous turbulence in (4.9), where $Sk_0/\epsilon_0 = 3.4$. NKE model results are compared with results from the SKE and LRR [51] models, and the LES of Bardina *et al.* [3].
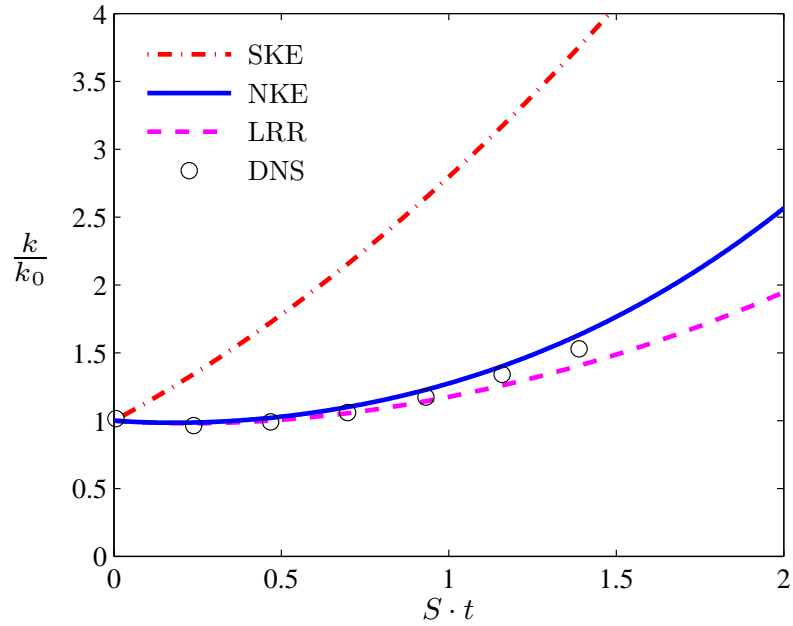
Figure 4.3: Turbulence kinetic energy $k(t)/k_0$ for initially-isotropic axisymmetrically-contracted homogeneous turbulence in (4.10), where $Sk_0/\epsilon_0 = 5.54$. NKE model results are compared with results from the SKE and LRR [51] models, and the DNS of Lee and Reynolds [55].
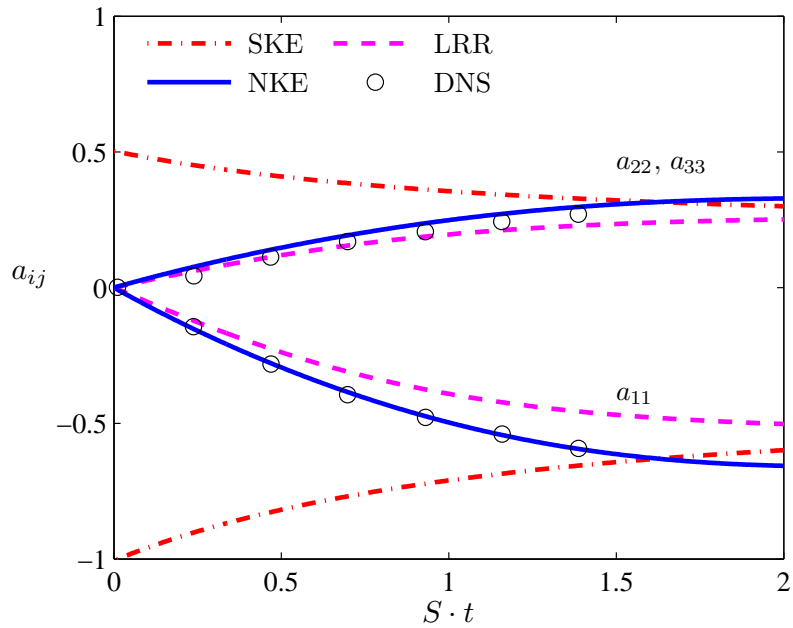


Figure 4.4: Anisotropy $a_{ij}$ for initially-isotropic axisymmetrically-contracted homogeneous turbulence in (4.10), where $Sk_0/\epsilon_0 = 5.54$. NKE model results are compared with results from the SKE and LRR [51] models, and the DNS of Lee and Reynolds [55].
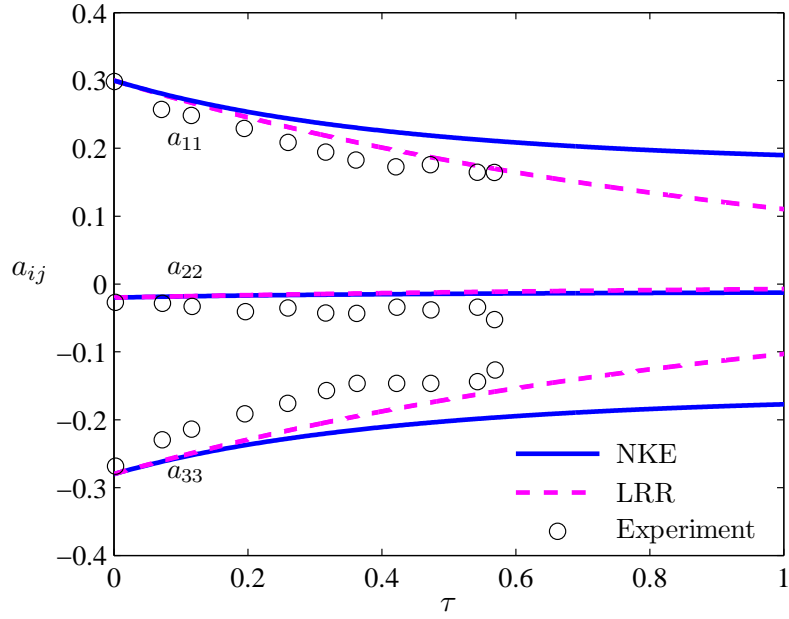
Figure 4.5: Decay of the anisotropy $a_{ij}$ in the plane strain experiment of Choi and Lumley [13]. NKE model results (using $C_\Lambda = 2$) are compared with experimental results [13] and results from the LRR [51] model.
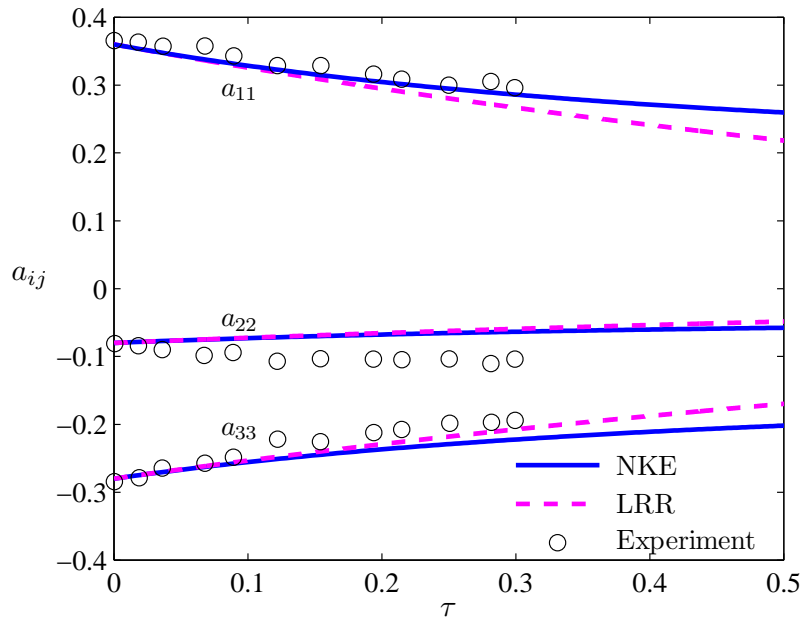


Figure 4.6: Decay of the anisotropy $a_{ij}$ in the plane contraction experiment of Le Penven *et al.* [75]. NKE model results (using $C_\Lambda = 2$) are compared with experimental results [75] and results from the LRR [51] model.
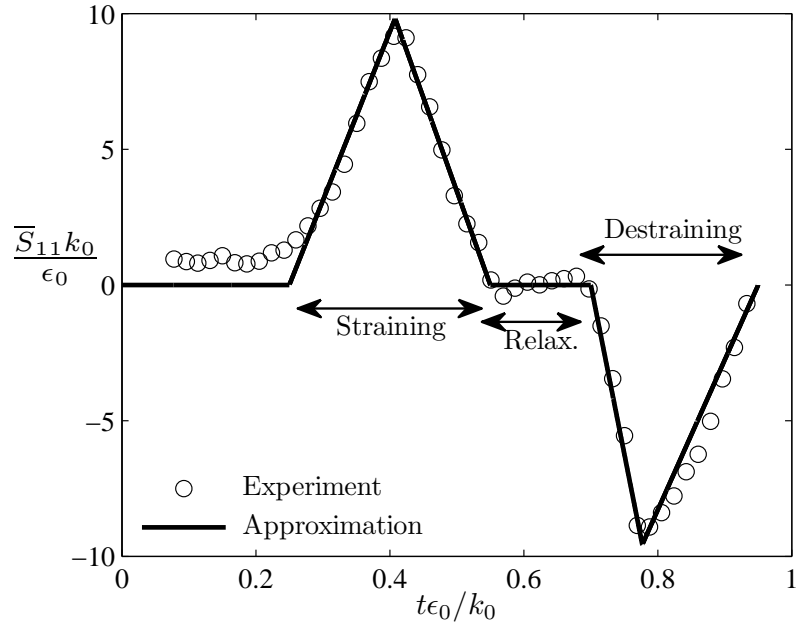
Figure 4.7: Imposed mean strain rate $\overline{S}_{11}(t)$ in strained, relaxed, and destrained turbulence experiment of Chen, Meneveau and Katz [11], with piecewise linear approximation used to permit analytical evaluation of equivalent strain rate $\widetilde{S}_{11}(t)$ via (4.1).
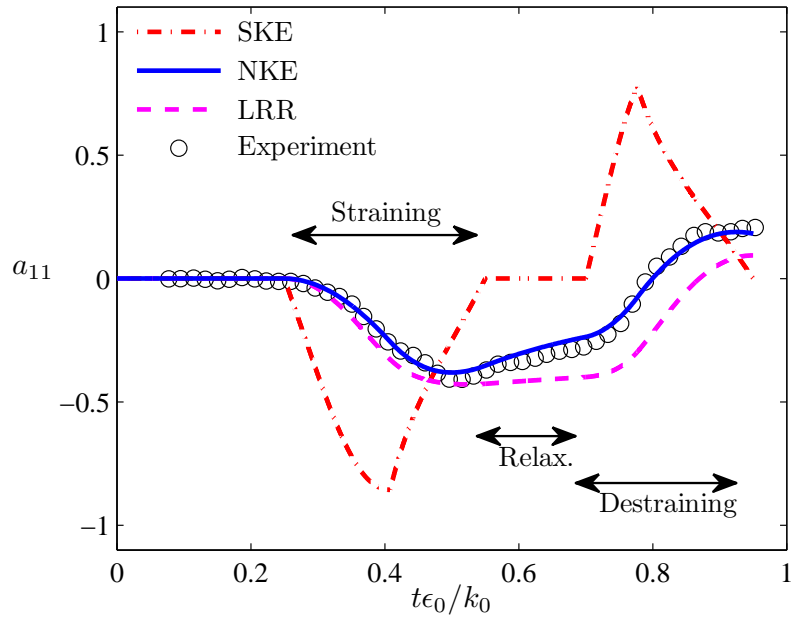


Figure 4.8: Anisotropy $a_{11}(t)$ in strained, relaxed, and destrained turbulence in Figure 4.7, showing comparisons of measured values from Chen *et al.* [11] with results from present closure in NKE model, from classical equilibrium closure in SKE model, and from the LRR model [51].
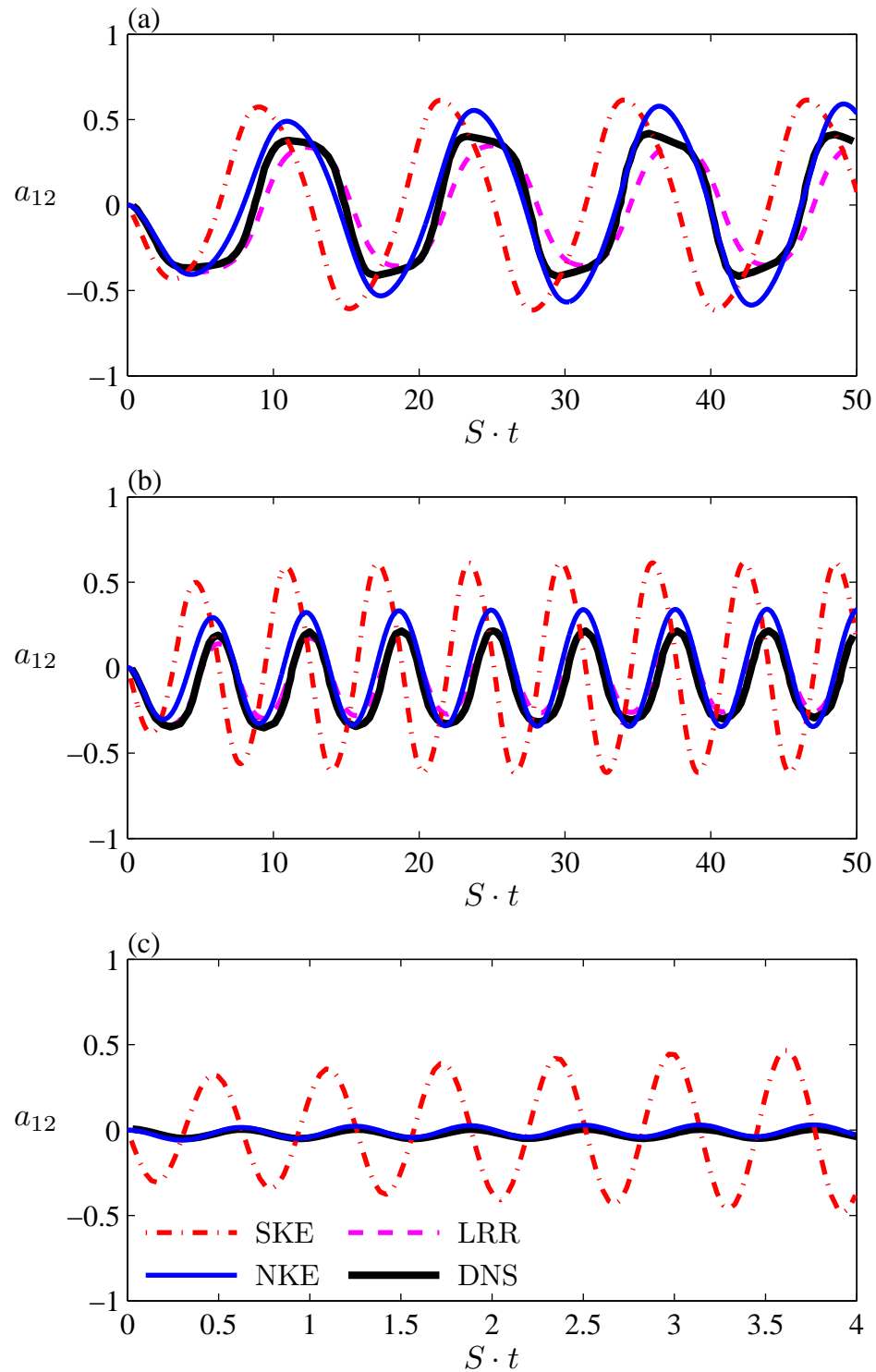
Figure 4.9: Anisotropy $a_{12}(t)$ in periodically sheared turbulence for relative shearing frequencies $\omega/S = 0.5$ (a), 1.0 (b), and 10 (c), comparing the present solution in (4.23) with results from the SKE and LRR [51] models, and with corresponding DNS results of Yu and Girimaji [115].
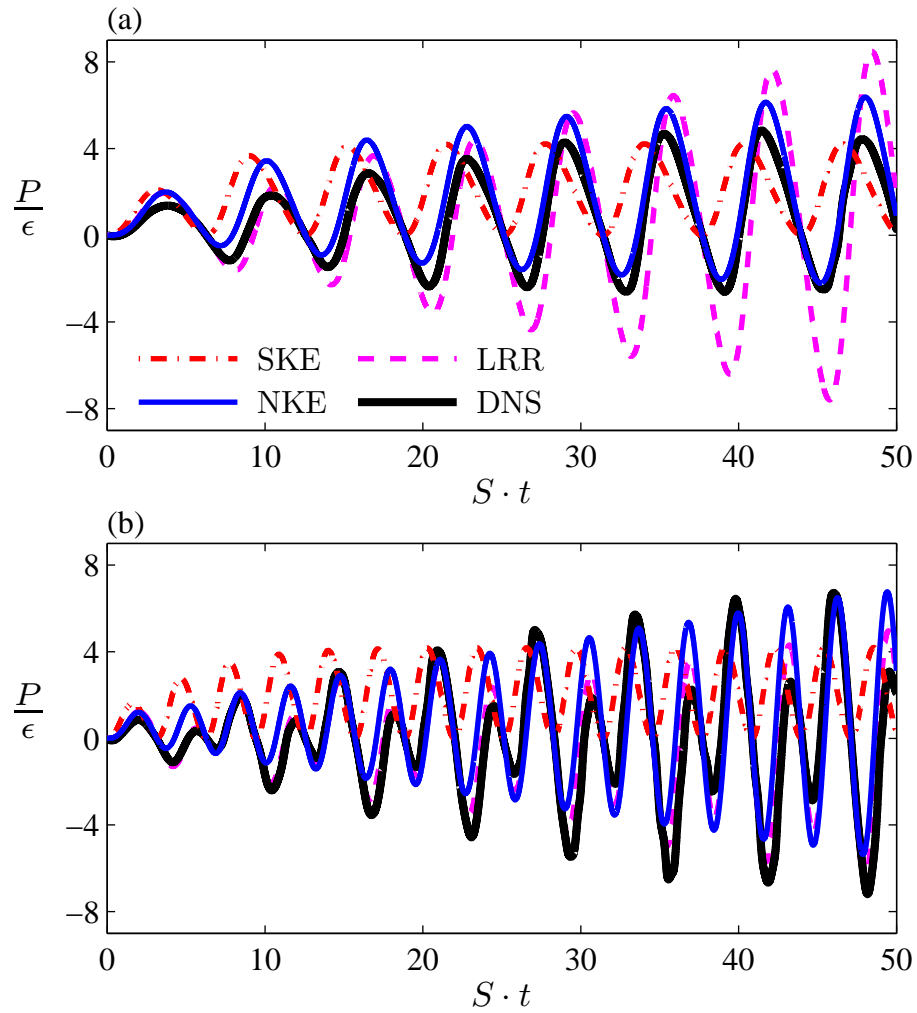
Figure 4.10: Time-evolution of the production-to-dissipation ratio $P/\epsilon$ from (4.26) for frequencies $\omega/S = 0.5$ ($a$) and $1.0$ ($b$), showing good agreement with DNS results of Yu and Girimaji [115]. Results from the SKE and LRR [51] models are also shown.
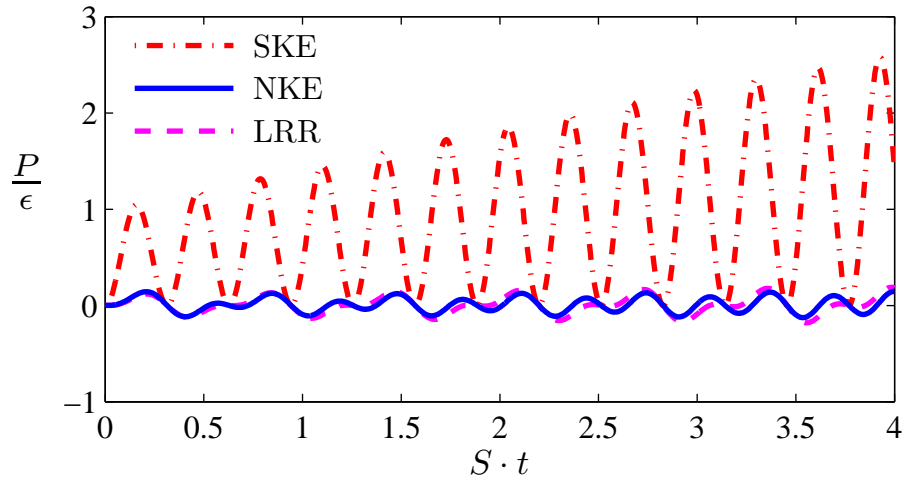
Figure 4.11: Time-evolution of the production-to-dissipation ratio $P/\epsilon$ from (4.26) for shearing frequency $\omega/S = 10$ showing good agreement of present closure with results from the LRR [51] model, while the SKE model significantly overpredicts the amplitude of $P/\epsilon$.
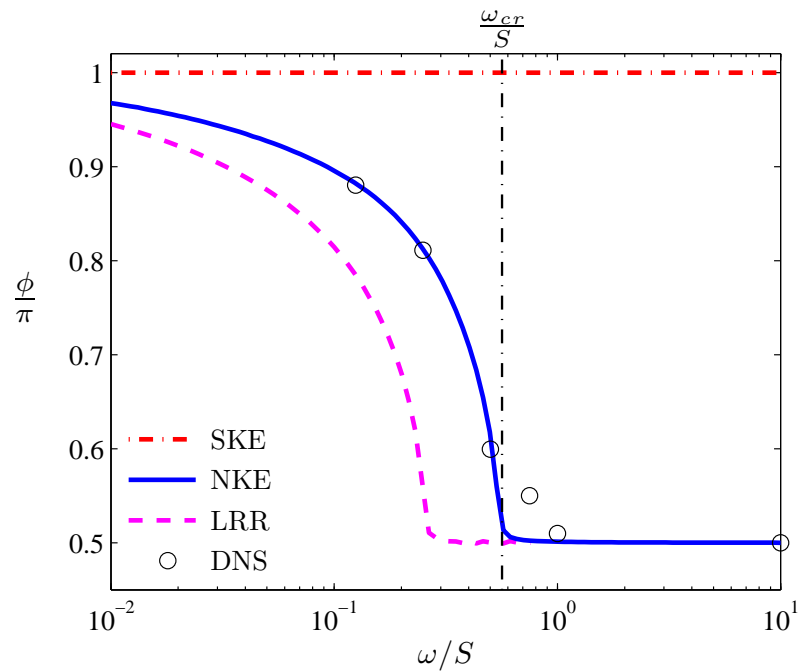


Figure 4.12: Phase difference between the shear stress anisotropy and the applied mean shear, showing good agreement of the present result in (4.28) with the DNS results of Yu and Girimaji [115], and comparisons with corresponding SKE and LRR [51] model results.

143
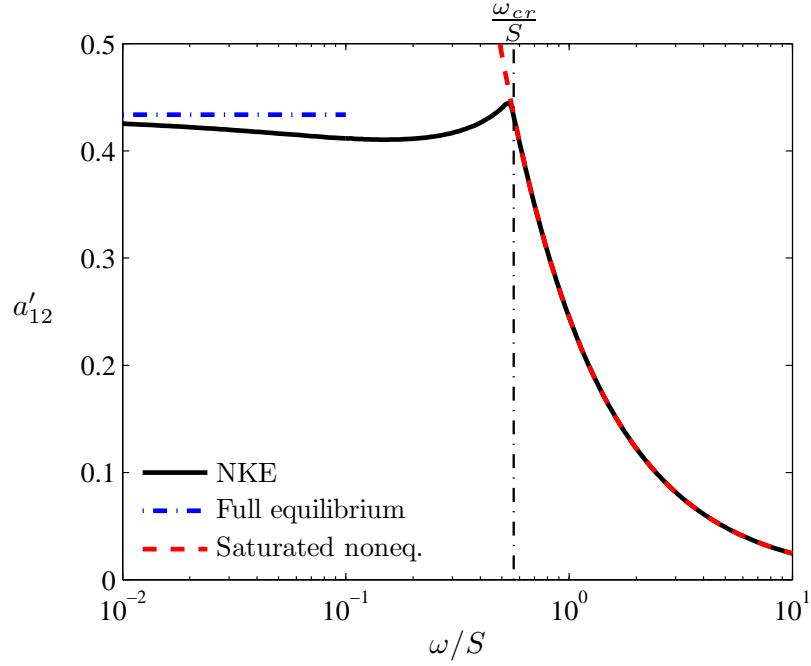
Figure 4.13: Rms amplitude of the long-time limit anisotropy from NKE model in (4.27), showing approach to equilibrium limit value in (4.35) and good agreement with form for the saturated nonequilibrium regime in (4.36) for $\omega > \omega_{cr}$.
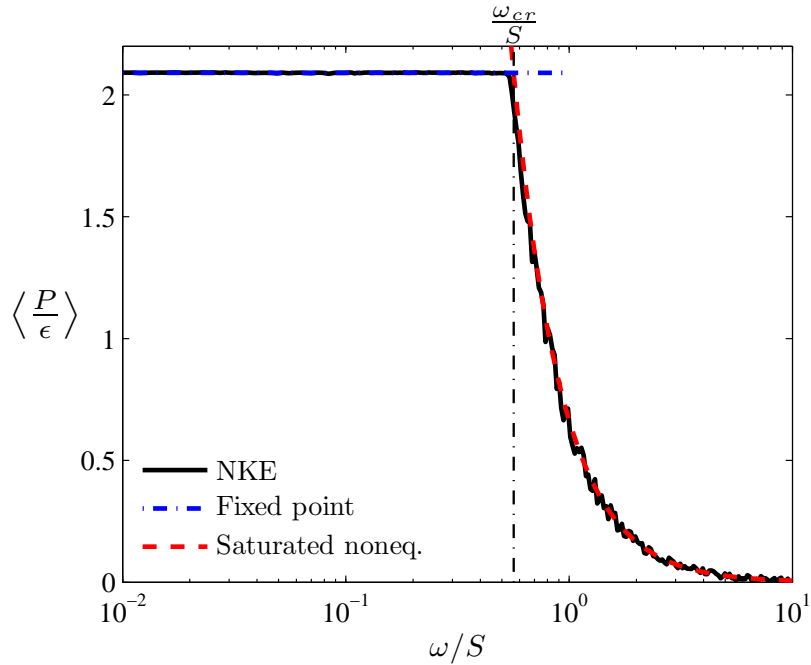


Figure 4.14: Cycle average of $P/\epsilon$ in long-time limit from NKE model in (4.37), showing also fixed point form in (4.43) for $\omega < \omega_{cr}$, saturated nonequilibrium form in (4.44) for $\omega > \omega_{cr}$, and abrupt transition at the critical frequency $\omega_{cr}$ given in (4.45) and (4.46).

144
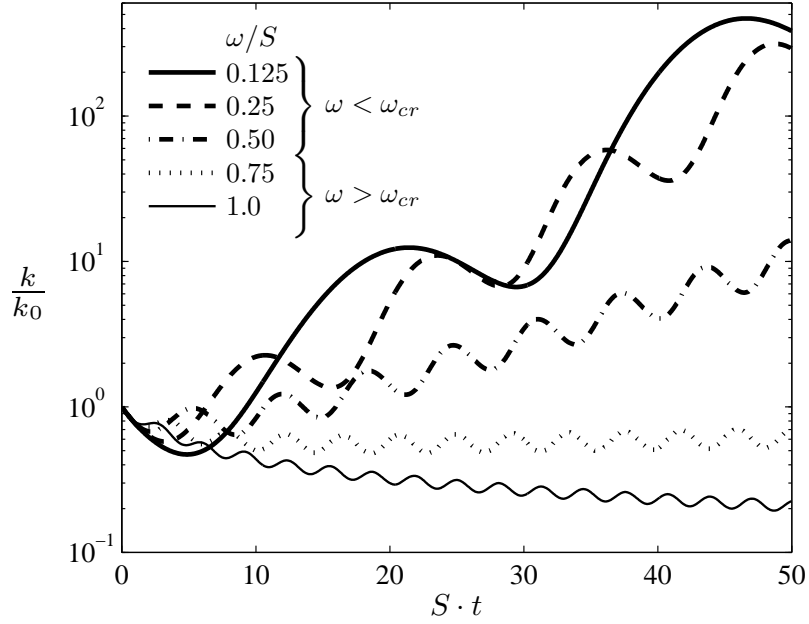
Figure 4.15: Kinetic energy evolution $k(t)$ from NKE model normalized by the initial value $k_0$ for various shearing frequencies $\omega/S$, showing the transition from kinetic energy growth ($\omega < \omega_{cr}$) to decay ($\omega > \omega_{cr}$) at the critical frequency $\omega_{cr}/S = 0.55$ from (4.45).
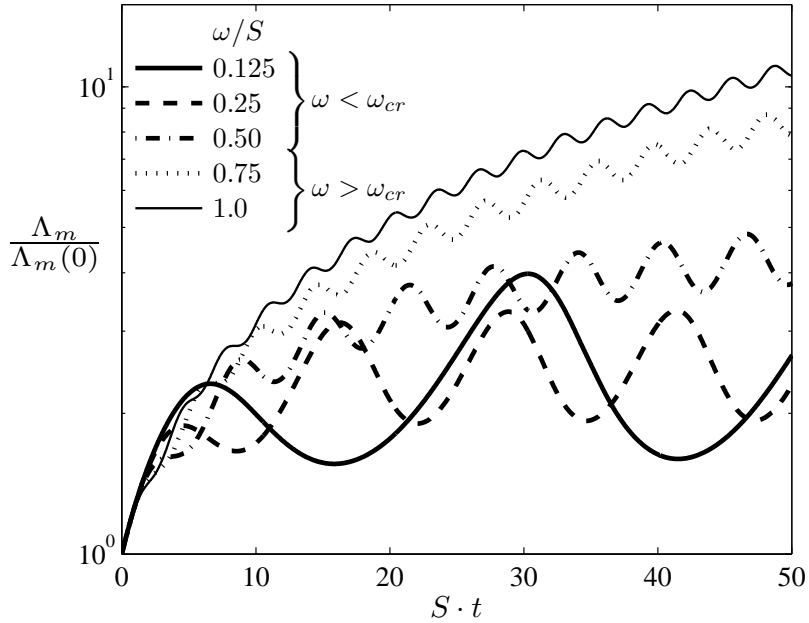


Figure 4.16: Evolution of the turbulence relaxation time scale $\Lambda$ from NKE model normalized by the initial value $\Lambda_0$ for various shearing frequencies $\omega/S$. The magnitude of $\Lambda$ becomes unbounded in the long-time limit for shearing frequencies above the critical value $\omega_{cr}/S = 0.55$.

145
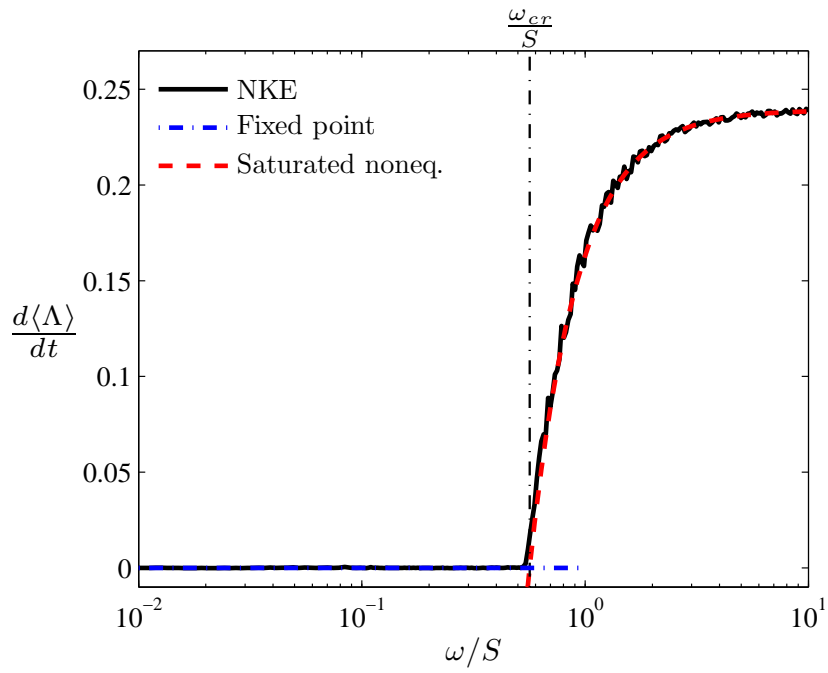
Figure 4.17: Frequency response of $d\langle\Lambda\rangle/dt$ in long-time limit from NKE model in (4.48), showing fixed point dynamics for $\omega < \omega_{cr}$ and good agreement with saturated nonequilibrium form in (4.49) for $\omega > \omega_{cr}$.
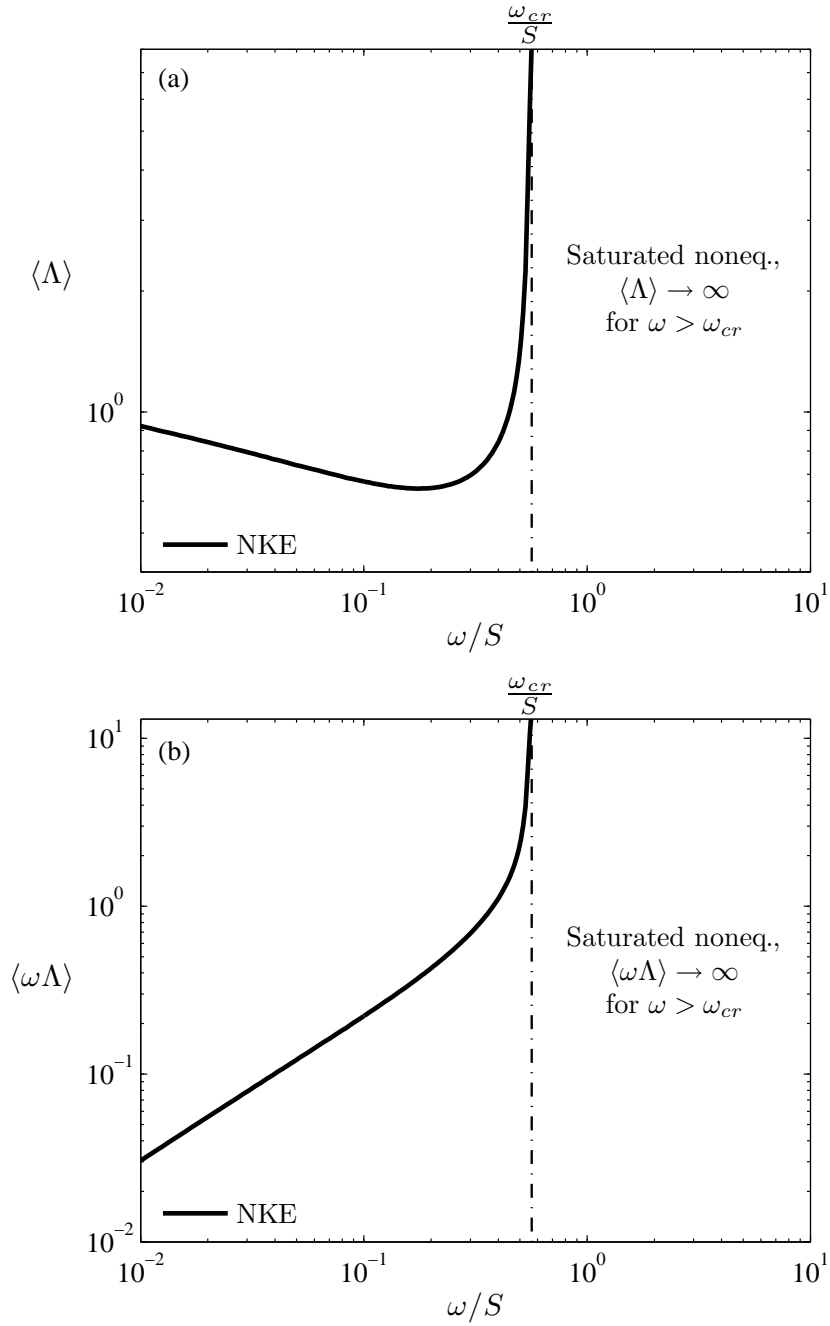
Figure 4.18: Variation in the cycle average of $\Lambda$ (a) and the nonequilibrium parameter $(\omega\Lambda)$ (b) from the NKE model in long-time limit with shearing frequency $\omega/S$, showing $\langle\Lambda\rangle \to \infty$ and $\langle\omega\Lambda\rangle \to \infty$ for all $\omega > \omega_{cr}$. Figure (b) shows monotonic increase in $\langle\omega\Lambda\rangle$ with increasing $\omega/S$.
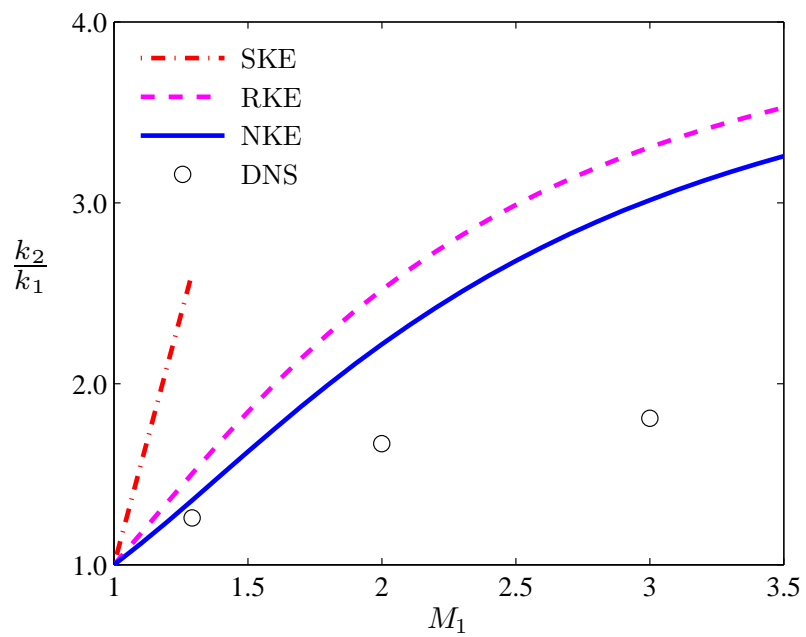
Figure 4.19: Amplification of turbulence kinetic energy $k$ across normal shock at various upstream Mach numbers $M_1$, comparing DNS [56, 60] with NKE model and classical equilibrium SKE [94] and RKE models.
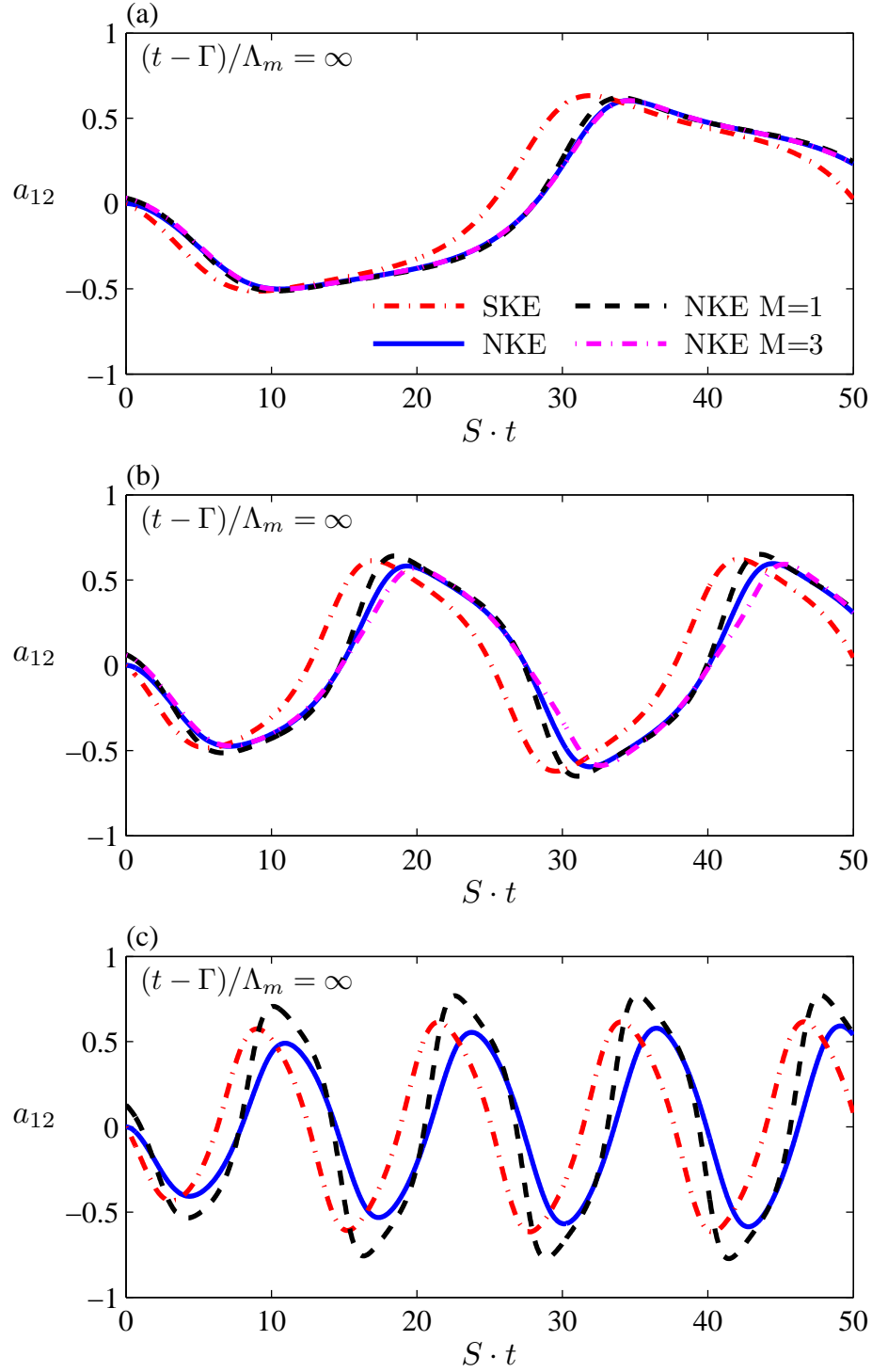
Figure 4.20: Temporal evolution of $a_{12}$ for shearing frequencies (a) $\omega/S = 0.125$, (b) $\omega/S = 0.25$, and (c) $\omega/S = 0.5$, showing results from $M = 1$ truncated closure in (4.58) (NKE $M = 1$), $M = 3$ closure in (4.59) (NKE $M = 3$), standard $k$-$\epsilon$ model in (4.21) (SKE), and full nonequilibrium closure in (4.23) (NKE). In all cases, $(t - \Gamma)/\Lambda_m = \infty$ has been used for the $B^{(m)}$ coefficients in (3.121). For $\omega/S = 0.5$, the $M = 3$ closure requires finite $(t - \Gamma)/\Lambda_m$; consequently $M = 3$ results are not shown in (c).
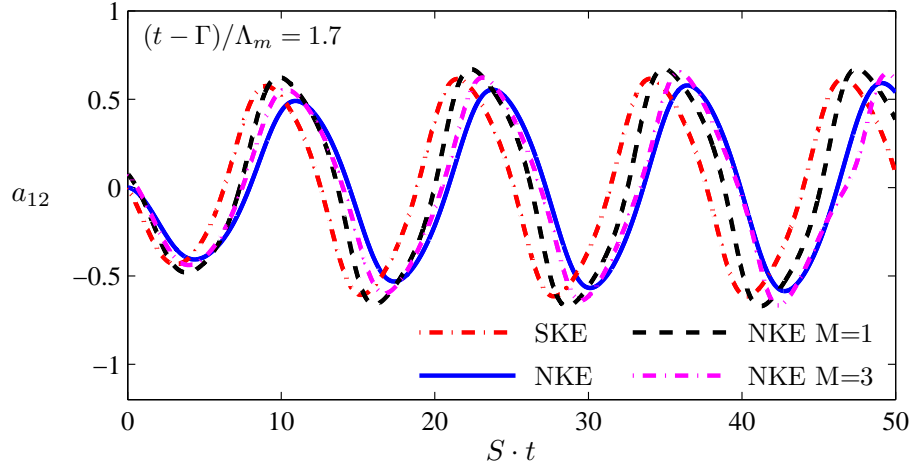
Figure 4.21: Temporal evolution of anisotropy $a_{12}$ for shearing frequency $\omega/S_{max} = 0.5$, showing results from $M = 1$ truncated nonequilibrium closure in (4.58) (NKE $M = 1$), $M = 3$ closure in (4.59) (NKE $M = 3$), standard $k$-$\epsilon$ model in (4.21) (SKE), and full nonequilibrium closure in (4.23) (NKE). The value $(t - \Gamma)/\Lambda_m = 1.7$ has been used for the $B^{(m)}$ coefficients defined in (3.121).
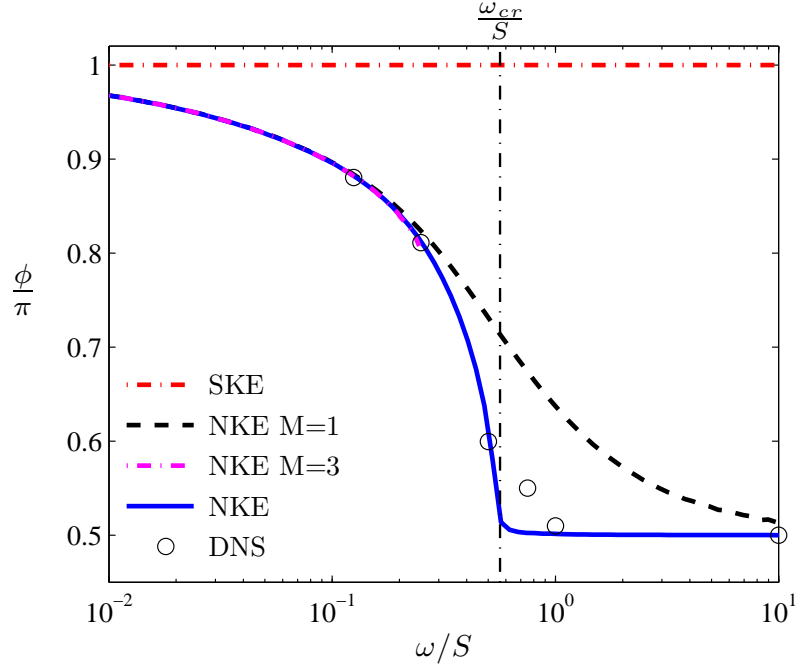


Figure 4.22: Phase difference between anisotropy $a_{12}$ and imposed mean shear $\overline{S}_{12}$ in periodically-sheared turbulence, comparing results obtained from $M = 1$ truncated nonequilibrium closure in (4.58) (NKE $M = 1$) and the $M = 3$ closure in (4.59) (NKE $M = 3$) with standard $k$-$\epsilon$ model in (4.21) (SKE), full nonequilibrium closure in (4.23) (NKE), and DNS results from Yu and Girimaji [115]. Due to the use of $(t - \Gamma)/\Lambda_m = \infty$, results from the $M = 3$ model are only shown up to $\omega/S \approx 0.25$.

150
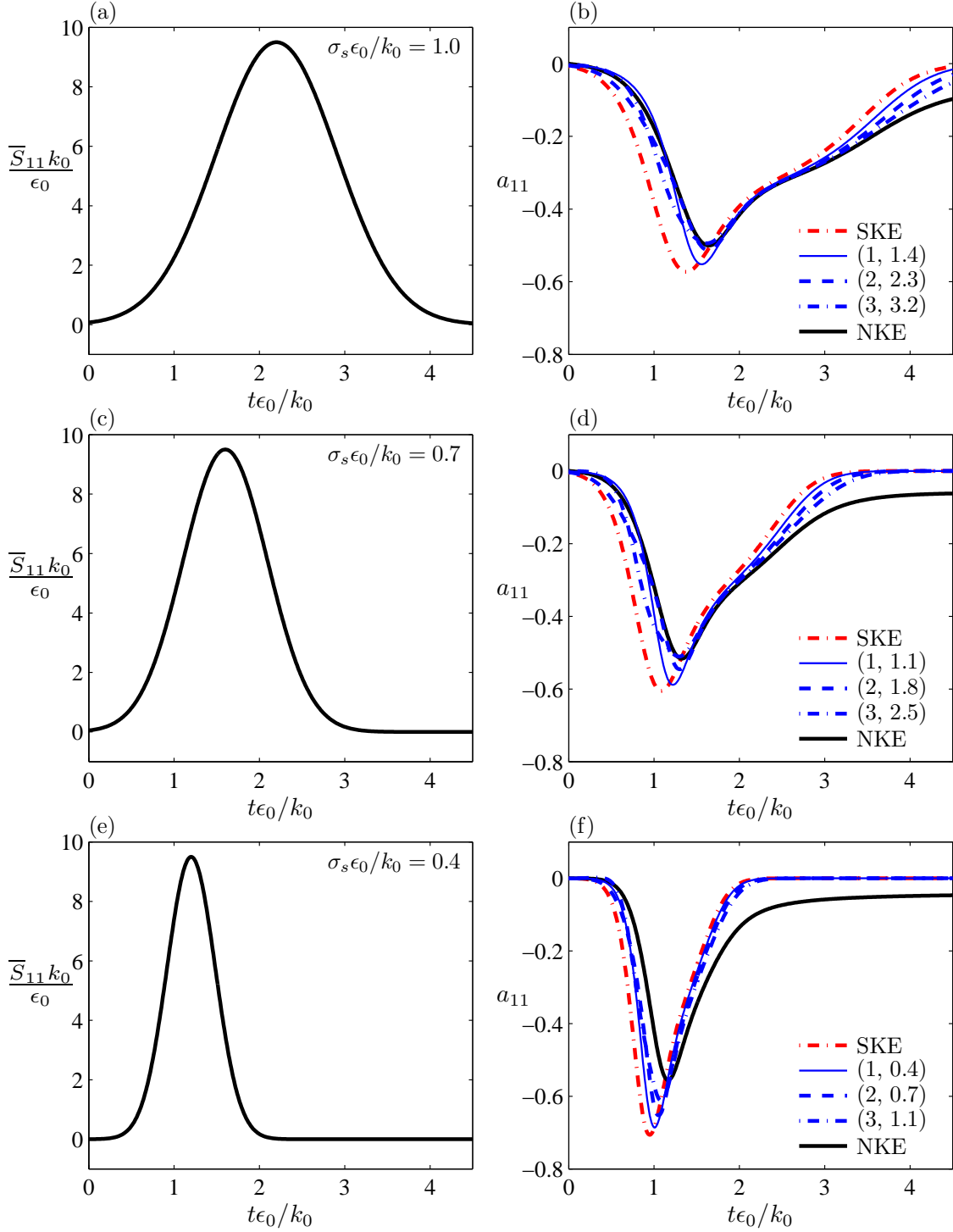
Figure 4.23: Temporal evolution of anisotropy $a_{11}$ (right column) for Gaussian applied strain from (4.60) (left column). The rows correspond to $\sigma_s \epsilon_0 / k_0 = 1.0$ (a) and (b), $\sigma_s \epsilon_0 / k_0 = 0.7$ (c) and (d), and $\sigma_s \epsilon_0 / k_0 = 0.4$ (e) and (f). Results are shown from the SKE closure and the $M = 1, 2, 3$ truncated closures in (4.65)-(4.67). The truncated closures are denoted in the legends by $(M, \gamma)$, where $\gamma \equiv (t - \Gamma)/\Lambda_m$ is used to obtain the $B^{(m)}$ coefficients in (3.121). Results are compared with the full NKE closure in (4.61) for all cases.

# CHAPTER V

# Computational Implementation and Nonlocal Tests of the Present Anisotropy Closure

The vast majority of practical turbulent flow problems are inhomogeneous, exhibiting often strong spatial variations in mean flow quantities. For example, in free-shear flows such as jets, mixing layers, and wakes the mean shear varies dramatically in the cross-stream direction. Similar strong spatial variations are also observed in the near-wall region of wall bounded flows such as turbulent channels and boundary layers. As discussed in Chapter III, such variations introduce substantial nonlocal effects on the anisotropy, which must be accurately predicted in order to obtain reliable, high-fidelity solutions of (1.2)-(1.4).

In order to assess the accuracy of the anisotropy closure outlined in Chapter III for addressing nonlocal effects in turbulent flows, fully-developed turbulent channel and the zero pressure gradient turbulent boundary layer are examined in the following. While nonequilibrium effects on the anisotropy are not significant in these flows, nonlocal effects are particularly important in both the channel and boundary layer cases since the mean strain varies rapidly in the near-wall region. As shown in Figure 1.2 for the channel flow, the classical local equilibrium closure in (1.35) provides relatively accurate predictions of the anisotropy away from the channel walls, but substantially over-predicts the anisotropy magnitude for $y^+ < 60$. This failure is due in large part to the neglect of nonlocal effects in the closure, as discussed in Section 1.3.3.

In the following, the present focus on nonlocal effects is shown to give substantially improved agreement with computational and experimental results in the turbulent channel and boundary layer cases when compared to results from the classical local equilibrium closure in (1.35). It is first shown how the present closure from (3.97) with (3.110) or (3.123) can be written for equilibrium flows. This closure is then applied analytically to the logarithmic velocity profile found near the wall in wall bounded flows, showing that the present nonlocal correction terms lead to a decrease in the anisotropy magnitude in the near-wall region compared to the local equilibrium closure in (1.35). The present closure is then evaluated using results from various fully-developed turbulent channel flow DNS studies, where all flow variables are obtained exactly from the DNS databases. This allows

152

a direct evaluation of the present closure formulation without concerns as to how $k$ and $\epsilon$ are obtained, or how (1.2)-(1.4) are solved to obtain $\overline{S}_{ij}$. Finally, the present closure is implemented in a full computational framework for solving (1.2)-(1.4), and results are shown for the zero pressure gradient boundary layer.

It should be noted before continuing that while the present closure is expected to provide improved predictions of the anisotropy in any flow with a spatially varying mean velocity gradient field, the turbulent channel flow and boundary layer are particularly attractive validation cases for a number of reasons. For the channel flow, the availability of a number of high-quality DNS databases makes it possible to accurately calculate several higher-order Laplacians of $\overline{S}_{ij}$ in (3.96). In general, calculation of these terms requires high-resolution data, and such data is simply not currently available for other canonical inhomogeneous flows, such as the turbulent jet and mixing layer. With respect to the boundary layer, the relative simplicity of this case allows straightforward implementation and testing of the present closure in a full computational framework for solving (1.2)-(1.4). At the same time however, the turbulent boundary layer is a fundamental flow of substantial engineering importance, and correctly predicting the anisotropy within the boundary layer (particularly in the near-wall region) has been problematic for nearly all prior turbulence model approaches.

## 5.1 Nonlocal Anisotropy Closure in Equilibrium Turbulence

The anisotropy closure in (3.97) expresses $a_{ij}$ in terms of the nonlocal and nonequilibrium effective strain $\widetilde{S}_{ij}$, which is given by (3.94) as a convolution integral over the entire history of the nonlocal tensor $T_{ij}$, defined in (3.87), along mean flow pathlines. For turbulent flows near equilibrium however, the turbulence memory time scale $\Lambda_m$ in (3.94) is much less than the time scale over which $T_{ij}$ varies, here denoted $\Lambda_T$. In such equilibrium flows the representation for $\widetilde{S}_{ij}$ from (3.94) becomes greatly simplified, and in particular nonequilibrium history effects on the anisotropy evolution can be neglected in the closure representation.

The effective strain can be written for equilibrium flows by taking the limit of $\widetilde{S}_{ij}$ in (3.94) as $(\Lambda_m/\Lambda_T) \to 0$. Making the change of variables $z = -(t-\tau)/(\Lambda_m/\Lambda_T)$, (3.94) can be written as

$$\widetilde{S}_{ij}(t) = \int_{-\infty}^{0} T_{ij}\left(t + \frac{\Lambda_m}{\Lambda_T}z\right) \frac{e^{z/\Lambda_T}}{\Lambda_T} dz. \tag{5.1}$$

In the limit $\Lambda_m/\Lambda_T \to 0$, (5.1) then yields the equilibrium relation

$$\lim_{\Lambda_m/\Lambda_T \to 0} \widetilde{S}_{ij}(t) = T_{ij}(t), \tag{5.2}$$

and consequently there is no longer any nonequilibrium history-dependence in $\widetilde{S}_{ij}$.

With (5.2) and the definition of $T_{ij}$ in (3.87), the present anisotropy closure is written

153

for equilibrium flows from (3.97) as

$$a_{ij} = -2\frac{\nu_T}{k}\left[\overline{S}_{ij} + \sum_{n=2}^{N}\frac{C_2^{(n)}}{\alpha_2}\Lambda^{2n-2}\left(\nabla^2\right)^{n-1}\overline{S}_{ij}\right], \tag{5.3}$$

where the $C_2^{(n)}$ are given by (3.67) for $N \to \infty$ and (3.118) for finite $N$, with $\alpha_2 = C_2^{(1)} - 4/3$. The first term in the square brackets is the local equilibrium response of the anisotropy, and corresponds to the classical closure in (1.35). By contrast to the classical closure however, the series of Laplacians in (5.3) additionally accounts for nonlocal effects due to variations in the mean strain rate tensor. It will be seen herein from the channel flow and boundary layer tests that these additional terms give dramatically improved predictions of the anisotropy when compared to results from the classical local equilibrium closure in (1.35).

## 5.2 Log-Layer Analysis

Both turbulent channel and boundary layer flows display a logarithmic velocity profile in the near-wall region, and this profile can be used to carry out a preliminary analytical evaluation of the nonlocal terms in (5.3) and their effect on predictions of the anisotropy in wall-bounded flows. Within the so-called "log-layer" region, the streamwise velocity is given by [78]

$$u^+ = \frac{1}{\kappa}\ln y^+ + B, \tag{5.4}$$

where $\kappa = 0.41$, $B = 5.2$, $u^+ \equiv \overline{u}/u_\tau$, and $y^+ \equiv yu_\tau/\nu$. The wall friction velocity $u_\tau$ is defined as $u_\tau \equiv \sqrt{\tau_w/\rho}$, where $\tau_w$ is the shear stress at the wall. The profile in (5.4) generally shows good agreement with DNS and experimental results well into the near-wall region [78], often down to $y^+ \approx 30$. Within the log-layer, the mean shear $\overline{S}_{12}$ is given from (5.4) as

$$\overline{S}_{12} \approx \frac{1}{2}\frac{\partial\overline{u}}{\partial y} = \frac{1}{2}\frac{u_\tau^2}{\nu}\frac{\partial u^+}{\partial y^+} = \frac{1}{2}\frac{u_\tau^2}{\nu}\frac{1}{\kappa y^+}, \tag{5.5}$$

where $\partial\overline{u}/\partial y \gg \partial\overline{v}/\partial x$ in turbulent channel and boundary layer flows. The shear anisotropy $a_{12}$ from (5.3) and (5.5) can thus be written as

$$a_{12} = -2\frac{\nu_T}{k}\overline{S}_{12}\left[1 - \frac{17}{21}\left(\frac{\Lambda^+}{y^+}\right)^2 - \frac{44}{7}\left(\frac{\Lambda^+}{y^+}\right)^4 - \frac{11400}{77}\left(\frac{\Lambda^+}{y^+}\right)^6 + \cdots\right], \tag{5.6}$$

where $\Lambda^+ \equiv \Lambda u_\tau/\nu$ and the $C_2^{(n)}$ coefficients from (3.67) have been used to obtain the result. By contrast, the local equilibrium closure in (1.35) gives the anisotropy in the log-layer as

$$a_{12} = -2\frac{\nu_T}{k}\overline{S}_{12}. \tag{5.7}$$

154

Comparison of (5.6) with (5.7) shows that the magnitude of $a_{12}$ is reduced in the log-layer by the nonlocal correction terms. As seen in Figure 1.2, the local equilibrium closure substantially over-predicts the anisotropy magnitude in the near-wall region of the turbulent channel, and the reduction in the magnitude of $a_{12}$ from (5.6) – which is fundamentally obtained by accounting for nonlocal effects on the anisotropy – may thus be sufficient to give better agreement with DNS and experimental results in wall-bounded flows.

## 5.3    Fully-Developed Turbulent Channel Flow

Fully-developed turbulent channel flow provides an ideal nonlocal test of the present anisotropy closure due to the substantial spatial variations in mean flow quantities in the near-wall region, as well as due to the availability of several high-resolution turbulent channel flow DNS data sets. Since the channel flow is fundamentally in equilibrium – as evidenced by the fact that flow properties do not change along mean flow streamlines and material derivatives $D/Dt$ of all flow properties are identically zero – the equilibrium form of the present nonlocal closure in (5.3) can be used to make quantitative comparisons of the anisotropy with results from DNS.

In the following, eight different Reynolds numbers from three different channel flow DNS databases are examined. The Reynolds number cases considered herein are ($i$) $Re_\tau = 150$, 300, 400, 650 from Iwamoto $et\ al.$ [39], ($ii$) $Re_\tau = 180$ and 395 from Moser $et\ al.$ [67], and ($iii$) $Re_\tau = 550$ and 950 from Hoyas and Jimenez [37]. Perhaps the main advantage of using these DNS databases for testing the present closure is that all flow variables, including $k$ and $\epsilon$, are provided exactly. The specific closure relation for the anisotropy can thus be tested without concerns as to the representations for the turbulence variables. This is in contrast to the various nonequilibrium test cases considered in Chapter IV, where $k$ and $\epsilon$ were obtained from transport equations such as those in (1.31) and (1.32).

### 5.3.1    Truncated Anisotropy Closure for Channel Flow Tests

As discussed in Section 3.5, as higher-order nonlocal terms are retained in the closure in (5.3), an increasing number of Laplacians of $\overline{S}_{ij}$ must be calculated. However, the resolution of the DNS can become an issue for large $N$, and in the following we will consider the $N = 2$ truncation of (5.3), which gives

$$a_{ij} = -2\frac{\nu_T}{k}\left[\overline{S}_{ij} + \frac{C_2^{(2)}}{\left(C_2^{(1)} - 4/3\right)}\Lambda^2\nabla^2\overline{S}_{ij}\right]\ ,\tag{5.8}$$

where $C_2^{(1)}$ and $C_2^{(2)}$ are given by (3.118) and we use $R/\Lambda = 0.86$, consistent with (3.125).

In turbulent channel flow the local Reynolds number can become small in the near-wall region, resulting in increasingly important viscous effects. As a result, $\Lambda$ in (3.36) is here

written as

$$\Lambda = \max \left[ 0.23 \frac{k^{3/2}}{\epsilon}, \, C_\eta \eta_K \right] , \tag{5.9}$$

where $\eta_K = \left( \nu^3/\epsilon \right)^{1/4}$ is the Kolmogorov length scale and it will be seen that

$$C_\eta = 12.4 \tag{5.10}$$

gives good agreement with DNS for all Reynolds numbers. This approach for addressing low-Reynolds number effects is similar to the formulation for $L$ in (3.131) used in elliptic relaxation models (e.g. [20, 21]). Note also that in obtaining (5.9) from (3.36) we have used the value for $C_\lambda$ in (3.39), which comes from comparison of the exponential $f(r)$ given by (3.38) with the inertial range form for $f(r)$ obtained from the Kolmogorov hypotheses, as discussed in Section 3.2.4.

The eddy viscosity $\nu_T$ in (5.8) is given by the standard form in (1.36) where here $C_\mu$ is given by the realizable Bradshaw hypothesis in (1.40). From the definition of $C_\mu$ in (1.37) it can be seen that $C_\mu \sim (P/\epsilon)^{-1}$, and thus $C_\mu$ must be limited in regions where $P/\epsilon$ becomes large. In reality, the magnitudes of $P/\epsilon$ and $Sk/\epsilon$ are closely linked, and the realizable $C_\mu$ in (1.40) provides a relatively straightforward way of accounting for the dependence of $C_\mu$ on $P/\epsilon$. Use of (1.40) is particularly important in the turbulent channel flow, since $Sk/\epsilon$ becomes large in the near-wall region and reaches a maximum value of $Sk/\epsilon \approx 18$ at $y^+ \approx 8$ as shown using DNS from Iwamoto $et\ al.$ [39] in Figure 5.1.

Finally, before proceeding to a full comparison of results from (5.8) with DNS, we can get a sense of where nonlocal effects are important in the turbulent channel by considering the parameter $\Psi$ from (3.105) as a function of $y^+$. Again using the DNS of Iwamoto $et\ al.$ [39], Figure 5.2 shows for four different values of $Re_\tau$ that $\Psi$ begins to increase and become substantially non-zero at $y^+ \approx 100$. Here $T_{ij}$ in the definition of $\Psi$ in (3.105) has been calculated from (3.87) by retaining only the leading order $n = 2$ nonlocal Laplacian term, consistent with the present truncated closure in (5.8). Figure 5.2 further shows that the degree of nonlocality in the channel peaks at $y^+ \approx 15$ where $\Psi \approx 1.2$. This thus indicates that nonlocal effects due to variations in the mean strain are important in the turbulent channel for $10 < y^+ < 100$, and that the present nonlocal anisotropy closure in (5.8) can be expected to give improved predictions of the anisotropy compared to the local equilibrium closure from (1.35) in this range.

### 5.3.2 Comparisons with DNS

Figure 5.3 compares the shear anisotropy $a_{12}$ as a function of $y^+$ predicted by the truncated closure described in the previous section – here denoted the NKE model – with results from DNS. Results from the standard $k$-$\epsilon$ (SKE) model from (1.35) and (1.36) with $C_\mu = 0.09$, and the realizable $k$-$\epsilon$ (RKE) model from (1.35) with $C_\mu$ given by (1.40) are also

156

shown. For all Reynolds numbers, the SKE model shows good agreement with DNS in the centerline of the channel, but dramatically over-predicts the anisotropy magnitude in the near-wall region. The RKE model shows somewhat improved agreement in the near-wall region due to the realizable $C_\mu$ in (1.40), which limits the anisotropy magnitude when $Sk/\epsilon$ becomes large near the wall. However, the RKE model fails to capture the decrease in the anisotropy magnitude as the wall is approached. By contrast, the NKE closure from (5.8) agrees with the DNS results for all Reynolds numbers down to $y^+ \approx 16$, consistent with the observed importance of nonlocal effects down to at least $y^+ \approx 15$ in Figure 5.2.

Below $y^+ \approx 16$ however, Figure 5.3 shows that the NKE closure over-predicts the anisotropy magnitude, resulting in poor agreement with the DNS. This poor agreement could be due to a number of factors, in particular the neglect of inhomogeneities in the turbulence variables, the neglect of the anisotropy in the dissipation tensor $\epsilon_{ij}$ (which can become significant as the local Reynolds number decreases in the near-wall region), and the increasingly two-dimensional nature of the turbulence near the wall. While the NKE closure from (5.8) does not explicitly address any of these effects, which are nevertheless discussed in more detail in Section 5.6, we can obtain a closure that agrees with DNS for $y^+ < 16$ by combining the present approach with prior anisotropy closures based on *ad hoc* wall damping functions. Such wall-damped closures were previously discussed in Section 1.3.3, and are here written in general form as

$$a_{ij}^{(f)} = -2f_\mu C_\mu \frac{k}{\epsilon} \overline{S}_{ij} \,, \tag{5.11}$$

where we have taken $\nu_T$ from the standard form in (1.36) and $f_\mu$ is a damping function that typically goes from $f_\mu = 0$ at $y^+ = 0$ to $f_\mu = 1$ for large $y^+$. The exact formulation for $f_\mu$ is usually determined and calibrated on an *ad hoc* basis from experimental or computational measurements of the anisotropy in wall-bounded flows.

As shown in Figure 5.3, the emphasis on nonlocal effects in the present closure from (5.8) gives good predictions of the anisotropy down to $y^+ \approx 16$. We can thus avoid the use of the *ad hoc* closure in (5.11) for nearly the entire flow, and can obtain better agreement for $y^+ < 16$ by resorting to prior damping function formulations in the extreme near-wall region only. Here we introduce the blending function $\phi$, which is 1 for small $y^+$ and 0 for $y^+$ greater than some cutoff value close to $y^+ \approx 16$, and write the anisotropy in blended form using (5.11) as

$$a_{ij}^{(\phi)} = \phi a_{ij}^{(f)} + (1 - \phi)a_{ij} \,, \tag{5.12}$$

where $a_{ij}$ on the right-hand side is given by the present closure in (5.8). The blending function $\phi$ can take on any form that gives the desired transition from $\phi = 1$ for small $y^+$ to $\phi = 0$ for large $y^+$, and here we use the hyperbolic tangent function

$$\phi = \frac{1}{2} - \frac{1}{2}\tanh\left[a\left(y^+ - b^+\right)\right] \,. \tag{5.13}$$

157

The blended closure in (5.12) with (5.13) allows the present nonlocal closure in (5.8) to be applied for $y^+ > b^+$ where $\phi = 0$, with $b^+$ set to a value close to $y^+ \approx 16$, while for $y^+ < b^+$ we obtain $\phi = 1$ and the standard wall-damped formulation for the anisotropy in (5.11) is used.

The damping function $f_\mu$ in (5.11) can be given by any number of possible forms, making it ideal for implementation in existing computational frameworks for solving (1.2)-(1.4). However, for the present fully-developed channel flow tests we consider the relatively simple van Driest form [19, 78] in (1.42), with $A^+ = 26$. Noting from Figure 5.3 that the present anisotropy closure begins to show disagreements with DNS in the range $y^+ \approx 15-20$, we here set

$$a \approx 0.4, \quad b^+ \approx 18, \tag{5.14}$$

which gives a moderately sharp transition from $\phi = 0$ to $\phi = 1$ near the wall using (5.13). The values of these constants are governed by the need to maintain a smooth transition from the nonlocal $a_{ij}$ in (5.8) to the wall-damped $a_{ij}^{(f)}$ in (5.11), and have been chosen to give good agreement with the channel flow and boundary layer cases considered herein. By using a relatively small value for $a$ and the more conservative cutoff for $b^+$ (as opposed to setting $b^+ = 16$ for instance), it is expected that the blending function in (5.13) with the constants in (5.14) will be accurate for a range of flows and a range of different formulations for $f_\mu$.

Figure 5.3 shows that the present nonlocal closure can be smoothly blended with the wall-damped anisotropy in (5.11) using (5.12)-(5.14) for all Reynolds numbers, giving good agreement with DNS results down to $y^+ \approx 3$. For $y^+ < 3$, the blended model shows poor agreement with the DNS results due to the behavior of the damping function in (1.42), which has been combined with the realizable $C_\mu$ in (1.40), near the wall. Improved agreement can be obtained through the choice of a different formulation for $f_\mu$. A number of alternative wall damping functions are summarized in Ref. [99] and the Speziale, Abid, and Anderson [97] form for $f_\mu$ will be used for the boundary layer tests in the next section. Nevertheless, the primary purpose of the blended closure in (5.12) is to allow integration to viscous walls in existing computational frameworks for solving (1.2)-(1.4), and Figure 5.3 shows that even with the van Driest function in (1.42) the present blended closure closely agrees with DNS for nearly the entire channel height, while only requiring an *ad hoc* treatment for the anisotropy at locations very close to the wall.

Finally, Figure 5.4 compares the shear anisotropy $a_{12}$ as a function of the nondimensional shear parameter $Sk/\epsilon$ from the present NKE closure model and the SKE and RKE models with corresponding results from DNS. The dependence of $a_{12}$ on $Sk/\epsilon$ is of particular importance because, as the DNS results in Figure 5.4 show, the relation between $a_{12}$ and $Sk/\epsilon$ becomes non-trivial near the wall, whereas the widely-used SKE model, based on the local equilibrium closure in (1.35), incorrectly predicts $a_{12} \propto Sk/\epsilon$ for all $Sk/\epsilon$. Figure 5.4 shows that the RKE model limits the anisotropy magnitude for large $Sk/\epsilon$, resulting

in better agreement with the DNS than the SKE model. However, the correct functional dependence of $a_{12}$ on $Sk/\epsilon$ is still not accurately predicted. By contrast, the present NKE closure from (5.8) shows good agreement with DNS even as $Sk/\epsilon$ increases, and substantial departures from the DNS results only occur at $y^+ \approx 16$ where $Sk/\epsilon \approx 12$. Consistent with the results in Figure 5.3, improved agreement is obtained using the blended anisotropy closure in (5.12).

## 5.4 Computational Implementation of Present Anisotropy Closure

The turbulent channel flow tests in the preceding section have provided a direct evaluation of the truncated closure in (5.8), revealing the importance of nonlocal effects on the anisotropy in inhomogeneous (specifically wall bounded) flows. In the channel flow tests $\overline{S}_{12}$, $k$, and $\epsilon$ were all obtained from the DNS databases, thereby allowing the closure in (5.8) to be directly evaluated without complications due to the numerical solution of (1.2)-(1.4) or the specific method by which $k$ and, in particular, $\epsilon$ are modeled.

However, practical use of the present anisotropy closure for typical engineering problems will, in nearly all cases, require implementation in a full computational fluid dynamics (CFD) code for solving (1.2)-(1.4). By contrast to the DNS studies in the previous section, $\overline{S}_{ij}$ in such cases is obtained from the solution of (1.2)-(1.4) for the mean velocity field $\overline{u}_i$, and $k$ and $\epsilon$ are obtained from modeled transport equations such as those in (1.31) and (1.32). It is thus of great interest to consider how the present closure performs when implemented in a full computational framework for solving (1.2)-(1.4), where numerical considerations such as convergence and stability are often as important as the physical accuracy of the closure itself.

Details concerning the computational implementation of the present closure in ISAAC (Integrated Solution Algorithm for Arbitrary Configurations) [66] are outlined in the following, with a view towards simulating the zero pressure gradient turbulent boundary layer in Section 5.5. Consideration of this case allows relatively straightforward initial implementation and testing of the present closure, while nevertheless still providing an evaluation of the closure accuracy and stability for simulations of practical turbulent flow problems.

### 5.4.1 Solver Details

ISAAC [66] is an upwind, structured grid, finite-volume CFD code that solves the Navier-Stokes equations in Favre-averaged form. The code provides an ideal test-bed for new turbulence modeling approaches, due primarily to its direct use of the full Reynolds stress tensor $\overline{u'_i u'_j}$ in (1.2)-(1.4) and in the production term $P \equiv \overline{u'_i u'_j}\, \overline{S}_{ij}$ in the transport equations for $k$ and $\epsilon$ [e.g. (1.31) and (1.32)]. Due to its widespread popularity and favorable numerical properties, the local equilibrium closure in (1.35) is often "hard-wired" into many solvers, in particular on the right-hand side of (1.3). Thus, for example, implementation of nonlinear

eddy viscosity models of the type noted in Section 1.3.2.1 can be complicated by the need to introduce higher-order terms on the right-hand side of (1.3). Similarly, the formulation of the present closure in (3.97), with the effective strain given by (3.110) or (3.123), introduces additional nonlocal and nonequilibrium terms that significantly complicate implementation in codes based on the local equilibrium closure. As a result, a code that evaluates and uses the Reynolds stress tensor directly, such as ISAAC, is preferred for implementation of the present closure.

Within ISAAC, primitive flow variables such as the pressure and mean velocities, denoted generally by $q_{i,j}$, are defined at cell centers at interior locations in the computational domain. For a grid with $idim \times jdim$ computational cell interfaces (including the outer boundaries), $q_{i,j}$ is defined at cell centers on the range $i = 2 : idim$ and $j = 2 : jdim$. The exact location of $q_{i,j}$ near boundaries depends on the type of boundary condition, but for viscous walls $q_{i,j}$ is defined on cell interfaces along the boundary itself. Thus, for a viscous wall along the bottom boundary of the computational domain, $q_{i,1}$ corresponds to the value of $q$ on the wall, which coincides with the south interface of the $j = 2$ cell. A schematic of the computational domain including all variable locations is shown in Figure 5.5, where it is clear that along the bottom viscous wall $q_{i,1}$ corresponds to the value of $q$ at the wall.

The metric terms $\eta_y$ and $\xi_x$ required to calculate the higher-order derivatives in generalized coordinates are defined on cell interfaces for the entire domain. The $\eta_y$ metrics are defined on north-south cell interfaces over the range $(i, j) = (2 : idim, 1 : jdim)$ and the $\xi_x$ metrics are defined on east-west interfaces on the range $(i, j) = (1 : idim, 2 : jdim)$. At boundaries such as viscous walls the location of the metrics is unchanged. Once again, the location of the metrics is shown schematically in Figure 5.5.

As with the $q_{i,j}$ variables, the cell volumes, denoted by $V_{i,j}$, are defined at cell centers for interior points in the computational domain. The location of $V_{i,j}$ at boundaries once again depends on the specific type of boundary, but for the bottom viscous wall in Figure 5.5, $V_{i,1}$ corresponds to the cell volume at the south cell interface, with $V_{i,j} = 0$ on viscous walls.

### 5.4.2 Implementation of Present Closure for Thin-Shear Flows

Implementation of the present anisotropy closure given by (3.97) with the effective strain in (3.110) or (3.123) requires the calculation of at least three derivatives of the mean velocity field in order to obtain the leading-order nonequilibrium and nonlocal terms $D\overline{S}_{ij}/Dt$ and $\nabla^2 \overline{S}_{ij}$, respectively. As shown in Chapter IV and Section 5.3, retaining even the first nonequilibrium and nonlocal correction terms gives substantially improved agreement with computational and experimental results when compared to predictions from the local equilibrium closure in (1.35). As a result, it is sufficient for initial computational testing of the present closure to consider only the first nonlocal and nonequilibrium terms, and consequently discretized derivatives of the velocity field up to third order are outlined

in the next section.

For initial computational implementation and testing of the present closure we will consider the zero pressure gradient turbulent boundary layer, a thin-shear flow that allows certain simplifications to the implementation of the nonlocal and nonequilibrium terms. Not only are nonequilibrium effects due to the $D\overline{S}_{ij}/Dt$ terms not large in thin-shear flows – thus allowing the use of the nonlocal equilibrium formulation for $a_{ij}$ in (5.3), or (5.8) in truncated form – but the mean strain rate tensor is dominated by the shear term $\overline{S}_{12}$ due to the two-dimensionality of the flow (resulting in $\overline{w} = 0$ and $\partial/\partial z = 0$) and the fact that $\partial/\partial y \gg \partial/\partial x$ and $\overline{u} \gg \overline{v}$ in thin-shear flows.

Working with the truncated nonlocal closure in (5.8), which was shown in Section 5.3 to give good agreement with DNS results for the fully-developed turbulent channel flow, computational implementation of the present closure for thin-shear flows requires the calculation of $\nabla^2 \overline{S}_{12}$, which can be approximated as

$$\nabla^2 \overline{S}_{12} \approx \frac{1}{2} \frac{\partial^3 \overline{u}}{\partial y^3} . \tag{5.15}$$

As a result, calculation of the first nonlocal term requires only the third derivative of the mean streamwise velocity $\overline{u}$ with respect to the cross-stream direction $y$. The simplicity of thin-shear flows also allows the use of cartesian grids, for which cross-derivative metric terms in the derivative formulations can be neglected. Thus, defining the generalized coordinates $\xi = \xi(x)$ and $\eta = \eta(y)$, it will be seen that formulating the derivatives in (5.15) requires only the metric term $\eta_y$.

### 5.4.3  Calculation of Cell-Center Derivatives

The Reynolds stress tensor $\overline{u'_i u'_j}$ is required at cell centers for calculation of the turbulence kinetic energy production term $P$, and at cell interfaces for calculation of the flux terms on the right-hand side of (1.3). In the following we outline formulations for cell-center derivatives up to third order, and provide formulations for the cell-interface derivatives in Section 5.4.4.

We can define a general formula for the $n$th order cell-center derivatives as

$$\left(\frac{\partial^n q}{\partial y^n}\right)_{i,j} = \frac{1}{V_{i,j}} \left[ (\eta_y)_{i,j} Q^{(n)}_{i,j} - (\eta_y)_{i,j-1} Q^{(n)}_{i,j-1} \right] , \tag{5.16}$$

where once again $q_{i,j}$ and $V_{i,j}$ are defined at cell centers and the metrics $(\eta_y)_{i,j}$ are defined at north-south cell interfaces. In the following we consider only derivatives with respect to $y$, consistent with the simplifications described in Section 5.4.2 for testing in thin-shear flows, and it is understood that while $q_{i,j}$ denotes a general flow variable, initial implementation of the present closure in ISAAC for the boundary layer case requires only derivatives of the mean streamwise velocity $\overline{u}$.

161

The variables $Q_{i,j}^{(n)}$ and $Q_{i,j-1}^{(n)}$ in (5.16) are defined at the north-south interfaces, and are given by different formulations depending on the order $n$ of the derivative on the left-hand side of (5.16). In the following we outline the formulation of $Q_{i,j}^{(n)}$ and $Q_{i,j-1}^{(n)}$ for $n = 1 - 3$, including values appropriate near viscous wall boundaries for $j = jdim$ and $j = 2$. Since initial testing of the present closure will focus on wall bounded flows, treatments of the derivatives near other types of boundaries will not be considered herein.

### 5.4.3.1  First Derivative $\partial q/\partial y$, $n = 1$

For the first derivative of $q$ with respect to $y$ we have

$$Q_{i,j}^{(1)} = \frac{1}{2}\left(q_{i,j+1} + q_{i,j}\right),\tag{5.17}$$

$$Q_{i,j-1}^{(1)} = \frac{1}{2}\left(q_{i,j} + q_{i,j-1}\right).\tag{5.18}$$

For $j = jdim$ and $j = 2$, which are the cell center locations immediately adjacent to the wall boundaries, we have

$$Q_{i,j}^{(1)} = q_{i,j+1},\quad\text{for}\quad j = jdim,\tag{5.19}$$

$$Q_{i,j-1}^{(1)} = q_{i,j-1},\quad\text{for}\quad j = 2.\tag{5.20}$$

### 5.4.3.2  Second Derivative $\partial^2 q/\partial y^2$, $n = 2$

For the second derivative of $q$ with respect to $y$ we have

$$Q_{i,j}^{(2)} = \frac{2}{(V_{i,j} + V_{i,j+1})}(\eta_y)_{i,j}\left[q_{i,j+1} - q_{i,j}\right],\tag{5.21}$$

$$Q_{i,j-1}^{(2)} = \frac{2}{(V_{i,j-1} + V_{i,j})}(\eta_y)_{i,j-1}\left[q_{i,j} - q_{i,j-1}\right].\tag{5.22}$$

These formulations are also valid for $j = jdim$ and $j = 2$ since $q_{i,j}$ (which is defined at cell-centers for interior locations) is defined on the computational boundaries (cell interfaces) for $j = 1$ and $j = jdim + 1$. As a result, the first derivatives given by (5.21) and (5.22) become one-sided derivatives at $j = 2$ and $j = jdim$, respectively, where $V_{i,j} = 0$ on viscous walls for $j = 1$ and $j = jdim + 1$.

### 5.4.3.3  Third Derivative $\partial^3 q/\partial y^3$, $n = 3$

For the third derivative of $q$ with respect to $y$ we have

$$Q_{i,j}^{(3)} = \frac{1}{2}\left[\left(\frac{\partial^2 q}{\partial y^2}\right)_{i,j+1} + \left(\frac{\partial^2 q}{\partial y^2}\right)_{i,j}\right],\tag{5.23}$$

$$Q_{i,j-1}^{(3)} = \frac{1}{2}\left[\left(\frac{\partial^2 q}{\partial y^2}\right)_{i,j} + \left(\frac{\partial^2 q}{\partial y^2}\right)_{i,j-1}\right].$$ (5.24)

All second derivatives on the right-hand sides of (5.23) and (5.24) are defined at cell centers. The derivative $\left(\partial^2 q/\partial y^2\right)_{i,j}$ which appears in both equations, has already been obtained from (5.16) with (5.21)-(5.22) and does not need to be recalculated. The derivatives $\left(\partial^2 q/\partial y^2\right)_{i,j+1}$ in (5.23) and $\left(\partial^2 q/\partial y^2\right)_{i,j-1}$ in (5.24) are straightforwardly calculated on interior cells (i.e. for $j = 3 : jdim - 1$) using the equations in (5.16) for $n = 2$ with (5.21) and (5.22).

For the cells adjacent to boundaries, namely for $j = jdim$ and $j = 2$, the variables $Q_{i,j}^{(3)}$ and $Q_{i,j-1}^{(3)}$ are equal to the value of the second derivative of $q$ on the cell boundary interfaces. Thus, for $j = jdim$ we have

$$Q_{i,j}^{(3)} = \frac{2}{(V_{i,j} + V_{i,j+1})}(\eta_y)_{i,j}\left[Q_{i,j}^{(2)} - \left(\frac{\partial q}{\partial y}\right)_{i,j}\right], \quad \text{for} \quad j = jdim, \quad (5.25)$$

where $Q_{i,j}^{(2)}$ is defined in (5.21) and $(\partial q/\partial y)_{i,j}$ has already been obtained from (5.16) with (5.17)-(5.20) and does not need to be recalculated. Similarly, for $j = 2$ we have

$$Q_{i,j-1}^{(3)} = \frac{2}{(V_{i,j-1} + V_{i,j})}(\eta_y)_{i,j-1}\left[\left(\frac{\partial q}{\partial y}\right)_{i,j} - Q_{i,j-1}^{(2)}\right], \quad \text{for} \quad j = 2, \quad (5.26)$$

where once again $(\partial q/\partial y)_{i,j}$ has already been obtained and $Q_{i,j-1}^{(2)}$ is defined in (5.22).

### 5.4.4 Calculation of Cell-Interface Derivatives

The general formula for the $n$th order cell-interface derivative is given by

$$\left(\frac{\partial^n q}{\partial y^n}\right)_{i,j} = \frac{2}{(V_{i,j} + V_{i,j+1})}(\eta_y)_{i,j}\left[Q_{i,j+1}^{(n)} - Q_{i,j}^{(n)}\right], \quad (5.27)$$

where the derivative on the left-hand side is defined at north-south cell interfaces and the variables $Q_{i,j+1}^{(n)}$ and $Q_{i,j}^{(n)}$ are defined at cell centers. In the following we outline formulations for $Q_{i,j}^{(n)}$ for $n = 1 - 3$. Note that by contrast to the cell center derivatives in the previous section, which are defined on $j = 2 : jdim$, here we must obtain the derivatives on all cell interfaces where $j = 1 : jdim$.

### 5.4.4.1 First Derivative $\partial q/\partial y$, $n = 1$

For the first derivative of $q$ with respect to $y$ we have simply

$$Q_{i,j+1}^{(1)} = q_{i,j+1}, \quad (5.28)$$

$$Q_{i,j}^{(1)} = q_{i,j} \,. \tag{5.29}$$

These relations are valid over the entire range $j = 1 : jdim$, since $q_{i,jdim+1}$ and $q_{i,1}$ are defined on cell interfaces at the boundaries and the derivatives from (5.27) thus become one-sided, with $V_{i,j} = 0$ at $j = 1$ and $j = jdim + 1$.

### 5.4.4.2  Second Derivative $\partial^2 q/\partial y^2$, $n = 2$

For the second derivative of $q$ with respect to $y$ we follow a similar approach to that employed for the first and third cell center derivatives and define

$$Q_{i,j+1}^{(2)} = \frac{1}{2}\left[\left(\frac{\partial q}{\partial y}\right)_{i,j+1} + \left(\frac{\partial q}{\partial y}\right)_{i,j}\right], \tag{5.30}$$

$$Q_{i,j}^{(2)} = \frac{1}{2}\left[\left(\frac{\partial q}{\partial y}\right)_{i,j} + \left(\frac{\partial q}{\partial y}\right)_{i,j-1}\right], \tag{5.31}$$

where now all first derivatives on the right-hand side of (5.30) and (5.31) are defined at cell interfaces. The derivative $(\partial q/\partial y)_{i,j}$ has already been obtained using (5.27) with (5.28) and (5.29) and does not need to be recalculated. At interior points (i.e. $j = 2 : jdim - 1$) the derivatives $(\partial q/\partial y)_{i,j+1}$ and $(\partial q/\partial y)_{i,j-1}$, which are defined on cell interfaces, are straightforwardly calculated using the relations in (5.27)-(5.29) for $n = 1$.

On the boundary interfaces, for $j = jdim$ and $j = 1$, we have

$$Q_{i,j+1}^{(2)} = \left(\frac{\partial q}{\partial y}\right)_{i,j}, \quad \text{for} \quad j = jdim\,, \tag{5.32}$$

$$Q_{i,j}^{(2)} = \left(\frac{\partial q}{\partial y}\right)_{i,j}, \quad \text{for} \quad j = 1\,, \tag{5.33}$$

where in both cases the derivative on the right-hand side has already been obtained from (5.27)-(5.29) and does not need to be recalculated.

### 5.4.4.3  Third Derivative $\partial^3 q/\partial y^3$, $n = 3$

For the third derivative of $q$ with respect to $y$, the variables $Q_{i,j}^{(3)}$ are obtained from the second derivative of $q$ at cell centers. Cell center second derivatives have been defined in (5.16) with (5.21) and (5.22), and from these relations we obtain

$$Q_{i,j+1}^{(3)} = \frac{1}{V_{i,j+1}}\left[(\eta_y)_{i,j+1}\left(\frac{\partial q}{\partial y}\right)_{i,j+1} - (\eta_y)_{i,j}\left(\frac{\partial q}{\partial y}\right)_{i,j}\right], \tag{5.34}$$

$$Q_{i,j}^{(3)} = \frac{1}{V_{i,j}}\left[(\eta_y)_{i,j}\left(\frac{\partial q}{\partial y}\right)_{i,j} - (\eta_y)_{i,j-1}\left(\frac{\partial q}{\partial y}\right)_{i,j-1}\right]. \tag{5.35}$$

164

Once again, all derivatives on the right-hand side of (5.34) and (5.35) are defined at cell interfaces. The derivative $(\partial q/\partial y)_{i,j}$ has already been obtained and does not need to be recalculated, while the derivatives at $(i, j+1)$ and $(i, j-1)$ can be obtained from (5.27)-(5.29) for interior points (i.e. $j = 2 : jdim - 1$).

On the boundary interfaces, for $j = jdim$ and $j = 1$, we have

$$Q_{i,j+1}^{(3)} = \left(\frac{\partial^2 q}{\partial y^2}\right)_{i,j}, \quad \text{for} \quad j = jdim, \tag{5.36}$$

$$Q_{i,j}^{(3)} = \left(\frac{\partial^2 q}{\partial y^2}\right)_{i,j}, \quad \text{for} \quad j = 1, \tag{5.37}$$

where once again the second derivatives on the right-hand side have already been obtained and do not need to be recalculated.

### 5.4.5  Validation of Derivative Formulas

We can assess the accuracy of the derivative formulas outlined in the preceding sections, as well as their implementation in ISAAC, using the polynomial test function $f(y)$ given by

$$f(y) = y + y^2 + y^3 + y^4. \tag{5.38}$$

Analytical calculation of the derivatives $d^n f/dy^n$ for $n = 1 - 3$ is straightforward, and numerical derivatives of $f(y)$ calculated using the formulas in Sections 5.4.3 and 5.4.4 can be compared with the analytical results to validate the computational implementation of the higher-order derivatives. In particular, derivatives of the function $f(y)$ are calculated using the ISAAC subroutines for the cell center and cell interface derivatives for both unstretched and stretched grids (such as the $65 \times 97$ stretched grid, shown in Figure 5.6, used for the boundary layer tests in the next section), using metric terms taken directly from ISAAC. This thus allows a direct test of not only the accuracy of the derivative formulations in Sections 5.4.3 and 5.4.4, but also the accuracy of their implementation in ISAAC.

Figure 5.7 shows results for unstretched and stretched grids, respectively, from the cell-center and cell-interface derivative calculations, compared with exact analytical results obtained from (5.38). It is clear from Figure 5.7(a) that for the unstretched grid, both the cell-center and cell-interface derivatives are in very good agreement with the exact results at interior points on the computational domain. At the boundaries however, the accuracy of the numerical derivatives begins to deteriorate and for $n = 3$ both the cell-center and cell-interface derivatives are in poor agreement with the analytical results.

Similar trends are seen in the stretched grid results in Figure 5.7(b), where once again the numerical derivatives are in good agreement with the analytical results at interior locations but the agreement becomes relatively poor near the boundaries. There is an additional small error for the third derivative on the stretched grid due primarily to errors introduced

by the calculation of the metric terms within ISAAC, as well as errors due to the decreased accuracy of the derivative formulations in Sections 5.4.3 and 5.4.4 for nonuniform cell spacings. However, these errors result in only small departures from the exact analytical result, and are not expected to pose problems for testing of the present closure in the boundary layer case.

The results in Figure 5.7 thus indicate that the derivative formulas outlined in Sections 5.4.3 and 5.4.4 are not only accurate representations for the exact derivatives at interior points on the computational domain, but have also been implemented correctly in ISAAC. However, it is also clear from Figure 5.7 that more sophisticated representations for the derivatives at cell boundaries are required. In particular, in obtaining the third derivatives in Sections 5.4.3.3 and 5.4.4.3, first-order accurate one-sided derivatives were used several times, resulting in substantially decreased accuracy at the boundaries. By increasing the stencil size of the one-sided derivatives, the final order of accuracy of the third derivatives may be increased.

It should be noted however, that the blended anisotropy formulation in (5.12) will be used for the boundary layer tests in Section 5.5. Due to the behavior of the blending function $\phi$ defined in (5.13), which effectively "de-activates" the present nonlocal closure at locations very near the wall, calculation of $\nabla^2 \overline{S}_{ij}$ at viscous walls is not required for the simulations of the boundary layer presented herein. As a result, the inaccuracies in the higher-order derivatives near boundaries shown in Figure 5.7 are not a problem for the initial implementation of the present closure approach.

### 5.4.6 Formulation of Present Closure in ISAAC

As with the channel flow tests in Section 5.3, the $N = 2$ truncated anisotropy closure in (5.8) is implemented in ISAAC, with the $C_2^{(1)}$ and $C_2^{(2)}$ coefficients given by (3.118). The corresponding nonlocal Laplacian term $\nabla^2 \overline{S}_{ij}$ is given from (5.15) using the derivatives formulated in the previous section. In order to allow integration to the bottom wall for the boundary layer case, the blended anisotropy formulation in (5.12) is used for implementation of the present closure in ISAAC. Here however, the truncated closure in (5.8) is blended with the two-equation $k$-$\epsilon$ model formulated by Speziale, Abid, and Anderson (SAA) [97], where $a_{ij}$ is given by the damped form in (5.11) with $f_\mu$ now written as

$$ f_\mu = \left[ 1 + \frac{3.45}{\sqrt{Re_T}} \right] \tanh \left( \frac{y^+}{70} \right) , \tag{5.39} $$

where $Re_T \equiv k^2 / \nu \epsilon$ is the turbulent Reynolds number. The turbulence kinetic energy $k$ is obtained from the standard form in (1.31), but the dissipation $\epsilon$ in the SAA model is obtained from

$$ \frac{D\epsilon}{Dt} = C_{\epsilon 1} P \frac{\epsilon}{k} - C_{\epsilon 2} f_2 \frac{\epsilon^2}{k} + \frac{\partial}{\partial x_j} \left[ \left( \nu + \frac{\nu_T}{\sigma_\epsilon} \right) \frac{\partial \epsilon}{\partial x_j} \right] , \tag{5.40} $$

166

where $f_2$ is given by

$$f_2 = \left[ 1 - \exp\left( -\frac{y^+}{4.9} \right) \right]^2 \left[ 1 - \frac{2}{9} \exp\left( -\frac{Re_T^2}{36} \right) \right]. \tag{5.41}$$

The blended anisotropy closure is obtained from (5.12), where $a_{ij}^{(f)}$ is given by (5.11) with (5.39), and the present $a_{ij}$ is given by the $N = 2$ truncated form in (5.8).

Given the shear-dominated nature of the boundary layer case, the nonlocal term in (5.8) is only included in the formulation for the shear anisotropy $a_{12} = a_{21}$, and the remaining components of $a_{ij}$ are represented in the same manner as the underlying SAA model, namely $a_{ij} = a_{ij}^{(f)}$. In the closure for $a_{12}$, the eddy viscosity is again given by the standard form in (1.36) using the realizable $C_\mu$ from (1.40). Here the turbulence integral scale $\Lambda$ is given from (3.36) and (3.39) as $\Lambda = 0.23k^{3/2}/\epsilon$, although the low-Reynolds formulation for $\Lambda$ in (5.9) may also be used in the future. The form for $\phi$ in (5.13) with the constants in (5.14) is again used to obtain the blended $a_{ij}$ from (5.12), despite the fact that $f_\mu$ was given by the van Driest form in (1.42) for the channel flow tests and is given here by (5.39) from the SAA model. The independence of the formulation for $\phi$ on the choice of $f_\mu$ reflects, in part, the relatively 'conservative' values of the blending constants in (5.14). For the specific representations for $\Lambda$ and $f_\mu$ used in the boundary layer case, it will be seen that $R/\Lambda \approx 0.9$, which is consistent with the value in (3.125), gives good agreement with experimental results. As with the tests of the present closure outlined in Chapter IV and Section 5.3, the closure implemented in ISAAC is herein denoted the NKE model.

## 5.5  Zero Pressure Gradient Turbulent Boundary Layer

In the zero pressure gradient boundary layer case, a turbulent boundary layer is allowed to develop over a viscous wall at the bottom of the computational domain. Experimental results for this case are available from Klebanoff [47], who measured the mean streamwise velocity $\overline{u}$ and Reynolds stresses $\overline{u'^2}$, $\overline{v'^2}$, $\overline{w'^2}$, and $\overline{u'v'}$ using hot-wire anemometry. As with the fully-developed turbulent channel flow tests in Section 5.3, the turbulent boundary layer is an essentially equilibrium flow where the anisotropy in the near-wall region is heavily influenced by nonlocal effects. In addition to providing a fundamental numerical test of the present closure in a full CFD framework, this case thus also tests the physical accuracy of the present closure for predicting nonlocal effects on the anisotropy in turbulent flows.

The turbulent boundary layer simulated herein consists of turbulent flow over a viscous wall of length $1.5L$, where the Mach number is $M = 0.2$ and the Reynolds number based on $L$ and the incoming flow velocity $U_\infty$ is $Re = 4.2 \times 10^6$. The incoming flow is introduced a distance $0.5L$ upstream of the start of the plate, and the outflow condition is applied a distance $0.5L$ past the location $x = L$, where all computational and experimental profiles are measured. This thus gives an overall width of $2L$ for the computational domain. The

height of the domain is $0.18L$, which will be seen to be on the order of ten boundary layer thicknesses at $x = L$. For all computations, the boundary layer flow is simulated by solving the two-dimensional thin-shear layer equations in ISAAC.

In the following CFD tests, the NKE closure model will be compared with results from "local equilibrium" and "realizable" anisotropy closures. In both these closures, the shear anisotropy $a_{12}$ is obtained from the blended form in (5.12), but the anisotropy away from the wall is given by

$$a_{12} = -2\,(0.09)\,\frac{k}{\epsilon}\overline{S}_{12}\,, \tag{5.42}$$

in the local equilibrium closure, which is based on the classical closure in (1.35), and by

$$a_{12} = -2C_\mu\frac{k}{\epsilon}\overline{S}_{12}\,, \tag{5.43}$$

in the realizable closure, herein denoted the RKE model, where $C_\mu$ in (5.43) is taken from the realizable Bradshaw hypothesis in (1.40). Comparison of results from the present NKE closure model described in Section 5.4.6 with results from the local equilibrium and RKE closures in (5.42) and (5.43), respectively, specifically allows the effect of the nonlocal Laplacian term on the anisotropy to be assessed, independent from effects due to other common aspects of the models, such as the blending function $\phi$, the damping function $f_\mu$, or the realizable $C_\mu$ used in the present closure and (5.43).

### 5.5.1   Computational Results

Computational results for the zero pressure gradient boundary layer are obtained using the $65 \times 97$ computational grid shown in Figure 5.6. The grid is stretched in the $y$ direction up to $0.05L$, and is evenly spaced in the $y$ direction for $0.05L - 0.18L$. The clustering of grid points near the wall gives the first grid point at $y^+ \approx 0.15$. The grid is evenly spaced in the $x$ direction for the entire computational domain. A grid-convergence study, shown in Figure 5.8, for the Reynolds shear stress $-\overline{u'v'}/u_\tau^2$ was carried out for two coarser grids and one finer grid using the present NKE closure. It is clear from Figure 5.8 that results from the $65 \times 97$ grid are in very close agreement with those from the higher resolution $97 \times 129$ grid, indicating that the $65 \times 97$ grid is sufficiently resolved for the boundary layer tests presented in the following.

Figures 5.9-5.15 show results for the mean flow and turbulence statistics in the boundary layer from the present NKE closure, the full SAA model, and the local equilibrium and RKE blended closures in (5.42) and (5.43), respectively. Experimental results for $\overline{u}$ and $\overline{u'v'}$ are available for comparison from Klebanoff [47], but in general close agreement with results from the SAA model can be taken as an indication of good model accuracy. This is because the SAA model has been specifically calibrated to give good predictions of the turbulent boundary layer [97], and in the absence of experimental results for $k$ and $a_{12}$, for example, the SAA model can be taken as a relatively accurate predictor of these variables. It should

be emphasized however, that agreement of either the NKE, local equilibrium, or RKE closures with the SAA model for $y^+ > b^+$ [where $b^+ = 18$ from (5.14)] is significant in that the SAA model requires the damping function $f_\mu$ in (5.39) for all $y^+$ in order to give accurate predictions of the anisotropy. Agreement between any of the closures tested herein with the SAA model is evidence that the flow physics have been accurately captured in the closure, thus removing the need for the *ad hoc* wall damping function for locations away from the wall.

Figure 5.9 shows the mean streamwise velocity fields predicted by the SAA, local equilibrium, and NKE models. All three models predict qualitatively similar fields, although it can be seen that the local equilibrium model predicts a slightly larger boundary layer thickness. The profile of $u^+$ versus $y^+$ in Figure 5.10 shows that the NKE model results are in good agreement with the SAA model and experimental results for all $y^+$, whereas the local equilibrium and RKE models typically under-predict $u^+$ at each $y^+$ value. Moreover, both the local equilibrium and RKE models incorrectly predict the wall friction velocity $u_\tau$, resulting in the under-prediction of $u^+$ in the free-stream, as shown for large $y^+$ in Figure 5.10.

Figure 5.11 shows contours of the shear stress $\overline{u'v'}/U_\infty^2$ for the SAA, local equilibrium, and NKE models. The magnitude of the stresses for the local equilibrium model is in general larger than the respective magnitudes from the SAA and NKE models, due to the absence of nonlocal effects which act to decrease the shear anisotropy in the near-wall region. The profile of $-\overline{u'v'}/u_\tau^2$ in Figure 5.12, measured at $x = L$, shows similar results, where both the SAA and NKE models are in good agreement while the local equilibrium and RKE models over-predict the shear stress magnitude for $18 < y^+ < 100$. Agreement with the available experimental results is generally fairly good for all models, although it is clear that there are substantial differences between the local equilibrium and RKE models compared to the SAA and NKE models for $y^+ < 100$, where experimental data is not available. Similar trends are seen for the profile of the shear anisotropy $-a_{12}$ in Figure 5.13, where once again the SAA and NKE models are in good agreement while the local equilibrium and RKE models significantly over-predict the anisotropy magnitude in the near-wall region. The over-predicted anisotropy magnitude from the local equilibrium and RKE models is consistent with the over-predicted anisotropy magnitude given by the SKE and RKE models for the turbulent channel flow results in Figures 5.3 and 5.4.

The contour plots of the turbulence kinetic energy $k$ in Figure 5.14 show that results from the present closure are once again in qualitatively better agreement with the SAA model results than results from the local equilibrium model in (5.42). Compared to the SAA and NKE models, the local equilibrium model predicts slightly larger kinetic energy magnitudes away the bottom wall and smaller magnitudes very near the wall. This is also shown in the kinetic energy profiles in Figure 5.15, where results for $k^+$ from the present closure are in good agreement with results from the SAA model, while the local equilibrium

and RKE models both under-predict the kinetic energy amplitude compared to the SAA and NKE results in the near-wall region.

Finally, with respect to the stability and convergence properties of the present closure approach, the nonlocal Laplacian term in the present closure generally imposes tighter restrictions on the time step used in the boundary layer simulations. A semi-implicit approximate factorization routine was used to solve the boundary layer case in ISAAC, and it was found that use of the present nonlocal closure typically required smaller Courant-Friedrichs-Lewy (CFL) numbers to obtain converged solutions for the mean flow and turbulent fields. However, for the same CFL number and grid resolution, it was observed that the convergence rate of the present approach was similar to that for the SAA, local equilibrium, and RKE models. In all cases, computational residuals at the last computational iteration were reduced by eight orders of magnitude compared to their initial values.

## 5.6   Further Considerations of the Anisotropy in Wall-Bounded Flows

The channel flow and boundary layer results presented herein show that by addressing nonlocal effects due to spatial variations in the mean strain rate tensor, the present anisotropy closure provides substantially improved predictions of the turbulence anisotropy in wall bounded flows. As first noted in Section 5.3 however, the present approach begins to over-predict the anisotropy magnitude in the extreme near-wall region of the turbulent channel at $y^+ \approx 16$. While it was shown that a closure valid for all $y^+$ could be obtained through the use of the blended anisotropy formulation in (5.12), the inaccuracies below $y^+ \approx 16$ reflect the importance of additional physical effects not accounted for by the present approach in the near-wall region. These additional physical effects most notably include low-Reynolds number and viscous effects, nonlocal effects due to inhomogeneities in the turbulence variables, and nonlinear effects on the anisotropy.

The decreasing local Reynolds number for $y^+ < 20$ poses perhaps the greatest issues for the present closure in the near-wall region. As the local Reynolds number decreases, viscous effects become increasingly important and many of the key assumptions used to obtain the effective strain formulation in (3.110) or (3.123) become inaccurate. While some viscous effects have been addressed by the formulation for $\Lambda$ in (5.9), additional improvements in the near-wall region may be achieved using the low-Reynolds number formulation for the $C_2^{(n)}$ coefficients in (3.70). The decreasing local Reynolds number also affects the accuracy of the high Reynolds number isotropic approximation for the dissipation tensor $\epsilon_{ij}$ in (1.20), since the anisotropic part of $\epsilon_{ij}$ can become significant for low Reynolds numbers. Finally, as viscous effects become increasingly dominant in the near-wall region, it may no longer be appropriate to neglect the viscous diffusion term $\nu \nabla^2 a_{ij}$ in the $D_{ij}$ transport term in (3.82). Retaining effects due to this term may provide improved anisotropy predictions in the near-wall region.

In order to derive the nonlocal rapid pressure-strain correlation on which the present

anisotropy closure is based, the effect of inhomogeneities in the turbulence variables, including $\Lambda$, were neglected. As discussed in Section 3.6.1, the nonlocal modification in (3.126) proposed by Launder and Tselepidakis may account for the first-order nonlocal correction due to turbulence inhomogeneities. Figure 3.8 provides a qualitative comparison of the correction terms due to inhomogeneities in the turbulence and mean strain rate, and it is clear that for $y^+ < 10$ effects due to the turbulence inhomogeneities may become dominant compared to nonlocal effects from spatial variations in the mean strain.

Finally, nonlinear effects on the anisotropy evolution can become important in instances where $P/\epsilon$ is large, or the higher-order terms of the form $a_{il}\overline{S}_{lj}$ and $a_{il}\overline{W}_{lj}$ are large with respect to the quasi-linear terms on the right-hand side of (3.84). Some nonlinear effects have already been accounted for indirectly through the use of the realizable $C_\mu$ from (1.40), which is motivated by the fact that $C_\mu$ scales as $(P/\epsilon)^{-1}$ and must therefore be limited in the near-wall region where both $P/\epsilon$ and $Sk/\epsilon$ become large. However, additional higher-order nonlinear terms have been neglected in obtaining the quasi-linear anisotropy equation in (3.84) from the full transport equation in (3.82). As noted in Chapter I, explicit algebraic stress models have been formulated to specifically address nonlinear effects due to these missing terms, and many such models are calibrated using DNS or experimental results of the anisotropy in wall bounded flows. Addressing nonlinearity in a similar fashion within the current nonlocal and nonequilibrium closure approach may provide further improvements to the predictions of the anisotropy in the near-wall region.

In conclusion, it is clear that the truncated anisotropy closure in (5.8), obtained from the full nonlocal, nonequilibrium closure in (3.97) with the effective strain from (3.110) or (3.123), is sufficient to give substantially improved predictions of the anisotropy down to $y^+ \approx 16$ in wall bounded flows. Below this location however, additional physical effects become important, and additional modifications to the closure are necessary in order to avoid the use of the blended anisotropy formulation in (5.12). Nevertheless, each of these issues can be addressed in a physically-meaningful and systematic fashion in future work, and it is expected that blended models based on *ad hoc* wall-damping functions will eventually be unnecessary.
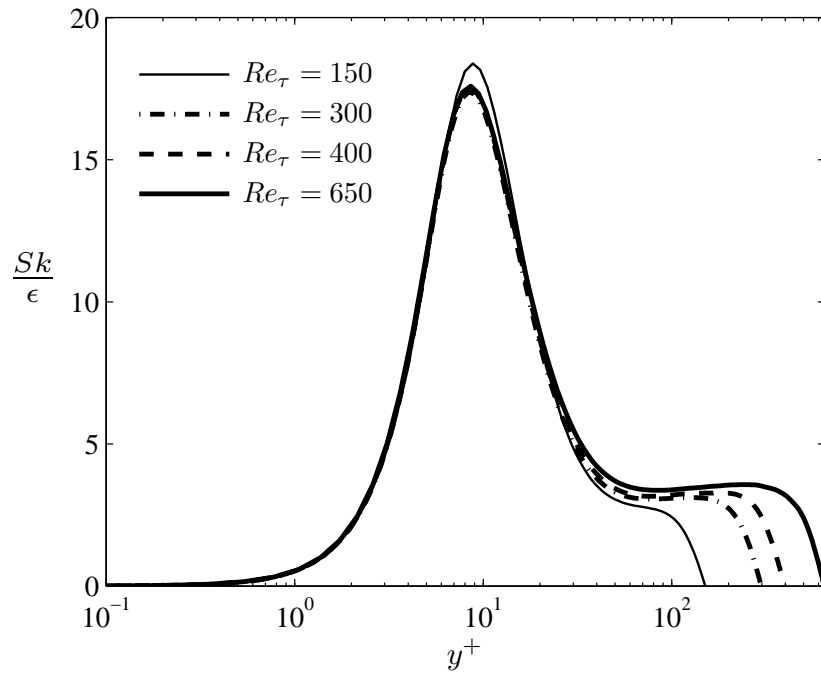
Figure 5.1: Nondimensional shear parameter $Sk/\epsilon$ as a function of $y^+$ for fully developed turbulent channel flow DNS from Iwamoto *et al.* [39].
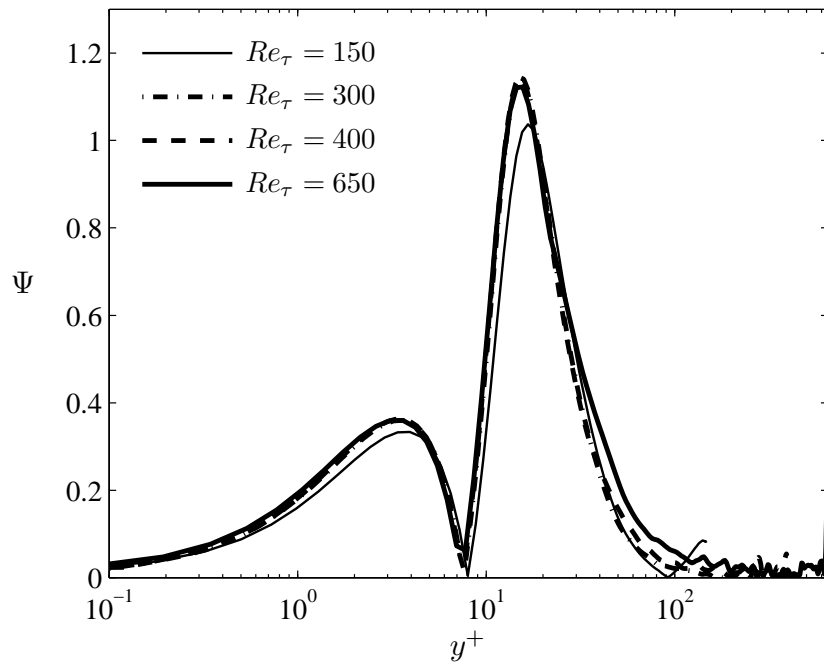


Figure 5.2: Nonlocal parameter $\Psi$ defined in (3.105) as a function of $y^+$ for fully developed turbulent channel flow DNS from Iwamoto *et al.* [39].
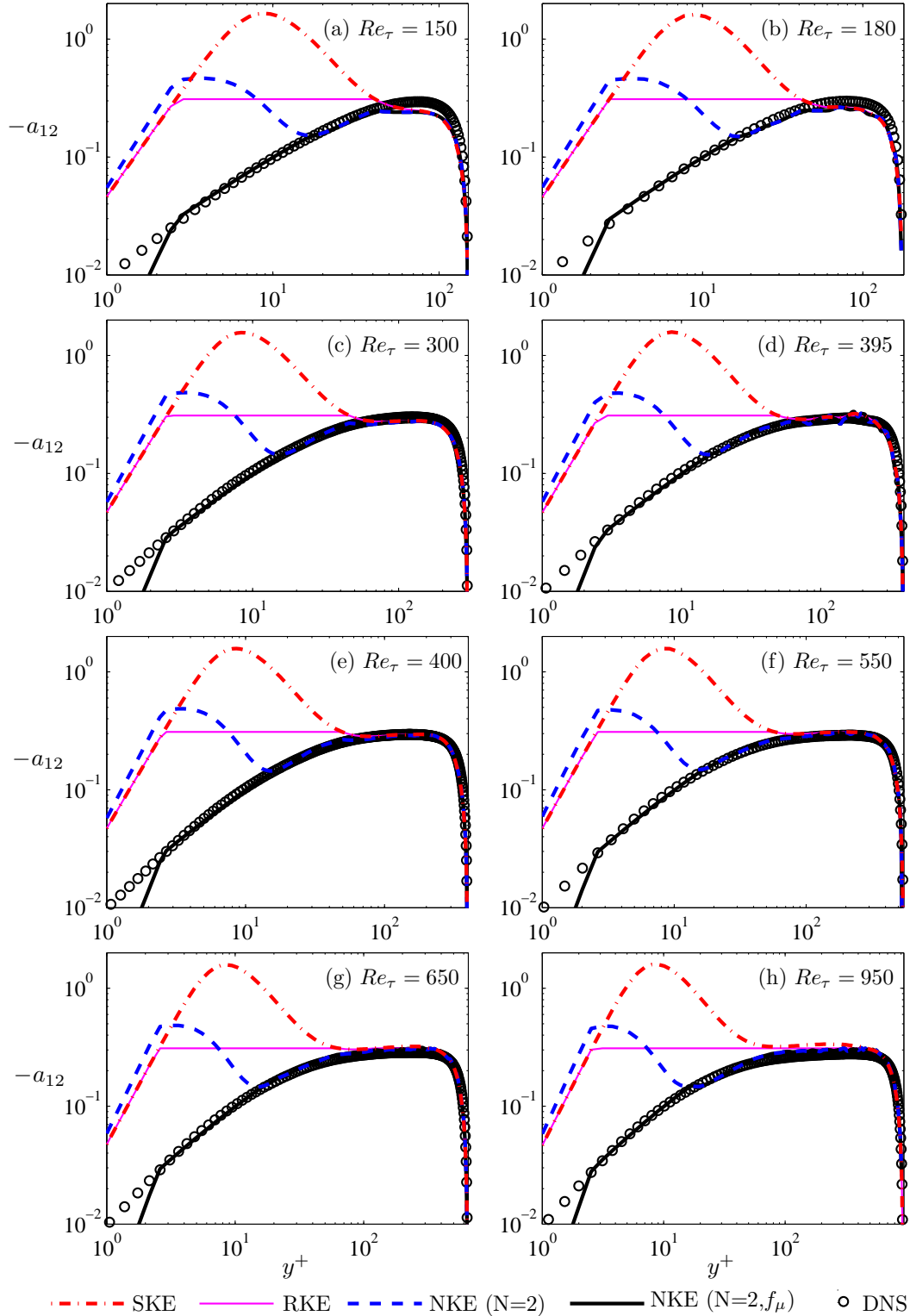
Figure 5.3: Shear anisotropy $-a_{12}$ as a function of $y^+$ for $Re_\tau = 150$ (a) – $Re_\tau = 950$ (h) in fully-developed turbulent channel flow. Results from the standard (SKE) and realizable (RKE) $k$-$\epsilon$ models, the present closure (NKE), and the blended NKE closure in (5.12) are compared with DNS results from Iwamoto *et al.* [39] ($Re_\tau = 150, 300, 400, 650$), Moser *et al.* [67] ($Re_\tau = 180, 395$), and Hoyas and Jimenez [37] ($Re_\tau = 550, 950$).
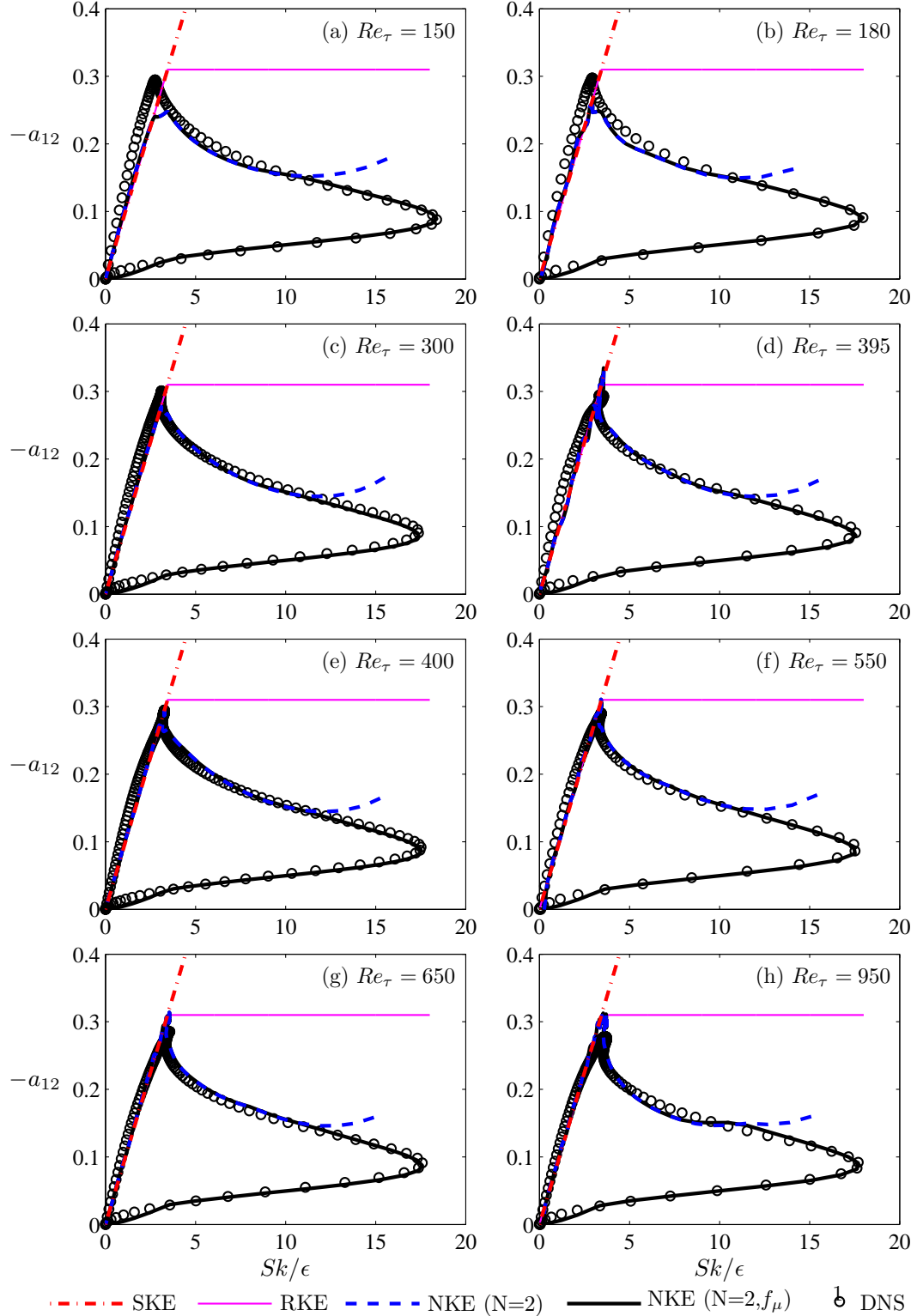
Figure 5.4: Shear anisotropy $-a_{12}$ as a function of $Sk/\epsilon$ for $Re_\tau = 150$ (a) – $Re_\tau = 950$ (h) in fully-developed turbulent channel flow. Results from the standard (SKE) and realizable (RKE) $k$-$\epsilon$ models, the present closure (NKE), and the blended NKE closure in (5.12) are compared with DNS results from Iwamoto *et al.* [39] ($Re_\tau = 150, 300, 400, 650$), Moser *et al.* [67] ($Re_\tau = 180, 395$), and Hoyas and Jimenez [37] ($Re_\tau = 550, 950$).

174
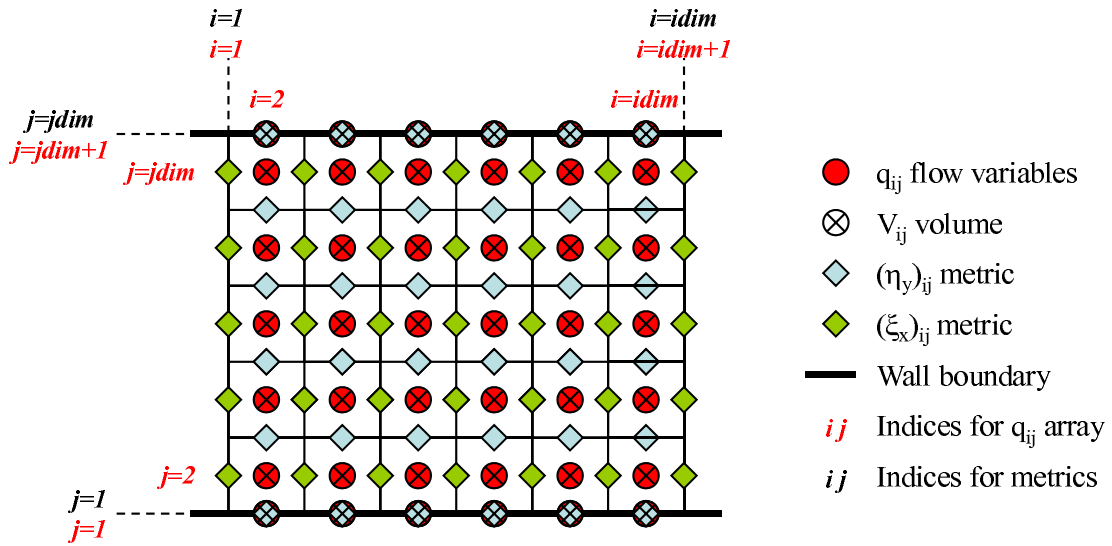
Figure 5.5: Schematic of the location of all variables and the numbering of the indices on the interior of the computational domain and on the cell boundaries.
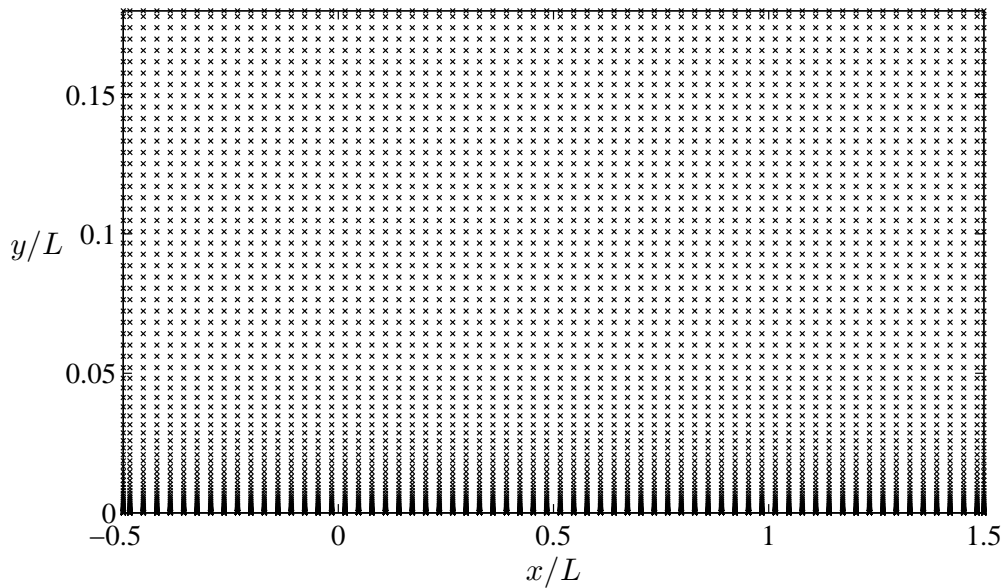


Figure 5.6: Computational grid for zero pressure gradient boundary layer case showing stretching in $y$ direction. Grid dimensions are $65 \times 97$.
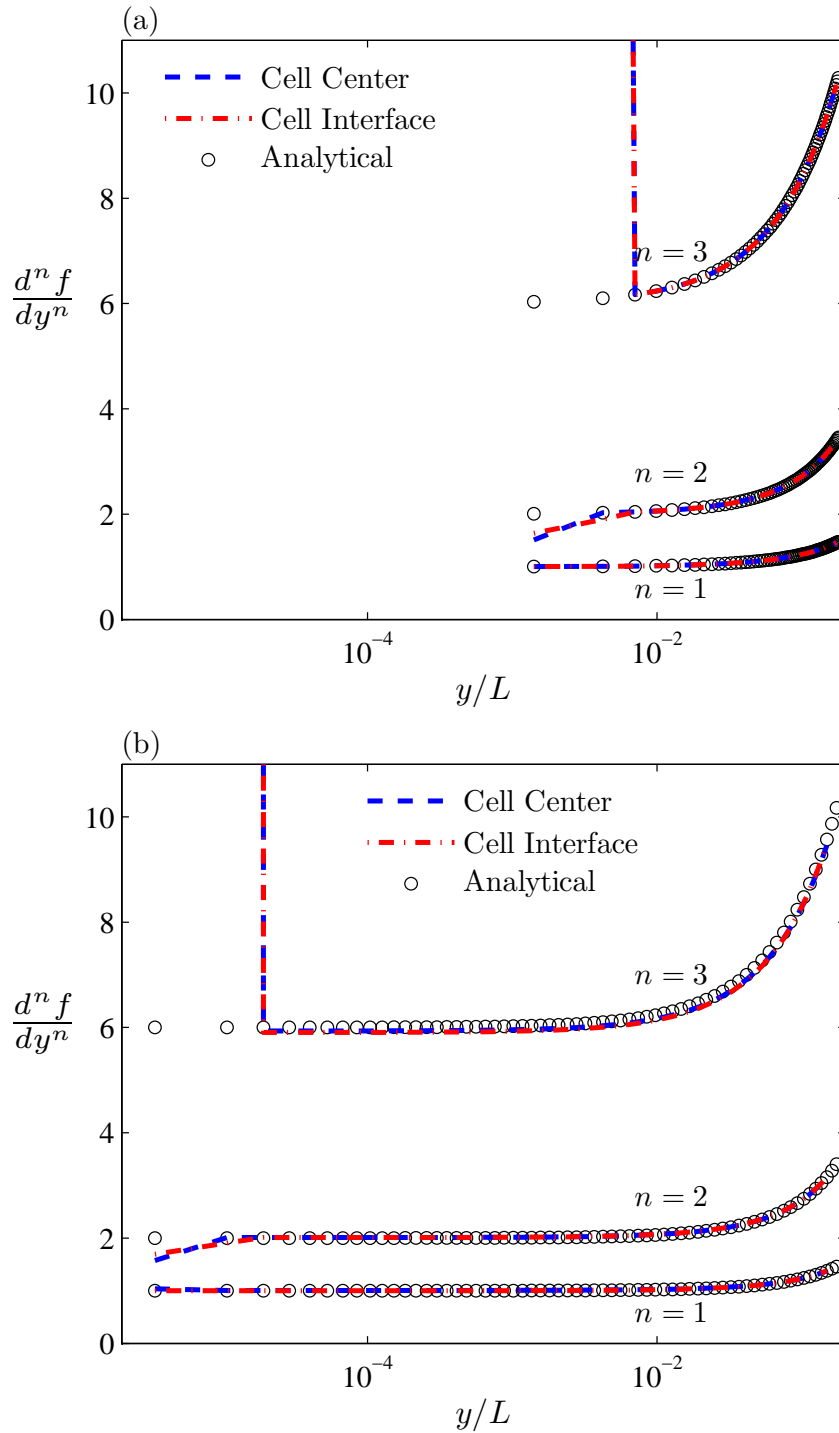
Figure 5.7: Accuracy of derivative calculations for the function $f(y)$ defined in (5.38) using evenly spaced (a) and stretched (b) computational grids.
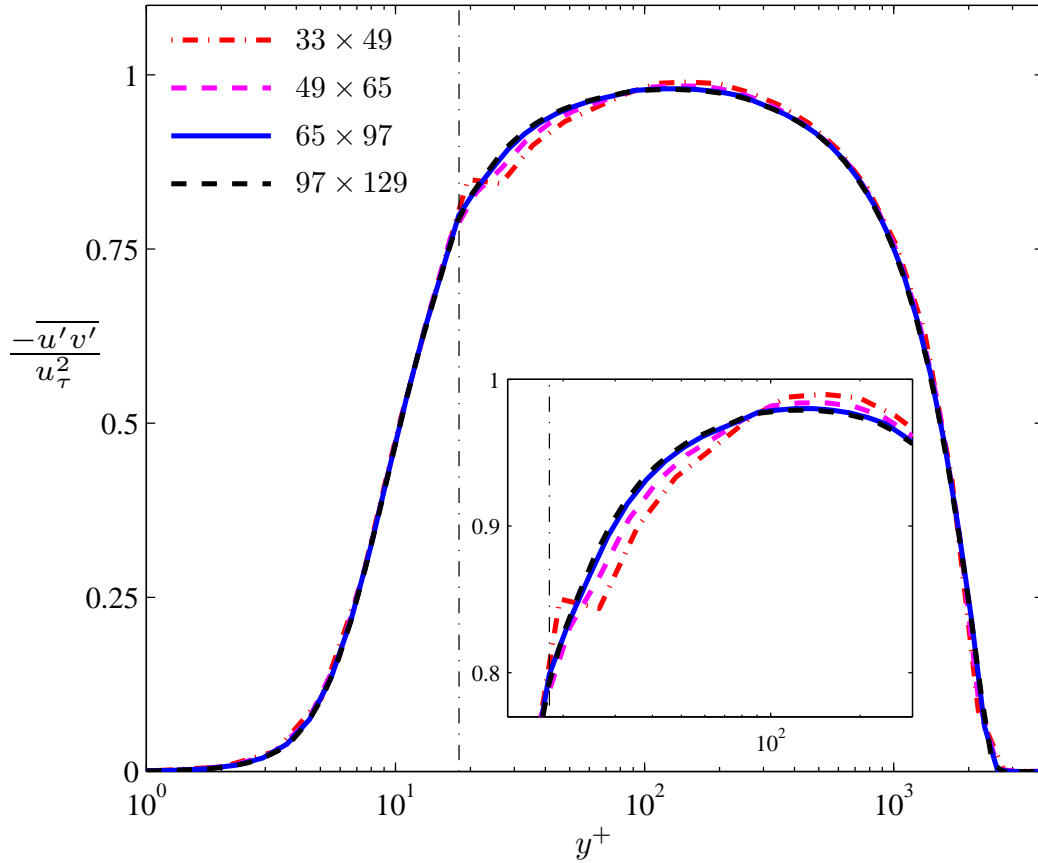
Figure 5.8: Profile of $-\overline{u'v'}/u_\tau^2$ at $x/L = 1$ for the zero pressure gradient boundary layer. Results from the blended NKE closure model are compared for four different grid resolutions, showing that the $65 \times 97$ grid in Figure 5.6 is sufficiently resolved for the present boundary layer simulations. The vertical dash-dot line denotes the transition point from the wall-damped $a_{ij}$ to the present nonlocal $a_{ij}$ at $y^+ \approx 18$, and the inset shows convergence of the computational results near this location as the grid resolution increases.
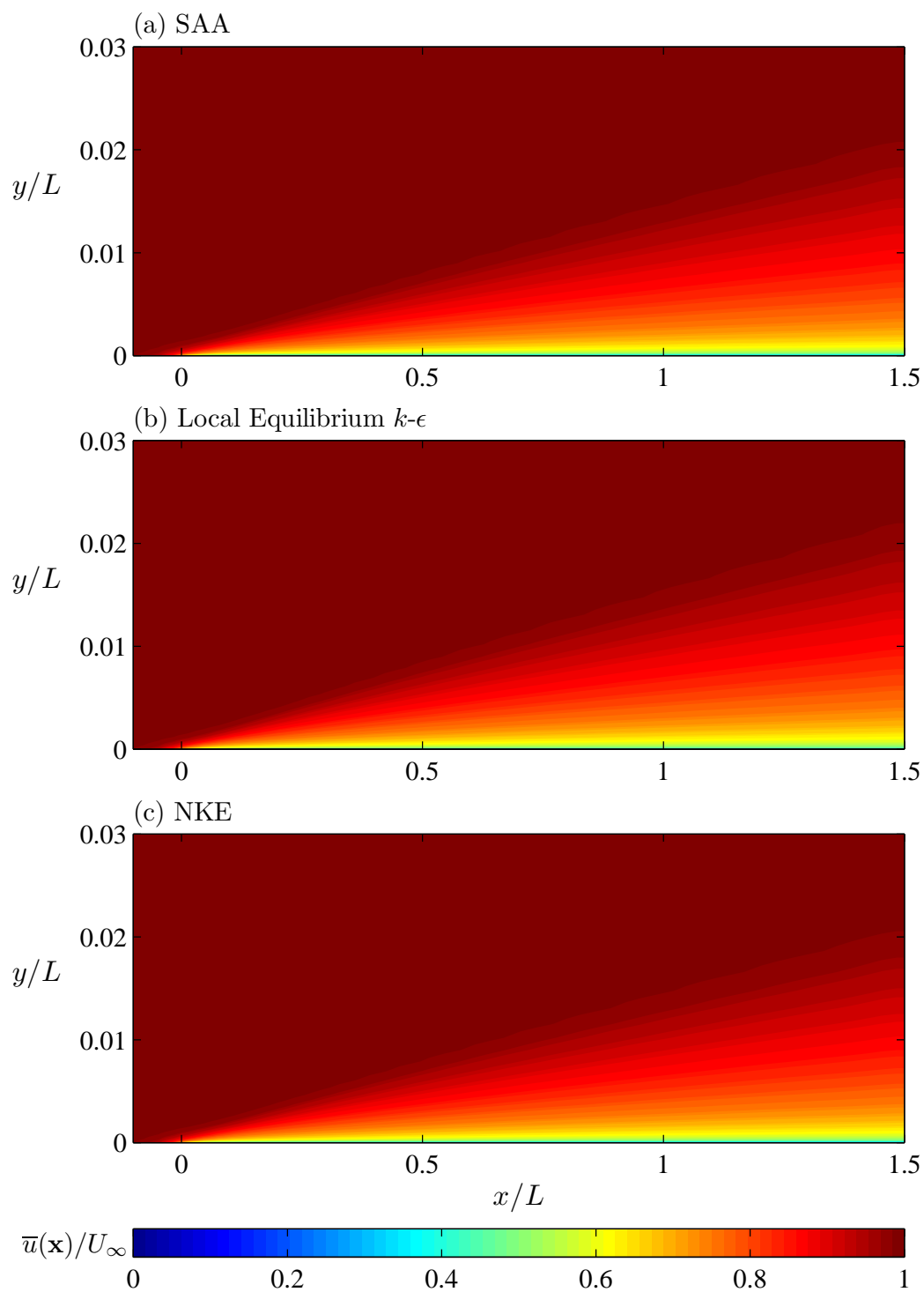
Figure 5.9: Mean streamwise velocity $\overline{u}/U_\infty$ for the zero pressure gradient boundary layer. Results are shown from the Speziale, Abid, Anderson (SAA) model [97] (a), the local equilibrium $k$-$\epsilon$ model in (5.42) (b), and the present blended closure (NKE) (c).
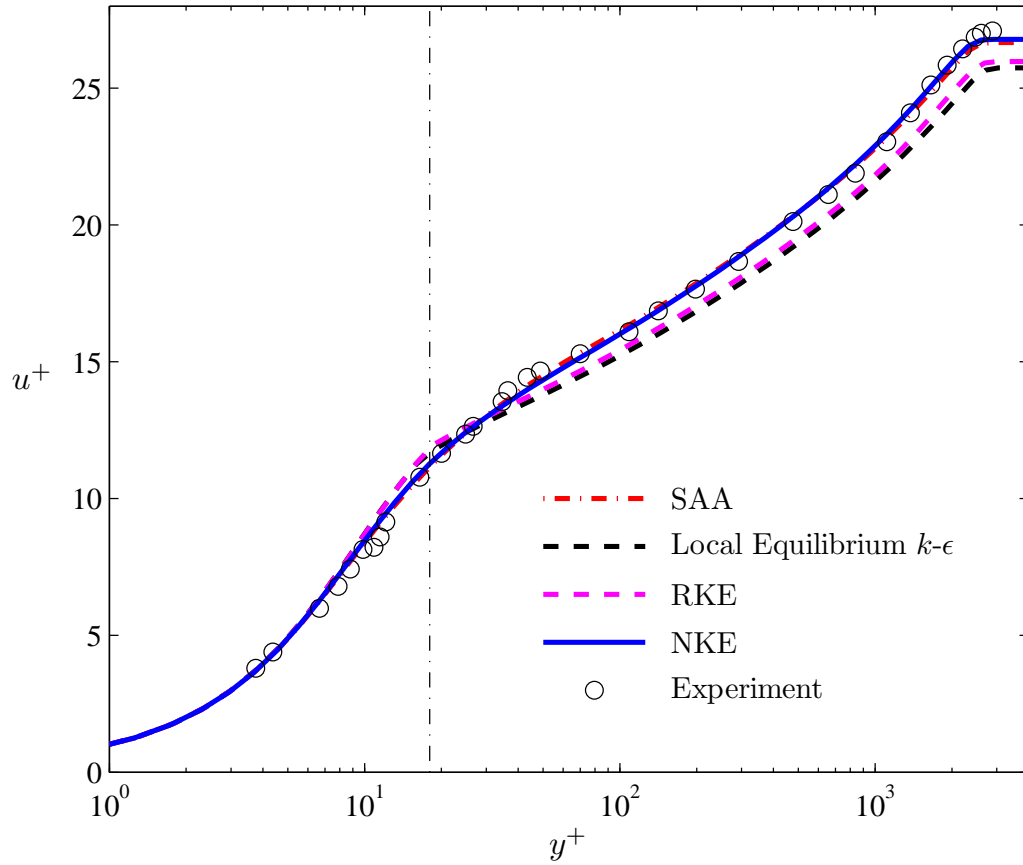
Figure 5.10: Profile of $u^+$ at $x/L = 1$ for the zero pressure gradient boundary layer. Results from the Speziale, Abid, Anderson (SAA) model [97], the local equilibrium $k$-$\epsilon$ model in (5.42), the realizable model in (5.43), and the present blended closure (NKE) are compared with experimental results from Klebanoff [47]. The vertical dash-dot line denotes the location $y^+ \approx 18$ at which the wall-damped $a_{ij}$ is blended with $a_{ij}$ from the local equilibrium, RKE, and NKE models.
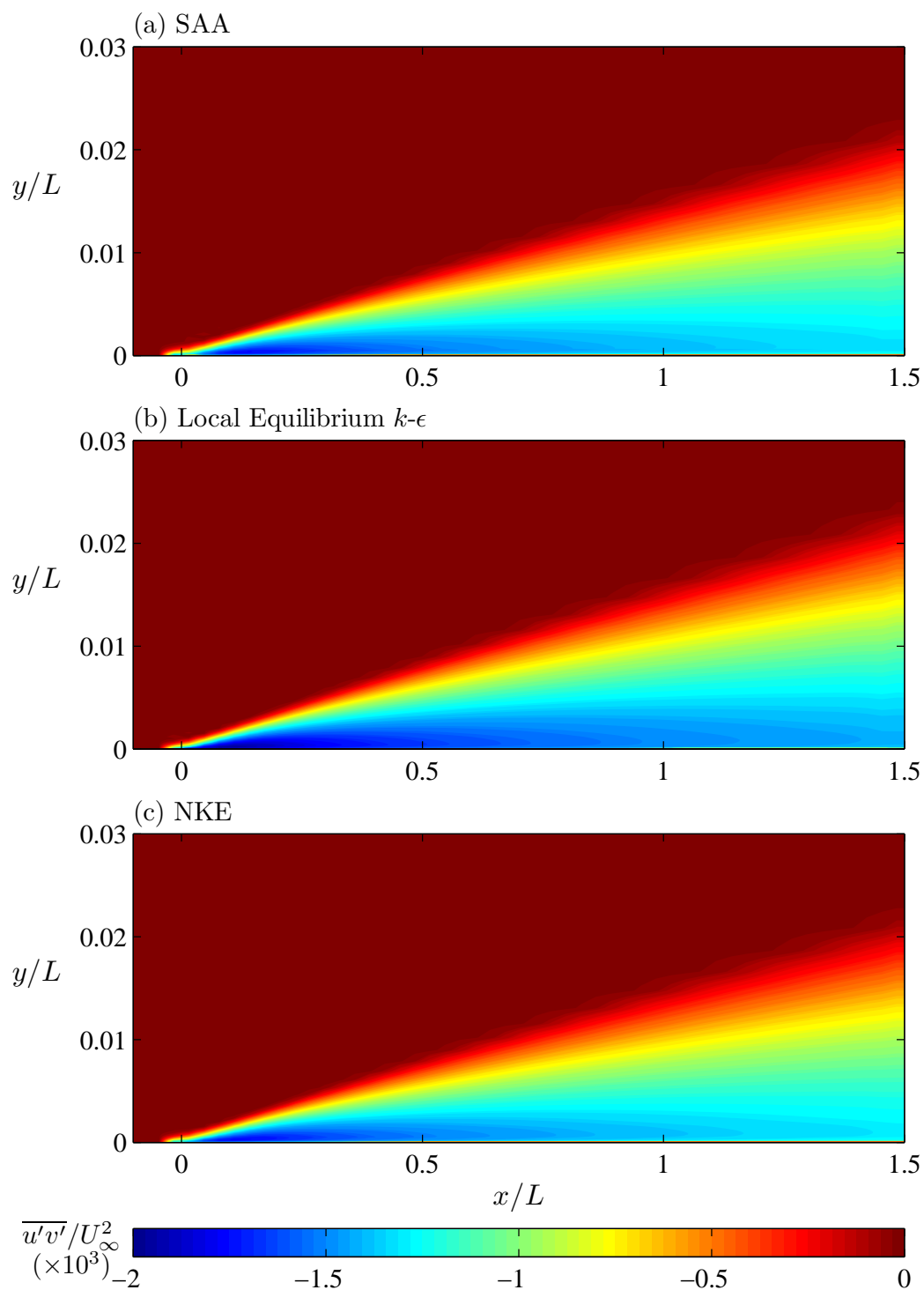
Figure 5.11: Shear stress $\overline{u'v'}/U_\infty^2$ for the zero pressure gradient boundary layer. Results are shown from the Speziale, Abid, Anderson (SAA) model [97] (a), the local equilibrium $k$-$\epsilon$ model in (5.42) (b), and the present blended closure (NKE) (c).
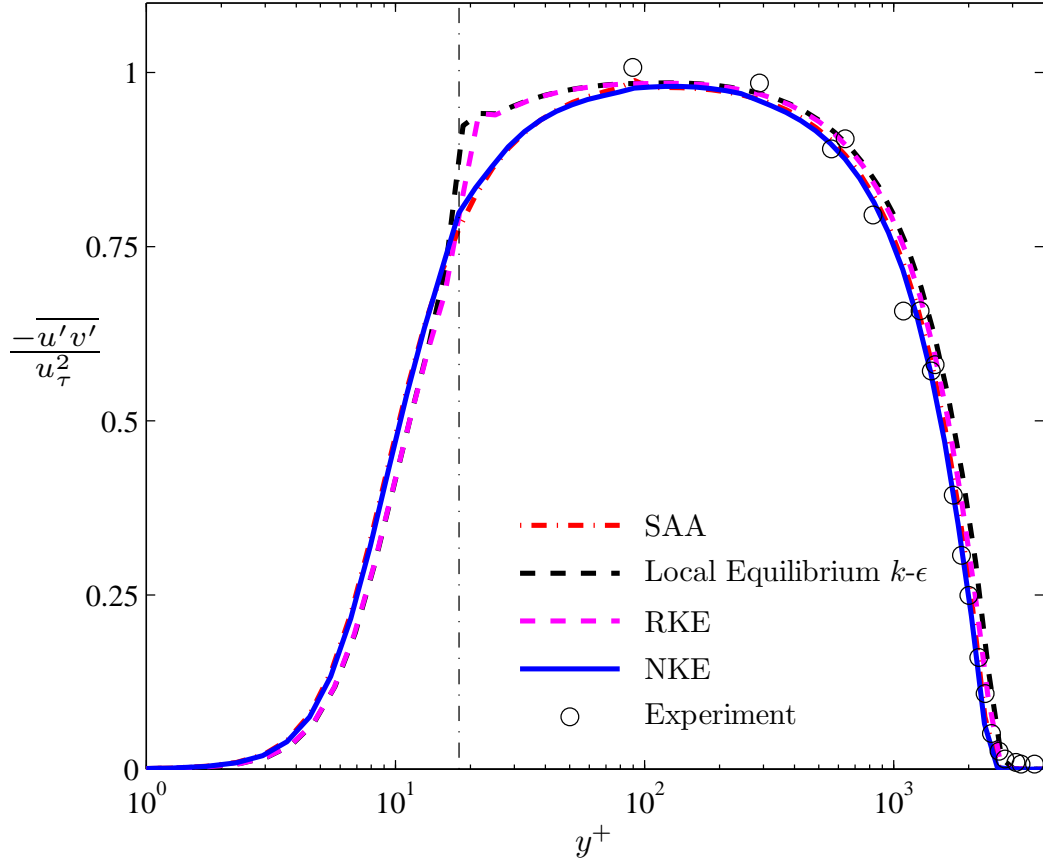
Figure 5.12: Profile of $-\overline{u'v'}/u_\tau^2$ at $x/L = 1$ for the zero pressure gradient boundary layer. Results from the Speziale, Abid, Anderson (SAA) model [97], the local equilibrium $k$-$\epsilon$ model in (5.42), the realizable model in (5.43), and the present closure (NKE) are compared with experimental results from Klebanoff [47]. The vertical dash-dot line denotes the location $y^+ \approx 18$ at which the wall-damped $a_{ij}$ is blended with $a_{ij}$ from the local equilibrium, RKE, and NKE models.
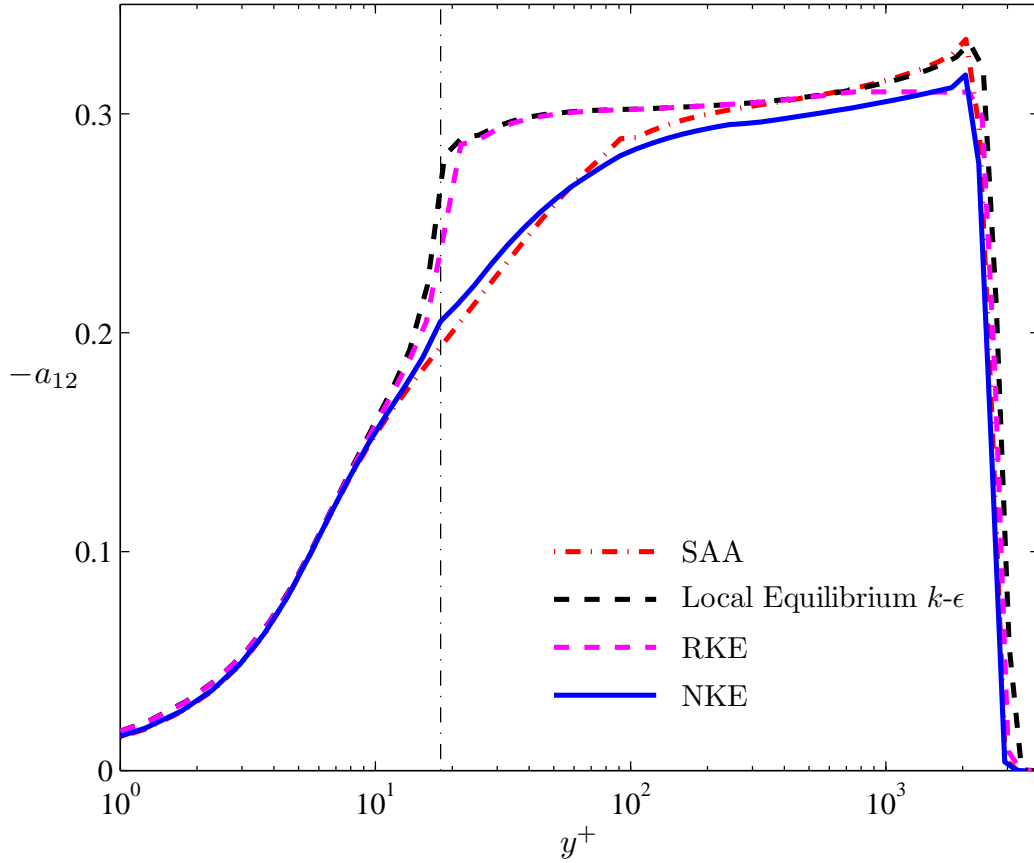
Figure 5.13: Profile of $-a_{12}$ at $x/L = 1$ for the zero pressure gradient boundary layer. Results are shown from the Speziale, Abid, Anderson (SAA) model [97], the local equilibrium $k$-$\epsilon$ model in (5.42), the realizable model in (5.43), and the present blended closure (NKE). The vertical dash-dot line denotes the location $y^+ \approx 18$ at which the wall-damped $a_{ij}$ is blended with $a_{ij}$ from the local equilibrium, RKE, and NKE models.
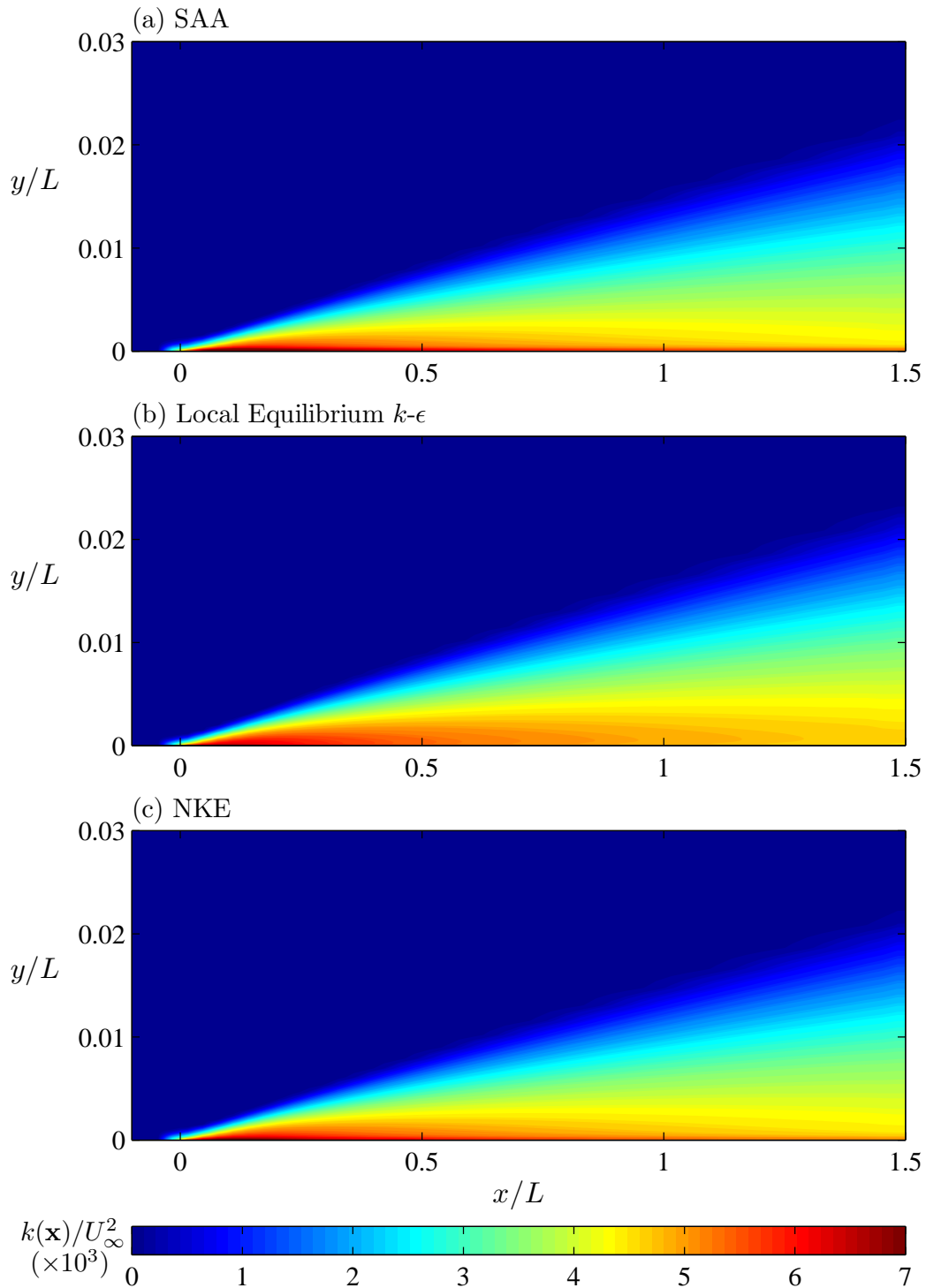
Figure 5.14: Turbulence kinetic energy $k/U_\infty^2$ for the zero pressure gradient boundary layer. Results are shown from the Speziale, Abid, Anderson (SAA) model [97] (a), the local equilibrium $k$-$\epsilon$ model in (5.42) (b), and the present blended closure (NKE) (c).
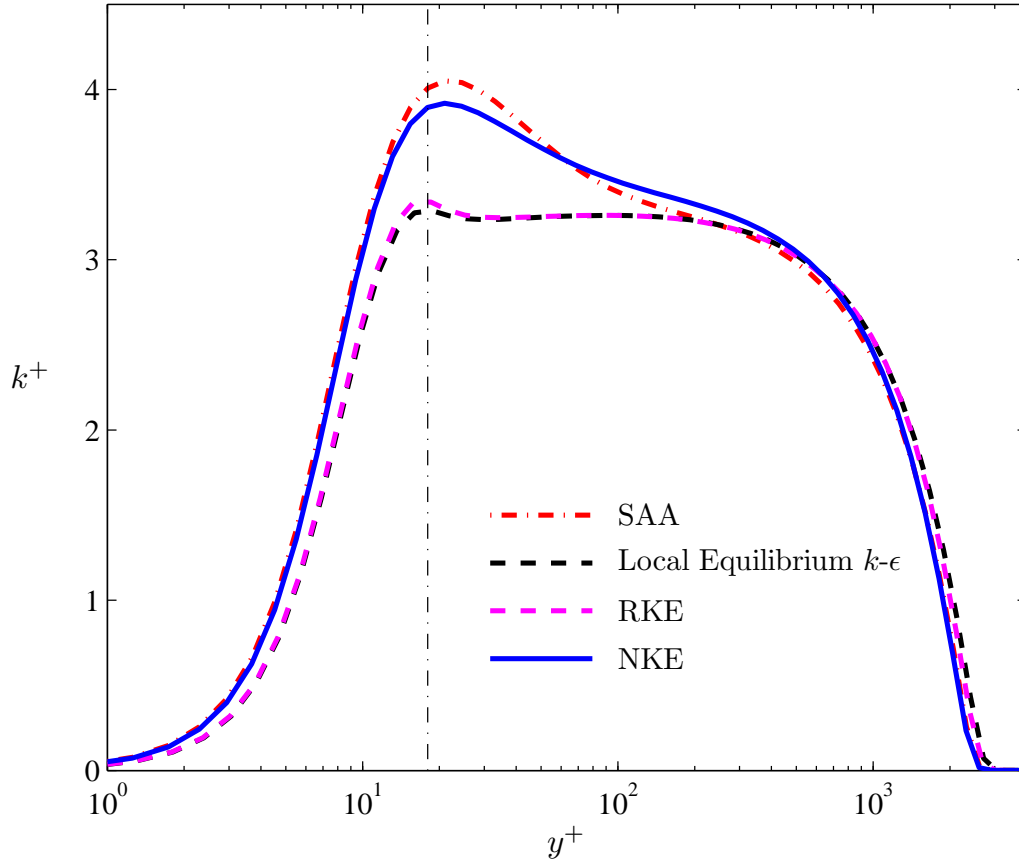
Figure 5.15: Profile of $k^+ \equiv k/u_\tau^2$ at $x/L = 1$ for the zero pressure gradient boundary layer. Results are shown from the Speziale, Abid, Anderson (SAA) model [97], the local equilibrium $k$-$\epsilon$ model in (5.42), the realizable model in (5.43), and the present blended closure (NKE). The vertical dash-dot line denotes the location $y^+ \approx 18$ at which the wall-damped $a_{ij}$ is blended with $a_{ij}$ from the local equilibrium, RKE, and NKE models.

# Conclusions and Future Research

The present study has outlined the derivation and validation of a new anisotropy closure for nonlocal and nonequilibrium effects in turbulent flows. This closure is motivated by fundamental studies of the vorticity alignment in turbulent flows, which have revealed a substantial nonlocal, quasi-linear aspect to the vorticity dynamics. This result suggests that the anisotropy evolution may also be understood as a quasi-linear system, where the anisotropy and vorticity are rigorously connected through the double Biot-Savart integral in (2.2).

Nonlocal effects on the anisotropy evolution have been accounted for through the derivation of a new nonlocal formulation for the rapid pressure-strain correlation. Using this formulation, a nonlocal transport equation for the anisotropy has been obtained, and a quasi-linear solution of this equation gives the present nonlocal, nonequilibrium anisotropy closure in (3.97). The anisotropy in (3.97) is written in an analogous form to the classical equilibrium closure in (1.35), except that the mean strain $\overline{S}_{ij}$ is replaced with the nonlocal, nonequilibrium effective strain $\widetilde{S}_{ij}$ defined in (3.96). Application of this new closure to a range of nonlocal and nonequilibrium tests provides significantly improved agreement with experimental and computational validation results than standard closure approaches. A nonlocal equilibrium form of the present closure has also been successfully implemented in a full computational framework for solving (1.2)-(1.4).

In the following a number of more detailed conclusions from the present work are outlined, followed by a brief discussion of future research directions.

## 6.1 Conclusions

($i$) Through decomposition of the total strain rate tensor into its local and nonlocal (background) constituents, it has been shown that there is a substantial nonlocal, quasi-linear contribution to the vorticity dynamics in turbulent flows. Through direct calculation of the local and nonlocal strain fields in high-resolution DNS using their respective Biot-Savart integrals, it has been shown that the vorticity preferentially aligns with the most extensional eigenvector of the background

strain rate tensor. This result reflects the importance of locally two-dimensional structures – such as Burgers vortex tubes and sheets – in turbulent flows, and is in contrast to the previously observed preferential alignment of the vorticity with the intermediate eigenvector of the total strain. Moreover, the alignment with the most extensional background strain suggests that the vorticity responds in a quasi-linear manner to the nonlocal strain field. Consideration of the nonlocal to local vortex stretching magnitudes indicates that in much of the flow there is a substantial nonlocal contribution to the vorticity dynamics, and this result is used to motivate the quasi-linear solution for the anisotropy that forms the basis of the present nonlocal, nonequilibrium closure outlined herein.

(*ii*) In addition to the direct approach for calculating the local and nonlocal strain fields, a systematic and exact expansion has been developed in (2.45) that allows the local and nonlocal contributions to the total strain to be disentangled. The approach is based on a series expansion of the vorticity field in a local spherical neighborhood of radius $R$ centered at the point $\mathbf{x}$. This allows the background strain field to be determined via a series of increasingly higher-order Laplacians applied to the total strain field. For the Burgers vortex test case, with increasing radius $R$ relative to the local gradient lengthscale $\lambda_\nu$ and with increasing order $n$, convergence of the resulting background strain tensor field to its theoretical form has been demonstrated.

(*iii*) Consistent with the results for the Burgers vortex, when the background strain expansion in (2.45) was used to determine the background strain in highly-resolved DNS of homogeneous isotropic turbulence, the alignment between the vorticity and the intermediate eigenvector of the total strain seen in previous DNS and experimental studies was substantially reduced, consistent with results obtained when calculating the background strain directly using a Biot-Savart integral. As a result, it can be concluded that (2.45) allows the local background strain to be determined in any flow.

(*iv*) Motivated by the importance of nonlocal effects on the vorticity dynamics, a rigorous and complete formulation for the rapid pressure-strain correlation $\Pi_{ij}^{(r)}$, including both local and nonlocal effects, has been obtained in (3.66) with (3.67) for $Re_\Lambda \gg 1$ or (3.70) for $Re_\Lambda \to 0$. Nonlocal effects are rigorously accounted for through Taylor expansion of the mean velocity gradients appearing in the exact integral relation for $\Pi_{ij}^{(r)}$ in (3.9). The derivation is based on the central hypothesis that the nonlocality in $\Pi_{ij}^{(r)}$ is substantially due to spatial variations in $\partial \overline{u}_k / \partial x_l$ in (3.9), and that in order to address this effect all other factors in (3.9) can be adequately represented by their homogeneous isotropic forms. The resulting rapid pressure-strain correlation in (3.66) takes the form of an infinite

186

series of increasing-order Laplacians of the mean strain rate field $\overline{S}_{ij}(\mathbf{x})$, with the $n = 1$ term recovering the classical purely-local form in (3.19), and with the remaining $n \geq 2$ terms accounting for all nonlocal effects due to spatial variations in the mean-flow velocity gradients $\partial \overline{u}_k / \partial x_l$.

$(v)$ Using the new nonlocal formulation for $\Pi_{ij}^{(r)}$ in (3.66) with (3.67) or (3.70), a nonlocal transport equation for the turbulence anisotropy has been obtained in (3.82) and (3.83). This equation can be solved by any number of standard methods, including full Reynolds stress transport or linear and nonlinear eddy viscosity approaches. The nonlocal anisotropy equation is aimed at providing substantially improved accuracy in simulations of inhomogeneous turbulent flows, including free-shear and wall-bounded flows, where strongly nonuniform mean flow properties and significant large scale structures introduce substantial nonlocal effects in the turbulence anisotropy.

$(vi)$ Applying physical insights obtained from the fundamental studies of vorticity alignment, a new anisotropy closure has been developed that includes both nonlocal and nonequilibrium effects on $a_{ij}$, but that can be readily implemented within existing computational frameworks based on the classical equilibrium closure in (1.35). Solution of a quasi-linear form of the nonlocal transport equation in (3.84) gives the anisotropy as a convolution integral over the strain history to which individual material elements have been subjected. The anisotropy is then given by (3.97), which is written in an analogous form to the classical equilibrium closure in (1.35) where the *local instantaneous* mean strain rate tensor $\overline{S}_{ij}$ appearing in the equilibrium closure is replaced with the *nonlocal, nonequilibrium effective* strain rate tensor $\widetilde{S}_{ij}$ defined in convolution integral form in (3.96).

$(vii)$ Careful attention has been paid to issues of practical model implementation, and the convolution integral for the effective strain in (3.96) has been written in equivalent time-local form in (3.110). This form for $\widetilde{S}_{ij}$ allows increasingly higher-order nonlocal and nonequilibrium effects to be included by retaining increasingly higher-order terms in the resulting series. Practical use of the present anisotropy closure will require truncations of (3.110), and it has been shown in Section 3.5.2 how the coefficients in the series expansions are modified for finite-order truncations of the expression for $\widetilde{S}_{ij}$ in (3.110).

$(viii)$ In Chapter IV the present closure from (3.97) with (3.96) was applied to a range of substantially different nonequilibrium homogeneous test cases. In all cases, results from the present closure showed dramatic improvements over the classical equilibrium closure in (1.35). For impulsively strained turbulence the

present closure captures the finite-time increase in the anisotropy magnitude immediately after the straining is applied, and gives predictions of the turbulence kinetic energy that are in better agreement with computational results than predictions from the equilibrium closure. In unstrained decaying anisotropic turbulence, the present closure predicts nonzero anisotropy for $t > 0$, whereas the equilibrium closure incorrectly predicts $a_{ij} = 0$ whenever the applied strain is zero. Additionally, the present closure produces much more accurate time lags and anisotropy magnitudes than the equilibrium closure in the straining, relaxation and destraining experiment of Chen, Meneveau and Katz [11] over the entire cycle. For periodically-sheared turbulence, the present closure correctly predicts the reduction in anisotropy magnitude and increase in phase lag with increasing straining frequency seen in the DNS results of Yu and Girimaji [115]. Moreover, the phase difference between the applied periodic shear and the resulting anisotropy is correctly produced over all straining frequencies from the equilibrium limit to the saturated nonequilibrium limit. In nearly all cases, results from the present closure were comparable to results from the more computationally intensive LRR [51] Reynolds stress transport model.

(ix) The present closure has permitted a detailed parametric study of the dynamics of initially-isotropic homogeneous turbulence subjected to periodic shear at any shearing magnitude $S$ and frequency $\omega$. The present frequency response analysis indicates that at the critical frequency $\omega_{cr}$, defined in (4.45), periodically sheared homogeneous turbulence abruptly enters a saturated nonequilibrium limit that persists for all $\omega > \omega_{cr}$. Moreover, for $\omega > \omega_{cr}$ the anisotropy amplitude decays as $\omega^{-1}$, the phase difference between the anisotropy and the applied shear reaches the frequency-independent value $\phi = \pi/2$, the cycle average of $P/\epsilon$ decays as $\omega^{-2}$, and the turbulence kinetic energy $k$ asymptotically approaches zero. This last result is in agreement with DNS [115], and indicates that turbulence cannot be sustained for shearing frequencies greater than the critical frequency $\omega_{cr}$.

(x) The nonlocal behavior of the present closure has been evaluated using tests in fully-developed turbulent channel flow in Chapter V. In the channel flow, the present anisotropy closure was evaluated for eight different Reynolds number cases, where $\overline{S}_{ij}$, $k$, and $\epsilon$ were obtained from DNS databases, allowing a direct assessment of the present approach. For all Reynolds numbers, the present closure approach shows good agreement with DNS results down to $y^+ \approx 16$, and agreement down to $y^+ = 0$ was obtained by blending the present closure with prior closures based on *ad hoc* wall damping functions.

(xi) The present closure was successfully implemented in a CFD code for solving

(1.2)-(1.4), and was used to simulate the zero pressure gradient boundary layer. Consistent with results for the turbulent channel flow, the present closure provided improved anisotropy predictions for $y^+ < 100$ in the boundary layer compared to models based on the local equilibrium closure in (1.35). By accounting for nonlocal effects on the anisotropy in a physically-accurate manner, the present closure could be integrated to $y^+ \approx 18$, and a wall-damping function was only required for locations very close to the wall. This is a significant improvement over many existing computational models, which require an *ad hoc* wall damping function for all $y^+$ in order to obtain accurate predictions of the anisotropy. While convergence of the present closure generally required smaller CFL numbers than models based on the local equilibrium closure in (1.35), the boundary layer results presented herein nevertheless show that the present closure can be stably implemented in existing CFD codes for solving practical turbulent flow problems.

($xii$) With respect to the two current areas of turbulence modeling research noted in Section 1.4.1, the present work has advanced both the physical representation for the anisotropy as well the method by which the anisotropy is obtained from this representation. Specifically, the present formulation for nonlocal effects in the rapid pressure-strain correlation gives the nonlocal anisotropy transport equation in (1.28), which accounts for nonlocal effects that essentially all prior approaches neglect. This equation is then solved in such a way as to retain nonequilibrium effects on the turbulence anisotropy, once again improving on many popular prior approaches that specifically neglect these effects by making equilibrium assumptions for the anisotropy dynamics.

## 6.2   Future Research

($i$) The background strain expansion in (2.45) is based on a Taylor series expansion of the vorticity within a spherical neighborhood of radius $R$ around any point $\mathbf{x}$. Such an expansion inherently involves derivatives of the total strain rate tensor field, which can lead to potential numerical limitations. If larger $R$ and correspondingly higher orders $n$ are needed to obtain accurate evaluations of background strain rate fields, then otherwise identical approaches based on alternative expansions may be numerically advantageous. For instance, an expansion in terms of orthonormal basis functions allows the coefficients to be expressed as integrals over the vorticity field within $r \leq R$, rather than as derivatives evaluated at the center point $\mathbf{x}$. (For example, wavelets have been used to test alignment between the strain rate eigenvectors and the vorticity gradient in two-dimensional turbulence [79].) This would allow a result analogous to (2.45)

189

that can be carried to higher orders with less sensitivity to discretization error.

(*ii*) The double Biot-Savart integral in (2.2) relating the Reynolds stresses to the two-point vorticity fluctuation correlation deserves deeper consideration. The time dynamics of the Reynolds stresses from this relation are entirely determined by the time dynamics of the two-point vorticity fluctuation correlation, and this may allow a direct and rigorous connection between the anisotropy and vorticity dynamics to be established. Nearly all prior approaches for obtaining rigorous representations for the anisotropy have focused on the exact anisotropy transport equation in (1.19) but, as noted in Chapter I, it has been difficult to obtain a closure from this equation due to the presence of unclosed pressure-strain, dissipation, and transport terms. Some progress may thus be made through further examination of the double integral relation in (2.2), perhaps using Taylor expansion techniques such as those employed in the derivation of the background strain tensor and nonlocal rapid-pressure strain formulation.

(*iii*) Despite the inclusion of some nonlocal effects due to the rapid pressure-strain correlation in the exact anisotropy transport equation in (1.19), research is still required to obtain more accurate representations for the pressure-strain, dissipation, and transport terms. In particular, additional nonlocal and anisotropic effects on the slow and rapid pressure-strain correlations are important in a number of flows, including wall bounded flows. With respect to nonlocal effects due to inhomogeneities in the turbulence, some progress may be achieved using the modified longitudinal correlation outlined in Section 3.6.1. New representations for the dissipation and transport terms were not addressed in the present work, but additional improvements in predictions of the anisotropy may be gained by accounting for additional physical effects in these terms. For instance, the dissipation is typically represented by its high-Reynolds number isotropic form, as discussed in Chapter I, but in locally low-Reynolds number regions, such as near walls, more sophisticated anisotropic representations for the dissipation are required.

(*iv*) It may be possible to derive more physically-accurate approaches for solving the nonlocal anisotropy transport equation in (3.82). In the present work a nonlocal, nonequilibrium representation for the anisotropy was obtained by solving the quasi-linear equation in (3.84), but this required much of the nonlinearity in (3.82) to be neglected. Following prior approaches for obtaining explicit algebraic stress models, it may be possible to obtain a closure for the anisotropy that accounts for nonlinear, nonlocal, and nonequilibrium effects in turbulent flows. An outline of how some basic nonlinear effects may be retained in the present closure approach is outlined in Appendix 6.2.

($v$) The continued implementation and testing of the present anisotropy closure in full computational frameworks for solving (1.2)-(1.4) is perhaps the most important direction for future research. Throughout this study, substantial attention has been paid to how the present closure will be implemented in existing codes for solving (1.2)-(1.4), and in Chapter V it was shown that the first nonlocal correction term, namely $\nabla^2 \overline{S}_{ij}$, could be stably applied in simulations of the turbulent boundary layer. Further work is required to implement additional higher-order nonlocal terms, as well as include nonequilibrium effects due to the $D^n \overline{S}_{ij}/Dt^n$ terms in (3.110) or (3.123). A more detailed study of the convergence and stability properties of the present approach is also required. Ultimately, simulations of complex turbulent flow problems of practical importance – where both nonlocal and nonequilibrium effects on the anisotropy may be significant – are the primary goal for future research involving the present closure approach.

# APPENDIX

# APPENDIX A

# Nonlinear Eddy-Viscosity for Present Nonlocal, Nonequilibrium Anisotropy Closure

The present closure in (3.97) with the effective strain $\widetilde{S}_{ij}$ given by (3.96), (3.110), or (3.123) accounts for nonlocal and nonequilibrium effects on the anisotropy in turbulent flows. However, the present closure is fundamentally obtained from the solution of the quasi-linear anisotropy transport equation in (3.84), and thus nearly all nonlinear effects on the anisotropy evolution have been neglected. There are a number of possible approaches for addressing at least some of this nonlinearity within the present nonlocal and nonequilibrium closure, and in the following we outline a nonlinear representation for the eddy viscosity that accounts for the dependence of $C_\mu$, which is rigorously defined in (1.37), on the production-to-dissipation ratio $P/\epsilon$.

## A.1 Formulation of Nonlinear $C_\mu$

It is well known that the the constant eddy viscosity coefficient $C_\mu$ defined in (1.39) – which is typically used with the representation for $\nu_T$ in (1.36) – is generally inaccurate in flows where the production-to-dissipation ratio $P/\epsilon$ becomes large [23, 42]. This can be seen explicitly by considering the representation for the eddy viscosity obtained from (1.36) and (1.37) with the $\alpha_i$ coefficients in (3.83), namely

$$\nu_T = -\left[\frac{C_2^{(1)} - 4/3}{2(P/\epsilon - 1 + C_1)}\right]\frac{k^2}{\epsilon}. \tag{A.1}$$

This form is rigorously connected to the nonlocal anisotropy equation in (3.82), where $C_2^{(1)}$ is given by (3.67) or (3.70) and $C_1$ is obtained from the choice of model for the slow pressure-strain correlation $\Pi_{ij}^{(s)}$.

The explicit dependence of $\nu_T$ on $P/\epsilon$ in (A.1) can be accounted for within the present anisotropy closure for nonlocal and nonequilibrium effects by noting that $P/\epsilon$ is given from

(1.18) as

$$\frac{P}{\epsilon} = 2\frac{\nu_T}{\epsilon}\widetilde{S}_{ij}\overline{S}_{ij}\,, \tag{A.2}$$

where the present closure in (3.97) has been used for the anisotropy $a_{ij}$. Substituting (A.2) in (A.1) and rearranging yields a quadratic equation for $\nu_T$ as

$$\frac{4\widetilde{S}_{ij}\overline{S}_{ij}}{\epsilon}\nu_T^2 + 2(C_1 - 1)\nu_T + \left(C_2^{(1)} - \frac{4}{3}\right)\frac{k^2}{\epsilon} = 0\,. \tag{A.3}$$

Defining the eddy viscosity as $\nu_T \equiv \widetilde{C}_\mu k^2/\epsilon$ we then obtain a corresponding quadratic equation for $\widetilde{C}_\mu$, namely

$$\widetilde{C}_\mu^2 + \frac{(C_1 - 1)}{\eta^2}\widetilde{C}_\mu + \frac{\left(C_2^{(1)} - 4/3\right)}{2\eta^2} = 0\,, \tag{A.4}$$

which has the solution

$$\widetilde{C}_\mu = \frac{(1 - C_1)}{2\eta^2} + \frac{1}{2\eta^2}\left[(C_1 - 1)^2 - 2\eta^2\left(C_2^{(1)} - \frac{4}{3}\right)\right]^{1/2} \quad \text{for} \quad \eta \neq 0\,, \tag{A.5}$$

$$\widetilde{C}_\mu = \frac{C_2^{(1)} - 4/3}{2(1 - C_1)} \quad \text{for} \quad \eta = 0\,, \tag{A.6}$$

where

$$\eta \equiv \frac{k}{\epsilon}\sqrt{2\widetilde{S}_{ij}\overline{S}_{ij}}\,. \tag{A.7}$$

The parameter $\eta$ contains both nonlocal and nonequilibrium effects due to its dependence on the effective strain $\widetilde{S}_{ij}$, in contrast to previous nonlinear approaches for the eddy viscosity that depend only on $\overline{S}_{ij}$. Following a somewhat similar approach to that used to obtain the realizable $C_\mu$ in (1.40), the value of $\widetilde{C}_\mu$ from (A.5)-(A.7) can be limited to values less than the standard value $C_\mu^* = 0.09$ in (1.39). This then gives $C_\mu$ as

$$C_\mu = \min\left[\widetilde{C}_\mu, C_\mu^*\right]\,. \tag{A.8}$$

where the eddy viscosity is still given in the context of a $k$-$\epsilon$ model framework by (1.36).

Figure A.1 shows the dependence of $C_\mu$ from (A.5)-(A.8) on the parameter $\eta$, where the LRR model [51] constants in (1.26) have been used to obtain $C_1$, and $C_2^{(1)}$ is obtained from (3.67). It is clear from Figure A.1 that at $\eta \approx 5.23$ the value of $C_\mu$ begins to decrease with increasing $\eta$. This is strongly reminiscent of realizable representations for $C_\mu$ such as that in (1.40), where $C_\mu$ is reduced for large values of $Sk/\epsilon$. Figure A.1 shows that the current nonlinear $C_\mu$ is in qualitative agreement with the realizable $C_\mu$ from (1.40), where the realizable $C_\mu$ has been plotted with respect to $Sk/\epsilon$ instead of $\eta$. The quantitative differences between the two representations for $C_\mu$ are due in large part to the choice of

$C_1$ from the LRR model in (1.26). Indeed, the present nonlinear $C_\mu$ has been rigorously derived from the nonlocal anisotropy transport equation in (1.28), whereas the realizable $C_\mu$ from (1.40) is empirically calibrated to give good agreement with turbulent channel flow results. Nevertheless, the resulting closure for the anisotropy using the eddy viscosity in (1.36) with $C_\mu$ from (A.5)-(A.8) and $a_{ij}$ from (3.97) accounts for nonlinear, nonlocal, and nonequilibrium effects on the turbulence anisotropy.

## A.2 Nonlinear $C_\mu$ in Impulsively-Sheared Homogeneous Turbulence

The accuracy of the nonlinear $C_\mu$ from (A.5)-(A.8) is readily evaluated for impulsively-sheared homogeneous turbulence, where the applied mean shear is given in (4.9). From (4.7), the present closure based on the convolution effective strain rate in (3.96) yields

$$a_{12}(t) = -C_\mu \frac{k}{\epsilon} S \left[ 1 - e^{-t/\Lambda_m} \right] . \tag{A.9}$$

It has already been shown in Figures 4.1 and 4.2 using the constant $C_\mu$ from (1.39) that the present closure provides better agreement with LES results [3] than the equilibrium form in (4.5). When $C_\mu$ from (A.5)-(A.8) is used instead of (1.39) in (A.9), we obtain the results for the kinetic energy evolution shown for four different values of the initial shear parameter $Sk_0/\epsilon_0$ in Figure A.2. As $Sk_0/\epsilon_0$ increases, the equilibrium closure in (4.5) and the nonequilibrium closure in (A.9) with constant $C_\mu = 0.09$ significantly overpredict the kinetic energy magnitude for all times when compared with LES and LRR model results. In the sense that (A.9) with $C_\mu$ given by (A.5)-(A.8) is intended as an approximate solution to the full modeled anisotropy transport equation in (1.28), we generally expect results using the nonlinear $C_\mu$ to be in good agreement with the underlying model used to obtain $C_1$, which in this case is the LRR model. Indeed, Figure A.2 shows that the LRR and nonlinear $C_\mu$ results are in good agreement for large shearing magnitudes in Figures A.2(a)-(c), and the agreement begins to deteriorate only for the *very* large shear in Figure A.2(d). Further improvements in the nonlinear model predictions require the $P/\epsilon$ dependence of $C_\Lambda$ to be addressed as well as the inclusion of higher-order nonlinear terms in the closure.

## A.3 Considerations of "Realizability" in Turbulence

In addition to the Bradshaw form for $C_\mu$ in (1.40), various other "realizable" turbulence models have been formulated to deal with the effects of large $P/\epsilon$ or $Sk/\epsilon$ (see, for example, the nonlinear realizable model developed by Shih *et al.* [93]). However, it is not clear that explicit considerations of realizability are an appropriate tool for turbulence model development [99]. It is of course important to ensure that the normal Reynolds stresses are strictly positive, but closure approaches that have been forced to agree with various aspects of the "Lumley triangle" [57] are not necessarily physically-accurate representations of real

turbulent flows. As discussed in Chapter I, it is preferable instead to base all closure approaches on the exact anisotropy transport equation in (1.19). As long as the models for the unclosed terms in (1.19) are carefully constructed, and not too much of the physics is neglected in obtaining a representation for the anisotropy (for example, the equilbrium closure in (1.35) neglects essentially all of the anisotropy dynamics, whereas the present closure retains important effects due to the $Da_{ij}/Dt$ term), then the resulting model must, by virtue of its physical accuracy, be "realizable." By this reasoning, realizable models seek simply to mitigate inaccuracies introduced by imperfect solutions of the exact transport equation for $a_{ij}$, rather than addressing the underlying problem – namely missing physics – at its source. Thus, here we simply note the similarity of the present nonequilibrium $C_\mu$ in (A.5)-(A.8) to prior models that have been derived solely from considerations of realizability, and claim that this connection is not surprising given that the current closure is inherently more "realizable" due to the present attempt at physical rigor.

It should also be noted that (A.5)-(A.8) is by no means the first attempt to develop a formulation for $C_\mu$ that accounts for nonequilibrium effects. Indeed, the various nonequilibrium eddy viscosity models outlined at the end of Chapter III all attempt to account for nonequilibrium effects on the anisotropy through new formulations for the eddy viscosity. For example, from the Yoshizawa and Nisizima [113] model in (3.137), an effective nonequilibrium coefficient $\widetilde{C}_\mu$ can be obtained as

$$\widetilde{C}_\mu = C_\mu \left[ \frac{1 - C(C_{\epsilon 2} - 2)}{1 + CC_\mu(2 - C_{\epsilon 1}) \left( \frac{Sk}{\epsilon} \right)^2} \right] , \tag{A.10}$$

where $C = 1.3$ and $\nu_T = \widetilde{C}_\mu k^2/\epsilon$. It is clear from Figure A.1 that (A.10) is in qualitative, if not quantitative, agreement with the realizable $C_\mu$ in (1.40) and the present form in (A.5)-(A.8). However, it should also be noted that (A.10) is fundamentally not a nonequilibrium formulation for $\nu_T$, since it depends only on the local, instantaneous value of $Sk/\epsilon$.

It is thus important to make a careful distinction between true nonequilibrium eddy viscosity models that account for effects due to *rapid* changes in $\overline{S}_{ij}$, as in (A.5)-(A.8), and "nonequilibrium" models of the type in (3.137), which are actually equilibrium models that simply reduce the eddy viscosity for large values of $Sk/\epsilon$. Taulbee [102] has developed a nonequilibrium eddy viscosity of the former variety and showed that $\widetilde{C}_\mu$ could be given by an expression of the basic form

$$\widetilde{C}_\mu = \frac{4/15}{C_1 + C_{\epsilon 2} - 2 + (2 - C_{\epsilon 1})P/\epsilon + (k/S\epsilon)DS/Dt} . \tag{A.11}$$

Once again $\widetilde{C}_\mu$ is limited for large values of $Sk/\epsilon$, but in contrast to (A.10) the denominator of (A.11) additionally accounts for first-order nonequilibrium effects via the $(k/S\epsilon)DS/Dt$ term. As noted in Chapter III however, Taulbee ultimately developed a nonlinear eddy viscosity model where, despite the nonequilibrium effects included in (A.11), the anisotropy

is written as a tensorial expansion in terms of the local and instantaneous $\overline{S}_{ij}$ and $\overline{W}_{ij}$. The resulting model is thus unable to account for certain nonequilibrium effects, such as the lag between the applied shear and the anisotropy for periodically-sheared turbulence in Figure 4.20.

Finally, the formulation in (A.5)-(A.8) is closely related to prior algebraic stress models for the anisotropy. In these approaches (e.g. [24, 27, 107]) an explicit algebraic expression for the anisotropy is obtained from the modeled anisotropy transport equation. The resulting closure is typically nonlinear in $\overline{S}_{ij}$ and $\overline{W}_{ij}$, and is inherently linked to the Reynolds stress transport model used to represent the pressure-strain correlation $\Pi_{ij}$ in the modeled equation for the anisotropy. Combination of (A.5)-(A.8) with the present closure in (3.97) and (3.96) results in a type of nonlocal, nonequilibrium algebraic stress model that is tied to the Reynolds stress transport model used to obtain $C_1$ in (A.5) and (A.6). Extension of the current closure for nonlocal and nonequilibrium effects to a full nonlinear algebraic stress framework is left as a direction for future research, as noted in Chapter VI.
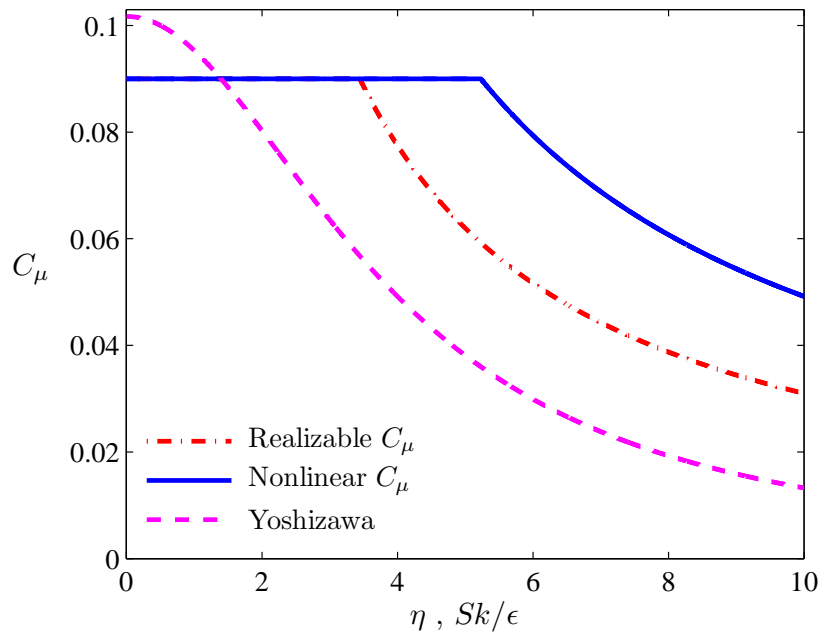
Figure A.1: Eddy viscosity coefficient $C_\mu$ as a function of $\eta$ or $Sk/\epsilon$, as predicted by the nonlinear, nonlocal, nonequilibrium model in (A.5)-(A.8) and the realizable Bradshaw hypothesis in (1.40).
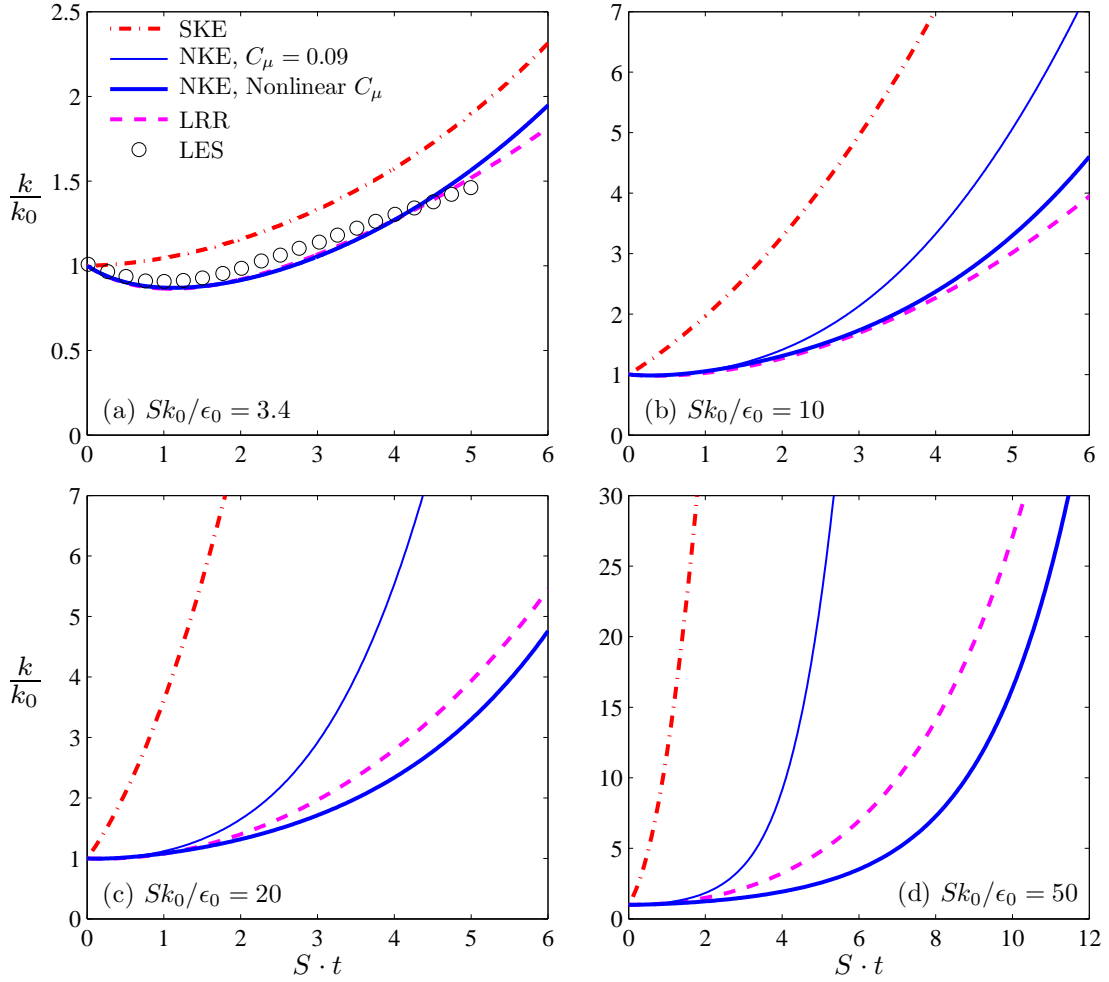
Figure A.2: Kinetic energy evolution for initially-isotropic impulsively sheared turbulence for initial shearing frequencies (a) $Sk_0/\epsilon_0 = 3.4$, (b) $Sk_0/\epsilon_0 = 10$, (c) $Sk_0/\epsilon_0 = 20$, and (d) $Sk_0/\epsilon_0 = 50$. Results from the standard $k$-$\epsilon$ model (SKE), the nonequilibrium $k$-$\epsilon$ model (NKE) with $C_\mu = 0.09$, and the nonequilibrium $k$-$\epsilon$ model with nonlinear $C_\mu$ given by (A.5)-(A.8) are compared with results from the LRR model [51]. LES results from Bardina *et al.* [3] are shown in (a).

# BIBLIOGRAPHY

# BIBLIOGRAPHY

[1] R. Abid. Evaluation of two-equation turbulence models for predicting transitional flows. *Int. J. Eng. Sci.*, 31:831–840, 1993.

[2] Wm. T. Ashurst, A. R. Kerstein, R. M. Kerr, and C. H. Gibson. Alignment of vorticity and scalar gradient with strain rate in simulated Navier-Stokes turbulence. *Phys. Fluids*, 30:2343, 1987.

[3] J. Bardina, J. H. Ferziger, and W. C. Reynolds. Improved turbulence models based on large-eddy simulation of homogeneous, incompressible turbulent flows. *Rep. No. TF-19*, Stanford University, 1983.

[4] G. K. Batchelor. Axial flow in trailing line vortices. *J. Fluid Mech.*, 20:645–658, 1964.

[5] G. K. Batchelor and A. A. Townsend. Decay of turbulence in the final period. *Proc. R. Soc. London Ser. A*, 199:238–255, 1948.

[6] R. B. Bird, R. C. Armstrong, and O. Hassager. *Dynamics of Polymeric Liquids, 2nd Ed.* John Wiley & Sons, 1987.

[7] P. Bradshaw, N. N. Mansour, and U. Piomelli. On local approximations of the pressure-strain term in turbulence models. *Proc. Summer Program, Center for Turbulence Research, Stanford University / NASA Ames Research Center*, pages 159–164, 1987.

[8] K. A. Buch and W. J. A. Dahm. Experimental study of the fine-scale structure of conserved scalar mixing in turbulent shear flows. Part 1. $Sc \gg 1$. *J. Fluid Mech.*, 317:21–71, 1996.

[9] J. M. Burgers. A mathematical model illustrating the theory of turbulence. *Adv. Appl. Mech.*, 1:171–199, 1948.

[10] B. J. Cantwell. Exact solution of a restricted Euler equation for the velocity gradient tensor. *Phys. Fluids A*, 4 (4):782–793, 1992.

[11] J. Chen, C. Meneveau, and J. Katz. Scale interactions of turbulence subjected to a straining-relaxation-destraining cycle. *J. Fluid Mech.*, 562:123–150, 2006.

[12] L. Chevillard and C. Meneveau. Lagrangian dynamics and statistical geometric structure of turbulence. *Phys. Rev. Lett.*, 97:174501, 2006.

[13] K. S. Choi and J. L. Lumley. Return to isotropy of homogeneous turbulence revisited. In *Turbulence and Chaotic Phenomena in Fluids*. North Holland, 1984.

[14] P. Y. Chou. On velocity correlations and the solutions of the equations of turbulent fluctuation. *Qrtly. of Appl. Math.*, 3:38–54, 1945.

[15] B. A. Croker. On the design of hypersonic inward-turning inlets. *Air Force Technical Report*, 2008.

[16] S. C. Crow. Viscoelastic properties of fine-grained incompressible turbulence. *J. Fluid Mech.*, 33:1–20, 1968.

[17] B. J. Daly and F. H. Harlow. Transport equations in turbulence. *Phys. Fluids*, 13:2634–2649, 1970.

[18] T. D. Dreeben and S. B. Pope. Probability density function and reynolds-stress modeling of near-wall turbulent flows. *Phys. Fluids*, 9:154–163, 1997.

[19] E. R. Van Driest. On turbulent flow near a wall. *J. Aerospace Sci.*, 23:1007–1011, 1956.

[20] P. A. Durbin. Near-wall turbulence closure modeling without "damping functions". *Theoret. Comput. Fluid Dyn.*, 3:1–13, 1991.

[21] P. A. Durbin. A Reynolds stress model for near-wall turbulence. *J. Fluid Mech.*, 249:465–498, 1993.

[22] P. A. Durbin and B. A. Pettersson-Reif. *The elliptic relaxation method*, chapter 4, in Closure Strategies for Turbulent and Transitional Flows, pages 127–152. Cambridge Univ. Press, 2002.

[23] T. B. Gatski. Constitutive equations for turbulent flows. *Theoret. Comput. Fluid Dynamics*, 18:345–369, 2004.

[24] T. B. Gatski and C. G. Speziale. On explicit algebraic stress models for complex turbulent flows. *J. Fluid Mech.*, 254:59–78, 1993.

[25] J. D. Gibbon, A. S. Fokas, and C. R. Doering. Dynamically stretched vortices as solutions of the 3D navier-stokes equations. *Physica D*, 132:497–510, 1999.

[26] M. M. Gibson and B. E. Launder. Ground effects on pressure fluctuations in the atmospheric boundary layer. *J. Fluid Mech.*, 86:491–511, 1978.

[27] S. S. Girimaji. Fully explicit and self-consistent algebraic Reynolds stress model. *Theoret. Comput. Fluid Dyn.*, 8:387–402, 1996.

[28] S. S. Girimaji, J. R. O'Neill, and D. Yu. Rapid distortion analysis of homogeneous turbulence subjected to rotating shear. *Phys. Fluids*, 18:085102, 2006.

[29] S. S. Girimaji and S. B. Pope. A diffusion model for velocity gradients in turbulence. *Phys. Fluids A*, 2 (2):242–256, 1990.

[30] I. Hadzic, K. Hanjalic, and D. Laurence. Modeling the response of turbulence subjected to cyclic irrotational strain. *Phys. Fluids*, 13 (6):1739–1747, 2001.

[31] P. E. Hamlington and W. J. A. Dahm. Reynolds stress closure for nonequilibrium effects in turbulent flows. *Phys. Fluids*, 20:115101, 2008.

[32] P. E. Hamlington and W. J. A. Dahm. Frequency response of periodically sheared homogeneous turbulence. *Phys. Fluids*, 21:055107, 2009.

[33] P. E. Hamlington, J. Schumacher, and W. J. A. Dahm. Direct assessment of vorticity alignment with local and nonlocal strain rates in turbulent flows. *Phys. Fluids*, 20:111703, 2008.

[34] P. E. Hamlington, J. Schumacher, and W. J. A. Dahm. Local and nonlocal strain rate fields and vorticity alignment in turbulent flows. *Phys. Rev. E*, 77:026303, 2008.

[35] K. Hanjalic and B. E. Launder. A Reynolds stress model of turbulence and its application to thin shear flows. *J. Fluid Mech.*, 52:609–638, 1972.

[36] J. O. Hinze. *Turbulence (2nd ed.).* McGraw-Hill, 1975.

[37] S. Hoyas and J. Jimenez. Reynolds number effects on the Reynolds-stress budgets in turbulent channels. *Phys. Fluids*, 20:101511, 2008.

[38] Y. N. Huang and H. Y. Ma. Reynolds stress model involving the mean spin tensor. *Phys. Rev. E*, 70:036302, 2004.

[39] K. Iwamoto, Y. Suzuki, and N. Kasagi. Reynolds number effect on wall turbulence: Toward effective feedback control. *Int. J. Heat and Fluid Flow*, 23:678–689, 2002.

[40] J. Jimenez. Kinematic alignment effects in turbulent flows. *Phys. Fluids A*, 4 (4):652, 1992.

[41] J. Jimenez, A. A. Wray, P. G. Saffman, and R. S. Rogallo. The structure of intense vorticity in isotropic turbulence. *J. Fluid Mech.*, 255:65, 1993.

[42] A. V. Johansson. Engineering turbulence models and their development, with emphasis on explicit algebraic Reynolds stress models. *Theories of Turbulence - CISM Courses and Lectures - No. 442*, Springer:253–300, 2002.

[43] W. P. Jones and B. E. Launder. The prediction of laminarization with a two-equation model of turbulence. *Int. J. Heat Mass Transfer*, 15:301–314, 1972.

[44] T. Jongen and T. B. Gatski. A unified analysis of planar homogeneous turbulence using single-point closure equations. *J. Fluid Mech.*, 399:117–150, 1999.

[45] S. Kida. Vortical structure of turbulence. In *Mechanics for a New Millenium.* Kluwer Academic Publishers, Dordrecht, 2001.

[46] J. Kim, P. Moin, and R. Moser. Turbulence statistics in fully developed channel flow at low Reynolds number. *J. Fluid Mech.*, 177:133–166, 1987.

[47] P. S. Klebanoff. Characteristics of turbulence in a boundary layer with zero pressure gradient. *NACA Report 1247*, pages 1135–1153, 1955.

[48] J. Knoell and D. B. Taulbee. Modeling the rapid pressure-strain correlation in homogeneous flows. *Phys. Fluids*, 13:2386, 2001.

[49] A. N. Kolmogorov. The local structure of turbulence in incompressible viscous fluid for very large Reynolds numbers. *Dokl. Akad. Nauk SSSR*, 30:299–303, 1941.

[50] B. E. Launder and S. P. Li. On the elimination of wall-topography parameters from second-moment closure. *Phys. Fluids*, 6 (2):999–1006, 1994.

[51] B. E. Launder, G. Reece, and W. Rodi. Progress in the development of a Reynolds stress turbulence closure. *J. Fluid Mech.*, 68:537–566, 1975.

[52] B. E. Launder and D. B. Spalding. The numerical computation of turbulent flows. *Comp. Meth. App. Mech. Eng.*, 3:269–289, 1974.

[53] B. E. Launder and D. P. Tselepidakis. Directions in second-moment modelling of near-wall turbulence. *AIAA Paper*, AIAA-91-0219, 1991.

[54] B. E. Launder and D. P. Tselepidakis. Application of a new second-moment closure to turbulent channel flow rotating in orthogonal mode. *Int. J. Heat and Fluid Flow*, 15 (1):2–10, 1994.

[55] M. J. Lee and W. C. Reynolds. Numerical experiments on the structure of homogeneous turbulence. *Stanford University Tech. Rep.*, pages TF–24, 1985.

[56] S. Lee, S. K. Lele, and P. Moin. Interaction of isotropic turbulence with shock waves: Effect of shock strength. *J. Fluid Mech.*, 340:225–247, 1997.

[57] J. L. Lumley. Toward a turbulent constitutive relation. *J. Fluid Mech.*, 41:413–434, 1970.

[58] T. S. Lundgren. Strained spiral vortex model for turbulent fine structure. *Phys. Fluids*, 25:2193, 1982.

[59] T. S. Lundgren. A small-scale turbulence model. *Phys. Fluids A*, 5:1472, 1993.

[60] K. Mahesh, S. K. Lele, and P. Moin. The influence of entropy fluctuations on the interaction of turbulence with a shock wave. *J. Fluid Mech.*, 334:353–379, 1997.

[61] R. Manceau, M. Wang, and P. Durbin. Assessment of non-local effect on pressure term in RANS modeling using a DNS database. *Center for Turbulence Research, Proceedings of the Summer Institute*, page 303, 1998.

[62] R. Manceau, M. Wang, and D. Laurence. Inhomogeneity and anisotropy effects on the redistribution term in Reynolds-averaged Navier-Stokes modelling. *J. Fluid Mech.*, 438:307–338, 2001.

[63] N. Mansour, J. Kim, and P. Moin. Reynolds-stress and dissipation rate budgets in a turbulent channel flow. *J. Fluid Mech.*, 194:15–44, 1988.

[64] J. Martin, A. Ooi, M. S. Chong, and J. Soria. Dynamics of the velocity gradient tensor invariants in isotropic turbulence. *Phys. Fluids*, 10:2336, 1998.

[65] G. L. Mellor and H. J. Herring. A survey of mean turbulent field closure models. *AIAA J.*, 11:590–599, 1973.

[66] J. H. Morrison. A compressible navier-stokes solved with two-equation and Reynolds stress turbulence closure models. Technical report, NASA CR-4440, 1992.

[67] R. D. Moser, J. Kim, and N. N. Mansour. Direct numerical simulation of turbulent channel flow up to $Re_\tau = 590$. *Phys. Fluids*, 11:943, 1999.

[68] J. A. Mullin and W. J. A. Dahm. Dual-plane stereo particle image velocimetry measurements of velocity gradient tensor fields in turbulent shear flow. II. Experimental results. *Phys. Fluids*, 18:035102, 2006.

[69] A. Naso and A. Pumir. Scale dependence of the coarse-grained velocity derivative tensor structure in turbulence. *Phys. Rev. E*, 72:056318, 2005.

[70] K. K. Nomura and G. K. Post. The structure and dynamics of vorticity and rate of strain in incompressible homogeneous turbulence. *J. Fluid Mech.*, 377:65–97, 1998.

[71] K. Ohkitani. Kinematics of vorticity: Vorticity-strain conjugation in incompressible fluid flows. *Phys. Rev. E*, 50:5107–5110, 1994.

[72] K. Ohkitani and S. Kishiba. Nonlocal nature of vortex stretching in an inviscid fluid. *Phys. Fluids*, 7 (2):411, 1995.

[73] M. E. Olsen and T. J. Coakley. The lag model, a turbulence model for nonequilibrium flows. *AIAA Paper*, 2001-2564, 2001.

[74] M. E. Olsen, R. P. Lillard, and T. J. Coakley. The lag model applied to high speed flows. *AIAA Paper*, 2005-101, 2005.

[75] L. Le Penven, J. N. Gence, and G. Comte-Bellot. On the approach to isotropy of homogeneous turbulence: Effect of the partition of kinetic energy among the velocity components. In *Frontiers in Fluid Mechanics*. Springer, 1985.

[76] B. A. Pettersson-Reif, T. B. Gatski, and C. L. Rumsey. On the behavior of two-equation models in nonequilibrium homogeneous turbulence. *Phys. Fluids*, 18:065109, 2006.

[77] S. B. Pope. A more general effective-viscosity hypothesis. *J. Fluid Mech.*, 72:331–340, 1975.

[78] S. B. Pope. *Turbulent Flows*. Cambridge University Press., 2000.

[79] B. Protas, K. Schneider, and M. Farge. Geometrical alignment properties in Fourier- and wavelet-filtered statistically stationary two-dimensional turbulence. *Phys. Rev. E*, 66:046307, 2002.

[80] A. J. Revell, S. Benhamadouche, T. Craft, and D. Laurence. A stress-strain lag eddy viscosity model for unsteady mean flow. *Int. J. Heat and Fluid Flow*, 27:821–830, 2006.

[81] J. R. Ristorcelli. A kinematically consistent two-point correlation function. *ICASE Report No. 98-5*, NASA/CR-1998-206909, 1998.

[82] R. S. Rivlin. The relation between the flow of non-Newtonian fluids and turbulent Newtonian fluids. *Quart. Appl. Math.*, 15:212–214, 1957.

[83] W. Rodi. A new algebraic relation for calculating the Reynolds stresses. *Z. Angew Math. Mech.*, 56:219–221, 1976.

[84] W. Rodi and N. N. Mansour. Low Reynolds number $k$-$\epsilon$ modelling with the aid of direct numerical simulation data. *J. Fluid Mech.*, 250:509–529, 1993.

[85] J. Rotta. Statistiche Theorie nichthomogener Turbulenz. 2. Mitteilung. *Z. fur Phys.*, 131:51–77, 1951.

[86] J. Rotta. Statistische Theorie nichthomogener Turbulenz. *Z. fur Phys.*, 129:547–572, 1951.

[87] J. Rotta. Recent attempts to develop a generally applicable calculation method for turbulent shear flow layers. *AGARD-CP-93*, North Atlantic Treaty Organization, 1972.

[88] R. Rubinstein and J. M. Barton. Nonlinear Reynolds stress models and the renormalization group. *Phys. Fluids A*, 2 (8):1472–1476, 1990.

[89] S. Sarkar and C. G. Speziale. A simple nonlinear model for the return to isotropy in turbulence. *Phys. Fluids A*, 2 (1):84–93, 1990.

[90] J. Schumacher. Sub-Kolmogorov-scale fluctuations in fluid turbulence. *Europhys. Lett.*, 5:54001, 2007.

[91] J. Schumacher, K. R. Sreenivasan, and V. Yakhot. Asymptotic exponents from low-Reynolds-number flows. *New J. Phys.*, 9:89, 2007.

[92] Z. S. She, E. Jackson, and S. A. Orszag. Structure and dynamics of homogeneous turbulence: models and simulations. *Proc. R. Soc. Lond. A*, 434:101–124, 1991.

[93] T. H. Shih, J. Zhu, and J. L. Lumley. A new Reynolds stress algebraic equation model. *Comput. Methods. Appl. Mech. Engrg.*, 125:287–302, 1995.

[94] K. Sinha, K. Mahesh, and G. V. Candler. Modeling shock unsteadiness in shock/turbulence interaction. *Phys. Fluids*, 15 (8):2290–2297, 2003.

[95] C. G. Speziale. On nonlinear $k$-$l$ and $k$-$\epsilon$ models of turbulence. *J. Fluid Mech.*, 178:459–475, 1987.

[96] C. G. Speziale. Analytical methods for the development of Reynolds-stress closures in turbulence. *Annu. Rev. Fluid Mech.*, 23:107–157, 1991.

[97] C. G. Speziale, R. Abid, and C. Anderson. A critical evaluation of two-equation models for near wall turbulence. Technical report, NASA CR-182068, ICASE Report No. 90-46, 1990.

[98] C. G. Speziale, S. Sarkar, and T. B. Gatski. Modeling the pressure strain correlation of turbulence: an invariant dynamical systems approach. *J. Fluid Mech.*, 227:245–272, 1991.

[99] C. G. Speziale and R. M. C. So. *The Handbook of Fluid Dynamics*, chapter 14, Turbulence Modeling and Simulation, pages 14.1–14.111. Springer, 1998.

[100] C. G. Speziale and X. H. Xu. Towards the development of second-order closure models for non-equilibrium turbulent flows. *Intl. J. Heat Fluid Flow*, 17:238–244, 1996.

[101] L. K. Su and W. J. A. Dahm. Scalar imaging velocimetry measurements of the velocity gradient tensor field in turbulent flows. II. Experimental results. *Phys. Fluids*, 8:1883, 1996.

[102] D. B. Taulbee. An improved algebraic Reynolds stress model and corresponding nonlinear stress model. *Phys. Fluids A*, 4 (11):2555–2561, 1992.

[103] A. Tsinober. *An Informal Introduction to Turbulence.* Kluwer Academic Publishers, Dordrecht, 2001.

[104] A. Tsinober, E. Kit, and T. Dracos. Experimental investigation of the field of velocity gradients in turbulent flows. *J. Fluid Mech.*, 242:169, 1992.

[105] P. Viellefosse. Internal motion of a small element of fluid in an inviscid flow. *Physica A*, 125:150–162, 1984.

[106] T. von Kármán and L. Haworth. On the statistical theory of isotropic turbulence. *Proc. R. Soc. London Ser. A*, 164:192–215, 1938.

[107] S. Wallin and A. V. Johansson. An explicit algebraic Reynolds stress model for incompressible and compressible turbulent flows. *J. Fluid Mech.*, 403:89–132, 2000.

[108] D. C. Wilcox. *Turbulence Modeling for CFD.* DCW Industries, 2000.

[109] I. Wygnanski and H. Fiedler. Some measurements in the self-preserving jet. *J. Fluid Mech.*, 38:577–612, 1969.

[110] I. Wygnanski and H. E. Fiedler. The two-dimensional mixing region. *J. Fluid Mech.*, 41:327–361, 1970.

[111] V. Yakhot, S. A. Orszag, S. Thangam, T. B. Gatski, and C. G. Speziale. Development of turbulence models for shear flows by a double expansion technique. *Phys. Fluids A*, 4 (7):1510–1520, 1992.

[112] A. Yoshizawa. Statistical analyis of the deviation of the Reynolds stress from its eddy-viscosity representation. *Phys. Fluids*, 27 (6):1377–1387, 1984.

[113] A. Yoshizawa and S. Nisizima. A nonequilibrium representation of the turbulent viscosity based on a two-scale turbulence theory. *Phys. Fluids A*, 5 (12):3302–3304, 1993.

[114] A. Yoshizawa, S. Nisizima, Y. Shimomura, H. Kobayashi, Y. Matsuo, H. Abe, and H. Fujiwara. A new methodology for Reynolds-averaged modeling based on the amalgamation of heuristic-modeling and turbulence-theory methods. *Phys. Fluids*, 18:035109, 2006.

[115] D. Yu and S. S. Girimaji. Direct numerical simulations of homogeneous turbulence subject to periodic shear. *J. Fluid Mech.*, 566:117–151, 2006.

[116] B. W. Zeff, D. D. Lanterman, R. McAllister, E. J. Kostellich R. Roy, and D. P. Lathrop. Measuring intense rotation and dissipation in turbulent flows. *Nature*, 421:146–149, 2003.